Universidad Autónoma de Madrid

Coupling quantum emitters to nanophotonic structures

Carlos González Ballestero

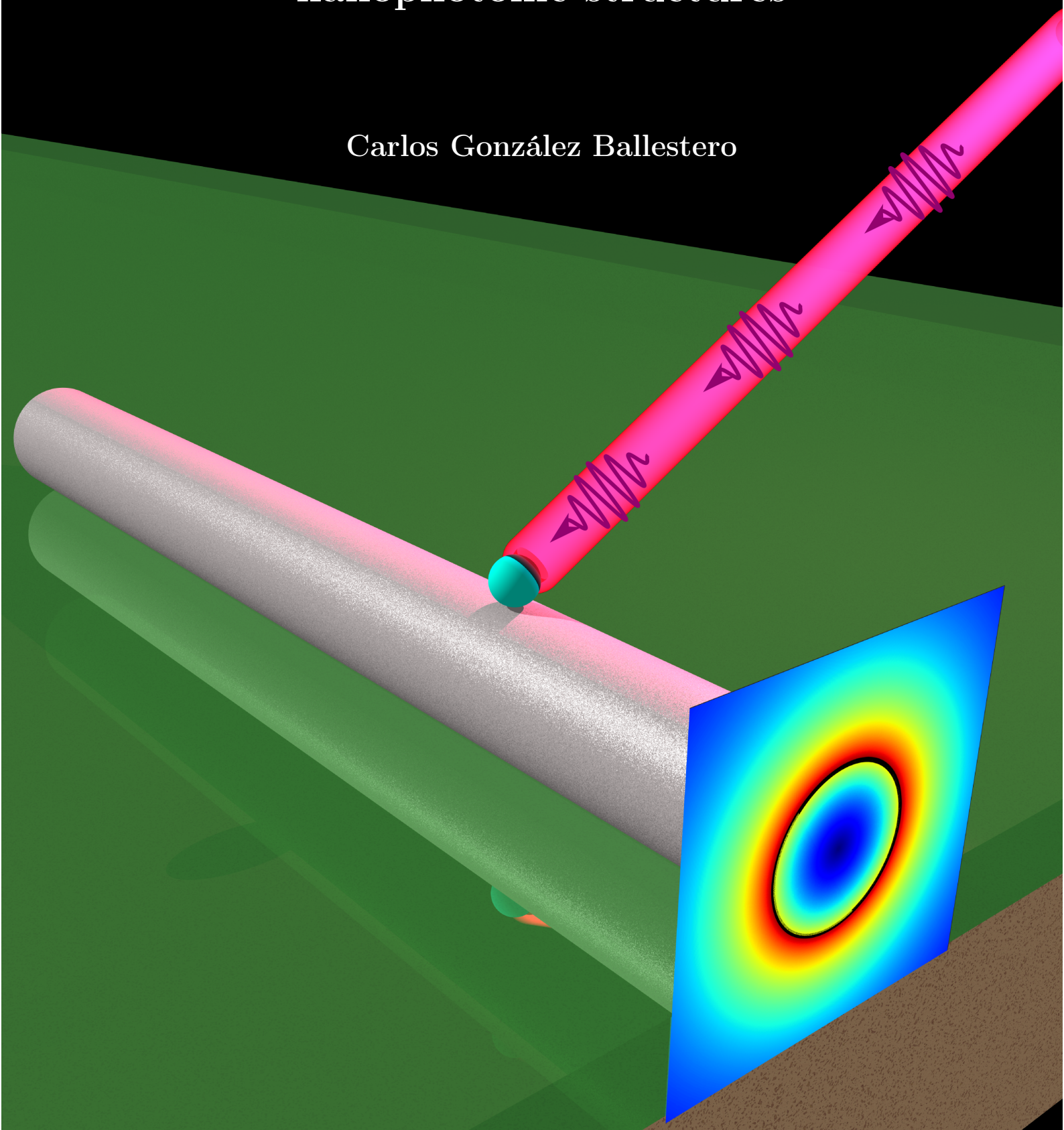

Universidad Autónoma de Madrid

Departamento de Física Teórica de la Materia Condensada

Condensed Matter Physics Center (IFIMAC)

Tesis doctoral dirigida por:

Francisco José García Vidal
Esteban Moreno Soriano

Madrid, November 2016

We are all agreed that your theory is crazy. The question that divides us is whether it is crazy enough to have a chance of being correct.

N. Bohr

Agradecimientos

En primer lugar, me gustaría agradecer a mis dos directores de tesis, Esteban y FJ, por enseñarme la combinación de trabajo duro e intuición en que se basa la investigación científica, así como a ser riguroso y honesto con los resultados obtenidos. Agradezco que se hayan esforzado en orientarme en este mundo extraño, sin dejar de animarme a seguir mis propias ideas e intuiciones. Quiero mencionar también el impacto que ambos tuvieron ya durante mis estudios de licenciatura, donde tuve la fortuna de asistir a sus clases. No deja de ser curioso para mí el haber acabado haciendo esta tesis bajo la supervisión de Esteban, que me habló por primera vez de un Hamiltoniano, y de FJ, que me habló por primera vez del formalismo de segunda cuantización. Hace por tanto mucho más de cuatro años que ambos participan en mi formación, un esfuerzo conjunto culminado en una tesis que no habría sido posible sin su ayuda.

Quiero también agradecer especialmente a todos los investigadores que han colaborado en diversas partes de esta tesis. Primero, a todo el equipo experimental que formó parte de nuestro trabajo con V-Grooves: los grupos del prof. Sergey Bozhevolnyi en la University of Southern Denmark y del prof. Romain Quidant en el ICFO, especialmente Esteban Bermúdez por su esfuerzo en comprender nuestra jerga teórica. También agradezco al Dr. Alejandro González-Tudela no sólo por toda su contribución en los trabajos de acoplo quiral, sino además por su amistad y por todo lo aprendido de él. Finalmente, es difícil sobreestimar la ayuda del Dr. Johannes Feist que, aparte de tener un papel fundamental en nuestros trabajos de strong coupling, ha sido un referente en estos últimos años de tesis. De él he podido aprender mucha física, métodos diferentes de aproximarme a los problemas y un montón de ipython (un área en la que ha tenido una especial paciencia, que le agradezco infinitamente).

I am also grateful to profs. Niek van Hulst, Arno Rauschenbeutel, Carlos Tejedor, Oriol Romero-Isart, and David Zueco for agreeing to take part in the defense of this thesis as jury members. Moreover, I thank Antonio Fernández Domínguez and Luis Martín Moreno for their availability as reserve members of this jury.

Haciendo *zoom out* al siguiente nivel, agradezco a todos los compañeros que han pasado por el grupo durante estos años: Juan Antonio, Javi Cuerda, Alex Delga, Jorge, Ricardo, Rocío, Ning, Felix y Pu. Gracias muy especiales a Antonio y sobre todo a Diego por sus valiosísimos consejos sobre comsol y por estar siempre disponible. También ha sido importante la relación con la gente de la universidad de Zaragoza, Luis y Edu, por interesantes discusiones sobre física y por los buenos momentos vividos en conferencias. Asimismo, quiero reconocer la ayuda de otras personas del departamento con los que me he sentido muy a gusto durante estos años: Milica, Guilherme, Elena, Pablo "Colin", Fabrice, Stefan "CentOS" Bilan, y Laura.

I have very good memories from my period at Cambridge, both on the academic and on the personal side, for which I would like to thank Florian Schröder and Alex Chin. Aparte del empujón que dió a mi motivación científica, Cambridge supuso para mí el darme cuenta de la buena formación que recibimos en este departamento, y de lo afortunado que soy por haber compartido estos años con otros estudiantes de doctorado, buenos colegas y excelentes investigadores. A ellos quiero agradecerles que hayan ayudado a crear un ambiente de trabajo agradable y estimulante, que hace de venir a la universidad un verdadero placer: Rubén S (S is for Sport), Victor "chanclas", María, Raúl, Dieguito, Sergio, Lucía, Camilo y David.

Es importante para mí agradecer también a todos mis compañeros de despacho, que han sido muchos a lo largo de esta tesis. En primer lugar, agradezco a los compañeros de mis primeros años, Delia, Ruth y Carlos por las conversaciones con el café mañanero. No me olvido del breve paso de los espectaculares Javi "Abe Lincoln", Jose "micelio", Edu y Raj. Finalmente, del equipo 301, Álvaro "Barca", el inolvidable RuiQi y, como mención especial, Javier Galego: no sólo por compartir mi sentido del humor hasta niveles alarmantes, sino por la combinación de constante alegría e inacabable vocación científica que hacen de él tan buen investigador. Aprovecho también aquí para agradecer a mi *lunch team* original: Blanquita, Antonio a.k.a. "the coolest" y mi bro Carlos Sánchez.

Sería injusto no dedicar un agradecimiento especial a tres amigos particularmente importantes. En primer lugar, mi hermana mayor académica Paloma, por su inestimable ayuda en más cosas de las que puedo enumerar, por su amistad, y por ser una referencia a la que aspirar tanto a nivel académico como a nivel personal. Del mismo modo, Mr. Javi del Pino, por compartir momentos buenos, malos y todo el espectro intermedio, sobre todo durante esos viajes en coche liberando presión. En él he encontrado un gran amigo y un sobresaliente investigador siempre dispuesto a compartir su extenso conocimiento teórico y bibliográfico. Finalmente, my bro Carlos Sánchez una vez más, cuyo camino intersecó el mío hace ya más de diez años en el primer curso de física, y cuyas cualidades

como amigo son sólo igualadas por su talento científico. A partir de ahora tendremos que seguir resonando a distancias intercontinentales.

A nivel más general, quiero agradecer a toda la gente que ha contribuído a esta tesis ofreciéndome su amistad durante estos años: los biólogos Hernán, Guille, Alba, María, Filip, Predes y Henna; the DESY people for the invaluable interdisciplinary feedback and undescribable experiences lived together, Ana, Felipe, Edyta, Mirek, Alina, Krzysiek, Curly, Leonardinho Estrella, and the british gentlemen Mr. Chaushev and Mr. Bożek; la gente de Alcalá, Mario, Alvarito, Juli, Sara, Diego y Kurt; el general Edu Grant y Nereida y, naturalmente el señor Francesco Mazza, por ese año de máster en que se convirtió en uno de mis mejores amigos.

Por último, pero no menos importante, agradezco a mi toda mi familia, especialmente a mis padres y mi hermana, por apoyarme para hacer lo que más me gusta e intentar entender el extraño mundo de la investigación. Y por supuesto, agradezco a Federica por apreciar mi lado utópico y, en realidad, todos mis otros lados; por animarme siempre a seguir soñando incluso en los momentos más oscuros, por creer intensamente en lo imposible hasta hacerlo realidad y, en resumen, por dar sentido a toda esta locura.

Madrid, 11 de noviembre de 2016

Contents

Abstract

English

This thesis is devoted to the study of different problems at the increasingly diffuse boundary between quantum optics and nanophotonics. The ability to tailor light-matter interaction at the quantum level lies at the heart of many key challenges in today physics, such as the realization of a quantum computer. Such precise control could in principle be achieved via photonic structures engineered at the nanoscale. Thus, in this thesis we address a variety of problems in quantum nanophotonics by means of different systems of quantum emitters coupled to photonic nanostructures.

First, we study the dissipative entanglement generation between two qubits coupled to a waveguide. By means of a full Hamiltonian approach, we illustrate the intrinsic non-Markovian behavior arising in some configurations, which is impossible to predict with usual formalisms in cavity quantum optics. Since such entanglement generation protocol is very sensitive to variations of the system parameters, we continue by proposing an alternative scheme, in which the generated entanglement is much more robust due to the chiral character of the qubit-photon couplings.

The second part of this work is focused on exploiting the photonic degrees of freedom in waveguide systems. We demonstrate how qubit-qubit entanglement can be generated by means of single-photon inputs, and how a second incoming photon allows for a temporal modulation of the entanglement profile. We also propose a scheme for entanglement detection via scattering of single photons. Finally, we introduce a four-port device in which chiral emitter-photon couplings allow for the realization of nonreciprocal few-photon devices based on quantum interference.

The third part of this work focuses on the study of the collective strong coupling regime, in which the system can only be described in terms of hybrid light-matter states called polaritons. We demonstrate how, when an ensemble of N quantum emitters interacts with a discrete set of electromagnetic modes, pure matter (dark) states can inherit the

spatial extension of the photonic modes, despite being uncoupled to them by definition. We then illustrate how the delocalized eigenstates of the strongly coupled system can be employed to largely enhance the exciton transport properties across the ensemble of emitters, and how this enhancement can be spatially tailored at the subwavelength scale by employing localized plasmonic resonances as photonic modes.

Finally, we study an experimentally feasible platform for efficient light-matter interaction, namely a plasmonic waveguide coupled to a nitrogen-vacancy centre in diamond. We present the theoretical study carried out in parallel with the experiment by our collaborators. The efficient coupling to guided plasmonic modes is demonstrated by both studies, with a figure of merit outperforming previous realizations in plasmonic structures.

Castellano

Esta tesis está dedicada al estudio de diferentes problemas en la cada vez más difusa frontera entre la nanofotónica y la óptica cuántica. La capacidad de modificar la interacción entre luz y materia a escala cuántica es esencial para muchos de los desafíos clave de la fisica actual, como por ejemplo la realización de un ordenador cuántico. Dicho control tan preciso podría en principio conseguirse a través de estructuras fotónicas diseñadas a escala nanométrica. Por esa razon, en esta tesis se afrontan una serie de problemas en nanofotónica cuántica utilizando diferentes sistemas de emisores cuánticos acoplados a nanoestructuras fotónicas.

Primero, estudiamos la generación disipativa de entrelazamiento entre dos bits cuánticos (qubits) acoplados a una guía de ondas. Utilizando un Hamiltoniano completo del sistema, mostramos el comportamiento no Markoviano que surge para ciertas configuraciones, y que resulta imposible de predecir por los formalismos habituales empleados en óptica cuántica en cavidades. Dado que este protocolo de generación de entrelazamiento es muy sensible a variaciones en los parámetros del sistema, proponemos a continuación un método alternativo, en el que el entrelazamiento resultante es mucho más robusto con respecto a variaciones de los parámetros del sistema gracias al carácter quiral del acoplo entre qubit y fotones.

La segunda parte de este trabajo se centra en aprovechar los grados de libertad fotónicos en sistemas de guia de onda. En este estudio demostramos cómo generar entrelazamiento entre dos qubits a través de paquetes de un fotón, y cómo un segundo fotón permite modular temporalmente el perfil de entrelazamiento creado. Asimismo, proponemos un método para detectar dicho entrelazamiento a través de paquetes de un fotón. Finalmente, introducimos un dispositivo de cuatro puertos en el que el acoplo quiral entre emisor y fotones permite diseñar dispositivos fotónicos no recíprocos basados en interferencia cuántica.

La tercera parte de este trabajo se centra en el estudio del régimen de acoplo fuerte colectivo, en el que un sistema sólo puede ser descrito en términos de estados híbridos de luz y materia llamados polaritones. Demostramos cómo, cuando un conjunto de emisores cuánticos interacciona con un conjunto discreto de modos electromagnéticos, estados puros de materia (estados oscuros) pueden adquirir la extension espacial de los modos fotónicos, a pesar de que por definicion no se acoplan a ellos. Después, ilustramos cómo los autoestados deslocalizados de dicho sistema fuertemente acoplado pueden ser usados para incrementar significativamente las propiedades de transporte de excitones a lo largo del conjunto de emisores, y cómo dicho incremento puede ser estructurado espa-

cialmente a escalas menores que la longitud de onda, a traves de resonancias plasmónicas localizadas.

Finalmente, estudiamos una plataforma experimentalmente realizable donde conseguir una interacción luz-materia eficiente, en particular una guía de onda plasmónica acoplada a un centro vacante-nitrógeno en diamante. Presentamos un estudio teórico llevado a cabo en paralelo al experimento realizado por nuestros colaboradores. El acoplo eficiente a modos plasmónicos guiados es demostrado por ambos estudios, con un factor de calidad superior al obtenido por previos estudios en estructuras plasmónicas.

List of acronyms

This is a list of the acronyms used in the text (in alphabetical order).

1D	One dimension
2D	Two dimensions
3D	Three dimensions
3LS	Three-level system
CPP	Channel plasmon polariton
DRE	Decay rate enhancement
EM	Electromagnetic
FEM	Finite Element Method
LSP	Localized surface plasmon
ND	Nanodiamond
NP	Nanoparticle
NS	Nanosphere
NV	Nitrogen-vacancy or Nitrogen-vacancy centre
NW	Nanowire
PW	Plasmonic waveguide
QE	Quantum emitter
QED	Quantum Electrodynamics
SC	Strong coupling
TC	Tavis-Cummings
VG	V-Groove

1 | General Introduction

1.1. Light and matter interaction in modern physics

The interaction of light with the charged particles conforming matter is responsible for most of the observable phenomena at the human energy scales. However, a complete understanding of how light and matter interact at a fundamental level was not attained until the twentieth century. The first relevant advances towards this profound comprehension correspond to the birth of quantum mechanics, where fundamental problems such as the structure of atomic spectra were solved based on a quantized picture only of matter [1]. Other relevant questions, such as the process behind atomic spontaneous decay, remained elusive until Paul Dirac introduced a full quantum description of both light and matter, laying the foundations of modern quantum electrodynamics (QED) at the atomic level [2]. This work would be generalized later on to any energy scale in what is nowadays considered one of the most accurate theories ever developed [3].

With a fundamental understanding of the basic phenomena at hand, a long way remained ahead in terms of exploiting and applying them. The decisive steps toward this goal were taken by a set of seemingly unrelated works in the decades of 1940-1960, which set the basis for many disciplines including quantum optics and nanophotonics. First, in the early works of Purcell [4], the spontaneous decay rate of quantum emitters, such as atoms and molecules, was suggested not to be an intrinsic property of such systems. The experimental confirmation of this effect would be achieved much later by Drexhage, who

observed a modification of the molecular emission lifetime in the vicinities of a mirror [5]. Additionally, theoretical works on simple models elaborated by Dicke [6] showed that collective ensembles of emitters may interact with light in a different way than as individual entities. Both these works demonstrated the possibility of tailoring the light-matter interaction at the micro and nanoscale. However, the flourishing of nanoscale optics had to wait until the first realization of the laser [7], one of the most relevant inventions of the last century, both for fundamental research and its impact in everyday applications.

The possibility of an efficient control of light and matter at the nanoscale was made a reality by the above discoveries, giving birth, among others, to the two disciplines this thesis will focus on. First, the study of light at the nanoscale, or nanophotonics, which along the last decades has been responsible for outstanding achievements such as e.g. plasmonic sensing [8], superresolution microscopy [9], or the discovery of metamaterials [10] and photonic crystals [11]. Second, the quantum theory of light, or quantum optics, which has provided a very important fundamental insight into the nature of light with, for instance, the resolution of the EPR paradox [12], or the experimental demonstration of the quantum nature of photons [13], as well as exciting applications such as ultrasensitive detectors based on squeezed light [14]. In the last decades, these traditionally distinct fields have partially overlapped in what we refer to as quantum nanophotonics. Due to the promising applications of full quantum circuits such as quantum computation [15], as well as their increasing miniaturization requirements for a future on-chip implementation, it has become necessary to interface nanometric photonic structures with quantum emitters. From the theoretical point of view, it is vital to understand the ever increasing number of processes arising in such nanostructures, as well as devising optimal strategies towards a future implementation of many quantum technologies.

The work I have developed in this thesis focuses on several open problems in quantum nanophotonics, from entanglement detection to excitonic transport. In this introductory chapter I will briefly summarize the relevant aspects of quantum nanophotonics and define some of the key concepts employed along the thesis. First, in section 1.2, I will comment on the different regimes of interaction between light and matter focusing on the most relevant for this thesis, namely the weak coupling and the strong coupling regimes. After, in section 1.3, I will give some details on the most two common structures employed for light-matter interaction, namely cavities and waveguides, as well as a brief comparative. Finally, in section 1.4, I will offer a brief outline of the thesis in the context of some relevant research areas in modern quantum nanophotonics.

1.2. Regimes of interaction between light and matter. Purcell effect and Strong Coupling.

A full quantum formalism describing the interaction between light and matter requires the quantization of the classical electromagnetic (EM) field in the presence of charged particles [16]. As detailed in appendix C, the quantum Hamiltonian resulting from this so-called canonical quantization procedure takes the form of a set of quantum harmonic oscillators representing the EM modes, interacting with the ensemble of particles described by fermionic energy levels [2]. Despite the apparent simplicity of the individual components, the combined system represents a formidable problem from the theoretical point of view. Indeed, the few situations in which an analytical solution exists, such as the Jaynes-Cummings [17] or Tavis-Cummings models [18], or some regimes of the Dicke Hamiltonian [6], have arisen as the reference models in the literature. Even in these extensively studied systems, new physics is being discovered nowadays. Despite the particular difficulties of each situation, some general statements can be made about the dynamics of light interacting with matter, especially regarding the different regimes of interaction.

Most of the light-matter interactions in nature occur within the so-called *weak coupling* regime, in which the light-matter coupling is very small and can be treated perturbatively [19]. This is the case, for instance, of atomic and molecular electronic transitions interacting with free-space EM modes, where the coupling rates g are usually much smaller than the transition frequencies ω_0. From the theoretical point of view, the analysis of systems in this regime is in principle simpler than in others, since the well-developed tools of weakly-coupled open quantum systems are applicable [20]. The usual route is to consider the ensemble of particles, or quantum emitters (QEs), as the relevant quantum system, which is weakly coupled to a dissipative environment representing the surrounding EM modes. If applied to, for instance, an excited QE radiating in free space, this model predicts an exponential decay and correctly reproduces the vacuum radiative decay rate γ_0 [21]. In general, any system in which the EM modes can be treated in such way is said to be in the weak coupling regime. Naturally, this applies to many setups in quantum nanophotonics, where QEs are placed close to nanostructures. Because such structures are formed by charged particles at the microscopic level, they always modify the EM density of states in a certain way [22]. In the language of open quantum systems,

this implies a modification of the free-space spectral density, which in turn results in a different interaction rate for light and matter. In the example of an excited QE in the vicinities of a nanostructure, this results in an exponential decay at a *modified* rate, γ. The enhancement or suppression of the intrinsic decay rates of QEs is known as Purcell effect, and is quantified via the Purcell factor [4],

$$P_F = \frac{\gamma}{\gamma_0}, \tag{1.1}$$

a key figure of merit in quantum nanophotonics.

Generally, in the weak coupling regime, any decay or field-mediated interaction has a similar structure as in free space, but displays nanostructure-dependent rates. Interestingly, it is possible to modify such rates independently, for instance favouring the interaction between an ensemble of QEs over their decay by photon emission [23]. Another possibility widely employed in nanophotonics consists on modifying the balance between the different decay channels of QEs, for example in waveguide nanostructures. In such case, a given QE can usually decay in various ways, i.e., we can write the total decay rate as $\gamma = \gamma_m + \Delta\gamma$. Here, γ_m represents the decay into "desired channel(s)", in this example the guided photonic modes, whereas $\Delta\gamma$ accounts for other relaxation processes such as decay to other nanostructure modes, free space radiation, or nonradiative loss [22]. In order to quantify the coupling efficiency of a QE to the preferred emission channel, a second crucial figure of merit is defined, namely the beta factor,

$$\beta = \frac{\gamma_m}{\gamma} = \frac{\gamma_m}{\gamma_m + \Delta\gamma}. \tag{1.2}$$

Note that analogous quantities can be defined in any system, and modified on demand by coupling to the adequate nanostructures.

The theoretical models described above represent no more than low-order perturbation theory for weak system-environment coupling. Thus, when the light-matter interaction increases above a certain level, they start to be inaccurate. If such interaction is still not very large, the light-matter dynamics can still be reproduced by means of perturbation theory, this time to higher order. This is the so-called intermediate coupling regime of light-matter interaction where, for instance, the decay of a QE deviates slightly from an exponential law, but still following a monotonically decreasing profile. Such a regime has been demonstrated experimentally [24] and can have an impact in some phenomena such as source emission control in plasmonic nanoparticles [25].

By definition, perturbative approaches break down for sufficiently large light-matter interaction rate, roughly when such rate overcomes the intrinsic losses of both light and

matter components [26]. At such point, systems are said to enter into the strong coupling regime, where the EM modes cannot be considered anymore a thermal, uncorrelated environment for matter, and an accurate description of the system can only be attained by means of dressed light-matter states. In this regime, the system is characterized by coherent or reversible dynamics, as opposed to the weak coupling case. In the case of an initially excited QE, the population does not show an exponential decay anymore, but in turn is coherently exchanged between field and QE, producing a characteristic oscillatory behavior. These so-called Rabi oscillations have a natural frequency Ω_R, proportional to the total light-matter coupling rate. The strong coupling regime is usually achieved by confining the EM modes in space in order to enhance their interaction rate with QEs, as we will see in the next section. Additionally, it is well known that the experimental requirements for achieving such regime are significantly reduced when light interacts with a large ensemble of N QEs, since the Rabi frequency is known to grow as $\sqrt{N}$ [27]. This is the reason why the first experimental demonstration of strong coupling was attained in atomic ensembles [28].

Like any population exchange between two levels in quantum mechanics, the Rabi oscillations indicate that the two entities exchanging probability, in this case light and matter, are not the eigenstates of the full system [29]. The natural states in a strongly coupled system are thus hybrid light-matter states called polaritons [30]. It is important to emphasize that this notation is often employed in a more general sense for any light-matter hybrid such as, for instance, surface plasmon polaritons, which combine light with a collective electronic vibration in metals [31]. Not all of the polaritons arise from strong coupling phenomena, and indeed a specific notation for the eigenstates identified in the Rabi splitting would be exciton-polaritons. However, due to their increasing popularity, many people refer to them simply as polaritons, and employ different names for other polaritonic excitations, e.g. plasmons. Unless stated otherwise, we will follow such custom along this thesis. Since polaritons display properties of both their constituents, they represent an invaluable resource for a light-matter interaction *à la carte*. One of the most active research areas associated to the strong coupling regime consists in creating and tailoring photon-photon interactions, giving rise to surprising phenomena such as Bose-Einstein condensates of light [32, 33] or polariton superfluidity [34].

In the last years, a significant research effort has been devoted to study new regimes beyond the well-understood strong coupling. Indeed, even in the strong coupling regime, some approximations are assumed that can break down for large enough light-matter interaction, e.g. the Rotating Wave Approximation (see appendix C). Therefore, when such interaction is increased above a critical value (the usual convention is 10% of the

typical transition energies of the QEs), new physics emerge as the Hamiltonian does not conserve the number of excitations anymore [35]. First observed in 2009 [36], this *ultra-strong* coupling regime displays a striking characteristic phenomenology, such as ground states with finite photon occupation [37] or saturation of decay rate enhancements [38]. As a consequence, the research on this regime is steadily growing, with demonstrations in different experimental systems [39–41] and application prospects in quantum computation [42]. Additionally, very recent works carry out interesting theoretical explorations beyond the ultra-strong coupling regime, where exotic physics has been uncovered in what has been denominated deep strong coupling regime [43]. Specifically, simple models predict a surprising decoupling between light and matter, in which QEs tend to repel the light modes in their close vicinities [44]. Despite this intriguing results, such regime is yet far from experimental reach, as it requires a light-matter coupling larger than the emission frequency of the QEs.

In this thesis we will focus on two of the above situations, namely the weak and the strong coupling regimes. On the one hand, the intermediate regime is not very distinct in terms of phenomenology, and is referred to only in very specific studies. On the other hand, both the ultra- and deep strong coupling regimes are not yet available in many systems at optical wavelengths. Therefore, the two situations we consider span in practice the vast majority of the present research in quantum nanophotonics. In general, the key requirement to exploit the advantages brought about by any of these regimes is a careful system engineering. Specifically, it is of vital importance to devise nanostructures whose EM modes satisfy the required conditions for an enhanced light-matter interaction, as well as to carefully select the most adequate QEs for the desired goal and integrate them in the adequate configuration.

1.3. Coupling light and matter. Optical cavities and waveguides

It is not easy to give a straight answer as to what is required to properly interface light and quantum emitters. Depending on the desired functionality, the requirements may vary enormously. For instance, for storing quantum information, the target emitter should have a very slow interaction rate, and hence one must devise a structure in which the density of states is strongly suppressed, e.g. the bandgap of a photonic crystal (see below). On the other hand, other applications such as single-photon sources can benefit

from a high emission rate, thus requiring large field confinements such as that offered by plasmonic structures. In general, the most used setups for engineering the EM density of states are cavities and waveguides.

1.3.1. Optical cavities

The simplest and more widespread optical element which allows for this engineering is an optical cavity as the one depicted in Fig. 1.1a. All the different available cavity systems (see Fig 1.1) rely on the same principle, namely the confinement of the EM field. It is possible to intuitively grasp the basic operation of these devices by considering a simple example, namely a QE placed between two parallel mirrors. In this elementary cavity, when the mirrors are placed very close to each other, the energy difference between the allowed EM modes (corresponding to wavelengths commensurate with twice the mirror-mirror separation) is very large, and such modes become discrete. As opposed to light in vacuum, which rapidly propagates away from QEs, these standing waves bounce back and forth between the mirrors for a long time, eventually being lost due to leakage out of the cavity. Consequently, the interaction probability with the QE is largely enhanced since, the time spent by the photons in the vicinities of the emitter is much larger than in free space. This argument can also be expressed formally in a quantum model of light-matter interaction. Indeed, the QE-light coupling g is proportional to the electric field intensity (see Appendix C)

$$g(\omega) \propto \mathbf{E}(\omega) = \sqrt{\frac{\hbar\omega}{2\varepsilon_0 V}}\mathbf{f}(\mathbf{r}), \tag{1.3}$$

where $\mathbf{f}(\mathbf{r})$ is an arbitrary normalized field profile, and the spatial extension of the mode is described by the *mode volume* V [19],

$$V = \frac{1}{\varepsilon_0 |\mathbf{E}_0|^2} \int dV U_{em}(\mathbf{r}), \tag{1.4}$$

$\mathbf{E}_0$ and U_{em} describing, respectively, the electric field amplitude and the electromagnetic energy density. Hence, by confining a photonic mode in a very small volume, such as that between two mirrors, the field intensity can be largely increased. The tradeoff between mode confinement and EM field intensity lies at the heart of quantum nanophotonics, and will be widely employed along this thesis.

The first cavity setups were implemented in the same way we have discussed above, namely by employing two mirrors to confine microwave photons. These setups were employed in the first measurement of cavity-induced Purcell enhancement on Rydberg

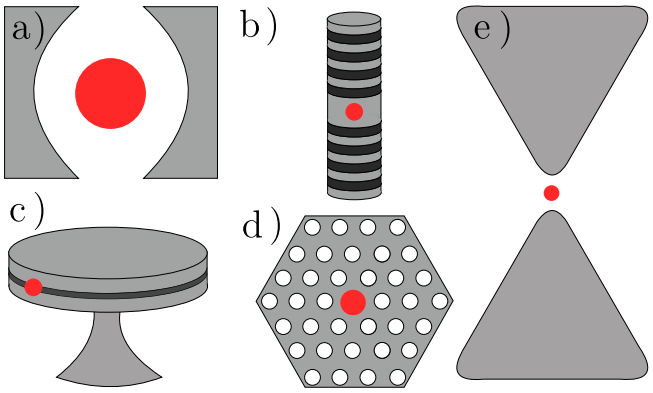

Cavity	λ (nm)	E (eV)	P_F	β	C	Ω_R (meV)
a	852	1.45	114	0.72	29	$3{\cdot}10^{-3}$
b	937	1.32	36	0.24	0.48	0.16
c	744	1.66	125	0.49	4.15	0.81
d	1182	1.32	441	0.24	0.45	0.17
e	660	1.9	~1000	0.23	0.4	125

Figure 1.1: Scheme of some usual cavity setups (QE shown in red) with the typical figures of merit: a) trapped atom. b) Micropillar cavity. c) Microtoroidal resonator. d) Photonic crystal slab cavity. e) Bowtie plasmonic cavity. The values of the table, extracted from Refs.[45, 46], show the emitter wavelength and energy, and Purcell and beta factors as defined in the main text. Additionally, we show an alternative figure of merit, namely the cooperativity $C = g^2/\gamma\kappa$, where g is the light-matter coupling rate and γ, κ the loss rates of QE and cavity, respectively. The last column in the table shows the measured Rabi splittings.

atoms [47], as well as in the first experimental demonstration of Rabi oscillations [28]. In the last years, the popularity of microwave experiments has faded in favour of optical cavity setups, mainly due to the inherent obstacles hampering microwave systems. First, they require very complex cryogenic apparatus which can hinder the coupling of photons in and out of the cavity at the quantum level [48]. Second, their dimensions of the order of the wavelength (∼mm) largely limit the scalability and integration in complex networks, a key requirement for quantum computation purposes as we will see below. Therefore, in this section we will only refer to optical cavities, since they clearly outperform microwave devices regarding quantum nanophotonics purposes. Finally, it is worth noting that microwave circuits have found a niche in the area of circuit QED, where the excellent degree of control they provide is employed to explore new physics of light-matter interaction, among others, the ultra-strong coupling regime [39].

Some of the problems enumerated above can be solved for mirror-mirror cavities interacting with optical atomic transitions. Indeed, these systems can have much smaller dimensions and thus represent a leap forward in terms of integration and scalability. In general, mirror-mirror cavities are the only setups suitable to host atoms, and thus these systems are widely employed in fundamental quantum optics since atoms are very well understood systems, their energy levels known and their decoherence mechanisms essentially identified. Regarding nanophotonics applications, however, such setups show some

critical disadvantages, namely the difficulty of trapping atoms, the required cryogenic apparatus and, regarding the cavity, the difficulty of aligning high-reflectivity mirrors. Some micron-sized mirror cavities are still employed for matrix-embedded molecular emitters [49], where the coupling is easily tuned through varying the mirror-mirror distance. However, for quantum nanophotonics at the few emitter level, many researchers have turned their attention to solid state cavities. Specially, semiconductors offer a very suitable platform since, among other interesting properties, they allow for the growth of built-in quantum dots inside the cavity setups [45]. Two main types of semiconductor resonators are particularly useful for quantum nanophotonics. First, pillar microcavities (Fig. 1.1b), in which photons are confined in the vertical direction through a Bragg grating and in the radial direction by total internal reflection [50]. These devices are very useful for controlling the EM modes, since photons can easily be pumped transversally and collected along the longitudinal direction. The second usual devices are whispering gallery resonators, either microtoroidal (Fig 1.1c) or spherical [51]. Although photonic inputs and outputs are not as easily controlled in these setups, they offer better performances in terms of Purcell factors [52]. In general, semiconductor resonators are widely used because of their flexibility, as well as their reasonably large Purcell factors and Rabi splittings (see table in Fig. 1.1).

Within semiconductors, a special mention is deserved by planar semiconductor microcavities, which are the basis of polariton applications [53]. These systems are typically tightly confined in one dimension while relatively extended in the other two, making them ideal to study the physics of propagating polaritons [30]. It does not do justice to these systems to talk about Purcell effect, since their focus is much wider than addressing single emitters. Indeed, a wide range of extraordinary phenomena has been reported on semiconductor microcavities which exploits collective polaritonic states [54, 55]. In chapter 4 we will offer a deeper perspective on these systems and the associated physics.

Initially predicted by E. Yablonovitch in 1987 [11], photonic crystal structures have revealed as extraordinary candidates for, among other uses, high-quality cavities. A photonic crystal is formed by a periodic modulation of the permittivity of some dielectric material. A typical example of a photonic crystal microcavity is a vacant within an ordered array of elements showing different refractive index in 1,2, or 3 dimensions, as schematically depicted in Fig. 1.1d. The periodicity of the lattice opens a photonic bandgap in which no photons can propagate, thus offering an excellent platform for decay rate suppression. On the other hand, light may be trapped inside the defect, effectively increasing the light-matter coupling. This makes these devices extremely flexible, with externally tunable [56] Purcell factors well within the regime $0.1 \lesssim P_F \lesssim 100$ [57, 58].

Photonic crystals are one of the best possible candidates for quantum nanophotonics, due to their good tradeoff between low loss, high field enhancement, and flexible control.

A last important type of cavities is that formed by metallic structures. Usually the schemes for high-performance cavities do not use metals even as mirrors, since their intrinsic losses hinder the photonic confinement. Despite their lossy character, metals are interesting since they can support hybrid modes between light and electronic oscillations, called surface plasmons, which are characterized by a large, and usually sub-wavelength, field profile [31]. Consequently, plasmonic cavities such as the bowtie antenna displayed in Fig. 1.1e can reach light-matter couplings orders of magnitude above those in dielectric systems. Since plasmons have been shown to display similar quantum phenomena than pure photons [59, 60], in principle these systems are employable for cavity QED. If their lossy character is kept under control by proper nanostructure engineering, plasmonic cavities can excel at some tasks, such as achieving much larger Rabi splittings [46] and Purcell factors up to 2000 according to theoretical predictions [61]. Additionally, plasmonic structures are easily fabricated and extremely well suited for dense integrated circuits due to their small dimensions. We will employ this kind of cavities in chapters 4 and 5.

1.3.2. Waveguides

Cavity systems are widely used in quantum computation-related areas since they can easily reach the strong coupling regime, where the coherent aspects of the system evolution dominate above the dissipative part. They also allow for a good control of the emission and losses. Additionally, the intra-cavity field can be prepared and monitored with high efficiency by using photons, which come out of the cavity containing information about the field inside. However, precisely because cavities excel at confining light, such photonic output is usually very slow, fundamentally limiting the speed of operation for quantum circuitry applications. For the same reason, an involved setup is often required to interconnect cavities in an efficient way, or to probe them by external sources. This is one of the main obstacles along the way towards a full quantum computer with cavities acting as computational nodes [62].

An interesting alternative proposed some time ago relies on tightly confining the EM field only in 2D, having thus a photonic waveguide. Although the smallest field confinement hinders the achievement of strong coupling, waveguides offer excellent properties from the point of view of quantum circuitry. Specifically, they allow for strong Purcell enhancements (see Fig. 1.2) and their propagating modes enable a high degree of exter-

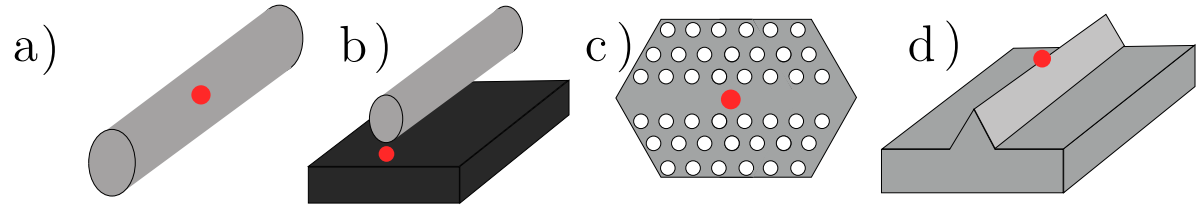

P_F	1.2	31	10	23
β	~ 0.25	0.8	0.98	0.7
L_p	100μm	6μm	30μm	15μm

Figure 1.2: Scheme of some usual waveguide setups (QE shown in red) with the typical figures of merit, obtained from the following experiments: a) Dielectric nanofibre [64] . b) Dielectric slot waveguide [65]. c) Photonic crystal waveguide [66]. d) Atomically structured plasmonic wedge [67]. In all the cases the QEs are quantum dots. The table shows the Purcell factor, beta factor, and mode propagation length corresponding to each case.

nal control. Indeed, the two open arms of the waveguide act as natural input and output ports for photons, which can be used to act upon coupled qubits or probe their properties. In the converse process, emitters coupled to waveguides can serve as quantum gates for photonic qubits propagating along the same built-in ports. All these reasons make waveguides excellent candidates for a photon-based quantum network [63].

Following the example of cavities, many different waveguide setups have been developed, each of them adapted to a particular application. Due to their simple fabrication, dielectric waveguides such as nanowires were among the first guided systems to be used in nanophotonics, mainly because of their low-loss rates and the extensive optical fibre technology available in the market [68]. Simple dielectric structures can display reasonably high Purcell and beta factors (see Fig. 1.2a), and their extremely long propagation lengths make them competitive platforms for quantum computation, especially the systems relying on silicon-based photonics [69]. Regarding few-photon/few-emitter precision setups, they are not the most popular choice since they are usually outperformed by other waveguides in terms of Purcell and beta factors. However, a lot of improvements have been made in the last years for structured dielectric devices, especially slot waveguides (Fig. 1.2b). These systems employ a very thin air gap to guide the photonic modes, achieving coupling efficiencies up to 80% due to an extreme field confinement [65]. As a consequence, however, the intrinsic propagation lengths are significantly reduced.

In the same way as a vacant in a photonic crystal acts as a cavity, and infinite linear channel along it forms a waveguide, as illustrated in Fig. 1.2c. Arguably one of the best guided systems for quantum applications, photonic crystal waveguides combine very low propagation losses with relatively easy interfacing with quantum dots [70]. Additionally, their modal dispersion can display very flat zones where the effective refractive index of the propagating photons is largely increased [66]. These slow light modes enhance light-matter couplings, with Purcell factors on the order of 10. Because emitters can be very well isolated in photonic crystal waveguides, these systems possess the record of highest beta factors to date, with coupling fractions $\beta > 98\%$ [66], largely above any other nanostructure. Their excellent properties regarding interaction with QEs, combined with the feasibility of creating complex three-dimensional waveguide networks [71] and devising basic quantum gates [72] make them excellent candidates for photonic quantum circuitry.

Last but not least, plasmonic-based waveguide systems are also a suitable candidate for a one-dimensional light-matter interface. One of their main advantages is their potential for compact integrated circuitry due to their subwavelength dimensions. Moreover, Purcell factors as high as ~ 25 have been reported due to the intense field confinement (see Fig. 1.2d). Although their properties strongly depend on the materials and fabrication techniques involved, some variations of plasmonic waveguides such as V-Grooves or wedges display relatively long propagation lengths, and can benefit from years of optimization in the area of plasmonic circuitry [73]. Additionally, they allow for the reaching of the strong coupling regime [74] and the design of elementary circuit devices [75]. Despite their high loss rate, which discards these systems for long-distance applications, some authors have proposed to combine their good properties with the large propagation lengths of dielectric waveguides by means of hybrid devices [76, 77].

1.3.3. Choosing the right quantum emitters

In an analogous way as when choosing the proper nanostructure, the election of an adequate emitter depends on the situation, since none among the large available variety objectively outperforms the others. In the end, the most adequate QE will be determined by the final purpose of the light-matter interface. For instance, if the objective is to devise a single-photon source whose emitted photons show a large degree of indistiguishability, the best option is to employ emitters with very narrow linewidths and few decoherence sources such as cold atoms. On the other hand, if the goal is to achieve large Rabi splittings to reach the strong coupling regime, large dipole moments are necessary such as

those provided by organic molecular QEs. Moreover, not all the QEs are easily integrated in every kind of nanostructure. Due to the vastness of this topic we will only briefly mention some of the most employed QEs, referring the reader to the excellent review in Ref. [78] for further read.

As we have seen above, from the fundamental point of view, trapped atoms or ions are the most desirable emitters, since their energy levels are well-known and easily controllable through EM fields. Additionally, they are little or even not sensitive at all to most of the decoherence sources arising in more complex emitters, such as dephasing, blinking, etc. Atoms show very good quantum optical properties such as strongly antibunched output light with a well-defined polarization and very high photostability [78]. As good as they are for single-photon sources, they are not the most suited for integrated nanophotonics since it is experimentally very involved to isolate, manipulate, and trap single atoms, requiring usually ultra-high vacuum and very low temperatures.

For quantum nanophotonics applications, three different QEs have deserved the majority of the attention at room temperature, namely organic molecules, colour centres and quantum dots. First, organic molecules are very common in applied nanophotonics, being the main ingredient of last generation solar cells [79], organic dye lasers [80], and many more. Their large dipole moment qualifies them also for enhanced light-matter interaction, with typical decay rates of $1 - 10\text{ns}^{-1}$. Despite their relatively large nonradiative decay rate, which is due to large dephasings and thermal fluctuations, they have remarkable properties as quantum emitters, with quantum yields above 90% and showing e.g. antibunching at room temperature [81]. For integrated circuits, these QEs can be problematic since they are usually not very stable under strong light pulses. However, by placing them in adequate matrices their photostability can be largely extended in time even under intense pulse illumination [82]. In general, these QEs are very useful in nanophotonics since they are extremely small, therefore excellent for applications at the nanoscale such as, for instance probing very localized fields [22].

An alternative choice for QEs are colour centres, which are defects of insulating inorganic crystals. The first single colour centre ever detected was a nitrogen-vacancy (NV) centre in diamond [83], and nowadays it is by far the most popular one. This defect originates by substituting two adjacent carbon atoms within a diamond lattice by a nitrogen atom and a vacant, respectively. Their bulk lifetime is around 12ns, although they are often used in nanocrystals $50 - 100\text{nm}$ in size, where the absence of total internal reflection phenomena extends their lifetime to around $20 - 30\text{ns}$ [84]. The stability of the NV-centres is excellent even at room temperature, because of the rigidity of the diamond lattice. One of their disadvantages is that high pulsed intensities can lead to

complex dark states, related to charge transfer processes and photochemical changes [85]. In general, they are very good candidates for quantum networks, and many researches are already employing them for this purpose [86, 87].

Finally, one of the most widely employed QEs are quantum dots, i.e., colloids or nanocrystalline samples to which the electronic confinement confers a discrete spectrum [88]. The variety of available types is huge, from colloidal semiconductor nanocrystals, usually a few nm in size, to self-assembled quantum dots, which can be grown to multiple sizes. Their lifetimes range from the tenths of picoseconds to $20 - 30$ns. In principle, quantum dots are much more flexible for nanophotonics applications, since they are usually easier to place or grow at a desired position within the nanostructure [88]. The major drawback in this context is their blinking, a phenomenon stemming from charge fluctuations which effectively switches off the emission properties of these QEs during a certain time window. Despite this fundamental flaw, which can be largely improved [89], quantum dots are in general very photostable and controllable, and nowadays they are probably the most employed emitters in quantum nanophotonics.

1.4. Context of this thesis in quantum nanophotonics

It is difficult to offer even a brief review of every active research area in quantum nanophotonics. Thus, in this last section of the introduction, we will focus on three very relevant aspects which are specially related with the content of this thesis, namely quantum computing and simulation, quantum photonic circuitry, and energy harvesting in organic compounds. In the following, we briefly introduce these three aspects, together with a small outline of the parts of this thesis related to each area.

1.4.1. Quantum computation and simulation

The constant increase in computational power achieved in the last years has been mainly supported by a continued size reduction of devices, which is believed to find its limit around 2019 [90], when it will probe the atomic scale. Rather than a disadvantage, this limit can become an asset as systems ruled by quantum mechanics may lead to more efficient computation techniques, labelled under the name of quantum computation and information [91]. As technology will arrive soon to the end of classical improvement of computing capabilities, the progress towards a full control of quantum devices addresses

one of the major future obstacles both for science and for everyday life. Many systems have been proposed as candidates to implement quantum computers, from trapped ions [15] and cavity QED systems [92] to superconducting circuits [93], among many others. All of them fundamentally rely on light matter interaction, since the role of basic computational unit, or qubit, is played by matter due to its inherent stability, whereas photons are used to control, address and interconnect them.

Currently, the theoretical research on quantum computation and information has developed many ideas, but only a small fraction of them are experimentally feasible at a large scale. This is mainly caused by the difficulty of exploiting quantum effects in a realistic setup. Among the different challenges for an experimental realization of complex quantum algorithms, two of the most important are the controlled generation of nonclassical states between qubits, and the efficient implementation of error correction protocols. Regarding the creation of nonclassical states, specifically entangled states, the main obstacle is their extreme sensitivity to decoherence, which intrinsically limits the capabilities of quantum computing [91]. Some works have proposed solutions in terms of decoherence-free subspaces [94, 95] whose existence, however, is only guaranteed under relatively strict conditions. A whole alternative approach known as topology-protected quantum computation has been theoretically introduced [96], but the possibility of implementing it in a realistic setup is still subject to debate. Regarding the actual experimental capabilities, a more practical strategy consists in minimizing decoherence by externally preparing long-lived nonclassical states in a system well isolated from its environment, and adding some error correction protocols *a posteriori* to account for the unavoidable loss of coherence [91]. This is one of the reasons why error correction protocols are essential in quantum computation, and hence are the subject of a large research effort. Designing such protocols is not straightforward, as classical schemes based on multiple copies of a bit cannot be applied in a quantum system due to the quantum no-cloning theorem [97]. Theoretical studies have been able to find a workaround by mapping the state of a qubit onto an entangled state of many additional *ancilla* qubits [98]. Thus, the experimental realization of these protocols also relies on the possibility of generating and controlling entangled states between qubits.

A closely related area to quantum computing and information is that of quantum simulation, which attempts to circumvent the fundamental problem of studying large quantum systems, namely the massive dimension of their Hilbert space. To deal with this intrinsic computational complexity of quantum mechanics, Feynman proposed to use quantum systems [99], already ruled by quantum laws, as analogue simulators. The idea relies on having a system at our disposal in which we could manipulate and engineer

interactions at will. If that is achieved, we would be able to make this system behave as the one we want to simulate, and subsequently predict the value of physical quantities by simply performing the appropriate measurements on our system. Again, tailored light-matter interactions are excellent for this purpose, and significant advances have been achieved in this regard with, for instance, cold atoms in atomic lattices [100].

Quantum simulation is already available in many systems such as in ion traps, where interesting physics of complex systems such as the Ising model have been uncovered [101]. Indeed, one of the straightforward applications of quantum simulation is to find ground states of complex Hamiltonians in condensed matter [102]. However, these problems are becoming increasingly attainable due to the recently developed computational tools which optimize the calculation of ground states, such as Density Matrix Renormalization Group or the more fundamental Tensor Network Algorithms [103]. It is thus much more interesting to use quantum simulation for studying the physics in regions of the Hilbert space where such powerful methods fail by definition, namely the highly entangled states arising e.g. close to a phase transition, where correlation lengths become increasingly large [104]. Once again, the ability to generate and engineer nonclassical correlations between the qubits forming the quantum simulator is of key importance for this goal.

As mentioned above, both quantum computation and quantum simulation rely on an efficient and controlled light-matter interaction, and therefore they are among the most active areas driving the research in quantum nanophotonics. The ability to use light modes to individually control qubits is extensively sought, either for initialization or readout, for performing measurements on the qubits, or for modifying the qubit-qubit interaction rates. Additionally, as mentioned above, the adequacy of a given nanostructure for both quantum computation and simulation relies on the possibility of efficiently generating entanglement between qubits, a problem which has received significant attention only in optical cavity systems [105]. In the last years, therefore, some researchers have focused on entanglement generation in alternative nanostructures such as waveguides [106, 107]. These structures are specially interesting since the possibility of employing them as active quantum optical elements is very promising for the implementation of efficient quantum networks [62]. The first part of this thesis is precisely devoted to a study of entanglement generation schemes in waveguide setups. We start in chapter 2 by revisiting the problem of dissipative entanglement generation in waveguides, and solving it by means of a full light-matter Hamiltonian. We demonstrate how this formalism is more adequate for waveguides since, as opposed to usual approaches in cavity setups, it is able to predict detrimental non-Markovian effects that arise under certain conditions. After, we propose an alternative protocol based on chiral waveguide-emitter couplings. A QE is

said to be chirally coupled to a waveguide if its guided photon absorption and emission rates depend on the propagation direction of such photon. This topic has attracted a lot of attention due to the recent experimental demonstrations of high-directional coupling [72, 108] as well as its potential impacts in quantum optics [109]. Finally, in chapter 3, we demonstrate feasible schemes for entanglement generation, manipulation, and detection based on the scattering of guided photons. Such scattering-based methods could represent an advantage since no initial preparation of the qubits is necessary.

1.4.2. Fast and small integrated photonic quantum circuits

In quantum computation and information, the term "quantum circuit" is often used to denote the set of photonic paths and gates that realize the desired operation over flying photonic qubits [91]. Here, we will use the same term in a more general sense, referring to any combination of photonic wires and devices able to improve the performance of present circuits by exploiting quantum effects. Aside from the evident applications in quantum computation, the achievement of fast and efficient nanoscale circuits could have a profound impact in many areas such as communications or data processing, a field in which optical fibres are already competing with traditional electronic circuits. Below the macroscopic scale, however, an adequate engineering of light-matter interaction is required. Many feasible candidates for quantum circuitry have been proposed within quantum nanophotonics and quantum optics, such as excitonic [110] and polaritonic circuits [111]. However, presently the most promising platforms in this regard are waveguides, due to their flexibility and demonstrated performance in a nanoscale tailoring of emitter-field interactions [62].

The natural starting point for the design of photonic quantum circuitry is the wide variety of existing photonic circuits already developed and optimized in classical nanophotonic waveguides. Indeed, many studies have been devoted in the past decades to the implementation of compact and efficient circuitry in almost any available waveguide [69, 71, 112]. Among these, three types stand out due to their remarkable properties, namely dielectric fibres, photonic crystal waveguides and plasmonic waveguides. Dielectric fibres are commonly employed as photonic transmission lines, since they display very low propagation loss and are extremely easy to fabricate. However, it is usually challenging to couple them efficiently to small nanophotonic devices due to a large modal mismatch, an issue that has been the object of an intense optimization effort (see e.g. [113] and references therein). For this reason, photonic crystal waveguides and plasmonic waveguides are usually preferred for nanophotonic circuits, since photonic de-

vices are more easily integrated in these systems. Circuits based on photonic crystals also have low propagation losses and are relatively easy to fabricate, allowing for some degree of engineering of the photonic dispersion relation. Additionally, their functionality as bare transmission lines can be extended into many other capabilities by means of integrated cavities. Indeed, side-coupled cavities can be used to reduce bending losses and devise photonic devices such as routers [114]. Despite their excellent properties as nanophotonic platforms, photonic crystal waveguides require a somewhat large surrounding matrix to generate the photonic band structure, fundamentally limiting their integration capabilities. In this regard, plasmonic waveguides are excellent substitutes due to their intrinsic field confinement, which in principle allows for an ultra compact circuitry at the subwavelength scale. Despite the large intrinsic losses of plasmonic systems, several works have demonstrated efficient plasmonic guiding along circuits [115], and remarkable achievements have been attained in terms of reducing bending losses and constructing elementary plasmonic networks [112].

In order to extend the above classical photonic circuits to the quantum regime, an enhanced light-matter interaction is required. In this regard, dielectric fibres are in principle not very efficient, since they usually show extremely small β factors when coupled to quantum emitters. Despite this disadvantage, several works have demonstrated photonic quantum devices in tapered nanofibres coupled to ensembles of neutral atoms [116], where the light-matter interaction is artificially enhanced by the large number of emitters [117, 118]. Moreover, at the few emitter level, some operations can also be implemented by means of coupling atom and nanofibre through an intermediate resonator, which enhances the coupling rate [119, 120]. This approach, however, limits the circuit scalability, as such resonators are usually much larger than the transverse section of the fibres. A simplest option in this case is to use either photonic crystal waveguides or plasmonic waveguides, both of which display large light-matter interaction at the single emitter level. As mentioned above, photonic crystals can achieve β factors close to unity by largely reducing the emission of QEs to free space modes [66]. As a consequence, many qubit-based photonic quantum gates have been already proposed in these systems, such as phase gates [72], circulators [121], and many more. On the other hand, plasmonic waveguides can also interact strongly with QEs due to their characteristic large field intensity, but the beta factors are usually much smaller, since emission to free space and nonradiative modes is not suppressed as efficiently. Nevertheless, in the last decades, the proposals of single plasmon devices [75] and the demonstration of efficient plasmon-photon conversion [122] have sparked a large research effort towards optimizing plasmonic systems for quantum circuitry [123, 124].

In this thesis, we tackle two open problems in quantum photonic circuitry. The first one regards the realization of non-reciprocal photonic devices, or gates, at the few photon level. Despite the large amount of gates existent in the literature, non-reciprocal devices such as diodes or transistors have received almost no attention, due to the intrinsic difficulty of engineering a non-reciprocal response at the quantum level. However, the recent demonstration of highly directional light-QE couplings for single emitters coupled to photonic crystal waveguides [72] and tapered dielectric nanofibres [108] paves the way for the implementation of non-reciprocal devices at the nanoscale. Thus, in the second half of chapter 3, we theoretically address the design of such devices based on the chiral coupling of a waveguide to a three-level system. We propose a four-port device in which both a diode and a transistor can be implemented, and demonstrate their high efficiency for realistic parameters. Our device is an example of the new capabilities brought by chiral light-QE coupling to waveguide-based photonic quantum circuitry, especially in photonic crystal or dielectric nanofibre systems.

The second problem we address is related to the usually low efficiency of hybrid light-matter interfaces based on plasmonic waveguides and single QEs. In such systems, the combination of moderate β factors and high propagation losses largely reduces the performance as compared to, for instance, photonic crystal systems. However, the potential advantages of plasmonic structures for compact quantum circuitry motivate the search for more efficient quantum plasmon-emitter platforms. For this reason, in the last chapter of this thesis (chapter 6) we study a system composed by a plasmonic groove waveguide coupled to a single nitrogen-vacancy centre. We demonstrate how the particular characteristics of such waveguide largely reduce the emission to free-space modes, whereas the diamond crystal surrounding the QE acts as a natural spacer reducing nonradiative decay. We theoretically predict that such a device can outperform previous realizations of plasmonic waveguide-QE systems, a prediction that has been confirmed by our experimental collaborators at ICFO and University of Southern Denmark [125].

1.4.3. Energy harvesting in organic compounds

The last decades have witnessed an exciting period in which physical and both biological and organic chemical sciences are starting to overlap. One of the areas where this synergy has produced more extensive research is the interaction of light with complex organic molecules, where promising applications such as advanced light-based techniques for medical imaging and detection [126] or the design of organic photovoltaic cells [127] are already available worldwide. Regardless of the complexity of the involved molecules,

the fundamental mechanism of light-matter interaction remains the same, namely the generation of an exciton via photon absorption, and the reverse process of relaxation accompanied by photon emission. This raises the question as to what is the role of quantum phenomena in such systems and, more interestingly, whether it is possible to control or harness such quantum effects in organic compounds. An increasing amount of researchers from different areas have devoted their attention to these ideas in the recent years, due to their interest both from the theoretical and the applied point of view. In the case of quantum nanophotonics, the study of these quantum effects could have a deep impact in, for instance, solar energy harvesting, either in artificial photovoltaic devices or in the understanding and exploiting photosynthetic complexes [128].

Regarding the field of artificial photovoltaics, a large research effort has already been carried out within classical nanophotonics with the aim of increasing the efficiency of solar cells. Such techniques usually focus on device engineering at a large scale, i.e., on improvements such as reducing the reflectivity by means of integrated resonators [129], or light trapping mechanisms [130]. The most efficient solar cells in the market usually combine many of these methods within a complex multilayer structure which, however, makes their fabrication very expensive [131]. It is thus becoming increasingly clear that, in order to have simple and highly efficient photovoltaic devices, their limitations have to be addressed at the nanoscale, e.g. by increasing the excitonic propagation length [132]. In this regard, a full quantum description of the involved light-matter processes is necessary.

The field of quantum photovoltaics is relatively young, but it has already provided some interesting studies aimed to enhance the capabilities of solar cells, and other exciton-based devices such as organic LEDs, at the quantum level. Such studies exploit different quantum mechanisms to reduce radiative recombination rates [133], as well as to increase the exciton generation rate [134] or the charge separation efficiency [135]. The interfacing of usual photovoltaic devices with quantum nanophotonic structures such as plasmonic nanowires or photonic crystals has also been shown to increase the light conversion efficiency [136, 137]. It is in principle possible to achieve a finer tuning of light-matter interaction at the quantum scale by an adequate engineering of such structures, in order to tailor the exciton transport properties across the material. Such possibility has been demonstrated in two recent works [138, 139], which illustrate how exciton transport efficiency can be enhanced by several orders of magnitude by strongly coupling an ensemble of QEs to a light mode.

Aside from the promising applications in photovoltaics, many fundamental problems could also benefit from a deeper insight on the exciton dynamics in organic molecules,

such as the study of natural light harvesting complexes [140]. The understanding of these complex molecules at the quantum level can shed light on key biological processes such as photosynthesis [128, 141], possibly uncovering new mechanisms applicable to artificial solar energy harvesting. Although this idea is currently only a long term goal, it motivates a lot of fundamental research in natural light-harvesting compounds. In the recent years, many interesting physics have been revealed in these systems, such as coherent exciton transport at room temperature [142–145], antibunched photon emission [146], or the possibility of dephasing assisted transport in ensembles of chromophores [147]. With the development of new advanced techniques in condensed matter physics able to explore higher degrees of complexity than ever before [148], it seems logical to expect that, in the following decades, we may be able to gain not only a deeper insight, but also certain degree of control over the properties of exciton transport in photosynthetic compounds.

In this thesis, we devote two chapters to the study of exciton transport in ensembles of organic molecules coupled to photonic nanostructures. Specifically, we deal with the phenomena associated to the strong coupling regime, which has already been experimentally reached in different nanophotonic systems. First, in chapter 4, we study the spatial extension of the polariton eigenstates of the above mentioned system, showing how the so called dark states can inherit the delocalized behavior of the photonic modes, despite being uncoupled to them by definition. These dark states are shown to very efficiently delocalize the excitonic wavepacket across the molecular ensemble, when the system is coherently pumped. After, we devote chapter 5 to the study of extraordinary exciton transport under incoherent pump. Taking the recent works demonstrating such effect [138, 139] as a starting point, we demonstrate the possibility of harvesting excitons in narrow spatial regions due to strong molecular coupling to spatially inhomogeneous fields. Finally, we illustrate how the fact that both the polaritons and the dark states are delocalized allows for a dephasing-assisted enhancement of the exciton transport properties under certain conditions.

2 | Waveguide-mediated entanglement generation

2.1. Introduction

Quantum entanglement is perhaps one of the most striking features of quantum theory. The quantum state of a given system is said to be entangled if it cannot be described as a separable combination of the individual states of the system constituents [149]. This intrinsically quantum correlation lies at the heart of quantum cryptography, quantum teleportation, and most of the logical gates required for a quantum computer [48, 91]. Entangled states were first exploited in optics [150], and in the late years they have become available in a wide variety of condensed matter systems such as Josephson junctions [151], spin or charge degrees of freedom in quantum dots [152–154], Cooper pair boxes [155], nitrogen-vacancy centres in diamond [156], or electrons in carbon nanotubes [157].

The ubiquity of entanglement, together with the wide range of promising applications, has sparked an intense research effort aimed towards efficient ways of generating entangled states between matter qubits [105]. Usually, the generation and control of entanglement is required across relatively large distances, a case in which the qubit-qubit interaction has to be mediated by an external common environment such as the ohmic reservoir of charge qubits [154, 158] or a common heat bath [159]. However, the most usual resource for such common environment is the electromagnetic field, due among other causes to its large degree of tunability. Light-mediated coupling between qubits has been already demonstrated in the microwave range for superconducting circuits [160], as

well as in the visible spectrum for quantum dots [161–163], NV centres [164], and many other emitters. The most popular systems for a controlled light-mediated interaction between qubits are based on optical cavities, where extensive studies on light-matter interaction have been carried out [160–163, 165]. Thanks to their advantageous properties, several protocols for cavity-assisted entanglement generation between quantum emitters have been proposed in the last decade [166–168]. These proposals belong to a large family of entanglement generation schemes based on the coherent interaction between the qubits [169–172].

Aside coherent interaction-based quantum protocols, a second option consists on the so-called dissipative or environment assisted schemes. The idea behind such protocols is based on engineering the dissipative dynamics associated with the coupling of the qubits to the common reservoir. If such environment manipulation is carried out properly, the system can evolve in time without additional external control into a desired target state, for instance the output of a quantum computation [173, 174]. Implementations of this idea have been exploited for the spontaneous generation of long-lived entangled states, both in theory [175–179] and experiment [180, 181]. These kind of entanglement generation schemes are advantageous since they require less external control and, therefore, they could in principle be more robust against other sources of decoherence. However, their implementation in cavity setups can be challenging, since achieving a long-lived entangled state requires an extremely precise tuning of the cavity mode frequency [182]. An interesting alternative platform for dissipative entanglement generation is offered by waveguides, where efficient light-matter coupling has already been achieved in numerous different systems such as nanofibres [183], photonic crystal waveguides [184, 185], plasmonic [186, 187] and semiconductor nanowires [188], and slot waveguides [189]. Moreover, the possibility of generating long-lived entanglement through dissipation has been already demonstrated in waveguide setups [106, 107].

The above mentioned studies on waveguide-mediated entanglement generation make use of a Markovian Master Equation formalism, a very successful and widespread framework in cavity systems [26]. The interesting results obtained in those works strongly motivate further research along two main lines. First, a deeper study of the limitations of the Master Equation in waveguide systems and, if necessary, the development of an alternative formalism beyond the Markov approximation. Second, the possibility of improving the generated entanglement between the qubits by means of further refinement of the protocol. We devote this chapter to a detailed analysis of these two aspects. In Section 2.2 we comment on the previous works on entanglement generation, illustrating the Lindblad Master Equation formalism and introducing the Wootters Concurrence as

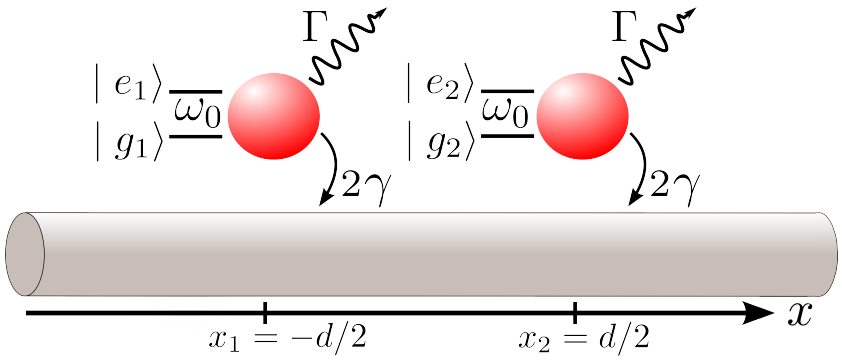

Figure 2.1: Basic waveguide QED setup for dissipative entanglement generation. Two qubits separated by a distance d are coupled to a waveguide with a coupling rate 2γ, and decay to free-space modes at a rate Γ.

an entanglement measure. After, in Section 2.3, we introduce the full Hamiltonian of a general waveguide QED system and diagonalize it in the single-excitation Fock space for the two cases of non-chiral and chiral couplings. Section 2.4 is devoted to the study of non-Markovian effects not reproduced by the Master Equation picture, and their impact on the generated entanglement. After, in Sec 2.5, we discuss the possibility of increasing the generated entanglement by means of a chiral waveguide-emitter coupling. Finally, our conclusions are presented in section 2.6.

2.2. Master Equation formalism for spontaneous entanglement generation.

In this section I will briefly explain the results obtained by previous studies in waveguide-mediated entanglement generation, namely Refs. [106, 107]. The basic system under study is depicted in Fig. 2.1. Two qubits with states $|g\rangle$ and $|e\rangle$ and a transition energy ω_0 are placed in the vicinities of a waveguide, separated by a distance d. They are coupled with the waveguide modes at a rate 2γ and to an additional lossy reservoir, to which they decay at a rate Γ. The factor 2 in the qubit-waveguide coupling will be used as a convention along this thesis, and emphasizes the fact that half of the total decay rate is due to coupling with right-propagating photons, and half to left-propagating photons. This convention will be very useful later on, when comparing chiral and non-chiral couplings. In principle, the waveguide can represent any one-dimensional collection of photonic modes, with a dispersion relation $\omega(k)$ and, in this approximation, infinite

propagation length. The loss rate Γ can be either due to nonradiative processes or to emission into free space modes, and defines the two relevant figures of merit in waveguide QED, namely the Purcell and beta factors

$$P_F = \frac{2\gamma + \Gamma}{\Gamma_0} \quad , \quad \beta = \frac{2\gamma}{2\gamma + \Gamma}. \tag{2.1}$$

Throughout this section, in order to study the basic dynamics of the qubits, we will neglect such losses for simplicity, i.e., we consider the limit $\beta \to 1$. As demonstrated in appendix C, the Hamiltonian of the system described above can be expressed as ($\hbar = 1$)

$$H = \int dk\omega(k)c^\dagger(k)c(k) + \sum_{j=1,2} \omega_0 \sigma_j^\dagger \sigma_j + \sum_{j=1,2} \int dk \left(V(k)c^\dagger(k)\sigma_j + H.c. \right), \tag{2.2}$$

where $H.c.$ stands for Hermitian conjugation. In the above expression, the first term represents the energy of the photonic modes, where $c^\dagger(k)$ is the bosonic creation operator of a photon with momentum k. Note that, in order for the dispersion $\omega(k)$ to have frequency units, the operators $c(k)$ are defined in units of $k^{-1/2}$. The second term in Eq. 2.2 accounts for the energy of the qubits by means of the spin creation operators $\sigma_j^\dagger$. Finally, the third term describes the qubit-photon interaction in the rotating wave approximation [26], where the coupling strength $V(k)$ is assumed equal for the two qubits. The coupling rate γ is a complicated function of $V(k)$ although, as we will see below, in the relevant case of a k-independent V and a linear dispersion relation they are related through $\gamma = V^2/v_g$, where v_g is the group velocity of the waveguide [190]. Unless explicitly mentioned, we ignore any direct coupling $\propto \sigma_i^\dagger \sigma_j$ between the two qubits.

2.2.1. Master Equation.

In order to study the qubit-qubit entanglement as a function of time, we have to calculate the system wavefunction $|\psi\rangle$ or, equivalently, the density matrix of the combined waveguide + qubits system [19],

$$\rho_t = |\psi\rangle\langle\psi|, \tag{2.3}$$

whose dynamics obeys the following Schrödinger equation,

$$\dot{\rho}_t = -i\left[H, \rho_t\right]. \tag{2.4}$$

Since the Hamiltonian 2.2 has many degrees of freedom, the solution of the above equation is usually challenging in practice. As a consequence, it is convenient to simplify the

problem by means of the Master Equation formalism. This method aims to eliminate all the variables of the photonic environment (in this case, the guided modes), in such a way that its whole effect appears as effective qubit-qubit interactions. In this formalism, an equation is obtained not for the whole density matrix ρ_t, but for the reduced density matrix of the two-qubit subsystem

$$\rho = \mathrm{Tr}_R[\rho_t] = \langle\emptyset|\rho_t|\emptyset\rangle + \int dk \langle k|\rho_t|k\rangle + \int dk_1 \int dk_2 \langle k_1 k_2|\rho_t|k_1 k_2\rangle + ..., \tag{2.5}$$

where Tr_R represents the partial trace operation taken over the environment modes [20], $|\emptyset\rangle$ is the photonic vacuum state, and we define $|k\rangle \equiv c^\dagger(k)|\emptyset\rangle$, $|k_1 k_2\rangle \equiv c^\dagger(k_1)c^\dagger(k_2)|\emptyset\rangle$, and so on. The reduced density matrix ρ has dimension 4×4 and contains the whole dynamics of the two-qubit ensemble, span by the states $\{|g_1\rangle \otimes |g_2\rangle, |g_1\rangle \otimes |e_2\rangle, |e_1\rangle \otimes |g_2\rangle, |e_1\rangle \otimes |e_2\rangle\}$.

Let us outline the procedure of tracing out the photonic degrees of freedom. For a detailed deduction we address the reader to, for instance, Refs. [19, 20, 26, 149]. First, we start by splitting the Hamiltonian 2.2 as $H = H_0 + V$, where

$$H_0 = \int dk \omega(k) c^\dagger(k) c(k) + \sum_{j=1,2} \omega_0 \sigma_j^\dagger \sigma_j, \tag{2.6}$$

and the interaction term is given by

$$V = \sum_j \int dk \left(V(k) c^\dagger(k) \sigma_j + H.c. \right). \tag{2.7}$$

The above definitions allow us to define the transformation from any general operator in the Schrödinger picture, $\mathcal{O}$, to the interaction picture, namely

$$\mathcal{O}^{(I)}(t) = e^{iH_0 t} \mathcal{O} e^{-iH_0 t}. \tag{2.8}$$

In the interaction picture defined above, Eq. 2.4 takes the simple form

$$\dot{\rho}_t^{(I)} = -i \left[V^{(I)}(t), \rho_t^{(I)} \right]. \tag{2.9}$$

We then proceed by formally integrating the above differential equation, and reintroducing the result back into Eq. 2.9. In this way we express the Schrödinger equation in the following integro-differential form,

$$\dot{\rho}_t^{(I)} = -i \left[V^{(I)}(t), \rho_t^{(I)}(0) \right] - \int_0^t dt' \left[V^{(I)}(t), \left[V^{(I)}(t'), \rho_t^{(I)}(t') \right] \right]. \tag{2.10}$$

The above expression is still exact, and therefore as difficult to solve as the original Schrödinger Equation 2.4. However, expression 2.10 has a very convenient form, which

allows to employ two important approximations in a more transparent fashion. First, the Born approximation [149], in which the emitter-field interaction is assumed to be weak. This assumption implies that the density matrix of the environment, $\rho_R^{(I)}(t)$, does not change from its initial value, i.e.,

$$\rho_t^{(I)} \approx \rho_R^{(I)}(0) \otimes \rho^{(I)}(t), \tag{2.11}$$

where the above factorization of the density operator is legitimate when the system and the environment are initially uncorrelated. The second and most relevant simplification is given by the so-called Markov approximation, which neglects any memory or backaction effect from the environment onto the system. In other words, the correlation time of the environment is approximated to zero, hence the bath can adapt instantaneously to any system variation. Physically, this implies the substitution of $\rho_t^{(I)}(t')$ by $\rho_t^{(I)}(t)$ in Eq. 2.10 and the extension of the integral to ∞. In this fashion the density matrix at a given instant does not depend on the state of the system at previous times. The above two approximations are sometimes referred to as a single, Born-Markov approximation. Finally, after taking the partial trace over the environment modes, Eq. 2.10 reads

$$\dot{\rho}^{(I)} = -i\mathrm{Tr}_R\left[V^{(I)}(t), \rho_R^{(I)}(0)\rho^{(I)}(0)\right] - \mathrm{Tr}_R\int_0^\infty dt' \left[V^{(I)}(t), \left[V^{(I)}(t'), \rho_R^{(I)}(0)\rho^{(I)}(t)\right]\right]. \tag{2.12}$$

The problem has therefore been reduced to a simple differential equation for which in principle all the coefficients can be explicitly calculated. Once they are determined, we can transform back into the Schrödinger picture, finally obtaining the so-called Master Equation [149],

$$\dot{\rho} = -i\left[H_s, \rho\right] + \sum_{i,j} \frac{\gamma_{ij}}{2}\mathcal{L}_{\sigma_i,\sigma_j}[\rho]. \tag{2.13}$$

The above equation describes the dynamics inside the Hilbert subspace span by the two qubits, where the effect of the guided photonic modes appears as effective qubit decays and qubit-qubit interactions. Indeed, the first term in the Master Equation contains a modified two-qubit Hamiltonian,

$$H_s = \sum_{j=1,2}(\omega_0 + \delta_j)\sigma_j^\dagger\sigma_j + \sum_{i\neq j} g_{ij}\sigma_i^\dagger\sigma_j, \tag{2.14}$$

where both an energy shift, δ_j, and a coherent interaction between the two qubits, g_{ij}, appear. The former, also called Lamb shift, is associated with the modification of the emitters self-interaction rate due to the environment. At optical frequencies, Lamb shifts are usually very small [22] and therefore can be absorbed into the frequencies ω_0 with

negligible effect. The second term in Eq. 2.13 is composed by the so-called Lindblad superoperators, which describe incoherent processes [26],

$$\mathcal{L}_{\sigma_i,\sigma_j}[\rho] = 2\sigma_j\rho\sigma_i^\dagger - \{\rho, \sigma_i^\dagger\sigma_j\}, \tag{2.15}$$

where the curly brackets denote the anticommutator. Here, the terms $i = j$ describe an environment-induced decay of the qubits into their respective ground states, with a rate γ_{ii}. On the other hand, for $i \neq j$ the Lindblad superoperator accounts for an incoherent transfer of population between both emitters. As we will see below, it is precisely this incoherent exchange that gives rise to spontaneous entanglement generation.

All of the rates determining the dynamics of the reduced density matrix, namely g_{ij} and γ_{ij}, depend on the photonic environment, and in the specific case considered in Refs. [106, 107] they are calculated as a function of the classical Green's tensor of the waveguide. In general, for two identical qubits with high β factors, and if the losses of the guided modes are small, these coefficients are very well approximated as

$$g_{12} = g_{21} = \gamma \sin\left(2\pi d/\lambda_0\right), \tag{2.16}$$

$$\gamma_{12} = \gamma_{21} = 2\gamma \cos\left(2\pi d/\lambda_0\right), \tag{2.17}$$

where $\gamma_{11} = \gamma_{22} = 2\gamma$, and $\lambda_0 = 2\pi v_g/\omega_0$ is the intrinsic emission wavelength of the two qubits, v_g being the group velocity. Interestingly, both interaction rates depend strongly on the qubit-qubit separation d, and both are cancelled out for certain values of the separation between emitters. It is therefore possible to tune the character of the interaction, from purely coherent (for $4d/\lambda_0 = 2n + 1$, $n \in \mathbb{Z}$) to purely dissipative (for $2d/\lambda_0 \in \mathbb{Z}$). This choice will have a deep impact on the generated entanglement, as we will see below.

2.2.2. Spontaneous entanglement generation.

The solution of the Master Equation 2.13 is more transparent in the basis formed by the eigenstates of H_s, namely $\{|g_1\rangle \otimes |g_2\rangle, |+\rangle, |-\rangle, |e_1\rangle \otimes |e_2\rangle\}$, where we define

$$|\pm\rangle = \frac{1}{\sqrt{2}}\left(|e_1\rangle \otimes |g_2\rangle \pm |g_1\rangle \otimes |e_2\rangle\right). \tag{2.18}$$

Note that the single-excitation states $|\pm\rangle$ are entangled. Expressed in the above basis, Eq. 2.13 takes the form of a rate equation describing the population exchange between the four states, as depicted schematically in Fig. 2.2. Note that the collective decay rates of the states $|\pm\rangle$ are different from the bare decay rate of the qubits, in this case

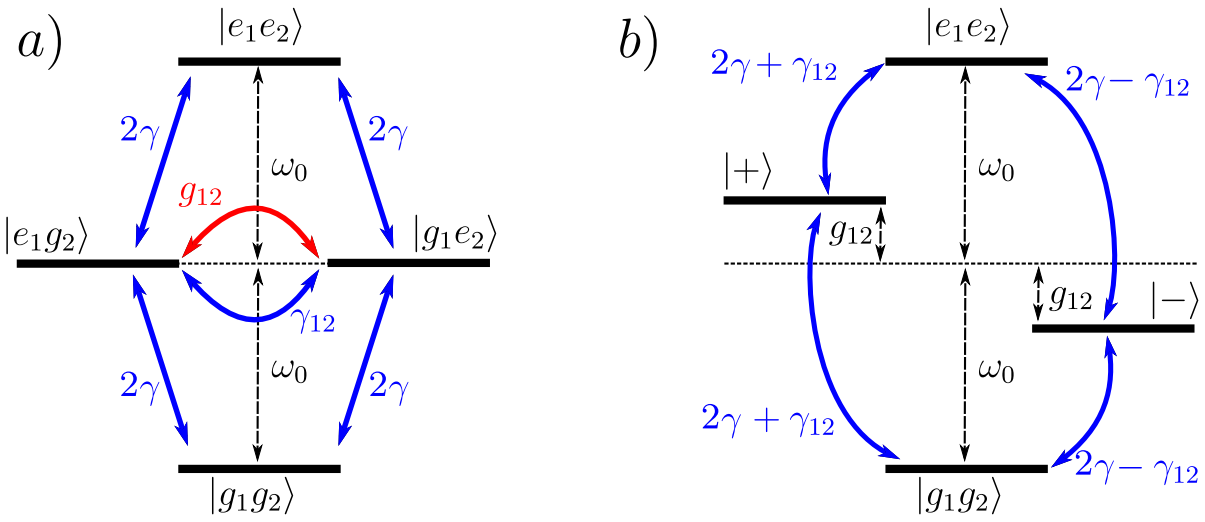

Figure 2.2: Schematic representation of the dynamics of the reduced density matrix of the two-qubit ensemble, as described by the Master Equation 2.13. a) In the product-state basis, all the levels decay at a rate 2γ, and a coherent (red) and incoherent interaction (blue) connects the two single-excitation states. b) In the eigenbasis of H_s the two single-excitation eigenstates have different energies and decay rates.

$\gamma_{\pm} = 2\gamma \pm \gamma_{12}$. This is a well-known collective phenomenon in which two states are formed with different decay rates, namely the superradiant state, which decays faster than the emitters, and the subradiant state, characterized by a slower decay [6, 191] (see chapter 4). Note that, since γ_{12} can be either positive or negative, both states $|\pm\rangle$ can be subradiant or superradiant, depending on the qubit-qubit separation.

In the level structure depicted in Fig. 2.2, two limiting cases are of special interest. First, if the qubit-qubit separation is chosen such that $\gamma_{12} = 0$, there is no sub- or superradiant state since both $|+\rangle$ and $|-\rangle$ decay at the same rate as the bare qubits, 2γ. In this situation $g_{12} = \gamma$, and the population dynamics is characterized by a coherent exchange between the two qubits. This situation is rendered in panel 2.3a for $d = \lambda_0/4$, where we show the time evolution of the populations of the two qubits and the two states $|\pm\rangle$, for the initial state $|\psi(t=0)\rangle = |e_1\rangle \otimes |g_2\rangle \equiv 2^{-1/2}(|+\rangle + |-\rangle)$. All of them are characterized by a rapid decay into the ground state, since the decay rate of the QEs dominates over the coherent interaction. On the other hand, when the separation between the qubits is tuned to cancel out the coefficient g_{12}, we have $\gamma_{12} = \pm 2\gamma$. In this limit, the subradiant state becomes totally uncoupled from the guided modes, thus forming a so-called dark state. Dark states (see also chapters 4 and 5) are extremely useful in these kind of systems, since they do not decay into the waveguide modes and therefore their

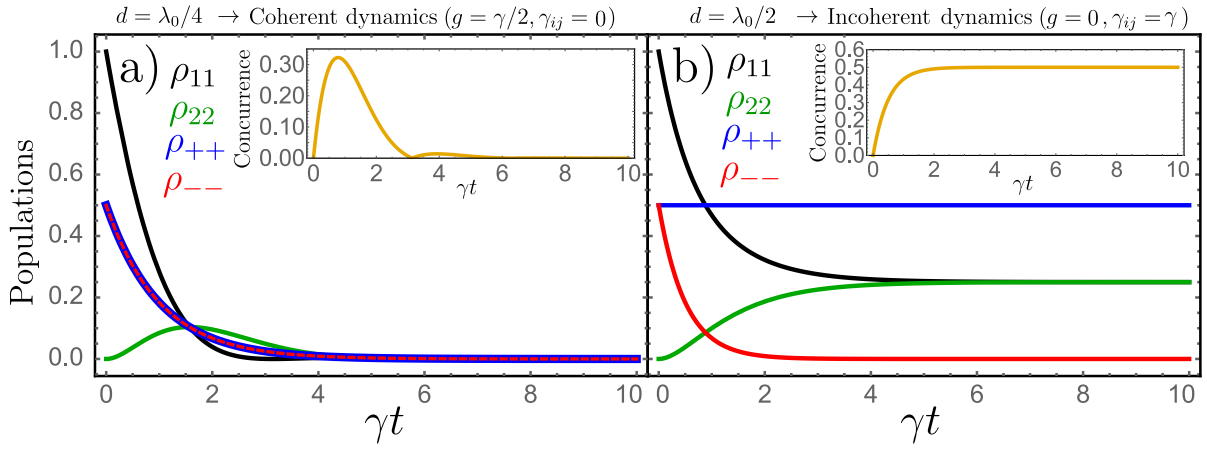

Figure 2.3: Population and entanglement dynamics of the two-qubits subsystem for the initial state $|e_1\rangle \otimes |g_2\rangle$. The different curves show the populations of the states $|e_1\rangle \otimes |g_2\rangle$ (black), $|g_1\rangle \otimes |e_2\rangle$ (green), $|+\rangle$ (blue), and $|-\rangle$ (red). The inset shows the generated entanglement measured through the Concurrence. a) Purely coherent interaction, $d = \lambda_0/4$. b) Purely incoherent interaction, $d = \lambda_0/2$.

population remains constant with time. Figure 2.3b shows an example of the system dynamics under these conditions, for the same initial state $|\psi(t = 0)\rangle = |e_1\rangle \otimes |g_2\rangle$, and a separation $d = \lambda_0/2$, which corresponds to $|+\rangle$ being the dark state. In this situation the superradiant state $|-\rangle$ decays with a rate 4γ and, therefore, for long times the only remaining population is that of the dark state $|+\rangle$. These results show how the system spontaneously evolves from an unentangled initial state into an entangled state with an infinite lifetime, a process known as dissipative entanglement generation. Note that in a realistic setup the emitters are subject to additional losses such as free space radiation, and the dark state has a small decay rate Γ. In such case the lifetime of the entangled state is finite, but very long for high β factors.

In order to determine the performance of the dissipative entanglement generation shown in panel 2.3b, we need to be able to quantify the quantum entanglement. For bipartite systems such as our two-qubit ensemble, many different measures have been proposed, but all of them are related [150]. In this thesis we choose the Wootters concurrence [192], which is defined as

$$C = \max\{0, \sqrt{\lambda_1} - \sqrt{\lambda_2} - \sqrt{\lambda_3} - \sqrt{\lambda_4}\}, \tag{2.19}$$

where $\{\lambda_1, \lambda_2, \lambda_3, \lambda_4\}$ are the eigenvalues of the non-Hermitian matrix $\rho(\sigma_y \otimes \sigma_y)\rho^*(\sigma_y \otimes \sigma_y)$ in decreasing order, σ_y being the $y-$Pauli matrix. The concurrence is a bounded measure of the quantum entanglement, being equal to 0 for product states and to 1 for

maximally entangled states such as $|\pm\rangle$. The inset panels in Figs. 2.3a and 2.3b show the concurrence $C(t)$ for the two cases discussed above. In the case of coherent interaction, the concurrence reaches a maximum value of $C \sim 0.3$, and is always characterized by a rapid decrease. On the other hand, when the interaction is purely incoherent, the population of the dark state is unable to decay, resulting in a stationary entangled state with concurrence $C = 0.5$. As we have commented above, for large β factors the concurrence lives for a long time even in the presence of losses, making the dissipative entanglement generation very advantageous. Note, finally, that the maximum generated concurrence can be increased up to 1, but only by means of an external pump [193].

2.3. Non-Markovian formalism for waveguide QED systems

The above results suggest that waveguide setups offer a reliable platform for entanglement generation purposes. However, a proper study of this kind of systems may benefit from a description beyond the Master equation formalism for various reasons. First, one of the advantages of waveguides with respect to optical cavities is the presence of input and output ports, through which a control of the photonic degrees of freedom is in principle possible. However, all the information about the guided modes is lost as they are traced out in the Master Equation. This could limit the potential of the formalism in terms of studying complex photon-qubit interactions. A second reason regards the Born-Markov approximation discussed above, intrinsic to the Master Equation formalism. For the two most studied cases in quantum optics, namely an emitter inside a single-mode cavity and an emitter in free space, such approximation is extremely accurate and equivalent to the assumption of weak emitter-field coupling [19]. However, for structured electromagnetic environments it may not necessarily hold, even in the weak coupling limit. For instance, an emitted photon in a 1D environment can be reflected by other emitters, finding its way back into its original source and thus exerting a backaction onto it, which is by definition a non-Markovian process. These two arguments suggest that a more adequate treatment of waveguide QED problems, and specifically entanglement generation, would require a general formalism in which the photonic modes are explicitly taken into account. We devote the rest of this chapter to the development of such formalism and its application to the problem of spontaneous entanglement generation.

2.3.1. Waveguide QED Hamiltonian in the position basis

The system we intend to solve is the same as depicted in Fig. 2.1. Although in principle our goal is to take into account the qubit losses, Γ, introducing them can be a delicate issue as we will see below. Therefore, we will first obtain the desired Hamiltonian in the lossless case $\Gamma = 0$, and introduce the losses a posteriori. The problem we face is thus the diagonalization of the bare waveguide-qubit Hamiltonian, Eq. 2.2. Previous works have dealt with this Hamiltonian in the context of photon scattering in waveguide QED, either by directly working in wavevector space [194, 195] or by transforming it into the position basis [186, 190, 196]. The latter method was much more developed until few years ago, and hence we will follow it along this thesis.

The detailed transformation of the Hamiltonian 2.2 into the position basis will be briefly summarized here, a detailed study being available in ref. [196]. Along such transformation, two main approximations have to be undertaken. First, we assume that the operating wavevector $|k_0|$ is far enough from $k = 0$, such that the right- and left- propagating eigenmodes of the waveguide, namely $|k_0|$ and $-|k_0|$, are clearly distinguishable. This is usually not a problematic assumption at optical frequencies, although technically it implies an upper bound on the cutoff frequency or, conversely, a minimum waveguide cross section [197]. The second approximation consists in linearising the dispersion relation, which is now formed by two independent branches,

$$\omega_{k\approx k_0} = \Omega_0 + v_g(k - k_0) \equiv +v_g k_R = \omega_{k_R}, \tag{2.20}$$

$$\omega_{k\approx -k_0} = \Omega_0 - v_g(k + k_0) \equiv -v_g k_L = \omega_{k_L}, \tag{2.21}$$

where the subindices R and L label, respectively, the right- and left-propagating branches, and we have chosen the arbitrary origin of energies at $\Omega_0 = 0$. In other words, this approximation assumes that the working bandwidth is small enough to approximate the dispersion relation to first order in k. Note that, as a consequence of having two independent branches, the bosonic operators $c(k)$ are split as well into two independent and commuting operators, namely $c(k_R)$ and $c(k_L)$, which can be transformed into the position basis via a standard Fourier transform,

$$c(k_\alpha) = \int_{-\infty}^{\infty} dx c_\alpha(x) e^{-ik_\alpha x}, \tag{2.22}$$

for $\alpha = R, L$. By introducing the above equality, together with Eqs. 2.20 and 2.21, into

the original Hamiltonian 2.2, we can rewrite it in the position basis as [196]

$$\begin{aligned} H = -iv_g \int dx \left(c_R^\dagger(x) \frac{\partial}{\partial x} c_R(x) - c_L^\dagger(x) \frac{\partial}{\partial x} c_L(x) \right) + \sum_j \omega_0 \sigma_j^\dagger \sigma_j \\ + \sum_{j=1,2} V \int dx \delta(x - x_j) \left(c_R^\dagger(x) + c_L^\dagger(x) \right) \sigma_j + H.c., \end{aligned} \tag{2.23}$$

where $\delta(x)$ is the Dirac delta distribution, and x_j is the position of emitter j (see Fig. 2.1). The new field operators $c_\alpha^\dagger(x)$ create an $\alpha-$propagating guided photon at position x. In order to obtain the equation above, we have assumed the qubit-waveguide coupling to be independent on the frequency, i.e., $V(k) \approx V$. This is equivalent to a *local* Markov approximation, in which we consider that the environment *per se* does not have any memory effects in the vicinities of the corresponding qubit. In other words, this Markov approximation is partial, only affecting the intrinsic structure of the electromagnetic field surrounding the emitter. As we will see below, the system as a whole can still display non-Markovian effects due to the interaction of the two locally Markovian systems.

In the entanglement generation scheme we want to explore, qubit 1 is initially excited, whereas qubit 2 is in the ground state. Since the above Hamiltonian conserves the total number of excitations, the whole system dynamics will thus remain in the single-excitation Hilbert subspace. This property enormously simplifies the problem, since the diagonalization of the Hamiltonian 2.23 is required only within such subspace.

2.3.2. Lossless, non-chiral situation. Scattering and localized eigenstates

Let us illustrate the diagonalization of Hamiltonian 2.23 in the single-excitation subspace. Since such Hamiltonian is invariant under parity, i.e., $[H, \Pi] = 0$, it is convenient to express it in terms of the parity-symmetric operators

$$c_{e,o}(x) = \frac{1}{\sqrt{2}} \left(c_R(x) \pm c_L(-x) \right), \tag{2.24}$$

$$\sigma_{e,o} = \frac{1}{\sqrt{2}} \left(\sigma_1 \pm \sigma_2 \right), \tag{2.25}$$

where the subindices e, o stand for the even or odd symmetry of the operators. Note that the qubit states $\sigma_{e,o}^\dagger |0\rangle$ correspond to the subradiant and superradiant states $|\pm\rangle$ studied in the previous section. The change into the even/odd basis has been successfully used to obtain the full spectrum of the Hamiltonian in the single-qubit case [198]. In this basis,

the Hamiltonian splits into two commuting contributions $H = H_e + H_o$, which can be expressed in a compact form as

$$\begin{aligned} H_m = \omega_0 \sigma_m^\dagger \sigma_m - i v_g \int dx c_m^\dagger(x) \frac{\partial}{\partial x} c_m(x) + \\ + V \int dx \left[\delta(x + d/2) + \eta_m \delta(x - d/2)\right] \left(c_m^\dagger(x)\sigma_m + H.c.\right), \end{aligned} \tag{2.26}$$

for $m = e, o$. In the expression above we have defined the variable

$$\eta_m = \begin{cases} 1 & \text{for} \quad m = e \\ -1 & \text{for} \quad m = o. \end{cases} \tag{2.27}$$

Since the even and odd subspaces are orthogonal by definition, we can diagonalize them separately. We start by writing the most general single-excitation eigenstate with parity m as

$$|\epsilon_m\rangle = \left(\int dx \phi_m(x) c_m^\dagger(x) + \alpha_m \sigma_m^\dagger \right) |0\rangle, \tag{2.28}$$

where the qubit amplitude α_m and the single-photon wavefunction $\phi_m(x)$ are the unknowns to be determined. The next step is to directly apply the time-independent Schrödinger equation $H_m|\epsilon_m\rangle = \epsilon|\epsilon_m\rangle$ to the eigenstate above, obtaining the following set of relations between the system coefficients,

$$(\epsilon - \omega_0)\alpha_m = V\left[\phi_m(-d/2) + \eta_m \phi_m(d/2)\right], \tag{2.29}$$

$$\left(\epsilon + i v_g \frac{\partial}{\partial x}\right) \phi_m(x) = V \alpha_m \left[\delta(-d/2) + \eta_m \delta(d/2)\right]. \tag{2.30}$$

The solution of the second equation above is clearly a piecewise plane wave, the Dirac delta distributions only imposing particular matching conditions at the position of the two qubits. Therefore, we can assume the following general form for the single-photon wavefunction,

$$\phi_m(x) = e^{i\epsilon x/v_g} \times \begin{cases} A_m(\epsilon) & \text{for} \quad x < -d/2 \\ t_{0,m}(\epsilon) & \text{for} \quad -d/2 < x < d/2 \\ t_{1,m}(\epsilon) & \text{for} \quad d/2 < x. \end{cases} \tag{2.31}$$

If we now integrate Eq. 2.30 around the two points $x = -d/2$ and $x = d/2$ and make use of the above expression, we obtain a system of algebraic equations given by

$$(\epsilon - \omega_0)\alpha_m = \tfrac{V}{2}\left[(A_m + t_{0,m})e^{-i\epsilon d/v_g} + \eta_m (t_{1,m} + t_{0,m}) e^{i\epsilon d/v_g}\right], \tag{2.32}$$

$$i v_g (t_{1,m} - t_{0,m}) e^{i\epsilon d/2} = V \alpha_m, \tag{2.33}$$

$$i v_g (t_{0,m} - A_m) e^{-i\epsilon d/2} = \eta_m V \alpha_m, \tag{2.34}$$

where we have used the convention $\phi(x_j) = [\phi(x_j + 0^+) + \phi(x_j - 0^+)]/2$, for $x_j = \pm d/2$. This final system of algebraic equations already gives information about the structure of the eigenstates. Indeed, note that the system is indeterminate, since we have three equations for 4 unknown coefficients. This implies that some energies can be degenerate and, if that is the case, we can label the different families of eigenstates with a free parameter, which we choose to be A_m for convenience. We will have two different solutions depending on this value.

Scattering eigenstates.

If the coefficient A_m is different from zero, we can normalize the other three unknowns to it, obtaining a fully determinate 3×3 system of equations. The solution of such system is given by

$$t_{0,m} = \frac{\epsilon - \omega_0}{\epsilon - \omega_0 + i\gamma\left(1 + \eta_m e^{i\epsilon d/v_g}\right)}, \tag{2.35}$$

$$t_{1,m} = \frac{\epsilon - \omega_0 - i\gamma\left(1 + \eta_m e^{-i\epsilon d/v_g}\right)}{\epsilon - \omega_0 + i\gamma\left(1 + \eta_m e^{i\epsilon d/v_g}\right)}, \tag{2.36}$$

$$\alpha_m = V e^{-\epsilon d/2v_g} \frac{1 + \eta_m e^{i\epsilon d/v_g}}{\epsilon - \omega_0 + i\gamma\left(1 + \eta_m e^{i\epsilon d/v_g}\right)}, \tag{2.37}$$

where $\gamma = V^2/v_g$ describes the decay rate of one qubit to either right or left propagating photons. The eigenstates described by the above coefficients correspond to the scattering of even or odd photons on the two-qubit system. Two examples of the photonic position probability density associated with these states are shown in Fig. 2.4, for a photon with an energy $\epsilon = 1.25\omega_0$ (panel a) and a photon in resonance with the qubits, $\epsilon = \omega_0$ (panel b). In the resonant case, the incoming photon cannot be transmitted through the two-qubit ensemble since the transmission coefficient $t_{0,m}$ vanishes, and therefore the position probability amplitude is 0 for $-d/2 < x < d/2$. This is a consequence of a well-known phenomenon in which a resonant single photon impinging over a two-level system is fully reflected. Perfect reflection is a result of a destructive interference between the two quantum processes which would lead to the photon being transmitted, namely direct transmission without qubit-photon interaction, and photon absorption followed by rightward reemission. This effect is well understood and has been demonstrated both theoretically (see appendix A, or Refs. [75, 199, 200]) and experimentally [201].

The branch of eigenstates described above has already been obtained in the context of photon scattering with one or two qubits [190, 196, 198, 202]. Indeed, we will name them *scattering eigenstates* $|\epsilon^{sc}\rangle$ since, as we will see below, they are sufficient to completely

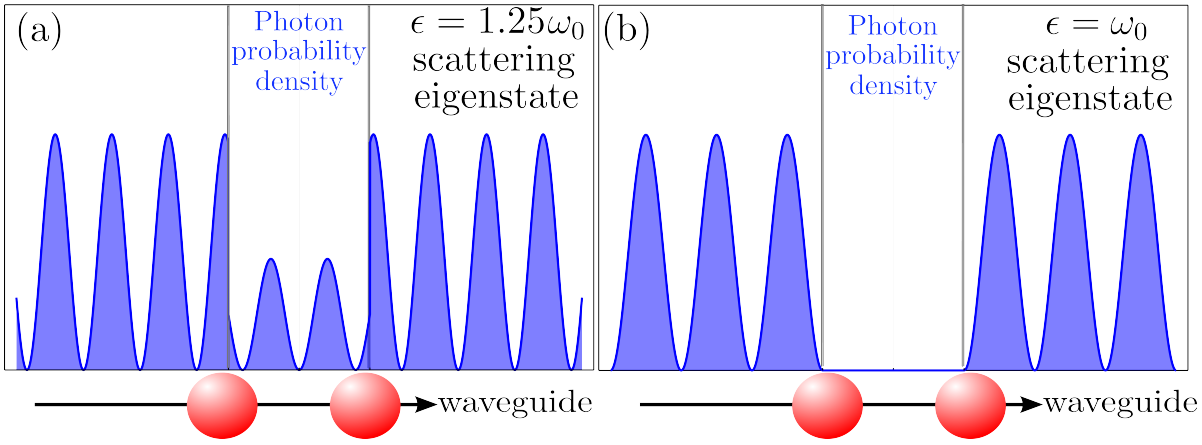

Figure 2.4: Photon position probability density for two scattering eigenstates. a) Non-resonant energy $\epsilon = 1.25\omega_0$. b) Resonant energy $\epsilon = \omega_0$, for which photons are fully reflected by the two qubits.

describe any scattering problem. However, when the initial state is not purely photonic, this scattering branch is not complete, and the second family of eigenstates comes into play.

Localized eigenstates.

An alternative solution of the algebraic system of equations 2.32-2.34 exists when the coefficient A_m is equal to zero. These eigenstates can appear only under a certain combination of parameters. More precisely, they only exist when the separation between the qubits is equal to half an integer multiple of the emitter characteristic wavelength, i.e., $d = n\lambda_0/2$ where $\lambda_0 = v_g/2\pi\omega_0$. We will refer to these as *resonant separations* (d_{res}) from now on. Additionally, a nontrivial solution requires the energy of such states to be $\epsilon = \omega_0$.

Provided that the conditions $\{d = d_{\text{res}}; \epsilon = \omega_0\}$ are satisfied, the algebraic system of equations 2.32-2.34 can be shown to have the following additional solution,

$$t_{1,m} = 0, \tag{2.38}$$

$$t_{0,m} = -i\eta_m \tfrac{V\alpha_m}{v_g} e^{i\pi(d/\lambda_0)}, \tag{2.39}$$

where the unknown coefficient α_m is determined by normalization. Since the two coefficients $A_m, t_{1,m}$ are equal to zero, these states are localized in the region between the two qubits. The appearance of such states is understood by recalling the above mentioned phenomenon where a single photon in resonance with a qubit is fully reflected. For the

scattering branch discussed in the previous section, this implied that no resonant photon could reach the region between both qubits, since such region becomes uncoupled with the outside. On the other hand, the eigenstates described by Eqs. 2.38-2.39 are exactly the opposite, since their photonic part only exists within the inter-qubit region. In order for such state to be stationary (and thus an eigenstate of the system), the standing wave condition must be fulfilled for this qubit-qubit *cavity*. This requirement is obviously satisfied for a photon of energy ω_0, and for the resonant separation condition $d = d_{\text{res}} = n\lambda_0/2$, in a complete analogy with a Fabry-Perot interferometer in classical optics.

Figure 2.5a shows the photon position probability distribution for this new localized eigenstate. Importantly, for half-integer resonant separations ($d = (2n-1)\lambda_0/2$), the localized state arises only in the even subspace, and for integer resonant separations $d = n\lambda_0$ it appears only in the odd subspace. Note that these states have the same characteristics as the dark states obtained in the Master Equation picture. Specifically, they are dark since they are uncoupled from the propagating guided modes. In this case, however, a more complete description of the system demonstrates that, for $d > 0$, these dark states have a photonic component, instead of being the pure qubit-states predicted by the Master Equation formalism. This is the first indication of an incomplete description of the system with the Master Equation, which we will study below in detail. Note, finally, that when the separation is not resonant, $d \neq d_{res}$, the existence of a photon with energy ω_0 in the region between both qubits is not possible because of destructive interference. This interesting effect has been exploited to fabricate an effective qubit-qubit cavity [203].

Completeness of the basis

The appearance of the localized eigenstates, which we will label $|\omega^L_{0,n}\rangle$, is essential in order to have a complete basis for some problems. As mentioned above, these eigenstates do not play a role in the dynamics of any scattering problem, i.e., for any initial state in which a photon is introduced through one of the ends of the waveguide. This is demonstrated by the orthogonality relation

$$\langle \epsilon^{sc} | \omega^L_{0,n} \rangle = 0, \tag{2.40}$$

which is in turn a direct consequence of the conditions $A_m, t_{1,m} = 0$ for the localized states. Additionally, for $d \neq d_{\text{res}}$ there is no localized eigenstate, and the scattering basis $\{|\epsilon_{sc}\rangle\}$ is complete to describe the evolution of the system for any possible initial

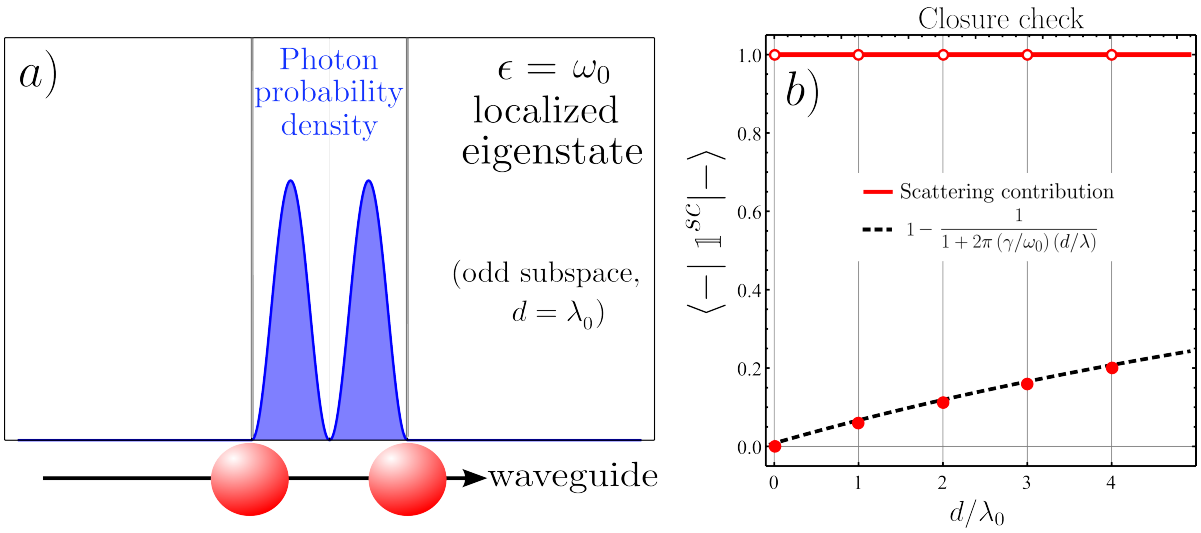

Figure 2.5: a) Photon position probability density for a localized eigenstate. Since the separation is $d = \lambda_0$, this state is a combination of localized photons and the odd qubit state $|-\rangle$. b) Completeness check ($\gamma = 10^{-3}\omega_0$). The closure relation formed only by the scattering eigenstates (red) is complete for any state with an initial qubit contribution, unless the separation is resonant, $d = n\lambda_0$. In such situation the localized eigenstates are required to complete the identity.

configuration. However, when the separation is resonant and the initial state contains some qubit contribution, the localized states have to be included. In order to demonstrate this, we construct the full closure relation

$$\sum_{m=e,o} \sum_{\epsilon} \frac{|\epsilon_m\rangle\langle\epsilon_m|}{\langle\epsilon_m|\epsilon_m\rangle} = \mathbb{1}. \tag{2.41}$$

Here, the norm of the eigenstates can be analytically calculated directly from their explicit expression, Eq. 2.28. The above identity can be split into two parts corresponding to the localized and the scattering branch, respectively. The contribution of the former, $\mathbb{1}^L$, is straightforward to calculate,

$$\mathbb{1}^L = \sum_{n\in\mathbb{Z}} |\omega^L_{0,n}\rangle\langle\omega^L_{0,n}| \left(\frac{\delta\left(d - [n-1/2]\,\lambda_0\right)}{|\alpha_e|^2 + d|t_{0,e}|^2} + \frac{\delta\left(d - n\lambda_0\right)}{|\alpha_o|^2 + d|t_{0,o}|^2} \right). \tag{2.42}$$

For the scattering branch, on the other hand, we have to take the continuum limit of the discrete sum,

$$\sum_{\epsilon} f(\epsilon) \to \int d\epsilon D(\epsilon) f(\epsilon), \tag{2.43}$$

where the prefactor $D(\epsilon)$ is the density of photonic states in the waveguide. We calculate this factor by considering the photonic modes in a periodic unit cell of length L in the waveguide, and taking the limit $L \to \infty$ at the end of the calculation. From the periodic boundary condition $n\lambda = L$ for integer n, we can write the energy of the n-th photonic state as $\epsilon_n = 2n\pi v_g/L$. The density of states will therefore be constant, $D(\epsilon) = (\epsilon_{n+1} - \epsilon_n)^{-1} = L/2\pi v_g$, and the closure relation for the scattering eigenstates is simply written as

$$\mathbb{1}^{sc} = \sum_{m=e,o} \frac{1}{2\pi v_g} \int d\epsilon |\epsilon_m^{sc}\rangle\langle\epsilon_m^{sc}|, \tag{2.44}$$

which is a length-independent result since the norm of the scattering states can be easily shown to fulfil $\lim_{L\to\infty}\langle\epsilon_m^{sc}|\epsilon_m^{sc}\rangle/L = 1$.

Once we have deduced the closure relation, we can check the completeness of the basis for an initial state with a qubit contribution. For illustration purposes, we choose the odd state $|-\rangle = \sigma_o^\dagger|0\rangle$, and calculate the following identity

$$\langle -|\mathbb{1}|-\rangle = \langle -|\mathbb{1}^L + \mathbb{1}^{sc}|-\rangle, \tag{2.45}$$

If the set of scattering and localized eigenstates is complete, the above value should be equal to unity. In Fig. 2.5b, we plot such identity together with the scattering contribution only, $\langle -|\mathbb{1}^{sc}|-\rangle$, as a function of the qubit-qubit distance d. As expected, for non-resonant distances the scattering basis is complete. On the other hand, when the distance between the qubits is equal to an odd-resonant separation, $d = n\lambda_0$, the scattering eigenstates are not sufficient to describe the system. For the particular case of an initial state with no photonic part, such as $|-\rangle$, the contribution of the localized states has a very simple expression,

$$\langle -|\mathbb{1}^L|-\rangle = \frac{1}{1 + 2\pi\,(\gamma/\omega_0)\,(d/\lambda_0)}. \tag{2.46}$$

The quantity $1 - \langle -|\mathbb{1}^L|-\rangle$ is displayed in the dashed line of Fig. 2.5b, demonstrating that the addition of the localized states makes the whole basis complete for any value of the separation d. Interestingly, when such separation is $d = 0$ the scattering eigenstates do not contribute to the overlap at all, whereas in the limit $d \to \infty$ the contribution of the localized states vanishes.

2.3.3. Introducing the qubit losses.

The issue of introducing the qubit losses Γ in a proper way is of key importance for the sake of comparison with realistic waveguide systems. All the works dealing with our

formalism in the context of photon scattering problems describe the losses in a simple way, by means of adding a small, non-Hermitian part to the frequency of the qubits,

$$\omega_0 \rightarrow \omega_0 - i\Gamma/2. \tag{2.47}$$

This approach works well for the above mentioned problems, as we will see below. However, it is not appropriate for the entanglement generation we study in this thesis. In particular, if one repeats the diagonalization in the above section for an imaginary ω_0, the resulting scattering branch of eigenstates becomes incomplete for *any* separation d. Since the localized eigenstates only exist for resonant separations, they are unable to compensate such incompleteness for any distance $d \neq d_{\text{res}}$. We are therefore constrained to employ a more thorough study of the losses which is able to fix this inconsistency.

Since the imaginary frequency approach is not applicable in this situation, we aim for a complete Hamiltonian description of the losses. Our model will be similar to that used in the previous section, now with the following total Hamiltonian,

$$H_T = H + H_r + H_c, \tag{2.48}$$

where H is the original lossless Hamiltonian, Eq. 2.23. The second term, H_r, is the contribution of the reservoir modes,

$$H_r = -iv \sum_{j=1,2} \int dz P_j^\dagger(z) \frac{\partial}{\partial z} P_j(z). \tag{2.49}$$

Here, we have modelled the free-space EM environment of each emitter j as one infinite continuum of photonic modes, whose creation operator is $P_j^\dagger(z)$. The above equation is similar to the Hamiltonian of two infinite waveguides, independent of each other and set along the z-axis. In this case, however, they would be *unidirectional* in the sense that they don't have two but a single propagation direction. This simplifies the calculations while keeping unaffected their main effect on the qubit populations, namely an exponential decay. Note that the above reservoirs are also Markovian, which is a good approximation for weakly coupled 3D environments. As a consequence, they are characterized only by a group velocity v which we consider equal to v_g for simplicity. Finally, the third term in Eq. 2.48 represents the coupling of each reservoir to its corresponding emitter,

$$H_c = K \int dz \delta(z) \sum_{j=1,2} \left[P_j^\dagger \sigma_j + H.c. \right], \tag{2.50}$$

where the coupling strength K defines the loss rate according to $\Gamma = K^2/v_g$. The interaction is set to take place at $z = 0$ for simplicity.

The diagonalization of the Hamiltonian 2.48 follows an analogous method as the one detailed in the previous sections. First, we express the reservoir operators in the even/odd basis as

$$P_m = \frac{1}{\sqrt{2}} \left(P_1(z) + \eta_m P_2(z) \right), \tag{2.51}$$

for $m = e, o$. Under this change of basis, both H_r and H_c split into independent even and odd contributions,

$$(H_r + H_c)_m = -iv_g \int dz P_m^\dagger(z) \frac{\partial}{\partial_z} P_m(z) + K \int dz \delta(z) \left[P_m^\dagger \sigma_m + H.c. \right], \tag{2.52}$$

which again allows for a separate diagonalization in the even and odd subspaces. The expression for the single-excitation eigenstate in this case reads

$$|\epsilon_m\rangle = \left(\int dx \phi_m(x) c_m^\dagger(x) + \alpha_m \sigma_m^\dagger + \int dz \psi_m(z) P_m^\dagger(z) \right) |0\rangle, \tag{2.53}$$

where $\psi_m(z)$ is the wavefunction associated with the reservoir modes. If we now apply the time-independent Schrödinger equation, we obtain a set of differential equations for the system coefficients, in the same way as in the previous section. The piecewise plane wave form for the wavefunction $\phi_m(x)$ is again given by Eq. 2.31, whereas the photonic wavefunction of the reservoir takes the general form

$$\psi_m(z) = e^{i\epsilon z/v_g} \begin{cases} a_m & \text{for} \quad z < 0 \\ b_m & \text{for} \quad z > 0, \end{cases} \tag{2.54}$$

with generic coefficients $\{a_m, b_m\}$. Upon introducing the above expression into the system of differential equations, we obtain an algebraic system of four equations with six unknowns. Again, the indeterminate character of such system implies that degenerate eigenstates arise, this time labelled by two free parameters which we choose to be A_m and a_m for convenience. It is straightforward to demonstrate that no solution exists for $A_m = a_m = 0$, and therefore only two possibilities remain.

Scattering branch, $A_m \neq 0$, $a_m = 0$.

In this case, by normalizing all the unknown coefficients to A_m, we obtain a 4×4 algebraic system. The solution for the coefficient of the reservoir is

$$b_m = -i\sqrt{\gamma\Gamma} e^{-\epsilon d/2v_g} \frac{1 + \eta_m e^{i\epsilon d/v_g}}{\epsilon - \omega_0 + i\Gamma/2 + i\gamma \left(1 + \eta_m e^{i\epsilon d/v_g}\right)}. \tag{2.55}$$

On the other hand, the solutions for the coefficients $t_{0,m}, t_{1,m}$, and α_m are identical to those obtained in the lossless case (equations 2.35-2.37), with an additional imaginary

part $-i\Gamma/2$ in the qubit frequency. In other words, by means of a complete description of the qubit losses, we demonstrate that the substitution $\omega_0 \to \omega_0 - i\Gamma/2$ correctly reproduces the physics of the scattering eigenstates, and is therefore adequate for any scattering problem. Note that in the limit $\Gamma \to 0$ we recover the results of the previous section.

Localized branch, $A_m = 0$, $a_m \neq 0$.

In this situation, the parameter a_m is still free, and we can normalize all the unknowns to it. Therefore, no additional constraint appears, and an eigenstate arises *for any energy*. As a consequence, we have a whole additional continuum branch of eigenstates, in substitution of the discrete set of localized states obtained in the lossless case. The expressions of the coefficients are

$$t_{0,m} = -i\frac{\sqrt{\gamma\Gamma}e^{i\epsilon d/2v_g}}{\epsilon - \omega_0 + i\Gamma/2 + i\gamma\left(1 + \eta_m e^{i\epsilon d/v_g}\right)}, \tag{2.56}$$

$$t_{1,m} = -i\frac{\sqrt{\gamma\Gamma}\left(e^{i\epsilon d/2v_g} + \eta_m e^{-i\epsilon d/2v_g}\right)}{\epsilon - \omega_0 + i\Gamma/2 + i\gamma\left(1 + \eta_m e^{i\epsilon d/v_g}\right)}, \tag{2.57}$$

$$\alpha_m = \frac{K}{\epsilon - \omega_0 + i\Gamma/2 + i\gamma\left(1 + \eta_m e^{i\epsilon d/v_g}\right)}, \tag{2.58}$$

$$b_m = 1 - i\frac{K}{v_g}\alpha_m. \tag{2.59}$$

The appearance of a continuous branch of eigenstates is a consequence of the natural widening of the qubit frequencies introduced by the lossy reservoirs. The majority of these eigenstates are not fully localized in the inter-qubit region, since $t_{1,m} \neq 0$ and, as a consequence, a certain amount of probability leaks into propagating waveguide modes. In Fig. 2.6a we show an example of one of these *quasi-localized* eigenstates. Despite the observed photon leakage toward the two ends of the waveguide, the quasi-localized eigenstates, $|\epsilon^{loc}\rangle$, remain orthogonal to the scattering eigenstates, i.e.,

$$\langle\epsilon^{loc}|\epsilon'^{sc}\rangle = 0. \tag{2.60}$$

Additionally, in the limit $\Gamma \to 0$ (i.e., $K \to 0$) we recover the physics of the lossless situation, as $t_{1,m} \to 0$ and a factor $\sim \delta(\epsilon - \omega_0)\delta(d - d_{\text{res}})$ appears in both α_m and $t_{0,m}$.

Interestingly, even in the lossy situation, it is possible to have a fully localized eigenstate, provided that $t_{1,m} = 0$. Note that this can be achieved for any value of the energy, by means of choosing the adequate distance between the qubits. The fully localized state obtained in such way is a dark state with respect to the waveguide, meaning that its

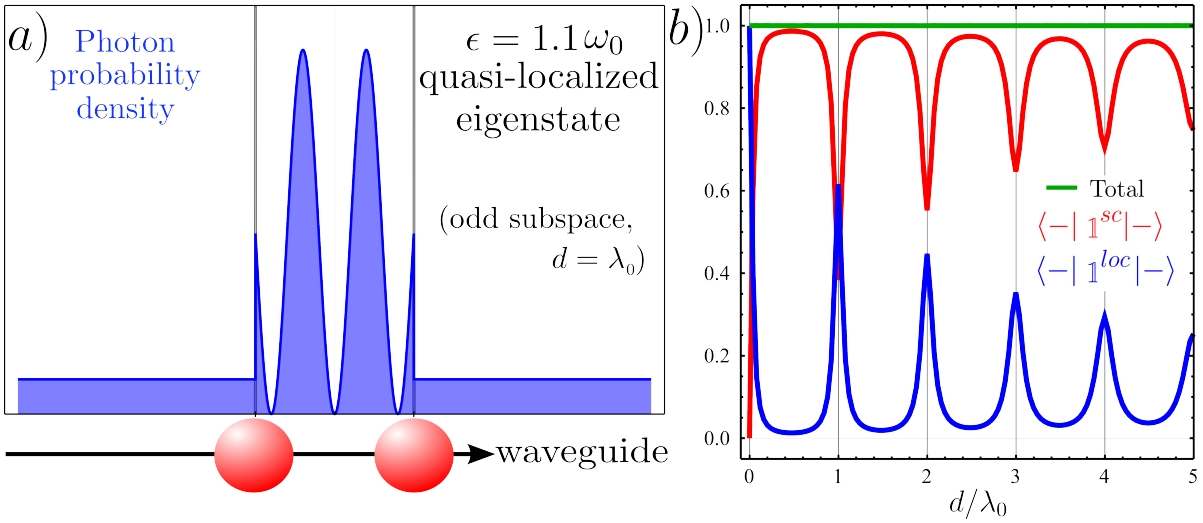

Figure 2.6: a) Photon position probability density for a quasi-localized eigenstate with energy $\epsilon = 1.1\omega_0$. b) Completeness check ($\gamma = 10^{-1}\omega_0, \beta = 0.98$). The contribution of the scattering branch (red line) is incomplete for any value of the qubit-qubit separation d. The basis is complete only when the quasi-localized branch of eigenstates (blue) is taken into account.

photonic contribution is fully confined between both qubits and uncoupled from the propagating waveguide modes. On the other hand, this state is not fully dark, since it still decays into the lossy reservoir at a rate Γ. Although a dark state of this kind can exist for any energy, the case of resonant conditions ($\epsilon = \omega_0, d = d_{\text{res}}$) is the most convenient for entanglement generation, for two main reasons. First, our entanglement generation scheme relies on initially exciting one of the qubits, therefore the emitted photons have a frequency spectrum centred at $\epsilon = \omega_0$. Second, the resonant conditions maximize the qubit populations according to Eq. 2.58, a fact which is advantageous for our protocol. We will therefore restrict to this case in forthcoming sections.

Finally, we can construct again the closure relation and study the contribution of both the localized and the scattering branches for an initial state with non-zero qubit component, which we again choose to be $|-\rangle$. The closure relation is calculated in an analogous way as in the lossless section, its final expression being

$$\mathbb{1} = \sum_{m=e,o} \sum_{b=sc,loc} \frac{1}{2\pi v_g} \int d\epsilon |\epsilon_m^b\rangle\langle\epsilon_m^b|. \tag{2.61}$$

The only difference between the above expression and its lossless counterpart in Eq. 2.44 is the continuous character of the quasi-localized branch. The appearance of a sum over the two branches, namely scattering and quasi-localized, simplifies the separation of the contributions of both these branches. In Fig. 2.6b we depict both of these contributions,

showing that indeed the quasi-localized branch must be included in a complete description of our problem, for any qubit-qubit separation d. Additionally, the results depicted in the figure demonstrate how the set of scattering and quasi-localized eigenstates form a complete basis.

As a final step toward studying the time evolution of the system variables, we must construct the time evolution operator $U(t)$. This operator determines the evolution of any initial state according to $|\psi(t)\rangle = U(t)|\psi(0)\rangle$, and is expressed formally as [29]

$$U(t) = e^{-iHt}. \tag{2.62}$$

An explicit expression can be obtained in a straightforward manner by employing the closure relation above, Eq. 2.61,

$$U(t) = \sum_{m=e,o} \sum_{b=sc,loc} \frac{1}{2\pi v_g} \int d\epsilon e^{-i\epsilon t} |\epsilon_m^b\rangle\langle\epsilon_m^b|, \tag{2.63}$$

The above equation will be employed for any time-dependent calculation in the following sections.

2.3.4. Solution for chiral couplings.

One of the aspects in which the versatility of waveguide systems will be useful for entanglement generation purposes is the directionality of the qubit-photon coupling. Several experimental works have demonstrated the possibility of chirally coupling quantum emitters to waveguides [72, 108, 204–206], inducing a preferential emission direction. Physically, this implies that our qubits have different coupling rates to right- and left-propagating photons, as depicted in Fig. 2.7. In this section we detail the diagonalization of the Hamiltonian in the case of chiral couplings.

In the absence of losses Γ, the Hamiltonian of the system in Fig. 2.7 is a modified version of the non-chiral expression 2.23,

$$\begin{aligned} H = -iv_g \int dx \left(c_R^\dagger(x) \frac{\partial}{\partial x} c_R(x) - c_L^\dagger(x) \frac{\partial}{\partial x} c_L(x) \right) + \sum_j \omega_j \sigma_j^\dagger \sigma_j + \\ + \sum_{j=1,2} \sum_{\alpha=R,L} V_{j\alpha} \int dx \delta(x - x_j) \left(c_\alpha^\dagger(x) \sigma_j + H.c. \right). \end{aligned} \tag{2.64}$$

Here, the first term, which describes the energy of the photonic modes, remains unchanged with respect to the non-chiral case. The second term is only modified to include an extra degree of freedom, namely a different frequency ω_j for both of the qubits, as

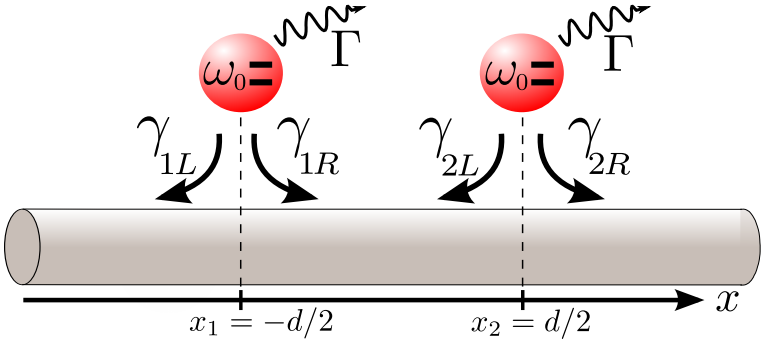

Figure 2.7: Scheme of the most general system for entanglement generation. The two qubits are chirally coupled to the waveguide, so that they interact with left- and right-propagating photons at a different rate.

this will be needed later on. Finally, the interaction term keeps its general form, but with independent coupling constants $V_{j\alpha}$ between qubit j and α-propagating photons. In this case, we have four coupling rates given by $\gamma_{j\alpha} = V_{j\alpha}^2/v_g$ $(j = 1, 2; \alpha = R, L)$, which define the figures of merit in chiral waveguide systems, namely the directionalities

$$D_j = \frac{\gamma_{jR} - \gamma_{jL}}{\gamma_{jR} + \gamma_{jL}}. \tag{2.65}$$

The diagonalization of the Hamiltonian 2.64 follows a similar procedure as the one detailed in the non-chiral case, although some fundamental differences deserve our attention. First, note that in this case the Hamiltonian is not parity-symmetric, and therefore the even/odd subspaces are not independent. Hence, we must tackle the whole problem by assuming the following general form for the single-excitation eigenstate,

$$|\epsilon\rangle = \left(\sum_{j=1,2} \alpha_j \sigma_j^\dagger + \sum_{\alpha=R,L} \int dx \phi_\alpha(x) c_\alpha^\dagger(x) \right) |0\rangle. \tag{2.66}$$

In the same way as described above, we apply the time-independent Schrödinger equation $H|\epsilon\rangle = \epsilon|\epsilon\rangle$ to obtain a system of differential equations. We can then substitute the photonic wavefunctions $\phi_\alpha(x)$ by their corresponding piecewise plane-wave expressions,

$$\phi_R(x) = e^{i\epsilon x/v_g} \begin{cases} A & \text{for} \quad x < -d/2 \\ B & \text{for} \quad -d/2 < x < d/2 \\ C & \text{for} \quad d/2 < x, \end{cases} \tag{2.67}$$

$$\phi_L(x) = e^{-i\epsilon x/v_g} \begin{cases} D & \text{for} \quad x < -d/2 \\ E & \text{for} \quad -d/2 < x < d/2 \\ F & \text{for} \quad d/2 < x, \end{cases} \tag{2.68}$$

to obtain an algebraic system of 6 equations for the 8 unknown coefficients $\{\alpha_1, \alpha_2, A, B, C, D, E, F\}$. Again, this system is indeterminate, and hence we can choose two of these coefficients to label the different branches of eigenstates. The natural choice are A and F, since the resulting eigenstates have a clear physical interpretation: for $A \neq 0$ and $F = 0$ the state $|\epsilon\rangle$ describes a scattering eigenstate where the incoming photon is impinging over the two qubits from $x = -\infty$. Conversely, the state corresponding to $A = 0$, $F \neq 0$ is an additional scattering eigenstate where the incoming photon travels leftwards from $x = \infty$. We name these two scattering branches $|\epsilon_{\rightarrow}\rangle$ and $|\epsilon_{\leftarrow}\rangle$, respectively.

The coefficients of these eigenstates can be written as a function of the two following quantities,

$$f_1(\epsilon) = e^{-i\epsilon d/2v_g} \frac{\left(\epsilon - \omega_2 + i\frac{\gamma_{2R}+\gamma_{2L}}{2} - ie^{i2\epsilon d/v_g}\tilde{\gamma}^2/\gamma_{1R}\right)}{(\epsilon - \omega_1 + i(\gamma_{1R}+\gamma_{1L})/2)(\epsilon - \omega_2 + i(\gamma_{2R}+\gamma_{2L})/2) + \tilde{\gamma}^2 e^{i2\epsilon d/v_g}}, \quad (2.69)$$

$$f_2(\epsilon) = e^{i\epsilon d/2v_g} \frac{\left(\epsilon - \omega_1 + i\frac{\gamma_{1L}-\gamma_{1R}}{2}\right)}{(\epsilon - \omega_1 + i(\gamma_{1R}+\gamma_{1L})/2)(\epsilon - \omega_2 + i(\gamma_{2R}+\gamma_{2L})/2) + \tilde{\gamma}^2 e^{i2\epsilon d/v_g}}, \quad (2.70)$$

where $\tilde{\gamma}^2 = \sqrt{\gamma_{2R}\gamma_{2L}\gamma_{1R}\gamma_{1L}}$. For the branch of eigenstates $|\epsilon_{\rightarrow}\rangle$, the coefficients normalized to A read

$$\alpha_j^{(\rightarrow)} = V_{jR} f_j, \quad (2.71)$$

$$B^{(\rightarrow)} = 1 - i\gamma_{1R} e^{i\phi} f_1, \quad (2.72)$$

$$C^{(\rightarrow)} = B^{(\rightarrow)} - i\gamma_{2R} e^{-i\phi} f_2, \quad (2.73)$$

$$E^{(\rightarrow)} = -ie^{i\phi}\sqrt{\gamma_{2R}\gamma_{2L}} f_2, \quad (2.74)$$

$$D^{(\rightarrow)} = E^{(\rightarrow)} - ie^{-i\phi}\sqrt{\gamma_{1R}\gamma_{1L}} f_1. \quad (2.75)$$

The coefficients of the second branch, $|\epsilon_{\leftarrow}\rangle$, are normalized to F in this case, and related to the coefficients above in the following way,

$$\begin{pmatrix} \alpha_1^{(\leftarrow)} \\ \alpha_2^{(\leftarrow)} \\ E^{(\leftarrow)} \\ D^{(\leftarrow)} \\ C^{(\leftarrow)} \\ B^{(\leftarrow)} \\ A^{(\leftarrow)} \end{pmatrix} = \mathcal{P} \begin{pmatrix} \alpha_2^{(\rightarrow)} \\ \alpha_1^{(\rightarrow)} \\ B^{(\rightarrow)} \\ C^{(\rightarrow)} \\ D^{(\rightarrow)} \\ E^{(\rightarrow)} \\ F^{(\rightarrow)} \end{pmatrix}, \quad (2.76)$$

where the left-to-right transformation $\mathcal{P}$ exchanges the frequencies and coupling rates according to $\{\omega_1, \omega_2, \gamma_{1R}, \gamma_{1L}, \gamma_{2R}, \gamma_{2L}\} \rightarrow \{\omega_2, \omega_1, \gamma_{2L}, \gamma_{2R}, \gamma_{1L}, \gamma_{1R}\}$ (see appendix A).

An interesting feature of the chiral Hamiltonian 2.64 is the absence of any localized states. Indeed, the existence of a solution for $A = F = 0$ necessarily implies $\gamma_{jR} = \gamma_{jL}$ for both $j = 1, 2$, and hence no dark state can arise in the chiral situation. This is understood by revisiting the non-chiral system, where a photon could be trapped between the qubits forming a dark state. Such possibility relied on the effect of perfect reflection of a resonant photon impinging over the qubits, which in turn was caused by a destructive interference in transmission. In the case of chiral coupling, however, the perfect reflection phenomenon disappears, since the imbalance between right- and left- coupling rates prevents the interference to be fully destructive, as demonstrated in appendix A. Therefore, no photonic state trapped between the qubits can be stationary. The absence of any localized eigenstate implies that a complete basis can be constructed with scattering eigenstates, thus easing the introduction of the qubit losses Γ. Indeed, in the previous section we have already demonstrated how for scattering states the losses could be introduced simply by adding a non-Hermitian contribution to the frequency of the qubits,

$$\omega_j \to \omega_j - i\Gamma/2. \tag{2.77}$$

By introducing the decay Γ in the above way, the diagonalization of the Hamiltonian is therefore complete.

A final remark is necessary before constructing the time-evolution operator, regarding the orthogonality of the two scattering branches we have obtained. In the chiral coupling case, the two scattering branches $|\epsilon_R\rangle$ and $|\epsilon_L\rangle$ are certainly linearly independent, since they are not a multiple of each other. However, they are not orthogonal, as they are not related through a symmetry operator of the Hamiltonian. Therefore, in order to construct the time evolution operator we must define the following overlap matrix,

$$S_{\alpha\beta} = \lim_{L\to\infty} \frac{\langle \epsilon_\alpha | \epsilon_\beta \rangle}{L}, \tag{2.78}$$

which can be analytically calculated. The time-evolution operator takes now the more involved expression

$$U(t) = \frac{1}{2\pi v_g} \sum_{\alpha,\beta=R,L} \int d\epsilon e^{-i\epsilon t} |\epsilon_\alpha\rangle \left(S^{-1}\right)_{\alpha\beta} \langle \epsilon_\beta|. \tag{2.79}$$

Finally, we can numerically determine that $U(0) = \mathbb{1}$, thus demonstrating the completeness of the basis formed by the two scattering branches.

2.4. Non-Markovian dynamics in entanglement generation

This section is devoted to a detailed study of the problem of spontaneous entanglement generation in terms of the full Hamiltonian formalism developed in the previous section. First, we will show how our model is able to recover the results obtained within the Master Equation picture in the adequate limit, namely $\gamma d/v_g \ll 1$. After, we will demonstrate how non-Markovian dynamics arise for large qubit-qubit separations, d, or large couplings, γ. Such effects, disregarded within the global Markov approximation, worsen the entanglement generation scheme and, in many physical systems, have to be taken into account.

The system we study in the first case is non-chiral, and therefore the time evolution operator is given by Eq. 2.63. We assume that qubit 1 is initially excited whereas qubit 2 is in the ground state, i.e., $|\psi(0)\rangle = |e_1\rangle \otimes |g_2\rangle$. By applying the time evolution operator $U(t)$ we can explicitly calculate the wavefunction of the system at any time. Since we are interested both in the dynamics of the qubit populations and in the Wootters concurrence C, we have to calculate the reduced density matrix of the two-qubit ensemble. We start with the definition of the density operator of the whole qubit+photon system,

$$\rho_t = |\psi(t)\rangle\langle\psi(t)|. \tag{2.80}$$

In order to obtain the reduced density operator for the two qubits, we must take the partial trace over the photonic modes, which in the position basis reads

$$\rho = \langle\emptyset|\rho_t|\emptyset\rangle + \sum_{\alpha=e,o}\int dx \langle\emptyset|c_\alpha(x)\rho_t c_\alpha^\dagger(x)|\emptyset\rangle. \tag{2.81}$$

The first and second terms in the expression above describe the contributions of the zero- and one-photon subspaces, respectively. Since the state $|\psi(t)\rangle$ never abandons the single-excitation Fock subspace, it is not necessary to include further terms in the partial trace. Finally, for the reduced density matrix determined in this way, the Concurrence can be explicitly calculated through its definition 2.19 as

$$C(t) = \frac{1}{2}\sqrt{[\rho_{++}(t) - \rho_{--}(t)]^2 + 4\mathrm{Im}\,[\rho_{+-}(t)]^2}, \tag{2.82}$$

where the individual elements of the density matrix are defined as $\rho_{ij} = \langle i|\rho|j\rangle$, and the sub- and superradiant states $|\pm\rangle$ have been defined in Eq. 2.18.

The dynamics of both the qubit populations and the Concurrence will be characterized by different intrinsic timescales. First, the inverse of the total emission rate of the qubits, $(2\gamma+\Gamma)^{-1}$. As we are interested in a system of qubits efficiently coupled to the waveguide modes, along this section we will keep the ratio Γ/γ fixed at $\Gamma = 0.1\gamma$, corresponding to a Purcell factor of $P_F = 21$ ($\beta = 0.95$). Although such β factors are slightly above the typical values in dielectric waveguides [207, 208], similar or larger Purcell enhancements have been reported in many other systems such as photonic crystal waveguides [209, 210], and slot [189] and plasmonic waveguides [211]. Apart from the intrinsic timescale $(2\gamma + \Gamma)^{-1}$, a second characteristic time arises due to the collective interaction between both qubits. Specifically, when more than one qubit is present in the vicinities of the waveguide, the propagation of the photons between both emitters requires a finite time d/v_g. Since the qubit-qubit interaction in our system is mediated by virtual photons, this retardation time will have a relevant role. The combination of these timescales will determine the system dynamics, as we will see below.

The full Hamiltonian picture we have developed in the previous section is able to recover the Master Equation predictions, as we illustrate in Fig. 2.8. Here, the qubit-waveguide coupling is very small as compared to the frequency of the qubits, $\gamma = 10^{-5}\omega_0$. Such a narrow emission linewidth is often characteristic of QEs in the optical range [22]. In panel 2.8a, we recover the results obtained within the Master Equation formalism in the case of purely coherent interaction (compare with Fig. 2.3a). In this situation, the rapid decay of the concurrence is a natural consequence of the non-resonant separation $d = \lambda_0/4$. For such a separation between the qubits, no dark state arises, and therefore the two single-excitation qubit states, namely $|+\rangle$ and $|-\rangle$, decay into guided modes. Note that for the particular separation considered in the figure, $d = \lambda_0/4$, the transmission probabilities $|t_{0,e}|^2$ and $|t_{0,o}|^2$ are equal. This indicates that the qubit-qubit cavity is as badly suited for confining odd photons than for confining even photons, since the distance d lies at the middle point between the closest even resonant value, $d = \lambda_0/2$, and the closest odd resonant value, $d = 0$. As a consequence, photons abandon the region between qubits at the same pace in both subspaces, and the populations ρ_{++} and ρ_{--} decay exactly at the same rate.

An example of the system dynamics for a resonant separation is shown in Fig. 2.8b, where $d = \lambda_0/2$. In this panel, the results of incoherent entanglement generation obtained in panel 2.3b are recovered, the only difference being a slow decay of the Concurrence due to the (now included) losses to free space Γ. The localized dark state in this situation is the state $|+\rangle$, whereas the superradiant state $|-\rangle$ decays at a rate $4\gamma + \Gamma$. Again, the entanglement dynamics is understood in terms of the localized dark state, as the initial

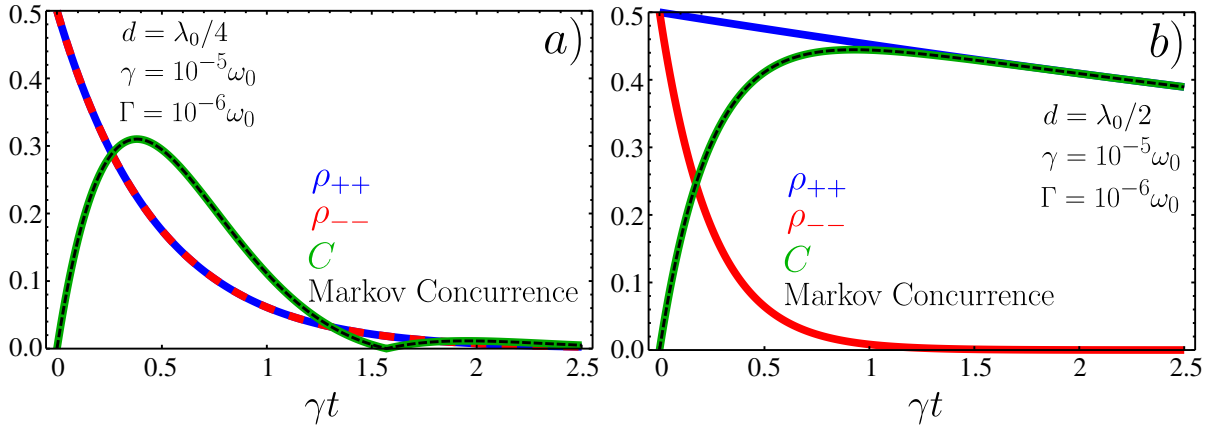

Figure 2.8: Dynamics of the two qubit ensemble initialized in the state $|e_1\rangle \otimes |g_2\rangle$, for an off-resonant separation $d = \lambda_0/4$ (panel a) and a resonant separation $d = \lambda_0/2$ (panel b). The blue and red curves show the population of the states $|+\rangle$ and $|-\rangle$, respectively. The green and dashed curves represent the generated Concurrence calculated using the full Hamiltonian picture and the Master Equation formalism, respectively.

population is evenly distributed between the superradiant state, characterized by a fast decay, and the dark state, which remains populated at long times. After the population of the state $|-\rangle$ abandons the vicinities of two-qubit ensemble, the entangled state $|+\rangle$ remains populated. As a consequence, qubit-qubit entanglement is generated due to an imbalance between the decay rates of the states $|+\rangle$ and $|-\rangle$.

It is insightful to calculate in this case the contribution of the localized state to the system dynamics, in a similar fashion as we did in Eq. (2.46). Although the full lossy formalism is employed in this section, for a more transparent explanation we will estimate such contribution by using the lossless expressions, where only a single, well defined dark state arises. In this situation, it is straightforward to show that

$$\left|\langle\psi(0)|\omega^L_{0,n}\rangle\right|^2 = \frac{1}{2} \times \frac{1}{1+|t_{0,e}/\alpha_e|^2}\delta(d - n\lambda_0/2) = \frac{1}{2} \times \frac{\delta(d-n\lambda_0/2)}{1+2\pi(\gamma/\omega_0)(d/\lambda_0)}. \tag{2.83}$$

The prefactor $1/2$ in the expression above arises from our particular choice of initial state, namely $|\psi(0)\rangle = (|+\rangle + |-\rangle)/\sqrt{2}$. Since the localized dark state belongs exclusively to either the even or the odd subspace, its contribution is upper bounded by $1/2$ as described by Eq. 2.83. Note that, for the parameters used in Fig. 2.8b, we have $|\langle\psi(0)|\omega^L_0\rangle|^2 \approx 1/2$. On the other hand, if we increase either the coupling γ or the separation between qubits, d, the contribution of the dark state becomes less important and, conversely, the relevance of the scattering states increases. This will be the origin of the non-Markovian effects we will see below. Note also that, in the limit of small γd, the localized state has practically

no photonic part since $|t_{0,e}/\alpha_e|^2 \ll 1$. It is now clear why in such regime the Master Equation results are recovered. First, for $\gamma d \ll v_g$, the photonic part of the localized state does not play any significant role in the dynamics, and the Markovian picture of the dark state as a pure qubit state, in this case $|+\rangle$, is very accurate. Second, in the limit $\gamma d \ll v_g$, the time required for a photon to travel from one qubit to another is much smaller than the respective lifetimes of both qubits. As a consequence, the photons mediating the interaction arrive instantaneously from qubit 1 to qubit 2, and the collective dynamics described by the Master Equation is turned on at time $t \approx 0$. As we will see below, both the above statements will lose validity when we abandon this regime, an effect which will give rise to non-Markovian effects.

According to the explanation above, upon increasing the coupling γ the Master Equation formalism begins to be inaccurate. This is illustrated in panel 2.9a, where we show the population dynamics and the concurrence as a function of time, when the qubit-qubit separation is resonant ($d = \lambda_0$) and the coupling is increased to $\gamma = 0.01\omega_0$. Note that, as opposed to the previous case, in this situation the dark state lies within the odd subspace. Interestingly, for very short times the populations ρ_{++} and ρ_{--} decay at the same rate, and they evolve differently from $t = d/v_g$ onwards. This is a natural retardation effect induced by the fast decay time of the qubits, $\sim 1/2\gamma$, which is now comparable to the time employed by the photons to cover the qubit-qubit separation. In other words, for such a large coupling γ, the first qubit has time to decay appreciably *before* the photons have time to reach qubit 2. As a consequence, both the qubit-qubit interaction and the corresponding collective effects turn on at a certain delayed time. This retardation effect is intrinsically non-Markovian and therefore impossible to predict by a Master Equation formalism. Besides retardation, note that according to Eq. (2.83), the contribution of the dark state to the total population is $\left|\langle\psi(0)|\omega_0^L\rangle\right|^2 \approx (1/2)0.94$. This implies that an appreciable amount of probability ($\sim 3\%$), which previously remained in the dark state, is now emitted in the form of odd-parity propagating photons. This leakage stems from the increased emission linewidth 2γ of the emitters, which spreads the emitted photonic population over a broader frequency range and, consequently, reduces the photonic occupation at the resonant frequency ω_0. Naturally, any emitted population out of resonance with respect to the frequency of the QEs does not fulfil the resonant conditions, and will eventually abandon the qubit-qubit cavity. Thus, the fraction of the emitted photonic population which remains trapped between both qubits decreases as compared with the Markovian case, and with it the population of the entangled dark state. Both the photon retardation and the spectral widening of the qubits is detrimental for entanglement generation since, as Fig. 2.9a shows, they result in lower values for the Concurrence.

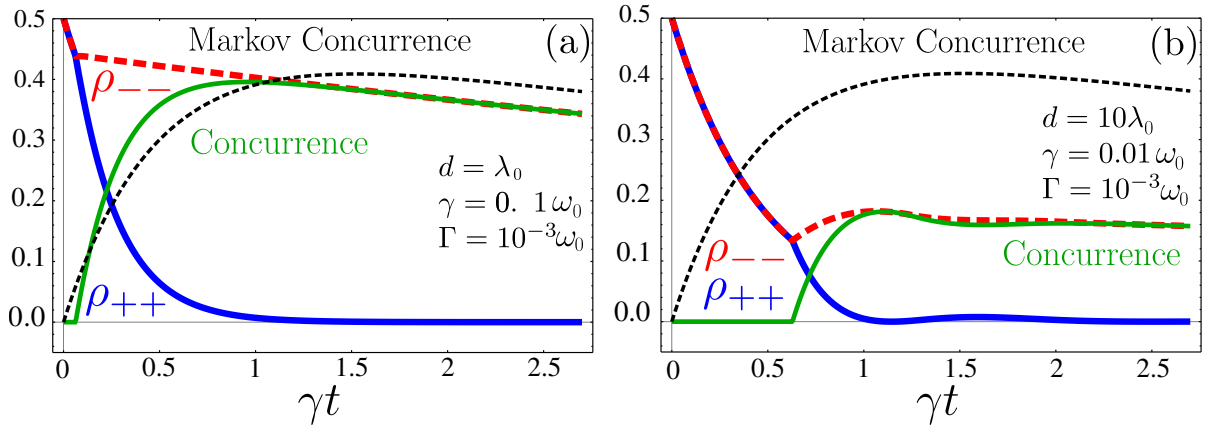

Figure 2.9: Non-Markovian dynamics of the two qubit ensemble initialized in the state $|e_1\rangle \otimes |g_2\rangle$, for a coupling rate $\gamma = 0.01\omega_0$ and separations $d = \lambda_0$ (panel a) and $d = 10\lambda_0$ (panel b). The blue and red curves show the population of the states $|+\rangle$ and $|-\rangle$, respectively. The green and dashed curves represent the generated Concurrence calculated using the full Hamiltonian picture and the Master Equation formalism, respectively.

The non-Markovian effects can be also enhanced by increasing the separation between the qubits, d (Fig. 2.9b), as this increases the time required for the photons to cover the distance between both qubits. Here, the Master Equation predictions completely fail to describe the behavior of the concurrence, which always remains below $C \approx 0.2$ within the complete formalism. Note that, in this situation, after the collective interaction is turned on, small beats can be observed in both the populations and the concurrence. Such oscillations arise when the first qubit has decayed significantly before the emitted photonic probability has reached emitter 2. Under these conditions a well-defined photonic wavepacket is formed, with a large spectral width given by 2γ. Since qubit 2 also has a large linewidth $\sim 2\gamma$, the photonic components with energies very close to ω_0 are likely to be reflected by qubit 2, oscillating back and forth a certain number of times before eventually leaving the qubit-qubit cavity. These metastable quasi-resonant photons induce a population exchange between the qubits, which eventually fades away when these photons abandon the vicinities of the QEs. The transient population exchange is the reason behind the oscillatory behavior observed in Fig. 2.9b.

Finally, an extremely non-Markovian case is shown in Fig. 2.10. For this combination of parameters, the populations of the states $|+\rangle$ and $|-\rangle$ evolve in a very similar way. First, both of them decay almost to zero, corresponding to a full decay of qubit 1 before the emitted photonic wavepacket is able to reach qubit 2. A full photonic wavepacket is therefore sent towards the second qubit and, by a process of reflection, bounces back

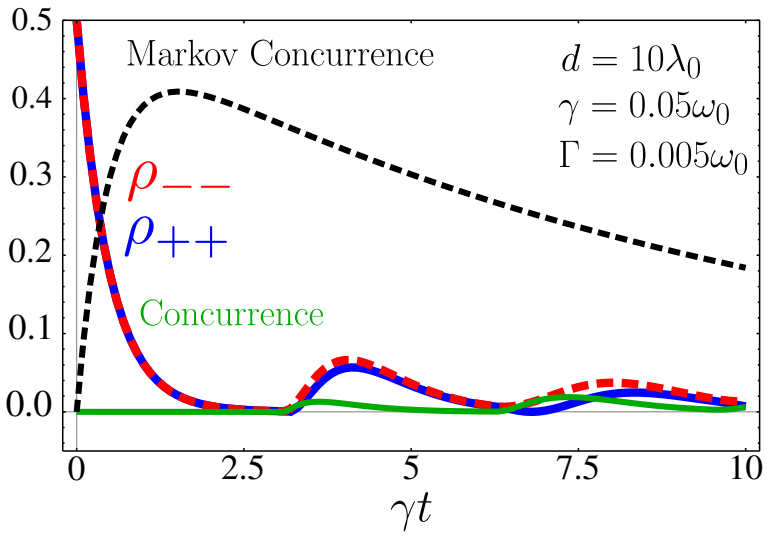

Figure 2.10: Extremely non-Markovian dynamics of the two qubit ensemble initialized in the state $|e_1\rangle \otimes |g_2\rangle$, for a coupling rate $\gamma = 0.05\omega_0$ and a separation $d = 10\lambda_0$. The blue and red curves show the population of the states $|+\rangle$ and $|-\rangle$, respectively. The green and dashed curves represent the generated Concurrence calculated using the full Hamiltonian picture and the Master Equation formalism, respectively.

and forth between both emitters, practically exciting only one at a time. This produces the sudden increases in both populations observed in the figure. Such population beats last for a very long time, since the extremely high coupling γ largely widens the reflectivity spectrum of the qubits. The photonic modes close to resonance are therefore very efficiently trapped between the QEs and only leak out for long times in the form of propagating photons. In the long time limit, the oscillations in the populations do eventually decay but, since almost no population remains in the qubit state $|-\rangle$, the concurrence will reach only extremely low values. In practice, this regime is thus characterized by an absence of collective behavior, in which the qubits behave mainly as individual entities and no correlations are able to arise.

One of the advantages of the full Hamiltonian picture we have developed is the possibility of studying also the dynamics of the photonic degrees of freedom in order to check the conclusions drawn above. In Fig. 2.11, we display the photon position probability density associated with the three regimes previously considered, namely full Markovian dynamics, retarded collective behavior, and no collective interaction at all. The first of these cases is shown in panel 2.11a, where the two qubits appear at the origin because of the stretched horizontal scale. This situation is characterized by an instantaneous rising of the collective state, in agreement with the Markovian predictions. Since the decay

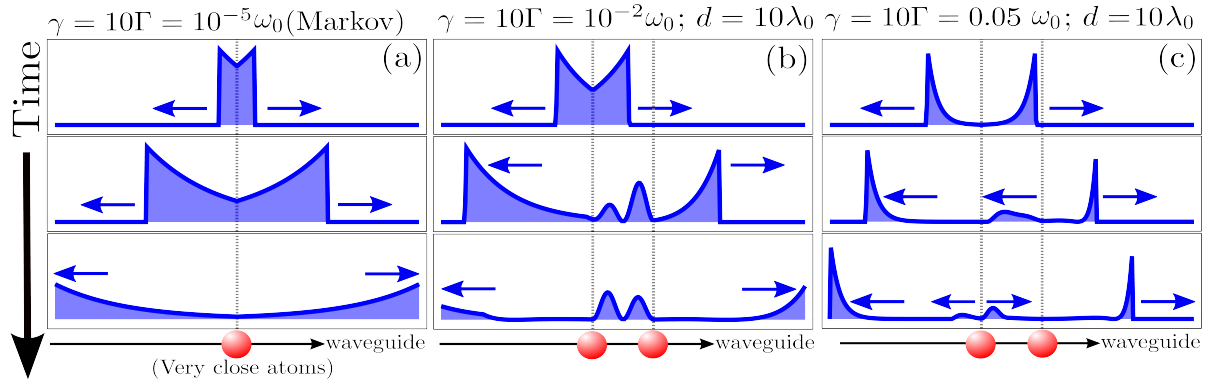

Figure 2.11: Photonic position probability density at different times. a) Markovian case. The collective regime starts instantaneously between the two qubits (here not distinguishable because of the stretched horizontal axis). b) Retarded interaction. After a few bounces back and forth, only the localized state remains. c) Extremely non-Markovian case. The collective interaction arises only for very long times, and plays a minor role in the dynamics.

rate of qubit 1 is small, the photons can reach the second qubit and establish the collective regime before the first emitter decays significantly. Therefore, the dark state $|-\rangle$ becomes uncoupled from the waveguide at $t \approx 0$. Conversely, the superradiant state $|+\rangle$ is formed instantaneously, and decays into guided modes in a similar fashion as a single qubit, but with a decay rate twice as large. This is reproduced by the emission profile in panel 2.11a, which mimics the single-qubit situation and thus confirms the collective behavior characteristic of Markovian dynamics.

The retarded collective regime is displayed in Fig. 2.11b. The first frame shows an early time, where qubit 1 is decaying into guided modes while qubit 2 is not yet playing any role in the dynamics. When the wavefront reaches the second emitter, a fraction of the population is reflected back towards qubit 1, interfering with the still incoming wavepacket. The photonic probability will bounce back and forth for some time and, eventually, all the probability not occupying the dark state will abandon the vicinities of the qubits. The last frame in panel 2.11b shows the long time behavior, where the resonant photons trapped between the qubits have reached the standing wave pattern characteristic of the localized state. Such photonic population profile will remain unchanged during the rest of the time evolution, apart from a slow global decay into free-space modes. Finally, the extremely non-Markovian case corresponding to Fig. 2.10 is shown in panel 2.11c. Here, no standing wave pattern is appreciable since the emitted photonic wavepacket has a very narrow spatial extension. In this case, the collective regime will be achieved only for very long times, were the tiny photonic contribution at the resonant frequency will

be the only one remaining population in the vicinities of the qubits.

To summarize, we have observed how non-Markovian behavior arises basically due to a competition between two timescales, namely the decay time of a single qubit $\approx 1/2\gamma$, and the delay time before the collective interaction arises, d/v_g. The ratio between these two quantities, $2\pi(\gamma/\omega_0)(d/\lambda_0)$, determines the system dynamical regime. In particular, the combination of two effects gives rise to non-Markovian behavior. First, the retarded onset of the collective interaction, which uncouples the dark state from the waveguide only after the delay time described above. Second, the large qubit linewidth γ, which results in an emitted wavepacket largely distributed in frequencies and, consequently, on a smaller contribution of the localized dark state, key for the long-lived entanglement generation. Thus, a large value of either γ or d has been shown to reduce drastically the accuracy of the Master Equation formalism. Non-Markovian effects decrease the efficiency of the entanglement generation scheme, with values of the concurrence that can lie well below the Markovian predictions. Note that the generated entanglement is also worsened by the presence of the losses Γ. In the same fashion, the propagation losses of the guided modes, which we have not considered here, would further reduce the generated concurrence, especially for long qubit-qubit separations d.

Let us discuss briefly on the relevance of the non-Markovian effects in realistic systems. First, note that the majority of setups operating in the optical range lie well within the Markovian regime, since the usual coupling rates rarely exceed $\gamma \approx 10^{-5}\omega_0$ [22]. In such systems, any inaccuracy in the Master Equation predictions would therefore arise only for extremely large qubit-qubit separations, $d \approx 10^4 - 10^5\lambda_0$. In usual experiments, however, much smaller separations are chosen in order to minimize the photon propagation losses. For these reasons, a Markovian formalism is very well suited to reproduce any system both in the optical or in the telecom (i.e., near infrared) regimes. On the other hand, non-Markovian effects could have an impact on the second relevant set of systems recently developed for quantum applications, namely microwave striplines attached to superconducting qubits. In such systems, couplings up to $\gamma \approx 0.01\omega_0$ have been reported [212] and, moreover, theoretical studies have predicted significantly larger values [213]. Here, for not so large qubit-qubit separations ($d \approx 10\lambda_0$), the Markovian regime is abandoned and the generated entanglement decreases. Note that the arising of non-Markovian effects has been already addressed to a first order approximation in ref. [77], which also contains a set of proposals for hybrid systems in the optical range where such effects could in principle be observable. Finally, let us remark that, although our formalism in the position basis is not necessarily required for optical waveguide systems, the explicit inclusion of the photonic degrees of freedom opens many possibilities from

the theoretical point of view, allowing e.g. for controlled photonic inputs. This degree of control will be exploited in chapter 3.

2.5. Entanglement generation with chiral qubit-waveguide couplings.

In the section above we have demonstrated how non-Markovian effects could severely reduce the efficiency of the entanglement generation scheme. Additionally, the existence of a long-lived entangled state relies on an extremely precise tuning of the qubit-qubit parameters into a resonant condition, namely identical transition frequencies ω_0, and resonant separations $d = d_{res}$. These reasons make the above protocol challenging to implement in some realistic setups, and motivate the exploration of alternative schemes with less pronounced sensitivity to external parameters. In this section we explore the possibility of spontaneous entanglement generation between qubits chirally coupled to a waveguide.

The system Hamiltonian in the chiral situation has already been diagonalized in section 2.3. There, we have demonstrated how, as opposed to the case of symmetric coupling, no localized dark state arises. Hence, we can expect the qubit dynamics not to depend so strongly on the coupling to a single, particular state. This suggests that non-Markovian effects do not affect the entanglement generation scheme in such a drastic way as in the non-chiral situation, a hypothesis that we will verify later on. Based on this supposition, we will describe the system in a first approximation by means of a Master Equation, leaving the full Hamiltonian solution for later discussion.

In the case of chiral coupling, this equation takes a more involved form than expression 2.13, namely [214]

$$\dot{\rho} = -i\left[H_{qb}, \rho\right] + \sum_{j=1,2} \gamma_j \mathcal{L}_{\sigma_j,\sigma_j}[\rho] + \sqrt{\gamma_{2R}\gamma_{1R}}\mathcal{L}_{\sigma_2,\sigma_1}[\rho] + \sqrt{\gamma_{2L}\gamma_{1L}}\mathcal{L}_{\sigma_1,\sigma_2}[\rho], \tag{2.84}$$

where we define $\gamma_j \equiv \left(\gamma_{jR} + \gamma_{jL}\right)/2$. The bare Hamiltonian of the qubits is given by $H_{qb} = \omega_0(\sigma_1^\dagger\sigma_1 + \sigma_2^\dagger\sigma_2)$ where, unless stated otherwise, the qubits are assumed to have the same frequency ω_0 for simplicity. In the above expression, the generalized Lindblad superoperators, $\mathcal{L}_{\sigma_a,\sigma_b}[\rho]$, are expressed as

$$\mathcal{L}_{\sigma_a,\sigma_b}[\rho] = \left(e^{-i2\pi l_{ab}}[\sigma_a, \rho\sigma_b^\dagger] - e^{i2\pi l_{ab}}[\sigma_a^\dagger, \sigma_b\rho]\right), \tag{2.85}$$

where $l_{ab} \equiv |x_a - x_b|/\lambda_0$. Due to the phase factor $2\pi l_{ab}$, the Lindblad terms contain a real and an imaginary part which originate, respectively, the coherent and incoherent

interaction contributions in the Master Equation. Note that in the non-chiral limit $\gamma_{jR} = \gamma_{jL}$ the usual expression 2.13 is recovered. In order to focus on the fundamental aspects of the chiral system, we will first particularize our study to the lossless case (i.e., $\beta_j = 1$), including the losses in the second part of the work.

Since dark states do not arise in the chiral situation, there is no particular advantage in using the even and odd basis. Hence, we will work in the basis of product states given by $\{|0\rangle, |1\rangle \equiv \sigma_1^\dagger|0\rangle, |2\rangle \equiv \sigma_2^\dagger|0\rangle, |3\rangle \equiv \sigma_1^\dagger\sigma_2^\dagger|0\rangle\}$. After expressing the density operator ρ in such basis, a careful examination of equation 2.84 reveals that the only non-zero elements are the populations ρ_{00}, ρ_{11}, and ρ_{22}, as well as the coherence ρ_{12}. Three of these quantities are coupled through the following system of differential equations,

$$\dot{\rho}_{11} = -2\gamma_1\rho_{11} - \sqrt{\gamma_{1L}\gamma_{2L}}\left(e^{i2\pi\tilde{d}}\rho_{21} + e^{-i2\pi\tilde{d}}\rho_{12}\right), \tag{2.86}$$

$$\dot{\rho}_{22} = -2\gamma_2\rho_{22} - \sqrt{\gamma_{1R}\gamma_{2R}}\left(e^{i2\pi\tilde{d}}\rho_{12} + e^{-i2\pi\tilde{d}}\rho_{21}\right), \tag{2.87}$$

$$\dot{\rho}_{12} = -(\gamma_1 + \gamma_2)\rho_{12} - \sqrt{\gamma_{1R}\gamma_{2R}}\rho_{11}e^{-i2\pi\tilde{d}} - \sqrt{\gamma_{1L}\gamma_{2L}}\rho_{22}e^{i2\pi\tilde{d}}, \tag{2.88}$$

with the normalized distance $\tilde{d} = d/\lambda_0$. The remaining component of the density matrix is obtained by conservation of probability, $\rho_{00} = 1 - \rho_{11} - \rho_{22}$. Once the above equations are solved, we can compute the qubit-qubit entanglement by means of the Concurrence, which in this basis takes the very simple form $C = 2|\rho_{12}|$, equivalent to Eq. 2.82. When the total couplings γ_1 and γ_2 are equal, the system of equations 2.86-2.88 can be analytically solved, and the concurrence as a function of the directionalities D_1 and D_2 can be expressed as

$$[C(t)]^2 = \sqrt{\frac{(1+D_1)(1+D_2)}{(1-D_1)(1-D_2)}}e^{-4\gamma t}\left(\sin^2\left[2q\gamma t\sin(2\pi\tilde{d})\right] + \sinh^2\left[2q\gamma t\cos(2\pi\tilde{d})\right]\right), \tag{2.89}$$

where $q \equiv (1-D_1^2)^{1/4}(1-D_2^2)^{1/4}$, and $D_j = (\gamma_{Rj} - \gamma_{Lj})/(\gamma_{Rj} + \gamma_{Lj})$ is the directionality of qubit j. The two terms in the sum above describe, respectively, the coherent and incoherent contributions of the waveguide-mediated interaction between the qubits.

The chiral and non-chiral cases are compared in the two panels of Fig. 2.12. In panel a, we display the time evolution of the concurrence in the non-chiral coupling scenario, where the behavior is essentially the same as that shown in Fig. 2.8. Here, the long-lived entangled state is achieved for the resonant separation $d = \lambda_0$, while for any other separation between qubits the concurrence is much smaller and decays in time. This strong dependence with the qubit-qubit separation is in contrast with the results obtained for a largely chiral coupling, displayed in panel 2.12b for directionalities $D_j =$

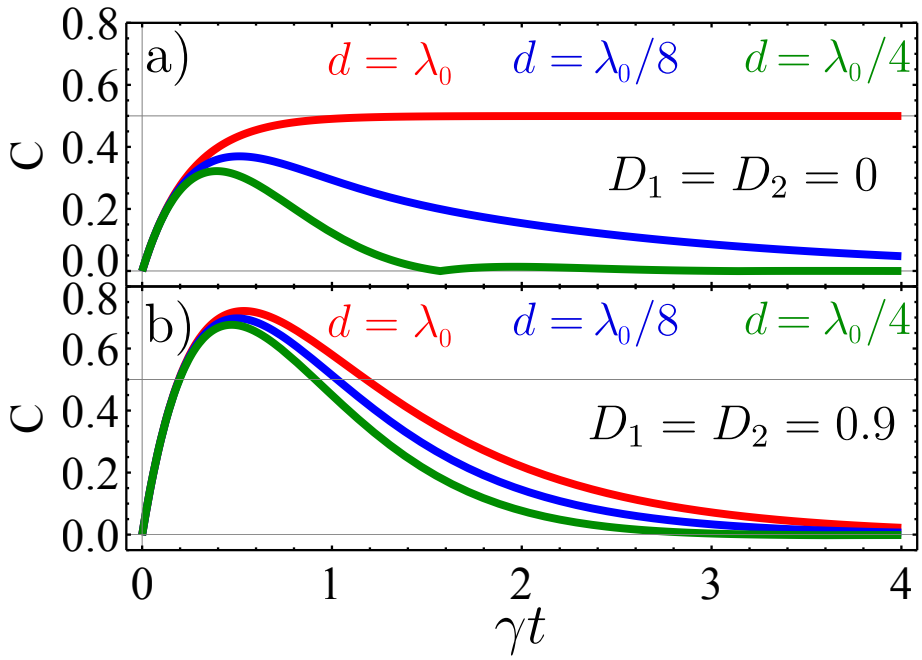

Figure 2.12: Time evolution of the concurrence, Eq. 2.89, for different qubit-qubit separations d, in the non-chiral (a) and chiral (b) cases.

0.9. In this case, as we have mentioned above, the appearance of a dark state is prevented by chirality. As a consequence, the dependence of the concurrence on the separation d becomes less critical. The chiral interaction also modifies the mechanism responsible for the entanglement generation, which now does not rely only on the incoherent part of the interaction. Indeed, in the chiral case the Lindblad superoperators can be shown to add an extra Hamiltonian term [214] which induces an additional, coherent transfer of excitations between the qubits. In other words, for chiral qubit-waveguide couplings the waveguide-mediated interaction always has a coherent contribution. As a result of this supplementary interaction, the concurrence is no more bounded by the overlap between initial and dark state, and is then able to reach higher values than in the non-chiral situation. Physically, it is possible to see the bound $C \leq 0.5$ of the non-chiral case as a consequence of qubit 1 emitting only half the initial population in the direction of the second qubit, and the other half into left-propagating modes. On the other hand, if the coupling is chiral, more than 50% of the initial population can be emitted towards qubit 2, hence the entangled state is able to reach a larger population.

The fact that no long-lived entangled state exists in the chiral coupling case produces the generated entanglement to have a finite decay rate for every separation d. Although in principle this could diminish the potential applications of the entanglement generation protocol, chirality also facilitates enormously the experimental implementation of the

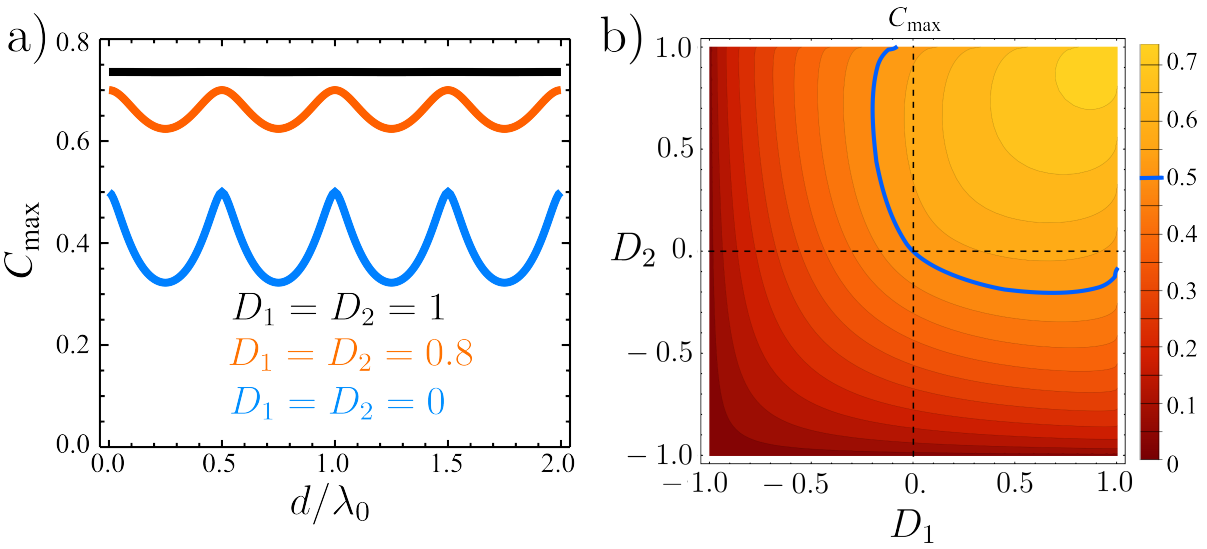

Figure 2.13: a) Maximum concurrence generated during the time evolution as a function of the qubit-qubit separation, d, for different values of the directionalities $D_1 = D_2$. b) Same quantity as a function of D_1 and D_2, for a resonant separation $d = \lambda_0$. The blue curve shows the maximum achievable value in the non-chiral case, $C_{\max}^{\text{chiral}} = 0.5$..

scheme since, as Fig. 2.12b shows, the dependence of the dynamics with the qubit-qubit separation is less critical than in the non-chiral case. In order to study the optimum separations d, we display in Fig. 2.13a the maximum concurrence achieved during the time evolution, $C_{\max}$, as a function of d. Clearly, the maximally chiral configuration $D_j = 1$ optimizes the entanglement generation scheme, as $C_{\max}$ reaches a maximum value which, additionally, is independent on d. For finite directionalities D_j, on the other hand, the concurrence is optimized for particular separations. Specifically, the concurrence $C_{\max}$ is maximized when the distance between the qubits is resonant, $d = n\lambda_0/2$. For these separations, an analytical expression for the maximum concurrence achieved along the time evolution can be extracted from Eq. 2.89,

$$[C_{\max}]^2 = \frac{(1+D_1)(1+D_2)}{1-q^2}\left(\frac{1-q}{1+q}\right)^{\frac{1}{q}}. \tag{2.90}$$

The dependence of $C_{\max}$ with the directionalities is shown in Fig. 2.13b, for a separation $d = \lambda_0$. Since initially qubit 1 is excited, negative directionalities have a detrimental impact on the generated concurrence. Indeed, in such case most of the initial population is emitted leftwards, and therefore is unable to reach the second qubit and, consequently, to populate the entangled state. Specifically, in the limit $D_j = -1$ the concurrence is strictly zero during all the time evolution, as the qubit j is coupled only to left-propagating modes and does not interact with its partner. On the other hand, however,

any values of the directionalities in the region $D_1, D_2 > 0$ result in an enhancement of $C_{\max}$ with respect to the non-chiral case, where $C_{\max}^{\text{non-chiral}} = 0.5$. Moreover, when both qubits are maximally coupled to right-propagating modes, i.e., $D_1 = D_2 = 1$, the maximum entanglement rises up to a very large value, which can be extracted from Eq. 2.90 as $\lim_{q\to 0} C_{\max} = 2/e \sim 0.73$. This is a significant result, as it shows that the maximum achievable concurrence can be enhanced by a factor of $\sim 50\%$ with respect to the non-chiral coupling scheme.

So far we have studied the entanglement generation protocol within the Markovian Master Equation formalism, in which we have been able to obtain an analytical expression for the maximum generated concurrence. Additionally, we have shown that the most promising feature of such scheme is its robustness against variations of the qubit-qubit distance, which eases the experimental implementation. For this reason, we focus our attention now on a detailed study of how the different system parameters, including the separation d, affect the generated concurrence. As we have seen above, for large values of $\gamma d/v_g$ non-Markovian effects arise, and a complete Hamiltonian formalism is required to accurately reproduce the system dynamics. Hence, we now reformulate the problem to properly assess the robustness of the proposed protocol in terms of the single-excitation eigenstates obtained in previous sections. Unless stated otherwise, we will assume equally coupled qubits, i.e., $\gamma_{1R} = \gamma_{2R}$ and $\gamma_{1L} = \gamma_{2L}$ and large directionalities ($D_j = 0.90$) in order to stay close to the optimum configuration. We also include explicitly the lossy modes in this part of our work, by fixing the decay rates Γ_j such that $\beta_j = (1 + \Gamma_j/(\gamma_{jR} + \gamma_{jL}))^{-1} = 0.98$. Note that the chosen values for both the directionalities and the beta factors have been experimentally reported [72, 108, 206, 215].

We focus our attention in three relevant parameters, namely the detuning between the frequencies of the emitters, the total coupling to the waveguide modes, $2\gamma = \gamma_R + \gamma_L$, and the separation d. First, we study the effect of the detuning between the qubits in Fig. 2.14a. For the corresponding calculations, the frequencies of both emitters are modified according to $\omega_1 = \omega_0 + \delta/2$, and $\omega_2 = \omega_0 - \delta/2$. Physically, we are shifting away the emission spectrum of qubit 1 from the absorption spectrum of qubit 2, keeping their linewidth constant. This decreases the population of the entangled state, since a large detuning δ suppresses the population exchange between the two qubits. We can understand this as consequence of the qubit coefficients in the system eigenstates, α_j, being peaked at the frequency ω_j, according to equation 2.71. Since the population transferred to the second qubit is given by $\propto \langle 0|\sigma_2 U(t)\sigma_1^\dagger|0\rangle \propto \alpha_2^*\alpha_1$, the concurrence naturally decreases for largely detuned qubits, as the frequency overlap between α_1 and α_2 decreases with δ. In Fig. 2.14, the detuning relative to ω_0 seems to be the most critical

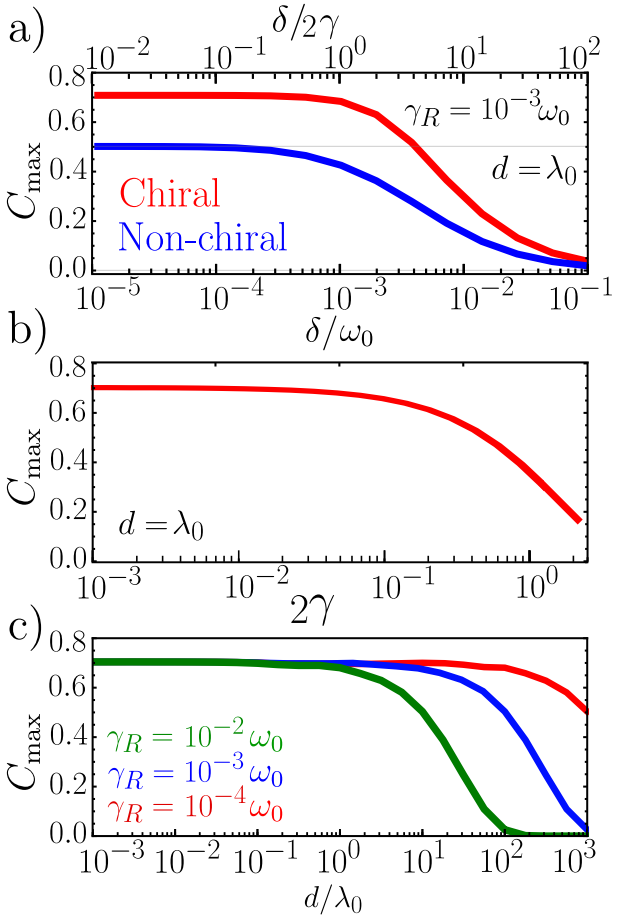

Figure 2.14: Robustness of the generated concurrence against variation of the system parameters, for $\gamma_{1R} = \gamma_{2R} \equiv \gamma_R$, $\beta_j = 0.98$ and $D_j = 0.9$. a) Effect of detuning δ between the frequencies of the two qubits. b) Dependence on the total waveguide-qubit coupling for a separation $d = \lambda_0$. c) Effect of the separation between the qubits, d, for different values of the coupling γ_R.

parameter as a change of $\sim 0.5\%$ in the frequency of the qubits is enough to reduce $C_{\max}$ below 0.5. However, the robustness against detuning is considerably large with respect to the qubits linewidth, 2γ. Indeed, whereas in the non-chiral case the concurrence is independent on the detuning for $\delta \lesssim 0.2\gamma$, for chiral couplings this range is increased by a factor of ~ 5. Additionally, in the chiral case, concurrences of $C_{\max} = 0.5$ are possible for detunings as large as $\delta \sim 5\gamma$. This is a crucial advantage with respect to non-chiral systems, especially for quantum emitters with a very narrow linewidth such as quantum dots.

The variation of $C_{\max}$ with the total qubit-waveguide coupling is displayed in Fig. 2.14b. For low values of 2γ, the concurrence is close to its theoretical maximum ($C_{\max} \sim 0.7$)

due to the large chosen directionalities. As we have discussed in the previous section, when the decay rate of the qubits 2γ is increased, the first qubit significantly decays before the photon reaches qubit 2 and, at any given time, at least one of the emitters is fairly depopulated. Thus, the concurrence $C = 2|\rho_{12}| \equiv 2\sqrt{\rho_{11}\rho_{22}}$ decreases for large values of 2γ. Note that, nevertheless, even for couplings as large as $\gamma \approx 0.05\omega_0$, the concurrence remains above 0.6. This result shows that chirality allows for a high level of concurrence not only in the optical regime, but also in systems where much larger couplings arise such as microwave striplines.

Finally, the variation of the maximum concurrence with the qubit-qubit separation d is shown in Fig. 2.14c. While in the non-chiral case a maximum concurrence of 0.5 was obtained only for particular values of d, for chiral couplings the entanglement generation scheme is shown to be robust for a wide range of separations. For large distances there is a decay in the concurrence, which responds to the same mechanism discussed above. Interestingly, for qubit-waveguide couplings in the optical regime ($\gamma \lesssim 10^{-4}\omega_0$), the entanglement generation scheme is practically independent on the distance d, allowing for concurrences above 0.6 for very large separations, e.g. around 60μm at $\omega_0 \approx 1$eV. The separation between the qubits is thus not a critical parameter anymore, allowing for a much easier implementation of this entanglement protocol.

2.6. Conclusion

The ability to generate quantum entanglement between qubits separated by long distances is essential for scalable quantum computing and quantum communication. For this purpose, the so-called dissipative entanglement generation protocols are promising since they rely on the internal degrees of freedom of the system and, in principle, reduce the requirements in terms of external manipulation of the qubits. Specifically, these schemes rely on coupling the qubits to a common structured reservoir, in such a way that the unperturbed time evolution of an initially disentangled state leads to the generation of entanglement. The situation in which waveguides play the role of such common reservoirs is very appealing as guided photons have been proposed as ideal building blocks for quantum networks, where they would interconnect the nodes formed by matter qubits. For this reason, we have devoted this chapter to the study of waveguide-mediated entanglement generation.

First, we have introduced previous results obtained by means of a Master Equation formalism. Here, the possibility of generating a long-lived entangled state between qubits

had been shown to rely on the appearance of a collective dark state, uncoupled from the waveguide modes. From that starting point, we have proposed an alternative, more complete formalism to describe such problem, in which the photonic modes are explicitly taken into account.

In the first part of our chapter, we have explicitly diagonalized the full system Hamiltonian in the single-excitation subspace. The arising of uncoupled dark states has been demonstrated also in this formalism, as well as their deep relation with the generation of entanglement. A complete model of the system has allowed us to certify that the predictions of the Master Equation are correct for most systems operating in the optical range. However, such formalism is critically inaccurate in describing the system dynamics when either the qubit-waveguide coupling or the distance between the qubits are sufficiently large. In this limit, non-Markovian effects arise not as a consequence of a locally structured environment for each QE, but because of the presence of more than one emitter in a one-dimensional photonic continuum. The unidimensional character of the waveguide allows for a photon emitted by one qubit to be reflected by the second. Such photon can thus impinge back into its original source, producing a memory effect that is intrinsically non-Markovian and, by definition, impossible to describe with a usual Master Equation. These effects can be very important in some systems such as strongly-coupled circuit QED setups, where the new entanglement generation schemes would be required.

In the second part of this chapter, we have applied the same Hamiltonian formalism to a system of two qubits chirally coupled to a waveguide. In such a situation, no dark state arises, and the entanglement generation contains a contribution from a coherent, waveguide-mediated interaction between the two qubits. Although in such case the entanglement lifetime is not as long as in the non-chiral situation, chirality brings about enormous advantages from the point of view of a feasible experimental implementation. First, in the chiral protocol the Concurrence is able to reach $\sim 50\%$ higher values than in the non-chiral equivalent. More importantly, the absence of a dark state removes the demanding requirements in terms of fine-tuning of the system parameters. Specifically, we have demonstrated how the generated entanglement is extremely robust against variations in the frequency of the qubits, the total waveguide-qubit couplings, and the separation between the two emitters. The full Hamiltonian picture introduced and employed along this chapter has thus revealed as a very powerful tool in waveguide QED, allowing for an extensive characterization and improvement of current entanglement generation protocols.

3 | Waveguide QED with photonic inputs: entanglement control and detection, and few-photon devices

3.1. Introduction

In the search for highly controllable setups for light-matter interaction, cavities and waveguides are frequent resources due to their flexibility and usually large field confinement. One of the particular advantages of waveguides, as we have previously discussed, consists on the natural input-output ports which allow for an easy introduction and extraction of information in the system. When a waveguide is coupled to an ensemble of QEs, it is in principle possible to introduce photons through one of the ends of such waveguide in order to generate or probe a particular quantum state of the qubits, as well as to modify their natural time evolution in a desired manner. Conversely, one could make use of the quantum emitters to act upon a particular photonic input, therefore constructing waveguide-based photonic quantum gates. We devote this chapter to exploring these possibilities, which have very interesting potential applications for integrated quantum circuitry.

The first section of this chapter (section 3.2) is devoted to the generation of entanglement between two qubits via an incoming single photon. This mechanism is different from the most common photon-assisted entanglement generation protocols, which normally rely either on a continuous wave pumping of a dissipative interaction scheme, such as the one studied in the previous chapter [106, 107], or in a heralded measurement of an entangled photon-qubit state [216–218]. The scheme we present here does not require the qubits to be initially prepared in a given state, and is demonstrated for an incoming photonic wavepacket equivalent to that produced by the decay of a two-level emitter acting as a source. This facilitates the implementation of such protocol in an integrated circuit with integrated single-photon sources.

The generation of entanglement induced by a single photon serves as a preliminary step towards more elaborate studies involving two-excitation states, first for entanglement manipulation in Section 3.3 and, subsequently, for entanglement detection in Section 3.4. We begin Section 3.3 by illustrating the process of diagonalizing the Hamiltonian in the two-excitation subspace, a problem tackled by other authors [77, 219] and where the bosonic nature of the photons is revealed to play a key role [198]. Specifically, the saturable character of the qubits allows for the formation of a two-photon bound state through a process of stimulated emission [220]. Once the two-photon solution has been computed, we study the entanglement dynamics of a two-qubit ensemble for a scattering input formed by two photons. Specifically, we find how the time window during which the qubits are entangled can be controlled on demand as a function of the delay time between both incoming photons. This mechanism is based on two related phenomena called, respectively, sudden death and revival of entanglement, which have been extensively studied in cavity setups both theoretically [221, 222] and experimentally [223, 224]. The possibility of entanglement manipulation, already available in cavities through other methods [225], is therefore introduced in waveguide QED systems.

Once we study how to generate and manipulate qubit-qubit entanglement through guided photons, in Section 3.4 we tackle the problem of detecting such entangled state by means of a single-photon probe. Entanglement detection is a necessary resource along the path towards quantum computing [226], and therefore has been the object of extensive research effort. The most elementary ways of detecting an entangled state rely on measurements related to Bell's inequalities [12, 227] or complete state tomography [228]. Both these methods are not optimal in terms of experimental implementation since they usually require many measurements in a very controlled environment. An alternative family of entanglement detection protocols is based on measuring directly the amount of entanglement, for instance the Wootters Concurrence, instead of the full quantum state

of the qubits. These schemes have been demonstrated for entangled photonic qubits [229–231], charge qubits in superconducting circuits [232], and matter qubits in cavity setups [233, 234]. Within the latter systems, an interesting proposal consists on detecting quantum correlations between two qubits through the spontaneously emitted photons leaking out of the cavity [235]. We introduce a related idea for waveguide systems. In our scheme, we study the scattering of a single photon by an initial arbitrary state of the two qubits, demonstrating how the two-photon detection probability at one end of the waveguide contains information about the concurrence of such state. Although for some initial states our method only offers a lower bound for the concurrence, the protocol is extremely robust against variations in any of the system parameters, thus being suitable for future experimental implementations.

In the remaining part of the present chapter, we leave the topic of entanglement generation to explore a different possibility open by the explicit control over the photonic degrees of freedom, namely the design of few-photon devices. Macroscopic optical devices are usually not optimal regarding possible implementations of quantum photonic circuitry, since a careful control of both the (small) photon numbers and their phase relation is often necessary [91]. It is thus of key importance to specially design optical devices to operate at the few-photon level. Waveguide QED setups provide an excellent platform for implementing operations on flying photonic qubits, due to the combination of open ports with an enhanced QE-photon interaction. Many recent works have already proposed waveguide-based single photon operations such as phase gates [77], as well as two-photon devices such as sequential transistors [75].

In the search for efficient few-photon devices, those whose behavior is intrinsically non-reciprocal, such as diodes, circulators or certain types of transistors, are specially interesting but, on the other hand, very challenging to devise. This is due to the requirement of a time-reversal symmetry breaking for the electromagnetic field [236], a very difficult achievement in nanoscale systems. Most of the recent proposals for single-photon diodes rely on two-qubit ensembles coupled to waveguides, and achieve an *effective* non-reciprocal behavior by breaking parity instead [237–241]. A truly non-reciprocal device has recently been achieved for a system of two externally pumped qubits [242], a work which uncovers the deep role of quantum interference in these kind of processes.

The operation of each of the setups mentioned above is constrained by severe requirements, such as a careful control of the state of the qubits [237, 242] or their separation and detuning [238, 241], unrealistically strong couplings in the optical range [240], or large photon numbers [239]. This motivates the search for devices showing a true spontaneous time-reversal symmetry breaking and, consequently, able to show nonreciprocal

behavior of light without a demanding external control. Some systems fulfilling these requirements have already been proposed such as cavity resonators in dielectric waveguides [243–247] or indentations in plasmonic waveguides [248], where the demonstration of partially asymmetric transmission indicates non-reciprocal behavior. However, most of these devices are micrometric or larger in size, which largely constrains their potential for compact integrated photonic circuitry. Recently, several experiments have taken a decisive step towards nanoscale non-reciprocal devices by demonstrating chiral coupling of an emitter to a waveguide [72, 108, 205, 206, 215] . Such a directional coupling manifests a breaking of time-reversal symmetry at the nanoscale [249] and even at the single atom level [204]. As we have seen in chapter 1, these experiments have spanned multiple works which exploit the potential of chiral couplings for quantum networks [214, 250], quantum optics [109, 251], and the study of spin systems [252]. Device-wise, many studies have proposed chirality-based few-photon operations in atomic ensembles [253, 254], and even implementations of efficient single-photon diodes [255] and circulators [121].

Sections 3.5 and 3.6 are thus devoted to a further exploration of the potential of chiral waveguide-QED couplings to design non-reciprocal few-photon devices. In section 3.5, we introduce a four-port setup in which we will demonstrate many different functionalities based on an engineered quantum interference. We continue by illustrating those regarding single-photon inputs, where we demonstrate both a robust single-photon rectifier as well as a single-photon diode. After, in section 3.6, we go one step further and explore the response of our device for a two-photon input. We show how a transistor-like behavior can be attained, therefore presenting the first two-photon device based on chirality. Finally, we detail our conclusions for the whole chapter in section 3.7.

3.2. Entanglement generation trough single-photon scattering.

In this section we devote our attention again to the problem of entanglement generation between two qubits coupled to a waveguide. As opposed to the previous chapter in which the qubits were prepared in an initially unentangled, single-excitation state, here we consider an in principle more feasible setup. Specifically, we aim to generate entanglement by means of a single-photon impinging over the qubits initially in their ground state, $|g_1 g_2\rangle$, as depicted in Fig. 3.1a. We consider the qubit-waveguide couplings to be non-chiral since, as we will see below, the arising of a dark state is particularly convenient

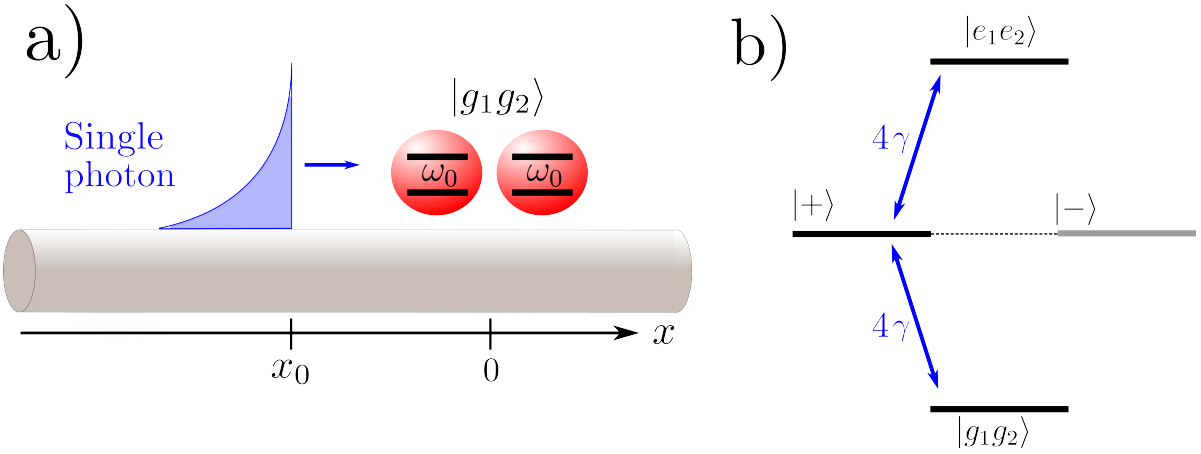

Figure 3.1: a) Scheme of the setup for single-photon entanglement generation: a single guided photon with a sharp wavefront impinges over two qubits initially in their ground state. b) Level structure of a system formed by two qubits separated by a distance $d \ll \lambda_0$.

in our case. Let us assume for simplicity that the qubits are both placed at $x = 0$, i.e., their separation fulfils $d \ll \lambda_0$. On the other hand, we consider that both emitters are still separated enough for their direct dipole-dipole interaction to be negligible. We will also assume that the qubit losses by emission to free space are much lower than the coupling to guided modes, i.e., $\Gamma \ll \gamma$ or, equivalently, $\beta \approx 1$. Both the above limits are optimum in terms of entanglement generation, as we have discussed in the previous chapter. Specifically, in such configuration the odd state of the qubits, $|-\rangle$, is a dark state and does not couple to the guided photons nor decay into the waveguide. As a consequence, the two-qubit ensemble acts as an effective three-level structure formed by the states $|g_1g_2\rangle, |+\rangle, |e_1e_2\rangle$ (Fig. 3.1b). Note that, in this case, the entanglement will be generated by populating the bright state $|+\rangle$, as opposed to the dissipative scheme of the previous chapter which relied on the occupation of the dark state $|-\rangle$. Along this whole chapter, thus, we will be dealing with transient entanglement instead of long-lived states, since the even qubit state has a finite lifetime and eventually decays into the guided modes.

The Hamiltonian of the system described above is the same as in the previous chapter, namely $H = H_e + H_o$, where according to Eq. 2.26 the even and odd components are given by

$$\begin{aligned} H_m = \omega_0 \sigma_m^\dagger \sigma_m - i v_g \int dx c_m^\dagger(x) \frac{\partial}{\partial x} c_m(x) + \\ + V \int dx \left[\delta(x + d/2) + \eta_m \delta(x - d/2)\right] \left(c_m^\dagger(x)\sigma_m + H.c.\right), \end{aligned} \tag{3.1}$$

$(m = e, o)$, with $\eta_e = -\eta_o = 1$. Note that, as expected, for $d \approx 0$ the odd Hamiltonian is already in diagonal form, since the qubit-waveguide coupling vanishes in this subspace. On the other hand, the total coupling in the even subspace is twice as large as that of a single qubit. Since our initial state, namely a single-photon impinging over the two qubits in their ground state, only has one excitation, the whole system dynamics occurs within the single-excitation subspace. As a consequence, we can employ the same diagonalization scheme undertaken in Section 2.3.2 of this thesis. In particular, the time evolution operator is calculated directly from Eq. 2.44 to be

$$U(t) = \sum_{m=e,o} \frac{1}{2\pi v_g} \int d\epsilon |\epsilon_m^{sc}\rangle\langle\epsilon_m^{sc}| e^{-i\epsilon t}, \tag{3.2}$$

where the localized states have been omitted since, as discussed in Chapter 2, they do not play a role if the initial state is formed exclusively by an incoming photon. The scattering eigenstates in this simplified problem are given by Eqs. 2.28, 2.31, and 2.35-2.37 in the even subspace, and by the following free wave in the odd subspace,

$$|\epsilon_o^{sc}\rangle = \int dx e^{i\epsilon x/v_g} c_o^\dagger(x)|0\rangle. \tag{3.3}$$

Note that the above eigenstate is not normalized. Additionally, the odd Hamiltonian allows for the extra solution $|-\rangle = \sigma_o^\dagger|0\rangle$, which corresponds to the localized dark state when the separation between qubits is $d = 0$.

The initial state of the system in our entanglement generation scheme is given by a single, right propagating photon,

$$|\psi(0)\rangle = \int dx \psi(x; x_0) c_R^\dagger(x)|\emptyset\rangle \otimes |g_1 g_2\rangle, \tag{3.4}$$

where $|\emptyset\rangle$ is the photonic vacuum, and the in principle arbitrary normalized wavepacket has been chosen as

$$\psi(x; x_0) = \sqrt{\frac{2\gamma_s}{v_g}} \theta(x_0 - x) e^{-\gamma_s x_0/2v_g} e^{(i\omega_s + \gamma_s)x/v_g}. \tag{3.5}$$

The election of the above wavepacket is not casual. Indeed, this pulse shape corresponds, apart from global phase factors, to a single photon emitted by an excited two-level system of transition frequency ω_s, placed at $x \to -\infty$, and non-chirally coupled to the guided photons at a total rate $2\gamma_s$. This fact has been shown both theoretically [190, 256] and experimentally [201, 257] and, additionally, is demonstrated step by step in Appendix A. The wavepacket given by Eq. 3.5 is thus a suitable choice regarding a possible implementation in integrated circuits or quantum networks, where single-qubits

have already been employed as single-photon sources [59, 258–260]. Additionally, note that the sharp wavefront of the pulse 3.5, given by the Heaviside theta function, causes the qubit-photon interaction to start at a well-defined time. Therefore, the choice of this type of wavepacket is also very convenient from the theoretical point of view, allowing a more transparent interpretation of the results.

Before continuing, let us briefly discuss the feasibility of generating the chosen wavepacket in a waveguide setup by means of an hypothetical source emitter placed infinitely far away from the two-qubit ensemble. Note that if we assume such configuration, then we have to take into account the fraction of the population emitted leftwards by the source, which in principle would prevent Eq. 3.5 to be normalized to unity. Therefore, for an efficient implementation, we must find a way to suppress such leftward emission, something we can achieve in a number of ways. First, by assuming the source emitter is chirally coupled to the waveguide with directionality 1, so that all the emission is directed rightwards (see Appendix A). A second, more elaborate alternative is to place a detector left of the source qubit. If no photons are detected, within the detector tolerance we can guarantee that the photon is propagating in the right direction. In other words, with a partial measurement we can induce the collapse of the photonic state into right or left propagation direction, obtaining the above wavepacket with a success rate of 50%. In either situation, the possibility of generating the wavepacket in Eq. 3.5 is feasible in realistic setups.

A second discussion should be made regarding the two-qubit Hamiltonian we employ in this problem, in which the hypothetical source of the incoming single photon is not explicitly included. This is not problematic since we have assumed such source to be placed at $x \to -\infty$, so that any possible role it may play in the dynamics occurs at infinitely long times and can thus be neglected. However, this picture can raise problems regarding the unavoidable photon propagation losses in the waveguide, which we are not taking into account here. Indeed, if the incoming photon is generated at $x \to -\infty$, then these losses would be critical and such photon would disappear before arriving to the two-qubit system. On the other hand, if the source was placed very close to the two-qubit ensemble in order to minimize propagation losses, the reflected photon could exert a backaction over the source in a relevant timescale, and such source would have to be included explicitly in the Hamiltonian. The problem of how to isolate a source from a system is very general and, in the case of waveguides, it can be also circumvented in various ways. The first option is to chirally couple the source to the waveguide with maximum directionality, as mentioned above. Then, any reflected component, which by definition propagates leftwards, would never interact with the original qubit, which

would remain *invisible* after emitting the photon. The source emitter could in this way be placed very close to the two-qubit ensemble without modifying its dynamics. A second option consists also in shortening the separation between source and system, but now introducing a non-reciprocal optical device between them such as an isolator or a circulator. This device allows the emitted photon to be transmitted rightwards but never leftwards, preventing the source qubit to play any role in the dynamics of the two-qubit ensemble. In section 3.5 we precisely illustrate how non-reciprocal few-photon isolators can be implemented in waveguide QED. Therefore, both the generation of a single-photon pulse with the shape given by Eq. 3.5 and the isolation of the source from the dynamics of the two-qubit ensemble are in principle experimentally feasible.

Let us now go back to our system and determine its dynamics, a straightforward calculation once we specify both the time evolution operator, Eq. 3.2, and the initial state Eq. 3.4. We can then construct the reduced density matrix of the two-qubit subsystem, in a similar fashion as in Section 2.4. In this simple problem, we can demonstrate the concurrence to be equal to the population of the even state,

$$C(t) = \rho_{++}(t) = |\langle +|\psi(t)\rangle|^2. \tag{3.6}$$

The possibility of entanglement generation is now clearly understood, since in the single-photon regime only two states participate in the dynamics, namely $|g_1\rangle \otimes |g_2\rangle$ and $|+\rangle$ (see Fig. 3.1b). When the single-photon arrives to the qubits, it induces the transition $|g_1\rangle \otimes |g_2\rangle \rightarrow |+\rangle$ from a product state into an entangled state, thus increasing the concurrence. In order to study how the parameters of the incoming wavepacket affect the generated entanglement, let us analyze in detail the overlap in expression 3.6,

$$\langle +|\psi(t)\rangle = \frac{1}{2\pi v_g}\int d\epsilon e^{-i\epsilon t}\left[\alpha_e^{sc}(\epsilon)\right]^* \langle \epsilon_m^{sc}|\psi(0)\rangle. \tag{3.7}$$

We assume that at $t = 0$ the qubit-photon interaction has not started yet. Thus, the initial position for the wavefront of the incoming wavepacket is placed at $x_0 < 0$. In such case, it is straightforward to demonstrate that the overlap $\langle \epsilon_m^{sc}|\psi(0)\rangle$ is simply given by the Fourier transform of the initial wavepacket (see Eq. 2.31 in previous chapter),

$$\langle \epsilon_m^{sc}|\psi(0)\rangle = \int dx e^{-i\epsilon x/v_g}\psi(x;x_0) \propto \frac{1}{\epsilon - \omega_s + i\gamma_s}, \tag{3.8}$$

corresponding to its frequency spectrum. If the incoming photon is assumed to be the result of the emission from a hypothetical source qubit, the above Lorentzian profile also has a clear interpretation as emission energy spectrum of such source. According to Eq. 3.7, the amount of population promoted to the state $|+\rangle$ is thus given by the

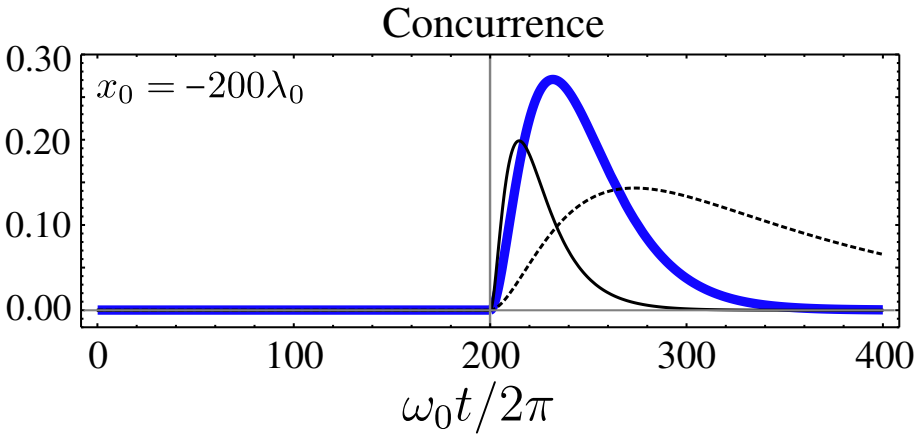

Figure 3.2: Generated concurrence for $\omega_0 = \omega_s$ and $\gamma = \omega_0/400$. The dynamics is determined by the ratio between the total rates $2\gamma_s$ and 4γ. We display the cases $2\gamma_s = 4\gamma$ (blue line), $2\gamma_s = 4 \times 4\gamma$ (solid black line), and $2\gamma_s = 4\gamma/8$ (dashed black line).

overlap between the frequency spectrum of the incoming wavepacket, Eq. 3.8, and the absorption/emission line shape of the even state $|+\rangle$, given by

$$\alpha_e^{sc} \propto \frac{1}{\epsilon - \omega_0 + i2\gamma}. \tag{3.9}$$

In order to maximize such overlap, and hence the generated concurrence, both Lorentzians must be equal. This is achieved by selecting the wavepacket parameters to fulfil $\omega_s = \omega_0$, $\gamma_s = 2\gamma$. The blue line in Fig. 3.2 shows the concurrence as a function of time for this choice of parameters, and a wavefront initially placed at $x_0 = -200\lambda_0$. Conversely, the solid back line represents the situation $\gamma_s = 8\gamma$, where the total rate at which the incoming photon *pumps* the transition $|g_1\rangle \otimes |g_2\rangle \rightarrow |+\rangle$, namely $2\gamma_s$, is larger than the natural absorption rate of such transition, 4γ. On the other hand, the dashed line shows the opposite situation, $\gamma_s = \gamma/4$, where the excitation rate is too slow to efficiently populate the even state.

The scheme for entanglement generation introduced in this section serves as an illustrative example of the possibilities brought about by a precise control of the natural input-output ports of the waveguide. In particular, we demonstrate the generation of entanglement in a simple setup through single-photon scattering. Note that a similar scheme has been proposed for plane-wave scattering in plasmonic waveguides [261]. Our protocol, however, demonstrates this possibility for a finite and realistic wavepacket, an important improvement towards an experimental realization. Note, additionally, that the scheme presented above still leaves room for optimization. Indeed, the maximum value $C \approx 0.27$ obtained in Fig. 3.2 could, for instance, be easily doubled if the incoming pulse

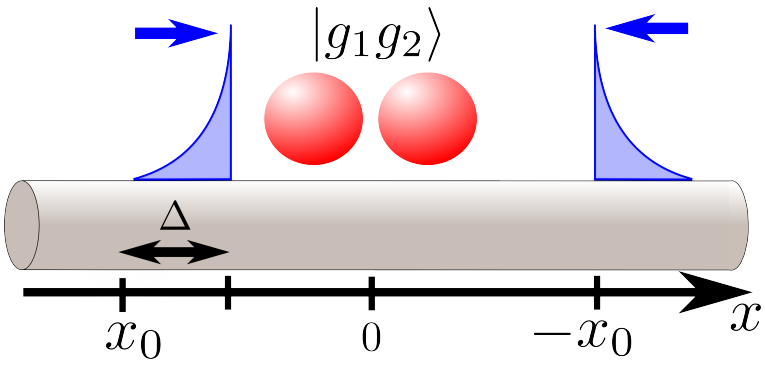

Figure 3.3: Basic setup for entanglement manipulation. A two-photon wavepacket impinges over the two-qubit ensemble in their ground state. The photon propagating rightwards is the first to arrive to the position of the qubits, whilst the leftward photon arrives at a later time Δ/v_g.

was not a right-propagating photon, but an even combination of right and left photons created through a beam splitter [262]. In any case, the dynamics of entanglement generation is well understood, and thus we continue by studying the interesting possibilities opened by this problem.

3.3. Entanglement manipulation with two-photon inputs.

Once we have demonstrated the possibility of generating entanglement through single-photon wavepackets, the question naturally arises as to whether it is possible to manipulate the time profile of the concurrence displayed in Fig. 3.2. In principle, one can do this by shaping the incoming single-photon pulse, but this usually requires a very precise control of the single-photon source [263]. Therefore, in this section we will employ a different approach. Our proposal is to introduce a two-photon wavepacket in which the individual photons arrive to the two-qubit ensemble with a time delay Δ/v_g, as depicted schematically in Fig. 3.3. In order to study the system dynamics in this situation, a diagonalization of the Hamiltonian in the two-excitation subspace is required.

3.3.1. Diagonalization of the Hamiltonian in the two-excitation subspace.

It is convenient to rewrite the system Hamiltonian in Eq. 3.1 for this particular case as

$$H = H_e + H_{o1} + H_{o2}, \tag{3.10}$$

where the three components represent respectively the Hamiltonian in the even subspace, and the two uncoupled parts of the Hamiltonian in the odd subspace, i.e.,

$$H_e = \omega_0 \sigma_e^\dagger \sigma_e - iv_g \int dx c_e^\dagger(x) \frac{\partial}{\partial x} c_e(x) + 2V \int dx \delta(x) \left(c_e^\dagger(x)\sigma_e + H.c. \right), \tag{3.11}$$

$$H_{o1} = -iv_g \int dx c_o^\dagger(x) \frac{\partial}{\partial x} c_o(x), \tag{3.12}$$

$$H_{o2} = \omega_0 \sigma_o^\dagger \sigma_o. \tag{3.13}$$

Importantly, the three operators above commute with each other,

$$[H_e, H_{o1}] = [H_e, H_{o2}] = [H_{o1}, H_{o2}] = 0, \tag{3.14}$$

which allows for an independent diagonalization in each subspace. For the single-excitation case, the eigenstates have already been calculated. For the first two Hamiltonians, these are the so-called *scattering eigenstates*, given respectively by

$$|\epsilon_e^{sc}\rangle = \left(\alpha_e \sigma^\dagger + \int dx \phi_e(x) c_e^\dagger(x) \right) |0\rangle, \tag{3.15}$$

$$|\epsilon_o^{sc}\rangle = \int dx e^{i\epsilon x/v_g} c_o^\dagger(x) |0\rangle, \tag{3.16}$$

where the coefficients α_e and $\phi_e(x)$ have been determined in the previous chapter. The eigenstate of the third Hamiltonian, H_{o2}, is simply the odd qubit state as mentioned above,

$$H_{o2}|-\rangle = \omega_0 |-\rangle. \tag{3.17}$$

In the two-excitation subspace, we can construct the eigenstates in two different ways. First, by taking the tensor product of single-excitation eigenstates belonging to different subspaces, i.e.,

$$|\epsilon^{(1)}\rangle = |(\omega_1)_e^{sc}\rangle \otimes |(\omega_2)_o^{sc}\rangle, \tag{3.18}$$

$$|\epsilon^{(2)}\rangle = |(\epsilon - \omega_0)_e^{sc}\rangle \otimes |-\rangle, \tag{3.19}$$

$$|\epsilon^{(3)}\rangle = |(\epsilon - \omega_0)_o^{sc}\rangle \otimes |-\rangle. \tag{3.20}$$

where in the first branch, $|\epsilon^{(1)}\rangle$, the energies of the two components fulfil $\omega_1 + \omega_2 = \epsilon$. The commutation relations in Eq. 3.14 guarantee that the above product states are eigenstates of the total Hamiltonian H. The second kind of eigenstates is formed by two excitations belonging to the same subspace. In the case of H_{o1}, the absence of any interaction term makes the eigenstate also a direct product,

$$|\epsilon^{(4)}\rangle = |(\omega_1)_o^{sc}\rangle \otimes |(\omega_2)_o^{sc}\rangle + |(\omega_2)_o^{sc}\rangle \otimes |(\omega_1)_o^{sc}\rangle, \tag{3.21}$$

where in this case the indistinguishability of the two photons has been taken into account through a bosonic symmetrization. The explicit expression of this eigenstate is

$$|\epsilon^{(4)}\rangle = \int dx_1 \int dx_2 \left(e^{ik_1x_1}e^{ik_2x_2} + e^{ik_1x_2}e^{ik_2x_1}\right) c_o^\dagger(x_1)c_o^\dagger(x_2)|0\rangle, \tag{3.22}$$

where $k_j = \omega_j/v_g$. The second odd space Hamiltonian, $H_{o,2}$ does not contain any interaction term either. However, in this case it is not possible to have any two-excitation eigenstate, since $H_{o,2}$ is the Hamiltonian of a fermionic two-level system which, by definition, cannot be doubly occupied as $\left(\sigma_o^\dagger\right)^2|0\rangle = 0$. Thus, no two-excitation eigenstate arises in this situation.

The fifth and last two-excitation eigenstate is the most laborious to obtain, and consists on two excitations in the subspace span by H_e. We follow the procedure of Ref. [198] and make the following Ansatz for this eigenstate,

$$|\epsilon^{(5)}\rangle = \int dx_1 \int dx_2 \phi_{ee}(x_1,x_2)c_e^\dagger(x_1)c_e^\dagger(x_2)|0\rangle + \int dx \alpha(x)c_e^\dagger(x)\sigma_e^\dagger|0\rangle + \beta\sigma_1^\dagger\sigma_2^\dagger|0\rangle, \tag{3.23}$$

where the bosonic symmetry is imposed through the condition $\phi_{ee}(x_2,x_1) = \phi_{ee}(x_1,x_2)$. The next step is to apply the even Hamiltonian (3.11) to this state and set the time-independent Schrödinger equation, $H_e|\epsilon^{(5)}\rangle = \epsilon|\epsilon^{(5)}\rangle$. We can then split such equality into the following system of equations:

$$(\epsilon - 2\Omega)\beta = 2V\alpha(0), \tag{3.24}$$

$$(\epsilon - \Omega + iv_g\partial_x)\alpha(x) = 2V\beta\delta(x) + 2V\phi_{ee}(0,x), \tag{3.25}$$

$$(\epsilon + iv_g\partial_1 + iv_g\partial_2)\phi_{ee}(x_1,x_2) = V\left[\delta(x_1)\alpha(x_2) + \delta(x_2)\alpha(x_1)\right]. \tag{3.26}$$

As we did in the previous chapter, we integrate the equations in the vicinities of $x = 0$ in order to get rid of the delta functions. After manipulating the result, we arrive to the following equivalent algebraic system:

$$(\epsilon - 2\Omega)\beta = 2V\alpha(0), \tag{3.27}$$

$$iv_g(\phi_{ee}(0^+,x)-\phi_{ee}(0^-,x))=V\alpha(x), \tag{3.28}$$

$$(\epsilon+iv_g\partial_1+iv_g\partial_2)\phi_{ee}(x_1,x_2)=0, \tag{3.29}$$

$$iv_g(\alpha(0^+)-\alpha(0^-))=2V\beta, \tag{3.30}$$

$$(\epsilon-\Omega+i2\gamma+iv_g\partial_x)\,\phi_{ee}(0^+,x)=(\epsilon-\Omega-i2\gamma+iv_g\partial_x)\,\phi_{ee}(0^-,x). \tag{3.31}$$

We proceed by using Eqs. (3.29) and (3.31) to solve for the two-photon wavefunction $\phi(x_1,x_2)=\phi(x_2,x_1)$. This has been done in detail in Ref. [198], where the wavefunction is determined with the exception of a free parameter C. We then have a system of three equations (3.27, 3.28, and 3.30) for the three unknowns $\alpha(x),\beta,C$, which is direct to solve. The final solutions are more easily written as a function of the coefficients $c_j^\pm=k_j-(\omega_0/v_g)\pm i\,(2\gamma/v_g)$, with $\epsilon=\omega_1+\omega_2=v_g(k_1+k_2)$, and are given by

$$\beta=4\frac{2\gamma/v_g}{c_1^+c_2^+}\frac{c_1^++c_2^+}{c_1^++c_2^+-i2\gamma/v_g}, \tag{3.32}$$

$$\alpha(x)=4\sqrt{\frac{\gamma}{v_g}}\begin{cases}\frac{e^{ik_1x}}{c_2^+}+\frac{e^{ik_2x}}{c_1^+} & \text{for}\quad x<0,\\ \frac{1}{c_1^+}\frac{1}{c_2^+}\left[c_2^-e^{ik_2x}+c_1^-e^{ik_1x}\right]+ & \\ +i\frac{\beta}{2}\frac{c_1^++c_2^-}{c_1^++c_2^+}e^{i(k_1+k_2-\omega_0+i2\gamma/v_g)x} & \text{for}\quad x>0.\end{cases} \tag{3.33}$$

$$\phi_{ee}(x_1,x_2)=\phi(x_1,x_2)\theta(x_2-x_1)+\phi(x_2,x_1)\theta(x_1-x_2), \tag{3.34}$$

$$\phi(x_1,x_2)=\begin{cases}e^{ik_1x_1+ik_2x_2}+e^{ik_1x_2+ik_2x_1} & \text{for}\quad x_1<x_2<0,\\ \frac{c_2^-}{c_2^+}e^{ik_1x_1+ik_2x_2}+\frac{c_1^-}{c_1^+}e^{ik_1x_2+ik_2x_1} & \text{for}\quad x_1<0<x_2,\\ \frac{c_1^-}{c_1^+}\frac{c_2^-}{c_2^+}\left(e^{ik_1x_1+ik_2x_2}+e^{ik_1x_2+ik_2x_1}\right)+ & \\ +\frac{2\gamma\beta}{v_g}\frac{c_1^++c_2^-}{c_1^++c_2^+}e^{(2\gamma-i\omega_0)(x_1-x_2/v_g)}e^{i\epsilon x_2/v_g} & \text{for}\quad 0<x_1<x_2.\end{cases} \tag{3.35}$$

As in the single-photon case, the purely photonic wavefunction Eq. 3.35 has the most transparent interpretation. In the region $x_1,x_2<0$, it is a boson-symmetrized plane wave corresponding to the incoming two-photon wavepacket, with wavevectors k_1,k_2. Then, when one of the photons crosses the boundary $x=0$, each term is multiplied by the corresponding single-photon transmission coefficient, $t_{1,e}(\epsilon=v_gk_2,d=0)=c_2^-/c_2^+$ (see Eq. 2.36 in the previous chapter). Finally, when both photons have interacted with the qubits ($0<x_1<x_2$), two contributions appear in the wavefunction: the first one is the linear term, in which the incoming wave is just multiplied by the two transmission coefficients c_1^-/c_1^+ and c_2^-/c_2^+. The second term is a two-photon bound state, for which the position probability amplitude is maximum at $x_1=x_2$ and decays exponentially when

the distance between the photons increases. Such bound state has a spatial extension $\sim v_g/2\gamma$, and arises from the discrete, fermionic nature of the qubits' energy levels, for which multiple occupation is forbidden. This nonlinear behavior appears when the second photon impinges on the two qubits while the excited state $|+\rangle$ is still populated, and thus is more pronounced when both photons arrive at the same time, $x_1 = x_2$. Conversely, if the delay between the two incoming photons is larger than the lifetime of the even qubit state, namely $\sim 1/4\gamma$, such state decays into their ground state when the second photon arrives, and the nonlinear effects are suppressed. This process of stimulated emission, in which a photon induces the transition $|+\rangle \rightarrow |g_1\rangle \otimes |g_2\rangle$, has been extensively studied in the literature [195, 220, 264, 265]. Generally, both the linear term and the bound contribution to the two-photon wavefunction $\phi(x_1, x_2)$ are relevant for the system dynamics as we will see below.

After the five different branches of eigenstates have been explicitly calculated, the time-evolution operator can be directly obtained in the two-excitation subspace. It is important to notice that, according to the expressions above, each eigenstate $|\epsilon^{(j)}\rangle$ is normalized to a different constant, and therefore their respective weights in the time evolution are different. After explicitly calculating the norms we can arrive to the following expression,

$$\begin{aligned} U(t) =& \frac{1}{2\pi v_g}\int d\epsilon e^{-i\epsilon t}\left(|\epsilon^{(2)}\rangle\langle\epsilon^{(2)}| + |\epsilon^{(3)}\rangle\langle\epsilon^{(3)}|\right) + \\ & \frac{1}{(2\pi v_g)^2}\int d\omega_1 \int d\omega_2 e^{-i(\omega_1+\omega_2)t}\left(\frac{|\epsilon^{(5)}\rangle\langle\epsilon^{(5)}| + |\epsilon^{(4)}\rangle\langle\epsilon^{(4)}|}{8} + |\epsilon^{(1)}\rangle\langle\epsilon^{(1)}|\right), \end{aligned} \tag{3.36}$$

which will be used throughout this chapter.

3.3.2. Entanglement manipulation

One we have calculated the time evolution operator in the two-excitation subspace, we can determine the system dynamics for any two-photon initial state. We choose the following initial configuration,

$$|\psi(0)\rangle = \int dx_1 \psi(x_1; x_0 + \Delta) c_R^\dagger(x_1) \otimes \int dx_2 \psi(x_2; -x_0) c_L^\dagger(x_2)|0\rangle, \tag{3.37}$$

where the wavepacket $\psi(x; x_0)$ is given by Eq. 3.5. The state above describes a photon coming from $x = -\infty$ and propagating rightwards, arriving to the two qubits earlier than a second photon originating from $x = +\infty$ and propagating leftwards. The time delay between the arrival of the two photons is given by Δ/v_g. By choosing the propagation

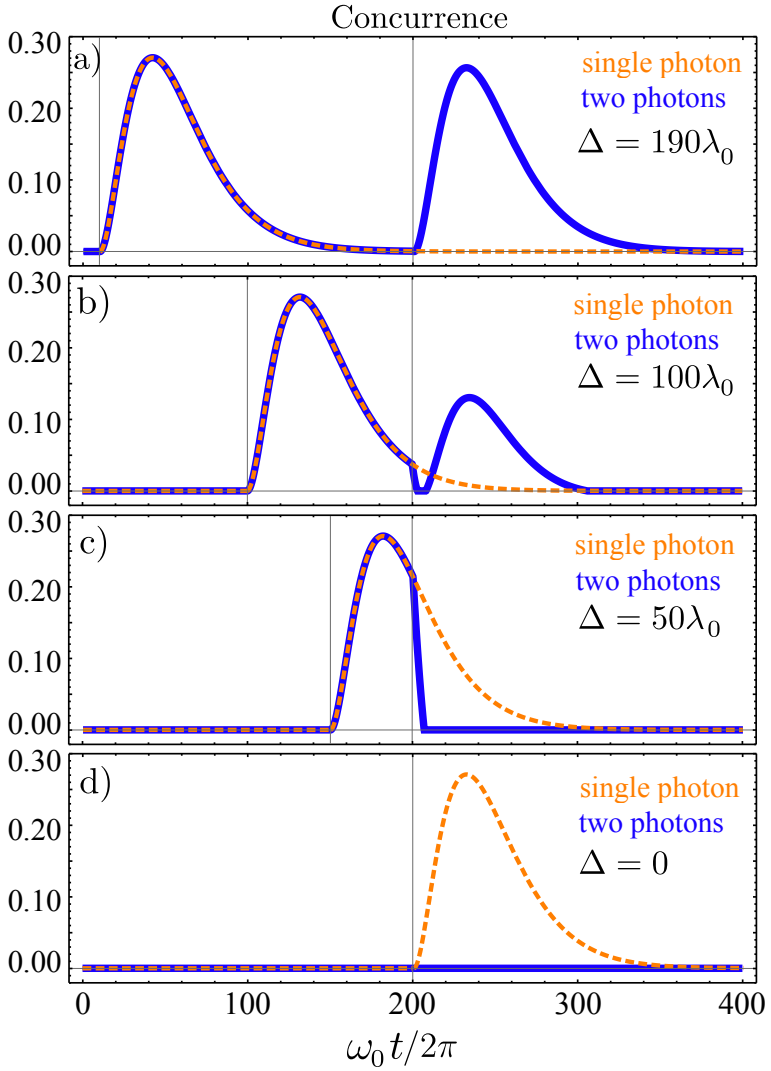

Figure 3.4: Time evolution of the generated concurrence for the two-photon wavepacket 3.37 (blue lines), as a function of the delay between both incoming photons ($x_0 = -200\lambda_0$). The arrival time of both photons is indicated by the vertical lines. The orange dashed line shows the effect of a single photon with the same shape.

quantum numbers (R,L) to be different, we make sure that the photons are distinguishable and thus the symmetrization of the initial state is not necessary. We will keep the same values for the parameters $\{\gamma, \omega_s\}$ as in Fig. 3.2, namely $\gamma = \omega_0/400$; $\omega_s = \omega_0$, and set $\gamma_s = 2\gamma$ in order to maximize the generated entanglement. The arrival time of the second photon will be fixed through the initial position of its wavefront, $x_0 = -200\lambda_0$. We will then explore the dependence of the system evolution with the delay Δ, which determines the arrival time of the first photon.

In this two-photon problem, after constructing the partial density matrix of the two-qubit subsystem, the concurrence takes a more complicated form,

$$C(t) = \max\left[0, \rho_{++}(t) - 2\sqrt{\rho_{gg}(t)\rho_{ee}(t)}\right], \tag{3.38}$$

where ρ_{gg} and ρ_{ee} represent, respectively, the population of the states $|g_1\rangle \otimes |g_2\rangle$ and $|e_1\rangle \otimes |e_2\rangle$. The amount of entanglement is thus given by two competing terms: it grows as the population of the even, entangled state $|+\rangle$ increases, while decreasing when the populations of the disentangled states $|g_1\rangle \otimes |g_2\rangle$ and $|e_1\rangle \otimes |e_2\rangle$ build up. As we will see below, this tradeoff will result in an interesting dynamical behavior which we can employ to manipulate the generated entanglement.

Each of the populations in Eq. 3.38 is analytically obtained from the time evolution of the initial state, Eq. 3.37. The concurrence generated by this two-photon wave packet is depicted in Figs. 3.4(a)–3.4(d) (solid line), together with the single-photon concurrence from the previous section (dashed line). For a large delay Δ (panel 3.4a), the two-photon curve is very similar to the sum of two identical single-photon pulses. This is an intuitive result which occurs because the state $|+\rangle$ excited by the first photon has time to relax to the ground state before the arrival of the second photon, as its lifetime $1/4\gamma$ is shorter than the delay time, Δ/v_g. In this regime, the arrival of each photon is sequential and the whole wavepacket creates a train of identical pulses in the concurrence. However, when the delay is reduced, the two pulses get closer and start to interact in a complex way, as seen in panels 3.4b and 3.4c. Here, the arrival of the second photon produces a very rapid decay of the entanglement which, in the case of panel 3.4b, is followed by a rebirth after a given time. In this intermediate delay regime, the concurrence profile displays a dip, which can even result in permanent cancellation of the entanglement as shown in panel 3.4c. This modifies the time duration of the entanglement pulse. Finally, when the two photons arrive to the qubits at the same time (panel 3.4d) no entanglement is generated. This means that, regarding the concurrence, the second photon fully suppresses the effect of the first one.

The interesting dynamics shown in Fig. 3.4b-d can be understood in terms of the possible transitions among the states of the two-qubit ensemble, depicted schematically in Fig. 3.5. A single photon induces the transition $|g_1\rangle \otimes |g_2\rangle \rightarrow |+\rangle$, thus generating entanglement between the qubits. When a second photon arrives, the population in such entangled state can undergo two different processes, namely further excitation $|+\rangle \rightarrow |e_1\rangle \otimes |e_2\rangle$, or stimulated emission $|+\rangle \rightarrow |g_1\rangle \otimes |g_2\rangle$. The importance of these two-photon processes depends on the population of the even state $|+\rangle$ at the arrival of the second

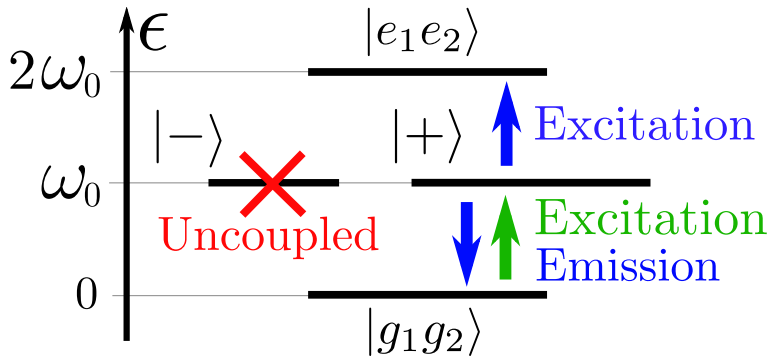

Figure 3.5: Level diagram of the two-qubit ensemble. The green arrow shows the transition induced by an incoming single-photon. When a second photon arrives, the population in the even state $|+\rangle$ can undergo two different processes (blue lines), namely further excitation or stimulated emission. Note that spontaneous emission processes are not shown in this scheme.

photon. Since such population spontaneously decays into the ground state, the delay Δ between the photons effectively controls the relevance of the two-photon processes, manifested in the tradeoff between the two terms in the Concurrence, Eq. 3.38.

The two competing contributions of the concurrence, ρ_{++} and $2\sqrt{\rho_{gg}\rho_{ee}}$, are displayed in Fig. 3.6 for the same values of the delay Δ considered in Figure 3.4. As we have explained above, for large delays (panel 3.6a), the state $|+\rangle$ excited by the first photon decays almost completely before the arrival of the second one. Hence, the qubit states probed by the first and the second photon are approximately the same, namely $|g_1\rangle\otimes|g_2\rangle$. As a consequence, the evolution of the concurrence with time displays two similar peaks which are formed almost exclusively by the contribution of ρ_{++}. When the delay is shortened as in panels 3.6b and 3.6c, the population of the state $|+\rangle$ is significant at the arrival of the second photon. In this situation, the transitions from this state, marked as blue arrows in Fig. 3.5, start to be relevant and thus the square root term in Eq. 3.38 increases. Eventually, the condition $2\sqrt{\rho_{gg}\rho_{ee}} > \rho_{++}$ is satisfied. At this point the concurrence vanishes in a phenomenon known as sudden death of entanglement. Two different situations may occur in this scenario. First, if the population of the state $|+\rangle$ at the arrival of the second photon is not too high (panel 3.6b), the square root term only becomes slightly larger than $\rho_{++}(t)$, since the two-photon processes are not very relevant. Thus, the transitions induced by the second photon are able to suppress the concurrence for a short time, but the entanglement rises again as the decay $|e_1\rangle\otimes|e_2\rangle \rightarrow |+\rangle$ repopulates the entangled state $|+\rangle$, producing a revival of the entanglement. Such a phenomenon, however, does not take place in panel 3.6c, where the two curves are

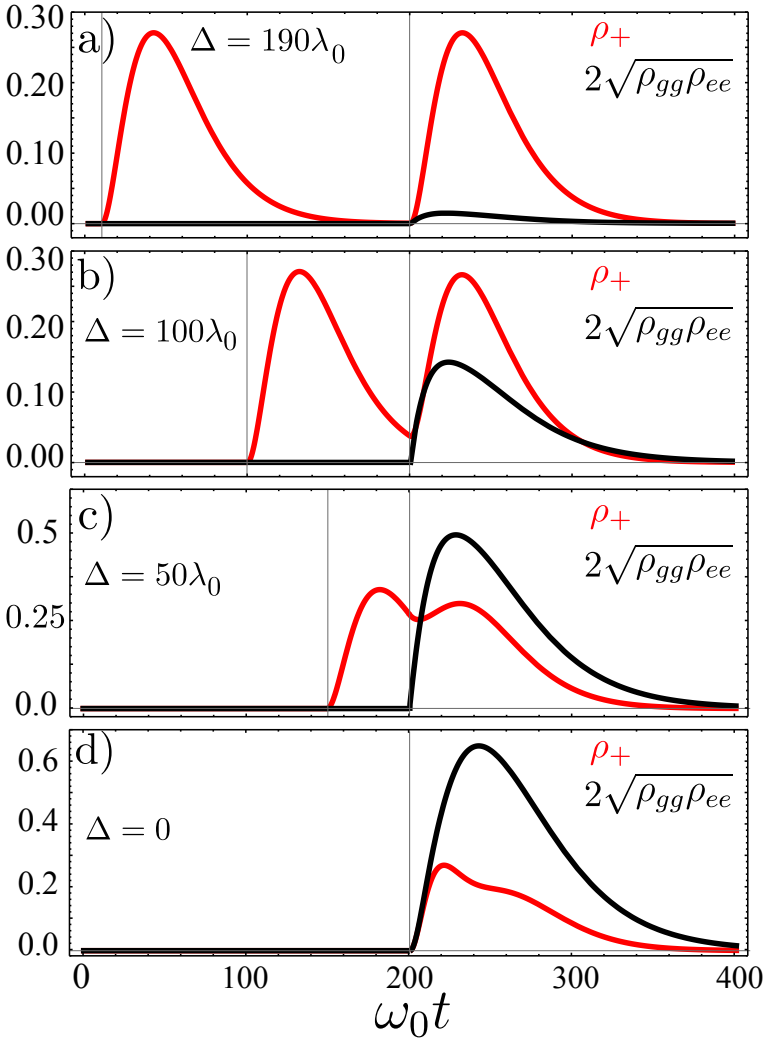

Figure 3.6: Time evolution of the two competing terms in the concurrence, Eq. 3.38, for different values of the delay between the two incoming photons, Δ. The vertical lines indicate the arrival time of both photons.

far apart from each other. Here, the second photon arrives when the state $|+\rangle$ has a large population. A significant amount of such population is irreversibly lost into guided modes through the stimulated emission process, $|+\rangle \rightarrow |g_1\rangle \otimes |g_2\rangle$. Thus, although some probability repopulates the entangled state after the decay of $|e_1\rangle \otimes |e_2\rangle$ (see the second maximum in the red curve), it is not enough to cause an entanglement revival and thus the concurrence suppression is permanent. Finally, in the zero-delay limit (panel 3.6d), the concurrence does never rise, as the condition $2\sqrt{\rho_{gg}\rho_{ee}} > \rho_{++}$ is fulfilled during all the time evolution. This is a consequence of the maximal efficiency of the double excitation process $|+\rangle \rightarrow |e_1\rangle \otimes |e_2\rangle$, and stimulated emission $|+\rangle \rightarrow |g_1\rangle \otimes |g_2\rangle$. The

situation of zero delay can be considered an extreme case of entanglement sudden death, in which the formation of an entangled state is completely suppressed. The phenomena of entanglement sudden death and revival are well-known processes in quantum optics, which have been theoretically studied [221, 222] and experimentally observed [223, 224] in cavity QED and other systems.

The analysis of Figs. 3.4 and 3.6 shows that we can easily tune the entanglement generation through the delay of the second photon. When selecting large values of Δ, photons act independently so we can generate a periodic train of pulses in the concurrence. However, by decreasing the delay time we are able to shorten the pulse to the desired duration via sudden death of entanglement, or even create a dip followed by a revival. Finally, for zero delay we are able to raise the population of the qubit levels without generating any entanglement.

3.4. Entanglement detection through single-photon scattering

So far we have demonstrated the possibility of generating an entanglement pulse in the two-qubit subsystem via the scattering of a single-photon, as well as modifying the properties of such pulse by means of a second photon. The relevance of these results relies on the possibility of the experimental detection of such entanglement. As we mentioned in the introduction to this chapter, several methods have been proposed in cavity setups, but a detection scheme specifically designed for waveguides is lacking. We devote this section to study the possibility of detecting entanglement by means of probing the two-qubit state with a single-photon.

We will consider an initial two-excitation state in which a single, right-propagating photon is travelling towards the two-qubit ensemble. We assume such ensemble to be in an arbitrary pure single-excitation state. The global initial state of the system is thus

$$|\psi(0)\rangle = \int dx \psi(x; x_0) c_R^\dagger(x) \otimes \left(\frac{\sigma_1^\dagger + \xi \sigma_2^\dagger}{\sqrt{1+|\xi|^2}} \right) |0\rangle, \tag{3.39}$$

where the incoming wavepacket has the same shape as Eq. 3.5, and the state of the qubits is parametrized by the complex number ξ (Fig. 3.7). The disentangled product states $|g_1\rangle \otimes |e_2\rangle$ and $|e_1\rangle \otimes |g_2\rangle$ correspond to $\xi = \infty$ and $\xi = 0$, respectively. Similarly, the even/odd entangled states $|\pm\rangle$ are obtained for $\xi = \pm 1$. Since the parameter ξ fully determines the state of the two qubits, it also univocally determines the concurrence of

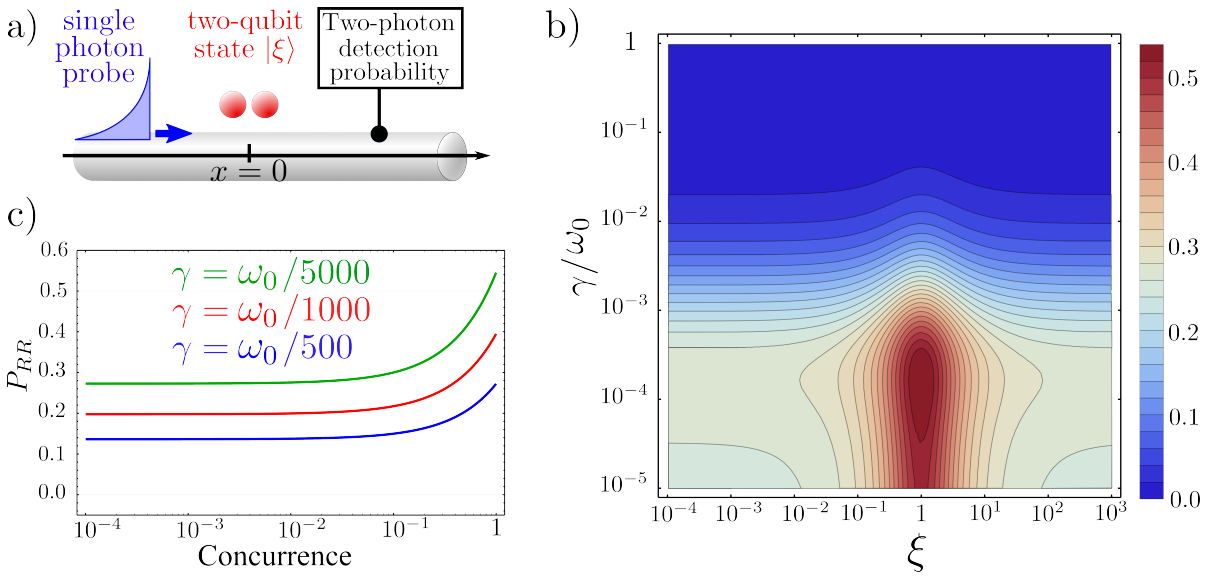

Figure 3.7: a) Setup for entanglement detection. A single-photon is scattered by the two-qubit ensemble, and the two-photon probability is measured at the right arm of the waveguide. b) Two-photon detection probability P_{RR} as a function of qubit-waveguide coupling, γ, and the state parameter ξ, for $\gamma_s = \omega_0/3000$. c) Relation between the probability P_{RR} and the concurrence of the initial state, for different values of the qubit-waveguide coupling.

such state, which reads

$$C = \frac{2|\xi|}{1+|\xi|^2}. \tag{3.40}$$

The idea behind the detection scheme is to relate the above expression with the photon scattering output. We thus calculate the time evolution of the initial state (3.39), $|\psi(t)\rangle$, by means of the two-excitation time evolution operator determined in Eq. 3.36.

In order to determine the initial concurrence $C(\xi)$ of the qubits from the scattering output, we set a detector at some position $x > 0$, as seen in Fig. 3.7a. This detector measures the total probability of collecting two photons propagating in the rightward direction, P_{RR}. We keep the detector open during the entire time evolution. This means that the total detected probability P_{RR} can be obtained by integrating the corresponding probability density over all positive positions,

$$P_{RR} = \lim_{t\to\infty} \int_0^\infty dx_1 \int_{x_1}^\infty dx_2 \frac{\langle\psi(t)|c_R^\dagger(x_1)c_R^\dagger(x_2)c_R(x_2)c_R(x_1)|\psi(t)\rangle}{\langle\psi(t)|\psi(t)\rangle}. \tag{3.41}$$

Note that the integrand is proportional to the second-order correlation function commonly used in quantum optics [26]. In the above expression, the long time limit is taken

to ensure that the photon-qubit interaction has finished, and our detector has collected any possible trace of the scattering output. Note that we only integrate over half the plane (x_1, x_2), since photons are bosonic in nature and therefore we must avoid double counting of states. To ensure that the state of the qubits has not decayed before being probed, we have assumed the initial condition $\gamma x_0 \ll v_g$, i.e., we consider the initial single-photon wavefront to be very close to $x = 0$. For simplicity, we also fix $\omega_s = \omega_0$ as in the previous sections, and set the linewidth of the incoming pulse to $\gamma_s/2 = \omega_0/3000$.

Let us first demonstrate that P_{RR} is indeed related to the concurrence. In Fig. 3.7b we show the behavior of the probability P_{RR} as a function of the qubit-waveguide coupling γ and the parameter ξ, which we assume real at the moment. The dependence of P_{RR} on ξ, and consequently on the initial entanglement between the qubits, is manifest. This dependence is more pronounced for $\gamma_s = 2\gamma$, where P_{RR} reaches a maximum as the decay/excitation rate of the two-qubit system is equal to the rate at which the pulse is arriving. Figure 3.7c depicts the two-photon detection probability as a function of the initial concurrence of the qubits for several values of the qubit-waveguide coupling γ . These curves show that, for a given γ and $\xi \in \mathbb{R}$, there is a biunivocal relation between P_{RR} and the initial concurrence. In this fashion, a measurement of the scattering output is able to retrieve information about the entanglement in the qubits.

So far we have schematically demonstrated the possibility of entanglement detection, but several issues remain obscure. First, the two-photon probability P_{RR} seems to be chosen *ad hoc*. This fact, along with the exact mechanism behind the relation between P_{RR} and ξ, requires an explanation. Second, note that the above scheme is unfavourable from the experimental point of view since, in order to implement it, a precise knowledge of the qubits frequency and linewidth, ω_0 and 2γ, is required. Moreover, we have to guarantee that the incident single photon has the shape in Eq. 3.5, with known parameters γ_s and ω_s. Finally, we need a dispersionless waveguide in order to keep the wavepacket shape during its propagation towards the detector. All these conditions suggest that a parameter-independent method would be much more useful. For this reason, in what follows we derive a very general result that does not depend on all those details, and provides a fundamental insight on the mechanism behind entanglement detection.

Our analysis stems from the results in Fig. 3.7c, which suggest there is an univocal relation between the two-photon detection probability and the initial concurrence of the two-qubit ensemble. Let us start by expressing our initial state Eq. 3.39 as a function of

the even and odd qubit operators,

$$|\psi(0)\rangle = \int dx \psi(x;x_0) c_R^\dagger(x) \otimes \left(\frac{(1+\xi)\sigma_e^\dagger + (1-\xi)\sigma_o^\dagger}{\sqrt{2}\sqrt{1+|\xi|^2}} \right) |0\rangle. \tag{3.42}$$

In the state above, the contribution associated to the odd symmetry qubit state does not interact with the incident photon nor decays into the waveguide, since the state $|-\rangle$ is completely uncoupled from the photonic modes. Thus, as the total number of excitations ($N = 2$) is conserved, the time evolution of the term proportional to $\sigma_o^\dagger|0\rangle$ will always correspond to a *one-photon state*, as one of the excitations remains permanently stored in the odd state of the qubits. This term will therefore not contribute to the two-photon detection probability in Eq. 3.41. On the other hand, the even term $\sigma_e^\dagger|0\rangle$ interacts with photons in a complex way but, as we have seen in the previous sections, any excitation in the even subspace will eventually decay into the waveguide. As a consequence, at time $t \to \infty$ this term will evolve into a *two-photon state*. Hence, by measuring any two-photon magnitude such as P_{RR} we project onto the subspace proportional to $\sigma_e^\dagger|0\rangle$. In this way we eliminate the contribution from the odd qubit state, and the dependence with the parameter ξ can be explicitly extracted out of P_{RR},

$$P_{RR} = \frac{|1+\xi|^2}{2(1+|\xi|^2)} \lim_{t\to\infty} \int_0^\infty dx_1 \int_{x_1}^\infty dx_2 \frac{\langle \psi_e(t)|c_R^\dagger(x_1)c_R^\dagger(x_2)c_R(x_2)c_R(x_1)|\psi_e(t)\rangle}{\langle \psi_e(t)|\psi_e(t)\rangle}. \tag{3.43}$$

Here, we have defined the $\xi-$independent state

$$|\psi_e(t)\rangle = U(t)|\psi_e(0)\rangle = U(t) \int dx \psi(x;x_0) c_R^\dagger(x)|\emptyset\rangle \otimes |+\rangle, \tag{3.44}$$

where $|\emptyset\rangle$ is the photonic vacuum state and $U(t)$ stands for the time evolution operator in Eq. 3.36. Note that the above factorization is not exclusive of the detection probability P_{RR}. Indeed, similar results would be obtained for any two-photon measurement such as P_{RL} or P_{LL}. Conversely, note that the opposite relation is not true, namely we cannot factor out the dependence with ξ in every photon measurement. This is the case of, for instance, single-photon observables, where we would be measuring contributions from two subspaces which evolve in time in different ways. Our entanglement detection scheme thus relies exclusively on two-photon probabilities and, among them, we choose P_{RR} for convenience.

Back to Eq. 3.43, note that not only have we factorized all the dependence with ξ, but we have also isolated the dependence with any other system parameters inside the integrals. This allows for the design of a parameter-independent entanglement detection

protocol. Hence, we can introduce a second measurement, namely the two-photon detection probability for an initially unentangled state, $P_{RR}(\xi = 0)$, and rewrite Eq. 3.43 as

$$P_{RR}(\xi) = \frac{|1+\xi|^2}{1+|\xi|^2} P_{RR}(\xi = 0). \tag{3.45}$$

We can finally rearrange the above equality in order to obtain

$$\left| \frac{P_{RR}(\xi)}{P_{RR}(\xi = 0)} - 1 \right| = \frac{2|\mathrm{Re}\,[\xi]\,|}{1+|\xi|^2}. \tag{3.46}$$

Let us focus first on the case in which the parameter ξ is a real number. In such situation, the expression above is equal to the concurrence 3.40, and thus the measurement of the normalized probability $P_{RR}(\xi)/P_{RR}(\xi = 0)$ fully determines the initial entanglement between the qubits. This situation is represented in Fig. 3.8, where the relation between concurrence (dashed line) and normalized probability (solid line) is shown. This method for measuring the entanglement between the qubits with only two measurements, namely $P_{RR}(\xi)$ and $P_{RR}(\xi = 0)$, does not require to fully determine the state of the two qubits, therefore being more feasible than full-state tomography. Additionally, our method is extremely powerful since the property Eq. 3.46 is independent of all the system parameters, whose global effect is accounted for in the measurement of $P_{RR}(\xi = 0)$. Indeed, this scheme is valid for any qubit frequency ω_0 or coupling γ. Moreover, it does not depend on the single-photon source, as the shape of the wavepacket can be completely arbitrary (provided that it has a steep increasing wavefront). The inclusion of free-space losses in the qubits or a non linear dispersion relation in the waveguide would not modify this equality either. The independence on all the relevant system parameters is remarkable, and it enormously facilitates the experimental implementation of this detection scheme. Note that the validity of this method relies on an efficient source of indistinguishable photons since, in order to normalize P_{RR} to $P_{RR}(\xi = 0)$, the two quantities must be measured exactly with the same single-photon wavepacket.

The above discussion applies only to states in which $\xi \in \mathbb{R}$. However, it is possible for the parameter ξ to have a non-zero imaginary part, a situation in which Eq. 3.46 is less restrictive. Indeed, in this case it is reduced to the inequality $C(\xi) > |P_{RR}(\xi)/P_{RR}(\xi = 0) - 1|$. This expression is still useful, as it provides a lower bound for the concurrence of the qubits. Note that we cannot obtain extra information about the concurrence with any other two-photon measurement such as P_{RL} or P_{LL}, since they are equivalent to P_{RR}. However, it is not difficult to conceive an extension of our protocol for any value of ξ in the complex plane, by means of state of the art techniques in cavity QED. We will only briefly outline the main lines here, since it goes beyond the scope of this

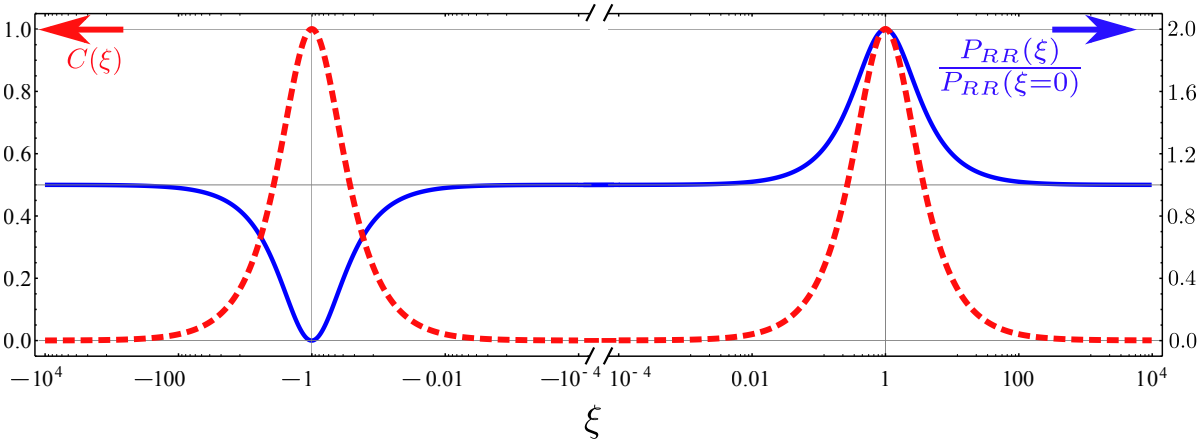

Figure 3.8: Concurrence (red dashed line) and normalized two-photon detection probability (blue line) as a function of the real parameter ξ.

thesis and the possibility of entanglement detection has already been demonstrated. The general scheme can be based on the possibility of adding an arbitrary phase $e^{i\theta}$ to the state of one of the two qubits, a trivial single-qubit operation which can be realized, for instance, through a detuned classical laser field acting upon the desired qubit [91]. Assuming this can be implemented in our setup, we can design a three step protocol for measuring the qubit-qubit entanglement. First, we create the state $(\sigma_1^\dagger + \xi\sigma_2^\dagger)|0\rangle$ and measure $P_{RR}/P_{RR}(\xi = 0)$, thus determining the real part of ξ. Second, we generate another copy of the original state, and perform a shift by a phase $e^{i\pi/2} = i$ on the second qubit, such that the new state is given by the parameter $\xi' = -\mathrm{Im}[\xi] + i\mathrm{Re}[\xi]$. Finally, we measure again $P_{RR}/P_{RR}(\xi' = 0)$, determining in this case the imaginary part of ξ. Although we will not go into further details of this implementation, it is important to stress that it is not only possible, but within the usual requirements for entanglement detection in cavities, namely different copies of the original state and auxiliary pump lasers [235].

3.5. Chirality-assisted single-photon devices

In this section we deviate from the topics studied above, in order to explore a different advantage brought about by our full control over the photonic degrees of freedom. Whereas in the previous sections we have focused our attention on using few-photon

inputs to modify or probe the state of quantum emitters, here we address the opposite problem. Our aim is to employ QEs to act upon single-photon states, therefore creating photonic devices specifically designed to operate at the single-photon level.

3.5.1. System, Hamiltonian, and solution of the single-photon scattering.

Instead of designing a different platform for each specific device, it is preferable regarding a possible future implementation to devise a setup in which many different operations can be performed. Inspired by their established performance and flexibility in waveguide-cavity systems [114, 244, 262], we will choose a four-port setup composed of two transmission lines, as depicted in Fig. 3.9a. Two waveguides, which we label u and d (up and down) respectively, form a four port arrangement in which each input/output port is labelled with the numbers 1 to 4 as shown in the figure. Each of the waveguides is coupled to one of the two transitions of a central three-level system (3LS) in a lambda configuration. The choice of a three-level structure in this case is not arbitrary, since the presence of two well-defined transitions is required for our devices. Additionally, although a two-qubit ensemble could achieve the desired effect, such implementation would introduce unwanted parameters such as separation or detuning, whose precise control may be experimentally challenging. In principle, we allow both transitions of the 3LS to be chirally coupled to their respective waveguides, and label the corresponding coupling rates to left- and right- propagating photons γ_{jL} and γ_{jR} $(j = u, d)$ respectively. These couplings define the total decay rate of the excited state $|e\rangle$ into each of the waveguides, γ_j, and the directionality of each transition D_j, given respectively by

$$\gamma_j = \gamma_{jR} + \gamma_{jL} \qquad ; \qquad D_j = \frac{\gamma_{jR} - \gamma_{jL}}{\gamma_j} \qquad (j = d, u). \tag{3.47}$$

Additionally, the excited state of the 3LS may decay into radiative modes outside of the waveguides at a rate Γ, which defines the β factor as

$$\beta = \frac{\gamma_d + \gamma_u}{\gamma_d + \gamma_u + \Gamma}, \tag{3.48}$$

equivalent to the definition employed in the previous chapter, Eq. 2.1.

The above system can be achieved in a number of ways, for instance, by using the appropriate symmetry of the system and the QE dipole moment to attain the desired selective coupling of the transitions $|g\rangle \leftrightarrow |e\rangle$ and $|s\rangle \leftrightarrow |e\rangle$ [54, 266]. Note that in this case our four port device can either represent two physically separated waveguides or,

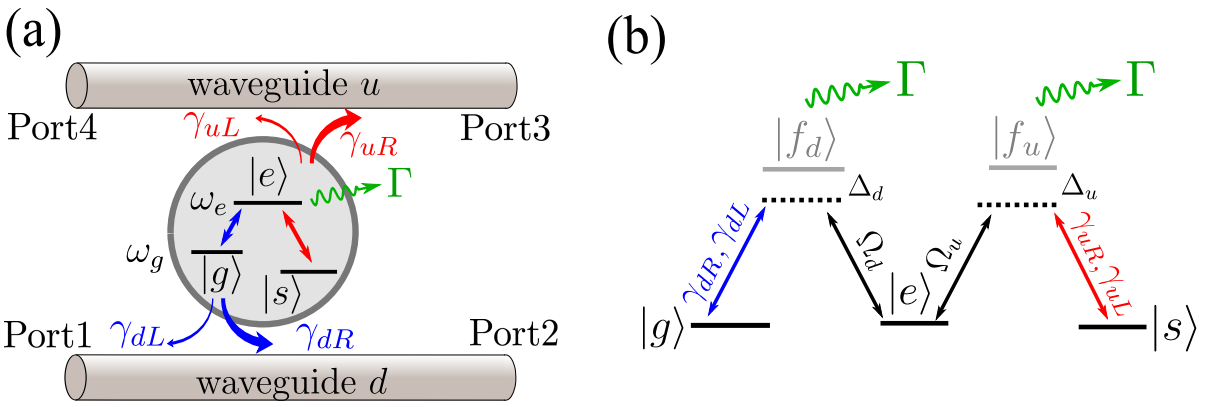

Figure 3.9: (a) Scheme of the system under study. A three level system in Lambda configuration interacts with two independent waveguides, labelled u and d. The transition $|g\rangle \leftrightarrow |e\rangle$, depicted in blue, is chirally coupled to the right- and left- propagating photons of the waveguide d, with coupling rates γ_{dR} and γ_{dL} respectively. The second transition, $|s\rangle \leftrightarrow |e\rangle$ (in red) is in turn chirally coupled to the waveguide u, with coupling rates γ_{uR} and γ_{uL}. Finally, the excited state $|e\rangle$ may decay radiatively into free space modes at a rate Γ. (b) Inverted W-system in which the three-level structure of panel a can be achieved by means of classical pump lasers.

alternatively, two modal branches belonging to the same waveguide. The latter is more efficient for avoiding crosstalk between the u and d reservoirs, although in the case of physically separated waveguides such crosstalk can also be largely reduced by an appropriate engineering of the crossing point between the waveguides [267–269]. Regarding the independent control of the different couplings $\gamma_{j\alpha}$ $(j = u, d; \alpha = R, L)$, it relies on the control of the total rates γ_j, since the directionalities are determined by the positions of the QEs within the nanostructure [108, 249]. Such degree of control can be achieved by means of an alternative implementation of a lambda 3LS, such as the one depicted in Fig. 3.9b in terms of a five-level system (also called W-system). Multilevel ladders of this kind are widely available in Zeeman hyperfine manifolds in atomic waveguide QED [204]. In our proposed implementation, two optically excited states $|f_{u,d}\rangle$ are respectively connected to both $|g\rangle$ and $|s\rangle$ through the d and u waveguides. Moreover, the states $|f_{u,d}\rangle$ are also connected with $|e\rangle$ by means of two off-resonant classical lasers with corresponding detunings $\Delta_{u,d}$ and amplitudes $\Omega_{u,d} \ll |\Delta_{u,d}|$. Under these conditions, the excited states are scarcely populated, and can be removed from the dynamics by means of adiabatic elimination [270]. The resulting three-level structure is characterized by an effective dynamics equivalent to that displayed in Fig. 3.9a, which incorporates the effect of the eliminated levels through renormalized waveguide decay rates $\gamma_{j\alpha} \to \frac{|\Omega_j|^2}{\Delta_j^2}\gamma_{j\alpha}$. Notice that the directionalities D_j remain unaltered by this renormalization but, on the other

hand, the β factor decreases since the transformation for the loss rate is $\Gamma \to \sum_j \frac{|\Omega_j|^2}{\Delta_j^2}\Gamma$. These reductions are usually not critical (for instance, less than 50% for $\gamma_1 = \gamma_2$), and are compensated by the advantages achieved by this adiabatic renormalization, namely the desired three-level structure with long-lived states $|g\rangle, |s\rangle, |e\rangle$, and tunable coupling rates γ_1 and γ_2.

The Hamiltonian describing this system is a generalization of the waveguide QED Hamiltonians we have used so far. Specifically, it can be expressed as the sum of five different contributions ($\hbar = 1$),

$$H = H_{3LS} + H_d + H_u + H_{Id} + H_{Iu}. \tag{3.49}$$

Here, the first term describes the bare 3LS,

$$H_{3LS} = (\omega_e - i\Gamma/2)|e\rangle\langle e| + \omega_g|g\rangle\langle g|, \tag{3.50}$$

where the losses Γ are described through a non-hermitian contribution accounting for the spontaneous emission of the excited state $|e\rangle$ into free space modes. As we have already determined in the previous chapter, this is a valid approximation for any photon scattering problem. In the above equation, the origin of energies is taken at the state $|s\rangle$ for convenience. The second and third terms in Eq. (3.49) describe the energy of the photonic modes in the two waveguides, given by

$$\begin{aligned} H_d &= -iv_g \int dx \left(c_R^\dagger(x)\partial_x c_R(x) - c_L^\dagger(x)\partial_x c_L(x) \right), \\ H_u &= -iv_g \int dy \left(b_R^\dagger(y)\partial_y b_R(y) - b_L^\dagger(y)\partial_y b_L(y) \right). \end{aligned} \tag{3.51}$$

Here, the operators $c_{R(L)}^\dagger(x)$ are employed to describe the photonic creation operators for right(left) photons in the waveguide d, whereas $b_{R(L)}^\dagger(y)$ represent the equivalent operators for the upper waveguide. The respective group velocities of both waveguides, v_g, can be considered equal with no loss of generality since, in this simple picture, the system dynamics is only determined by the coupling rates $\gamma_{j\alpha} \propto v_g^{-1}$, and therefore a different group velocity simply rescales the couplings to one of the waveguides with respect to the other. Note that the Hamiltonians H_d and H_u are completely equivalent, the only difference being a deliberate change in notation for both operators and position coordinates. This distinction aims to ease the identification of quantities belonging to each of the two independent waveguides.

The last two terms in Eq. (3.49) represent the coupling between the two waveguides

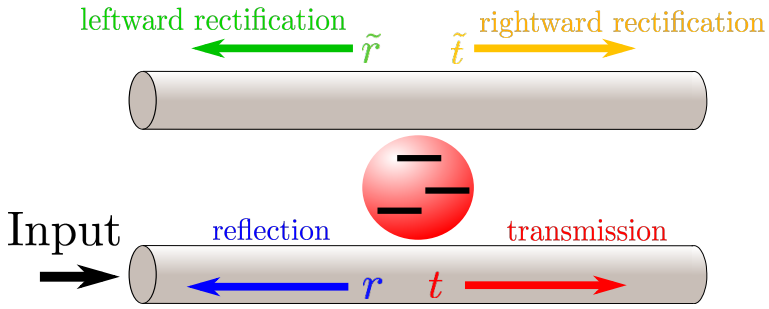

Figure 3.10: (a) General definition of the scattering coefficients. The usual reflection and transmission are labelled as r and t, respectively. The processes by which the photon *jumps* into the neighbouring waveguide have amplitudes $\tilde{r}$, for backward propagation, and $\tilde{t}$ for forward propagation.

and the 3LS, which takes place at $x = y = 0$. They are expressed as

$$\begin{aligned} H_{Id} &= \sum_{\alpha=R,L} \int dx \delta(x) V_\alpha c_\alpha^\dagger(x) |g\rangle\langle e| + H.c., \\ H_{Iu} &= \sum_{\alpha=R,L} \int dy \delta(y) W_\alpha b_\alpha^\dagger(y) |f\rangle\langle e| + H.c., \end{aligned} \tag{3.52}$$

Here, the four coupling constants $\{V_R, V_L, W_R, W_L\}$ are related to the coupling rates through the usual relation $\gamma_{d\alpha} = V_\alpha^2/v_g, \gamma_{u\alpha} = W_\alpha^2/v_g$ for $\alpha = R, L$. Let us emphasize that a key feature of this Hamiltonian is that each transition of the 3LS interacts only with one of the waveguides. Specifically, the transition $|g\rangle \leftrightarrow |e\rangle$ is coupled to the bottom waveguide, whereas the transition $|s\rangle \leftrightarrow |e\rangle$ is coupled to the upper waveguide. Note that this coupling structure, essential for the rest of the chapter, does not isolate one waveguide from another, as they can exchange probability through the excited state $|e\rangle$.

The complete Hamiltonian of Eq. (3.49) can be fully diagonalized in the single-excitation subspace. In order to study the single-photon scattering, we can restrict the problem to a photon incoming from an arbitrarily selected port, in this case port 1. The solutions corresponding to an input through ports 2 to 4 are not detailed here, as their calculation follows an analogous procedure (see Appendix B). Note that, if the 3LS is initially in the state $|s\rangle$, it does not interact with the photons in the bottom waveguide, and the scattering solution in this case is reduced to an unperturbed free wave travelling from port 1 to port 2. Henceforth, our interest is focused on the situation in which the 3LS is initially in the state $|g\rangle$. In this situation, the photon can be scattered into the four different ports. These four scattering possibilities are characterized by their respective probability amplitudes, which are schematically depicted in Fig. 3.10.

In order to avoid repeating very similar calculations as those performed in previous sections, we detail the step by step diagonalization of the Hamiltonian in the single-excitation subspace in Appendix B. The single-photon wavefunction has a similar form as in the previous cases,

$$|\epsilon\rangle = \alpha_e|e\rangle + \sum_{\alpha=R,L}\int dx\phi_\alpha(x)c_\alpha^\dagger(x)|g\rangle + \int dy\psi_\alpha(y)b_\alpha^\dagger(y)|s\rangle, \tag{3.53}$$

and is completely determined by the four probability amplitudes for each of the possible scattering processes defined in Fig. 3.10, given by

$$t(\omega) = \frac{\omega-\omega_{eg}+i\Gamma/2+i(\gamma_{dL}-\gamma_{dR}+\gamma_{uL}+\gamma_{uR})/2}{\omega-\omega_{eg}+i\Gamma/2+i(\gamma_{dL}+\gamma_{dR}+\gamma_{uL}+\gamma_{uR})/2}, \tag{3.54}$$

$$r(\omega) = \frac{-i\sqrt{\gamma_{dR}\gamma_{dL}}}{\omega-\omega_{eg}+i\Gamma/2+i(\gamma_{dL}+\gamma_{dR}+\gamma_{uL}+\gamma_{uR})/2}, \tag{3.55}$$

$$\tilde{t}(\omega) = \frac{-i\sqrt{\gamma_{dR}\gamma_{uR}}}{\omega-\omega_{eg}+i\Gamma/2+i(\gamma_{dL}+\gamma_{dR}+\gamma_{uL}+\gamma_{uR})/2}, \tag{3.56}$$

$$\tilde{r}(\omega) = \frac{-i\sqrt{\gamma_{dR}\gamma_{uL}}}{\omega-\omega_{eg}+i\Gamma/2+i(\gamma_{dL}+\gamma_{dR}+\gamma_{uL}+\gamma_{uR})/2}, \tag{3.57}$$

where ω is the energy of the incoming photon, and $\omega_{eg} = \omega_e - \omega_g$ is the energy of the transition $|g\rangle \leftrightarrow |e\rangle$. It is straightforward to check that the probability is conserved as $|t|^2+|r|^2+|\tilde{t}|^2+|\tilde{r}|^2 = 1$ when $\Gamma = 0$. The dependence of the above coefficients with the system parameters allows us to tune them in order to perform the desired operations on the photons.

3.5.2. Single-photon rectification

In this section we will show how to tune the scattering coefficients to devise a single-photon router or rectifier, able to direct the input photon from port 1 to port 3. For a clearer interpretation of the physical mechanisms involved, let us consider for now the ideal case in which the couplings are maximally chiral and the losses of the 3LS are negligible, i.e., $D_j = 1$ and $\beta \to 1$ (or, equivalently, $\gamma_{dL} = \gamma_{uL} = 0$ and $\Gamma = 0$). In this simple situation, both coefficients r and $\tilde{r}$ vanish, and the photon can only be scattered rightwards. The remaining two scattering amplitudes become

$$t(\omega) = \frac{\omega-\omega_{eg}+i(\gamma_{uR}-\gamma_{dR})/2}{\omega-\omega_{eg}+i(\gamma_{dR}+\gamma_{uR})/2}, \tag{3.58}$$

$$\tilde{t}(\omega) = \frac{-i\sqrt{\gamma_{dR}\gamma_{uR}}}{\omega-\omega_{eg}+i(\gamma_{dR}+\gamma_{uR})/2}. \tag{3.59}$$

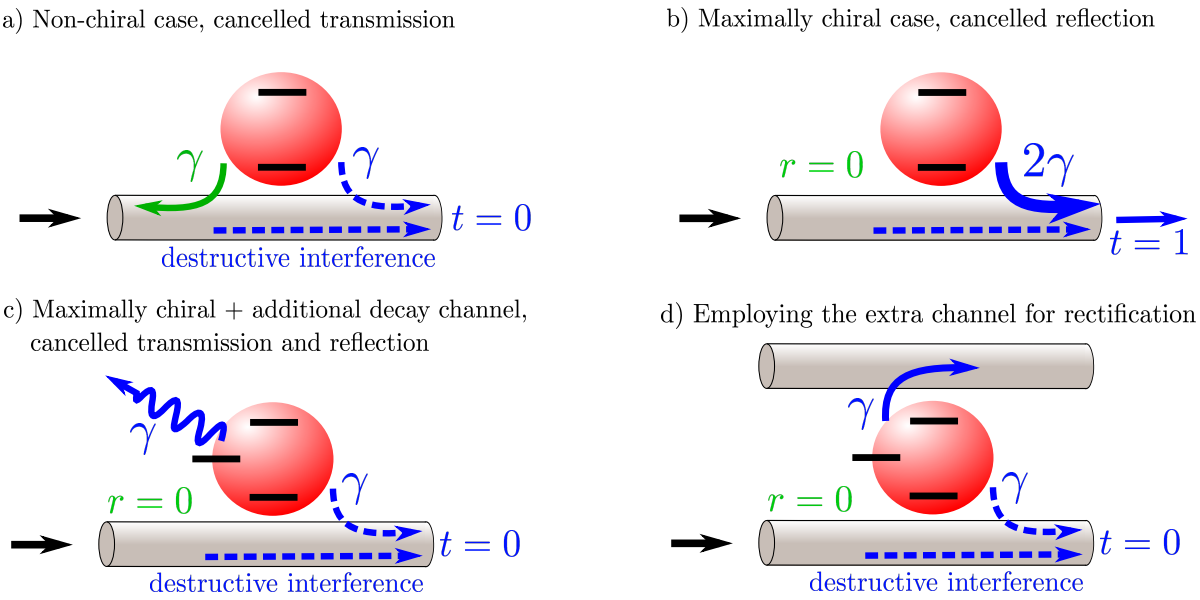

Figure 3.11: a) The single-photon transmittance for a qubit non-chirally coupled to a waveguide vanishes due to a destructive interference. b) When the coupling is maximally chiral, however, the reflection is cancelled and the balance between the previously interfering amplitudes is broken, resulting in full transmission. c) If an extra decay channel is added to the qubit, perfect interference can be achieved again, and both transmission and reflection are cancelled. d) Our scheme uses a second waveguide to collect the photon emitted through the extra channel, achieving full rectification.

From the formulas above, it is straightforward to see that when the frequency of the incoming photon is resonant with the transition $|g\rangle \leftrightarrow |e\rangle$ ($\omega = \omega_{eg}$) and the two remaining couplings are chosen equal ($\gamma_{dR} = \gamma_{uR}$), the transmission coefficient t also vanishes. In this particular case, three out of the four scattering amplitudes cancel out ($r = \tilde{r} = t = 0$), and the incoming photon is directed to Port 3 with probability $|\tilde{t}|^2 = |-1|^2 = 1$. Thus, by means of this simple tuning, we have achieved a *single photon rectifier* which allows for a deterministic switch of a given input photon into a second waveguide[1]. This device, also known as single-photon router in the literature [272–274], has been extensively researched for its evident applications in photonic quantum networks.

The underlying physical mechanism of rectification can be understood in terms of quantum interference. In order to develop a clear picture of this mechanism, we first

[1]Note that since $\tilde{t} = -1$, the rectification also effectively performs a so-called $\pi-$ phase gate operation on the incoming *photonic qubit*. We will not explore this possibility further, since simpler realizations have been already proposed in both chiral [72] and non-chiral [271] waveguide setups.

recall the situation of a two-level system (2LS) symmetrically coupled to a single waveguide, as shown in Fig. 3.11a. As mentioned in the previous chapter, in this case an incoming photon whose frequency is resonant with that of the 2LS will be reflected with probability 1 (see Appendix A for a formal demonstration). Such perfect reflection is a direct consequence of the destructive interference between two quantum processes, namely the direct transmission of the photon without interaction with the 2LS and, on the other hand, an absorption of the photon by the 2LS followed by rightward reemission. The amplitudes of these two processes, shown in dashed lines in Fig. 3.11a, cancel out as they are equal in magnitude an opposite in sign. Since one of the two scattering channels, namely transmission, is cancelled by this interference, the only possible process is reflection which therefore must account for 100% of the probability.

The situation can be turned around when we allow the qubit-waveguide coupling to be chiral, as Fig. 3.11b shows. Whenever a photon is absorbed by the 2LS, the chiral interaction introduces an imbalance between the right- and left- reemission probabilities. Hence, while the amplitude of the direct transmission process (dashed blue line) remains unchanged, the absorption+rightward reemission amplitude (solid blue line) increases or decreases in magnitude with respect to the non-chiral situation, depending on whether rightward emission is favoured or hindered by chirality. In Fig. 3.11b, the maximally chiral limit is displayed, where the coupling asymmetry is pushed to its maximum, i.e., no photons can be emitted leftwards. In such situation, since the reflection of the photon at resonant frequency is impossible, the rightward reemission amplitude (thick blue line) is now maximized in magnitude, and the transmission probability tends to unity. This is also demonstrated analytically in Appendix A. Chirality thus allows for a complete inversion of the scattering output as compared to the non-chiral case of Fig 3.11a.

Interestingly, it is possible to cancel out *both* transmission and reflection coefficients by adding an extra decay channel (Fig. 3.11c). Here, the coupling to left-propagating photons is again set to 0 to prevent reflection, but we now allow the excited state to decay into a second and in principle arbitrary environment. If we now choose the decay rate of the upper state into this environment equal to the decay rate into right-propagating waveguide modes as shown in the figure, only half of the probability absorbed into the excited state will decay back into rightward guided modes. But as the discussion in Fig. 3.11a revealed, this is exactly the fraction of reemitted probability which leads to perfectly destructive interference in transmission. Hence, the transmission coefficient is 0 again and, having no option of being either reflected or transmitted, the incoming photon is redirected into the secondary environment with maximum probability. The only remaining task in order to recover our four port system is to assume that the

extra environment is a second waveguide, as depicted in Fig. 3.11d. With this addition we introduce the possibility of addressing the rectified photon to a particular port for further use.

The rectification device is thus achieved by cancelling both transmission and reflection coefficients, therefore forcing the photon to *switch* into the second waveguide. Note, however, that the vanishings of r and t respond to very different causes, in the first case to chirality alone (through $\gamma_{dL} = 0$), and in the second to destructive quantum interference. In any case, chirality is essential both to extract the photon from the initial waveguide and to redirect it to the selected output port after the rectification.

Let us now study the performance of the single-photon rectifier in a more realistic scenario, in which the device operation is affected by losses $\Gamma \neq 0$ as well as imperfect directionalities $D_j < 1$. In principle, we consider the four coupling rates $\gamma_{j\alpha}$ to be different in this case. First of all, note that even in this general situation we can tune the system parameters so that the transmission coefficient vanishes. Indeed, from Eq. (3.54) it is straightforward to see that $t = 0$ for an incoming photon in the resonance condition ($\omega = \omega_{eg}$) whenever the couplings fulfil

$$\gamma_{dR} = \gamma_{dL} + \gamma_{uL} + \gamma_{uR} + \Gamma. \tag{3.60}$$

This requirement is understandable from the argument given above related to quantum interference. Here, the decay rate to rightward guided modes, γ_{dR}, has to be equal to the decay rate of the excited state $|e\rangle$ into the rest of the possible channels combined, such that only half of the probability is reemitted rightwards. Note, however, that this condition is limited by physical constraints, and cannot be always achieved. Indeed, if we rewrite Eq. (3.60) in terms of β factor and directionalities,

$$\gamma_u = \gamma_{dR} - \gamma_{dL} - \Gamma = \gamma_d \left(\beta(D_d + 1) - 1\right), \tag{3.61}$$

it is clear that a physical solution (i.e., $\gamma_d, \gamma_u > 0$) requires the β factor to fulfil

$$\beta \geq \frac{1}{D_d + 1}. \tag{3.62}$$

In other words, there is a threshold for the β factor above which the rectification condition $t = 0$ can be achieved. The reason behind this fundamental constraint is the physical impossibility for the state $|e\rangle$ to emit half of its population into rightward modes in the waveguide d, when losses surpass a certain value. Indeed, if Γ is so large as to represent more than half of the total decay rate of $|e\rangle$, there is no possible way of distributing the couplings γ_{jR}, γ_{jL} in order to fulfil the $t = 0$ requirement. Equation (3.62) thus determines the regime of operation of the single-photon rectifier.

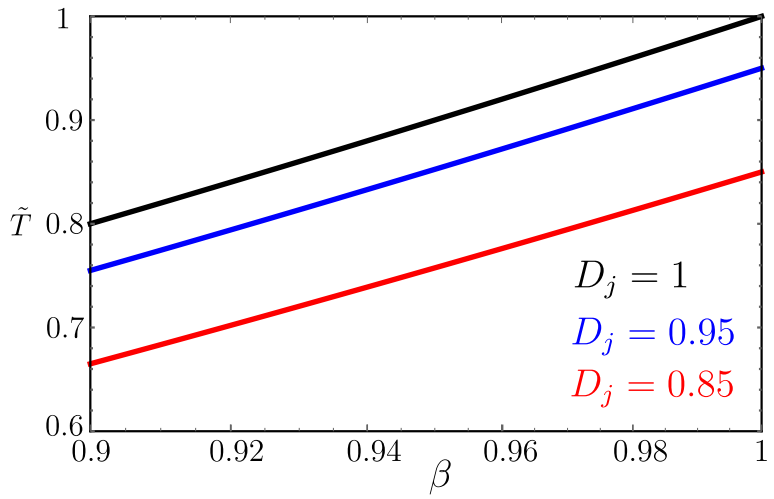

Figure 3.12: Total probability of rectification into port 3 versus β factor, for different directionalities $D_d = D_u$.

In practical terms, the limitation expressed by Eq. (3.62) is not very restrictive for a wide variety of realistic systems. Indeed, for perfectly directional couplings ($D_j = 1$) we can achieve the rectification condition $t = 0$ for β factors as low as $1/2$, whereas for usual experimental values of $0.8 < D_j < 0.98$ [72] the limit only increases up to $\beta \gtrsim 0.56$. These β factors are very common in most waveguide systems, where values as high as $\beta \sim 0.98$ have been reported [66]. Therefore, from now on we will consider the case in which the assumption $t = 0$ is fulfilled. By doing so, the only two factors decreasing the performance of the rectifier will be the losses Γ, and the leakage into ports 1 and 4 caused by imperfect directionalities. Note, additionally, that the efficiency of the device also be diminishes if the incoming photon is detuned with respect to the transition frequency ω_{eg}, a situation in which the transmission towards port 2 would not completely vanish. However, this is a minor problem as compared to the finite directionalities and the free-space losses. Indeed, the effect of the detuning is only relevant if such detuning is large as compared to the emission linewidth of the state $|e\rangle$, namely $\gamma_d + \gamma_u + \Gamma$. However, for the system to behave as a rectifier, we must tune the coupling rates to fulfil Eq. (3.62), a condition that can be also written as $\gamma_d + \gamma_u + \Gamma \geq \Gamma(D_d^{-1} + 1)$. Therefore, the emission linewidth of the state $|e\rangle$ is always relatively large for an operating rectifier, making it intrinsically robust against small variations of the resonance condition $\omega = \omega_{eg}$.

The efficiency of the single-photon rectifier can then be quantified through the total rectification probability which, under the conditions $\omega = \omega_{eg}$ and $t = 0$, is given by

$$\tilde{T} = |\tilde{t}|^2 = \frac{1 + D_u}{1 + D_d} \left(\beta(D_d + 1) - 1\right) \qquad \left(\text{for } \beta \geq \frac{1}{D_d + 1}\right). \tag{3.63}$$

Note that in the ideal case ($\beta \to 1$ and $D_j \to 1$) the efficiency defined above is equal to 1, whereas in a realistic case the probability leakage into the undesired channels (free-space, as well as ports 1 and 4) will reduce this value. The scattering probability $|\tilde{t}|^2$ is displayed in Fig. 3.12 as a function of the β factor and for different values of the directionalities D_d and D_u, considered equal for simplicity. The rectification probability is shown to remain rather close to unity for realistic directionalities, for instance as high as $\sim 80\%$ for easily achievable values of $\beta = 0.93$, $D_j = 0.9$.

3.5.3. Single-photon diode

The four-port setup presented above can also act as a single photon diode or isolator as defined in Ref. [253], in this case with respect to the waveguide d. This behavior is achieved already in the rectifier configuration with no further parameter tuning. Let us explain its basic operation in the ideal scenario, where the directionalities are maximized ($D_j = 1$) and the system is lossless ($\Gamma = 0$). As we have seen above, by choosing the coupling rates to fulfil $\gamma_{dR} = \gamma_{uR}$ we are able to achieve perfect rectification of a photon from port 1 into port 3. In such configuration, a non-reciprocal behavior spontaneously arises for the photons in the bottom waveguide. Indeed, if an input photon ($\omega = \omega_{eg}$) is introduced from port 1 it will not be able to reach port 2, since it is extracted from the waveguide d by means of the rectification process. On the other hand, the same input introduced along port 2 will be perfectly transferred towards port 2, since the maximum directionality $D_d = 1$ implies $\gamma_{dL} = 0$ and, as a consequence, the 3LS is unable to interact with the left-propagating photon. These two alternative photonic paths, depicted in Fig. 3.13, are respectively labelled $l \to r$ and $r \to l$. Note that in this situation a single-photon *current* can be transmitted past the 3LS only in one direction, namely $r \to l$. Consequently, the system acts as a single-photon diode.

In order to determine the diode efficiency in a realistic situation ($D_j < 1$, $\Gamma > 0$), we must take into account the loss-inducing processes along each path. We will assume the $t = 0$ condition, Eq. 3.60, is fulfilled. For a photon incoming along the path $l \to r$ (Fig. 3.13a), this automatically cancels the transmission probability. However, some noise can be added to the device when such photon is reflected back towards port 1. Any other scattering process, including loss to free-space, extracts the photon from the waveguide d, thus representing a desired output. The performance of the diode along the path $l \to r$ will then be quantified only by the reflection probability $R_{l\to r} = |r|^2$, where the reflection coefficient r is given by Eq. 3.55. For a photon in resonance and under the condition

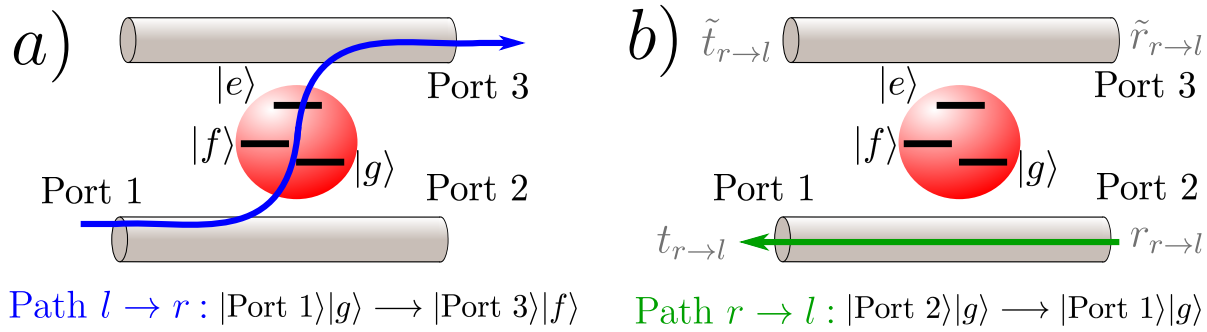

Figure 3.13: Scheme of the operation of the system as a single-photon diode. a) A single photon incoming through port 1 is rectified to port 3 with maximum probability, and therefore is not able to reach port 2. b) A photon introduced along port 2 reaches port 1 undisturbed. The grey labels at each port define the scattering coefficients in this situation.

$t_{l\to r} = 0$ this coefficient reads

$$R_{l\to r} = \frac{1 - D_d}{1 + D_d} \qquad \left(\text{for } D_d > 0 \text{ and } \beta \geq \frac{1}{D_d + 1}\right). \tag{3.64}$$

Let us now focus on the second photon path, $r \to l$ (Fig. 3.13b). In this case, the scattering coefficients are different from Eqs. 3.54-3.57, and have to be determined independently (see Appendix B). For a photon in the resonance condition, $\omega = \omega_{eg}$, and provided that $t_{l\to r} = 0$, they are equal to

$$t_{r\to l} = 1 - R_{l\to r}, \tag{3.65}$$
$$r_{r\to l} = r_{r\to l}, \tag{3.66}$$
$$\tilde{t}_{r\to l} = \tilde{r}_{l\to r}\sqrt{R_{l\to r}}, \tag{3.67}$$
$$\tilde{r}_{r\to l} = \tilde{t}_{l\to r}\sqrt{R_{l\to r}}. \tag{3.68}$$

In this case, two different factors affect the performance of our diode. The first is a possible reflection of the incoming photon back into port 2, which introduces noise as discussed above. The probability of this event, according to Eq. 3.66, is exactly the same as for the opposite path, i.e., $R_{l\to r}$. The second decrease in performance comes from the rest of the processes which prevent the photon from reaching port 1. The efficiency of the transmission is quantified by the probability

$$T_{r\to l} = |t_{r\to l}|^2 = (1 - R_{l\to r})^2. \tag{3.69}$$

Surprisingly, the performance of the diode as quantified through Eqs. 3.64 and 3.69 is a function *only* of the directionality D_d, through the reflection probability $R_{l\to r}$. This

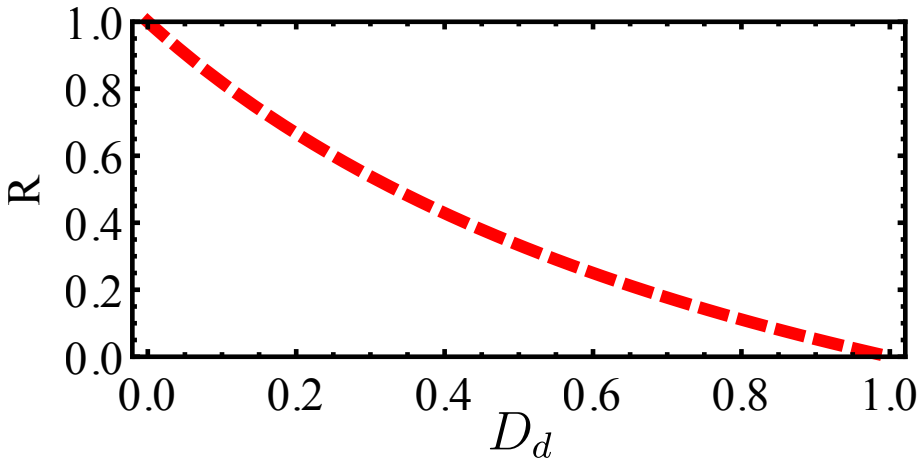

Figure 3.14: Single-photon reflection probability versus directionality of the bottom waveguide. This is the only parameter determining the performance of a single-photon diode.

implies the diode is more robust as a device than the rectifier, a fact that is easily understood by comparing the requirements for both devices. In the case of the diode, its operation relies on the photon incoming through port 1 being removed from the waveguide d in any manner. On the other hand, the rectifier requires such photon to be extracted from the bottom waveguide *and* to be directed to a specific port in waveguide u. This makes the diode less sensitive to the particular parameters associated with the photon reemission from the state $|e\rangle$. Specifically, the operation of the diode is not dependent on the particular value of Γ, γ_{uR}, and γ_{uL}, but on the total external loss rate for photons within the bottom waveguide, $\gamma_{uR} + \gamma_{uL} + \Gamma$. Since such rate is related to D_d through the $t = 0$ condition (see Eq. 3.60), the performance of the diode depends exclusively on the parameter D_d. In Fig.3.14 we display the probability R versus the directionality D_d. For usual directionalities $D_d \gtrsim 0.9$ the reflection losses are very low, $R \sim 5\%$, and the transmission probability along the path $r \to l$ remains at $T_{r\to l} \sim 90\%$. On the other hand, in the best experimental values up to date in photonic crystal waveguides, $D_j \sim 0.98$ [72], the reflection-induced noise is reduced to 1% while the transmission probability goes above 0.98. This single-photon diode based on quantum interference is therefore very robust and could be already implemented in state of the art experimental setups.

3.6. Chirality-assisted two-photon transistor.

The promising properties of or four port device at the single photon level rise the question as to how does it perform for two-photon inputs. In this section we will first characterize the two-photon response of our system by means of detection probabilities. Then, we will show how this device can also act as a transistor for the bottom waveguide, that enables a single photon to be transmitted to a desired port only if a second *gate* photon is present.

3.6.1. Scattering of a two-photon state.

First of all, we need to solve the scattering eigenstate associated with a two-photon input, i.e., two waves with well defined momentum k_1 and k_2 incoming through Port 1, the initial state of the 3LS being $|g\rangle$. Following the same steps as in the previous sections of this chapter, we define the general two-excitation eigenstate for our problem,

$$\begin{aligned}|\epsilon\rangle = &\int dx_1 \int dx_2 \left(\sum_{\alpha=R,L} \phi_{\alpha\alpha}(x_1,x_2) c_\alpha^\dagger(x_1) c_\alpha^\dagger(x_2) + \phi_{RL}(x_1,x_2) c_R^\dagger(x_1) c_L^\dagger(x_2) \right) |g\rangle \\ &+ \int dx \int dy \sum_{\alpha,\beta} \psi_{\alpha\beta}(x,y) c_\alpha^\dagger(x) b_\beta^\dagger(y) |s\rangle + \int dx \sum_{\alpha=R,L} \varphi_\alpha(x) c_\alpha^\dagger(x) |e\rangle.\end{aligned} \tag{3.70}$$

In the above equation, the wavefunctions $\phi_{\alpha\beta}$ correspond to states in which both photons are in the bottom waveguide. Two of these functions are subject to the bosonic symmetry constraint $\phi_{\alpha\alpha}(x_1,x_2) = \phi_{\alpha\alpha}(x_2,x_1)$. The wavefunctions $\psi_{\alpha\beta}$ describe states with one photon in each of the waveguides, whereas the functions φ_α account for states in which one of the excitations is in the state $|e\rangle$ of the 3LS. The explicit calculation of the wavefunctions above is detailed in Appendix B. In a similar way as in the simpler two-photon state calculated in Eq. 3.23, the corresponding wavefunctions $\phi_{\alpha\beta}$, $\psi_{\alpha\beta}$, and φ_α will be defined piecewise, containing a possible input term (in this problem, only in ϕ_{RR} since both input photons are introduced along port 1), transient terms where only one of the incoming photons has interacted with the 3LS and, finally, the asymptotic terms in which such interaction is finished for both photons. Only the latter contributions describe the scattering outputs of the system.

The above distinction between input, transient and output terms in the two-photon

eigenstate allows for the splitting of such eigenstate into two contributions,

$$|\epsilon\rangle = |\epsilon_i\rangle + |\epsilon_o\rangle. \tag{3.71}$$

The first term in the above equation is labelled *input state* $|\epsilon_i\rangle$, and contains by definition *both* the input and the transient contributions to the eigenstate $|\epsilon\rangle$. The second term is referred to as the scattering *output state* $|\epsilon_o\rangle$, which contains the asymptotic behavior mentioned above in which both photons have already interacted with the 3LS. As detailed in Appendix B, $|\epsilon_o\rangle$ is constructed by removing from $|\epsilon\rangle$ all the terms containing a right-propagating photon in $x < 0$, from where the calculation of the state $|\epsilon_i\rangle$ follows by simple substraction.

The definition of the input and output states is very useful in the two-photon case, since the two-photon wavefunctions have a complicated form and, consequently, their scattering outputs are not straightforward to quantify. Hence, instead of particular scattering coefficients, we make use of the general detection probabilities P_{mn}, which represent the total probability of detecting one photon in port m and another photon in port n after the scattering event occurs. These quantities have been used by other authors [198] and are expressed in terms of the output state $|\epsilon_o\rangle$. Note that we have already made use of such a concept for entanglement detection (Eq. 3.41). In that case, no explicit reference to input and output states was necessary since, due to the fact that the incoming photon was a wavepacket and not a plane wave, for large enough times (note the limit $t \to \infty$ in Eq. 3.41) both input and transient terms disappeared and the output naturally remained as the only contribution.

Let us detail the extraction of one of the detection probabilities P_{mn} by using a particular example, namely P_{23}. The photons detected at port 2 will be those propagating rightwards in the bottom waveguide. In the same fashion, photons addressed to port 3 are right-propagating modes of the upper waveguide. Therefore, we can write the position probability density associated with one photon in port 2 and another in port 3 as the following second order correlation function,

$$\rho_{23}(x,y) = \frac{\langle \epsilon_o | b_R^\dagger(y) c_R^\dagger(x) c_R(x) b_R(y) | \epsilon_o \rangle}{\langle \epsilon_o | \epsilon_o \rangle|_{\Gamma=0}}. \tag{3.72}$$

The normalization constant is fixed to the lossless output state, since a loss-induced decrease of the norm can never contribute to increase the detection probabilities. This normalization is required for a correct description of the system behavior. Note that, although it has not been necessary to explicitly mention it up to this point, such normalization is implicit in all the scattering problems solved with this formalism, both in the

literature [77, 198, 199, 220, 265], and along this thesis for the cases of one and two photons. The total probability of detecting two photons in ports 2 and 3 is straightforwardly obtained as

$$P_{23} = \int_{-L/2}^{L/2} dx \int_{-L/2}^{L/2} dy \rho_{23}(x, y), \tag{3.73}$$

where L is the total length of the waveguides. Although we always consider the limit $L \to \infty$, for reasons related to the eigenstate normalization (see Appendix B) it is convenient to keep the notation L and take such limit at the end of our calculation. Note that, in principle, by extending the limits of integration above to $-L/2$ we may be including processes not corresponding to scattering out of ports 2 and 3. However, this is not the case, since the probability density only contains the asymptotic scattering outputs, and thus it automatically fulfils $\rho_{23} \propto \theta(x)\theta(y)$.

The rest of the detection probabilities in this case are given by a similar expression as Eq. 3.73. We can obtain a general formula by defining a generalized coordinate

$$z_j = \begin{cases} x & \text{for} \quad j = 1, 2 \\ y & \text{for} \quad j = 3, 4, \end{cases} \tag{3.74}$$

as well as generalized photonic operators

$$a_i(z_i) = \begin{cases} c_L(z_i) = c_L(x) & \text{for} \quad i = 1 \\ c_R(z_i) = c_R(x) & \text{for} \quad i = 2 \\ b_R(z_i) = b_R(y) & \text{for} \quad i = 3 \\ b_L(z_i) = b_L(y) & \text{for} \quad i = 4. \end{cases} \tag{3.75}$$

By using these definitions we can obtain a general expression for both the position probability density in ports m and n and the corresponding detection probability, P_{mn}, as

$$\rho_{mn}(z_m, z_n) = \frac{\langle \epsilon_o | a_m^\dagger(z_m) a_n^\dagger(z_n) a_n(z_n) a_m(z_m) | \epsilon_o \rangle}{\langle \epsilon_o | \epsilon_o \rangle |_{\Gamma=0}}, \tag{3.76}$$

$$P_{mn} = \frac{1}{1 + \delta_{mn}} \int_{-L/2}^{L/2} dz_m \int_{-L/2}^{L/2} dz_n \rho_{mn}(z_m, z_n). \tag{3.77}$$

In this expression, the factor $(1 + \delta_{mn})^{-1}$ prevents a double counting of the states subject to a bosonic symmetry constraint. Although in principle there are 16 possible values of P_{mn} corresponding to the different combinations of indices $m, n \in [1, 4]$, not all of them represent independent processes. Indeed, we can reduce the number to 10 by noticing that some probabilities represent the same scattering output ($P_{mn} = P_{nm}$). Additionally,

from the general form of the eigenstate in Eq. (3.70) we can immediately deduce that, for the considered input,

$$P_{33} = P_{34} = P_{44} = 0, \tag{3.78}$$

as the Hamiltonian does not allow for two photons to be rectified. Therefore, only 7 possible scattering outputs remain, namely P_{1n} and P_{2n}, in which one photon is addressed to port n and the second is reflected or transmitted, respectively. Note, finally, that these probabilities describe the only possible output processes, as we formally demonstrate in Appendix B. This is manifested in the fact that, in the absence of free-space losses Γ, these probabilities add up to unity,

$$\sum_{m=1,2}\sum_{m=n}^{4} P_{mn}\Big|_{\Gamma=0} = 1. \tag{3.79}$$

Because of this completeness, the probabilities P_{mn} play a similar role in the two-photon scattering process as the scattering probabilities $T, R, \tilde{T}, \tilde{R}$ did in the single-photon case. Finally, let us comment that the definition of the probabilities P_{mn} in terms of an output state $|\epsilon_o\rangle$ is necessary, as otherwise our results would not be consistent with any of the alternative available methods in which the transient terms do not arise, such as LSZ reduction [194] or input-output formalism [275–277].

3.6.2. Operation and performance of the two-photon transistor.

Let us consider first the ideal case in which the 3LS is lossless and the directionalities are maximized, i.e., $\Gamma = 0$ and $D_j = 1$. Additionally, we will always assume the frequency of both incoming photons to be resonant with the transition $|g\rangle \leftrightarrow |e\rangle$. Under these conditions $R = \tilde{R} = 0$, and the detection probabilities have very simple expressions,

$$P_{11} \propto R^2 = 0, \tag{3.80}$$

$$P_{12} \propto RT = 0, \tag{3.81}$$

$$P_{13} \propto R\tilde{T} = 0, \tag{3.82}$$

$$P_{14} \propto R\tilde{R} = 0, \tag{3.83}$$

$$P_{24} \propto \tilde{R}(1+T) = 0, \tag{3.84}$$

$$P_{22} = T^2 \quad , \quad P_{23} = 1 - P_{22}. \tag{3.85}$$

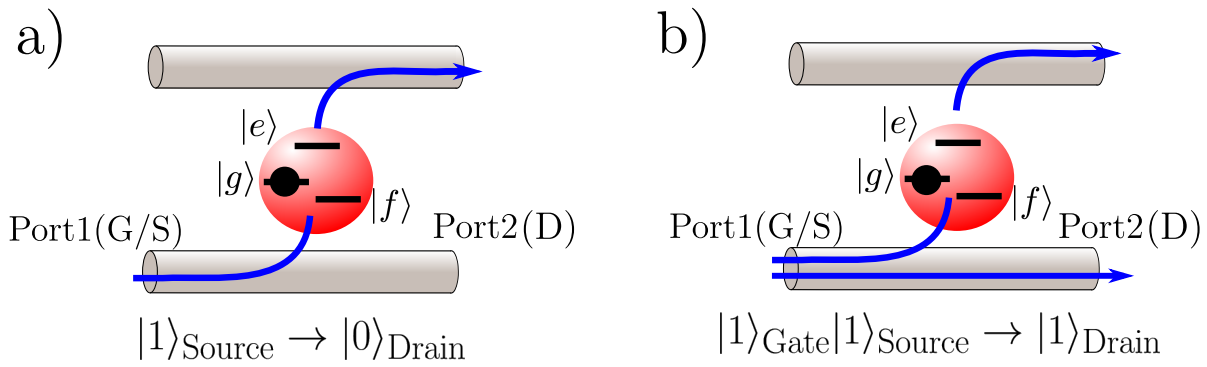

Figure 3.15: Scheme of operation of the two-photon transistor. Port 1 plays the role of both Gate (G) and Source (S), whereas port 2 represents the Drain (D). The transmission of a single photon from the source to the drain is only possible when a second, gate photon opens the transmission channel.

Here, we have defined $\{T, R, \tilde{T}, \tilde{R}\} \equiv \{|t(\omega_{eg})|^2, |r(\omega_{eg})|^2, |\tilde{t}(\omega_{eg})|^2, |\tilde{r}(\omega_{eg})|^2\}$, where $t, r, \tilde{t}$, and $\tilde{r}$ are the single-photon scattering coefficients defined in Eqs. (3.54-3.57). Naturally, all the processes involving the reflection coefficients r or $\tilde{r}$ vanish in the limit $D_j = 1$, and only two processes remain. First, direct transmission of two photons towards port 2, with probability $P_{22} = T^2$, and second, the process by which one of the photons is rectified into port 3 and the second is transmitted to port 2, with probability $P_{23} \propto 1 - T^2$.

The ideal situation described above can be extremely useful under the rectification condition discussed in the single-photon case, where the transmission probability T also vanishes if the couplings are adequately tuned. When this condition ($T = 0$) is fulfilled, the probability P_{22} also vanishes, and only one possible scattering output remains, namely the one described by P_{23}. In other words, there is only one possible path for the two-photon wavepacket, with probability 100%. This surprising result can be used to build a transistor-like device. For the sake of comparison with an ordinary three-terminal transistor, let us name port 1 the Source/Gate and port 2 the Drain, as depicted in Fig. 3.15. For a single photon input in port 1 (the source), transmission towards port 2 is prevented by the rectification process as discussed in previous sections. However, if we introduce a second photon through port 1, one of the input photons is rectified while the second is addressed to port 2. In this way, a transmission channel between ports 1 and 2 can be opened by means of a gate photon. A single-photon transistor has therefore been achieved which, in the ideal situation we are considering, has an efficiency of 100%. Note that, although similar ideas have been proposed in non-chiral waveguide setups [75] they heavily rely on a careful external manipulation of the system through classical driving of the 3LS and, additionally, their operation requires a sequential arrival of the

two photons in order to avoid spurious nonlinear effects caused by the two-photon bound states. Our device, on the other hand, makes use of the passive chiral qubit-waveguide coupling to achieve the same operation which, additionally, is independent on the time separation between the arrival of the two photons.

In order to characterize the performance of the transistor, we now consider the more realistic system in which the directionalities are not perfect and the β factor is lower than unity, i.e., $D_j < 1$ and $\Gamma \neq 0$. As we have discussed above, the rectification process is a key requirement for the operation of the device. Hence, we will assume again that the system parameters have been tuned to fulfil the rectification condition $T = 0$ (Eq. 3.60). In this situation, the probabilities P_{mn} can be expressed in terms of both the directionalities and the β factor as

$$P_{23} = \tilde{T} = \frac{1 + D_u}{1 + D_d} \left(\beta(D_d + 1) - 1\right), \tag{3.86}$$

$$P_{11} = Q_d^2, \tag{3.87}$$

$$P_{13} = Q_d P_{23}; P_{24} = Q_u(1 + Q_d)P_{23}; P_{14} = Q_d Q_u P_{23}, \tag{3.88}$$

$$P_{12} = P_{22} = 0, \tag{3.89}$$

where we have defined $Q_j = (1 - D_j)(1 + D_j)$.

The efficiency of the single-photon transistor is determined by the probability P_{23}, which is displayed in Fig. 3.16a as a function of the two directionalities D_d and D_u and for different values of the β factor. Note that, whereas D_u can have any value between 0 and 1, the allowed interval of directionalities D_d is restricted by the constraint $T = 0$, as described by the condition Eq. 3.62. Moreover, the probability P_{23} depends more dramatically on the directionality D_d than on D_u. The reason behind this imbalance is that a value $D_u < 1$ introduces losses only in the path of the rectified photon, but not in the photon travelling towards port 2. On the other hand, when D_d decreases below 1, both the transmission and rectification probabilities are affected, increasing the losses of the device in a more drastic way. Therefore, an adequate optimization of D_d is a crucial step towards an efficient photon transistor. In Fig. 3.16b we show the total efficiency as a function of the β factor, for different values of the directionalities $D_d = D_u$. The dependence is clearly linear, each curve intersecting the horizontal axis when the β factor reaches its fundamental limit for rectification, Eq. 3.62. For the current record values obtained experimentally, namely $\beta = 0.984$ and $D_j = 0.98$ [66, 72], the efficiency of the device reaches $P_{23} \approx 95\%$. This makes our single-photon transistor a feasible device for state of the art experimental techniques.

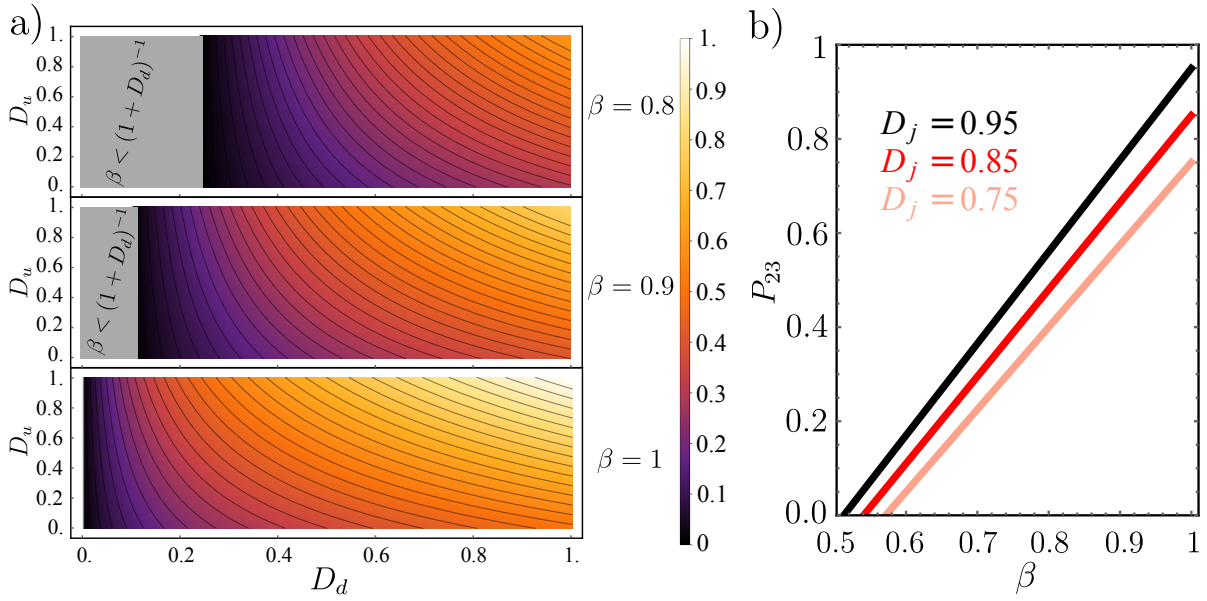

Figure 3.16: Performance of the single-photon transistor. a) Success probability P_{23} as a function of the directionalities D_d and D_u. Each subpanel corresponds to a different value for the β factor, and has a domain is constrained by the fundamental limit Eq. (3.62). b) P_{23} versus β factor, for different values of the directionalities $D_d = D_u$.

3.7. Conclusion

This chapter has been devoted to exploiting the advantages brought about by the full Hamiltonian description of waveguide QED systems, namely the complete control over the photonic degrees of freedom. With the prospectives of quantum applications in mind, this control can be utilized to operate on each of the two components of any hybrid light-matter systems. Specifically, the first three sections of this chapter show how propagating guided photons can exert different operations on two-qubit ensembles, while the two following sections employ quantum emitters to manipulate photonic inputs in a desired way.

Regarding light-on-matter operations, we have focused our attention on devising an efficient platform for generating, manipulating, and detecting entanglement between two matter qubits. First, we have shown how qubit-qubit entanglement can be generated in a simple way with a single-photon pulse. Moreover, the possibility of shaping and even suppressing the generated entanglement by means of a second single-photon has been demonstrated. Additionally, we have presented a scheme for entanglement detection based on analysing the single-photon scattering output. As opposed to the dissipative spontaneous entanglement generation presented in the previous chapter, only transient

entangled states can be created by means of propagating photons, even in the absence of losses. However, this is compensated by the enormous advantages of the method proposed in this chapter, namely the high degree of control and the demonstration of a complete platform in which entanglement can not only be generated, but also manipulated in time domain and detected, all within the same integrated waveguide QED setup. The protocols introduced in this chapter are an optimum complement to the previously studied dissipative schemes, since in principle both could be combined in the design of complex networks according to the desired functionality of each component.

In the second part of this chapter, we have turned the situation around in order to employ a quantum emitter to perform operations over flying photonic qubits. By engineering the system parameters to produce certain quantum interference processes, we achieve deterministic non-reciprocal behavior of the photonic inputs. We employ this to devise both a diode and a rectifier for single photons. Moreover, we introduce a chirality-based photonic transistor for a two-photon input. Whereas efficient and linear operations were already available on waveguide-resonator systems [245, 247], the miniaturization of such devices is challenging due to their intrinsically larger size. On the other hand, hybrid devices based on electronic degrees of freedom suffer from intrinsic nonlinearities which give rise to usually unwanted bound photonic states, as we have demonstrated in the diagonalization of two-photon inputs. However, we have shown the possibility of avoiding such nonlinearity in our two-photon transistor which, contrary to previous proposals, is unaffected by the time delay between both photons as long as they are highly monochromatic. Additionally, although we have not explored further, the full control over the chiral couplings in our four-port setup allows for the design of many more functionalities, from phase gates to beam splitters, frequency shifters, and others.

In conclusion, we have demonstrated the controlled and efficient performance of waveguide QED setups when realizing both light on matter and matter on light operations. Both the platform for entanglement generation, manipulation, and detection, and the non-reciprocal few-photon devices we have introduced could in principle be implemented on-chip in a compact, integrable setup, and therefore be employed as basic elements in quantum networks. Unlike usual cavity QED systems, waveguides offer the possibility of employing the photonic degrees of freedom in a simple manner. Therefore, waveguide-based systems represent an excellent component for quantum computation purposes.

4 | Collective phenomena: Strong Coupling and dark state delocalization.

4.1. Introduction

Up to this point, we have focused our attention in light-matter interaction for a reduced number of QEs. In the optical range, the coupling of such emitters to nanophotonic structures is usually small due to their reduced dipole moment, and hence the light-matter interaction remains within the weak coupling regime. The eigenstates of the light-matter Hamiltonian in this situation do not significantly differ from the natural states of one of the two constituents, i.e., either they are matter states slightly affected by the photonic environment, or vice-versa. In the previous chapters, we have shown how an adequate engineering of the EM environment in the weak coupling regime allows for a light-matter interaction tailored on demand, thus illustrating the wide range of applicability of weakly coupled systems.

As discussed in chapter 1, the phenomenology associated to light-matter interaction can drastically change, however, if the coupling rate between the EM modes and the QEs is increased beyond their respective linewidths. In this situation, the hybrid system enters the strong coupling regime, where light and matter become intertwined and thus indistinct from each other [48]. Indeed, the eigenstates of such a strongly coupled system are quantum superpositions of both constituents, and display hybrid light-matter properties. This gives rise to surprising phenomena such as Rabi oscillations [278]. In

general, it is difficult for single optical QEs to reach the strong coupling regime even in high-quality cavities, where the field intensity at the position of the QEs is largely enhanced. The usual approach to reach this regime is to couple the EM modes not to one, but to large ensembles of N quantum emitters, which results in a coupling constant $\sqrt{N}$ times larger [18]. This was the case for the first experimental demonstration of Rabi oscillations [28]. Although the same phenomenon was demonstrated a decade after for a single atom [279], the strong coupling regime remains more accessible for collective ensembles of QEs and is therefore a widely used strategy nowadays.

The possibility of reaching the *collective strong coupling* (CSC) regime between light and a large ensemble of QEs is very interesting aside from practical reasons, mainly due to fundamental differences with respect to the single QE case. Specifically, the phenomenology of CSC is much richer due to the nature of the system eigenstates, or polaritons [30]. For a single QE, the polaritons are hybrid states formed by a superposition of a photonic state and a localized exciton in the QE. On the other hand, when the cavity field is coupled to a large ensemble of QEs, the polaritons can be composed by photons and *delocalized* excitonic states, which are distributed among many QEs. In such extended systems, these polaritons propagate with a given dispersion relation in the same way as any other quasiparticle, and interact with each other in a controlled way [280]. As a consequence, they have been shown to display very interesting effects such as superfluidity [34], Bose-Einstein condensation [33, 281, 282] or polariton lasing [283]. The tunability of their hybrid properties also makes them very good candidates for quantum processing and quantum computation purposes, with applications such as polaritonic circuits [111], polariton logic gates [284], dispersionless transmission as solitonic packets [285], and many more. Moreover, it has recently become clear that polaritons can also display complex emergent phenomena inherited from their matter constituents, a property already exploited even at the cutting edge of condensed matter with, for instance, spin hall effect [286] or topological polaritonics [287]. In the last years, polariton physics has become a large research field due to its enormous potential for both applied and fundamental research [53].

A second interesting property of systems in the CSC regime is the appearance of dark states. It is well known that each EM mode couples to a single collective state of the ensemble of QEs [16]. In this process, many other states of the QEs (dark states) remain totally uncoupled to the light and thus keep their purely matter nature. The almost ubiquitous dark states are usually disregarded in the applications of CSC since, as opposed to the polaritons, they are assumed not to benefit from the light-matter interaction. Indeed, these states are usually only seen as a source of polariton losses

through dephasing [288] or, in terms of applications, only as passive elements such as qubit storage for quantum memories [289]. In this chapter we will challenge such view by demonstrating how, under the appropriate conditions, dark states can inherit polaritonic properties.

This chapter is organized as follows. First of all, we devote section 4.2 to review the key concepts in theory of CSC. Here, we will introduce the light-matter Hamiltonian, and briefly study one of the simplest cases, namely the Tavis-Cummings Hamiltonian. This will allow us to define the relevant concepts such as bright and dark states, polaritons and Rabi splitting. We will also discuss and compare the different ways of modelling losses and external driving of the system, as well as our approximated Hamiltonian for lossy EM excitations such as surface plasmons. After, in section 4.3, we study the example of an ensemble of molecular QEs strongly coupled to a plasmonic nanowire. Our results demonstrate that, for systems with a continuous dispersion relation, dark states are strongly localized and do not propagate along the ensemble of QEs. We then analyze the same problem in a finite nanostructure in section 4.4, specifically a plasmonic nanoparticle. Here, we show how for discrete EM spectra the dark states are delocalized among all the ensemble of QEs, thus inheriting the extended character of the photonic modes. Finally, our conclusions are presented in section 4.5.

4.2. Theory of collective strong coupling in arbitrary nanostructures.

The objective of this section is to briefly introduce the methods we will employ in the study of strongly coupled systems along the following chapters. Most of the contents in the present section are well-known in quantum optics, and therefore we drop a rigorous analysis in favour of a schematic presentation of the key points. First, we introduce the complete light-matter Hamiltonian, in which the corresponding light-matter coupling rate is determined from first principles. This fundamental picture is more adequate for the chapters devoted to strongly coupled systems, as opposed to the simplified version of such Hamiltonian employed in chapters 2 and 3, where the coupling rate was treated as a free parameter. We will continue by introducing the basic definitions in this field, such as bright and dark states, polaritons, and Rabi splitting. Finally, we will focus on the study of the different possible methods of including loss and pump in our theoretical model, and discuss their respective advantages and disadvantages.

4.2.1. Light-matter Hamiltonian and Tavis-Cummings model.

The study of strongly coupled systems requires a physically accurate theoretical calculation of the light-matter coupling constant in realistic situations. In order to do so, we need to obtain from first principles the quantum Hamiltonian characterizing a system of EM modes coupled to an ensemble of QEs. Such a Hamiltonian can be deduced from fundamental arguments in what is known as the canonical quantization of the EM fields, as demonstrated by Dirac [2]. Since the detailed calculations are involved, we have performed them in appendix C. In such appendix we show that the Hamiltonian of a system of N dipolar QEs interacting with a set of EM modes is given by the following expression ($\hbar = 1$),

$$H = H_{qe} + H_{em} + H_I = \sum_{\alpha} \omega_\alpha \sigma_\alpha^\dagger \sigma_\alpha + \sum_{\alpha\beta} \left(V_{\alpha\beta} \sigma_\alpha^\dagger \sigma_\beta + H.c. \right) + \sum_{\mathbf{k}} \omega(\mathbf{k}) a_{\mathbf{k}}^\dagger a_{\mathbf{k}} + \sum_{\alpha,\mathbf{k}} \left(g_\alpha(\mathbf{k}) a_{\mathbf{k}}^\dagger \sigma_\alpha + H.c. \right). \tag{4.1}$$

in the two-level and rotating wave approximations (see Appendix C for details). The first two terms describe the Hamiltonian of the N QEs, H_{qe}, through their spin creation and annihilation operators $\sigma_\alpha^\dagger$ and σ_α ($\alpha = 1, 2, ...N$), respectively. Such a Hamiltonian contains the self energies ω_α of the QEs, and the coherent coupling between QEs induced by the dipole-dipole interaction,

$$V_{\alpha\beta} = \frac{1}{4\pi\varepsilon\varepsilon_0 |\mathbf{r}_\alpha - \mathbf{r}_\beta|^3} \left(\boldsymbol{\mu}_\alpha \cdot \boldsymbol{\mu}_\beta - 3 \frac{(\boldsymbol{\mu}_\alpha \cdot [\mathbf{r}_\alpha - \mathbf{r}_\beta])(\boldsymbol{\mu}_\beta \cdot [\mathbf{r}_\alpha - \mathbf{r}_\beta])}{|\mathbf{r}_\alpha - \mathbf{r}_\beta|^2} \right), \tag{4.2}$$

where $\boldsymbol{\mu}_\alpha$ and $\mathbf{r}_\alpha$ describe, respectively, the dipole moment and the position of the α-th QE. The third term in Eq. 4.1 contains the energy of the EM modes, H_{em}, described as independent quantum harmonic oscillators labelled by a mode index $\mathbf{k}$. Each mode $\mathbf{k}$ has a frequency $\omega(\mathbf{k})$ and is represented by bosonic creation and annihilation operators $a_{\mathbf{k}}^\dagger$ and $a_{\mathbf{k}}$, respectively. Finally, the fourth and last contribution H_I describes the light-matter interaction term, where the coupling rate between the emitter α and the mode $\mathbf{k}$ is given by

$$g_\alpha(\mathbf{k}) = -\sqrt{\frac{\hbar\omega(\mathbf{k})}{2U_{em}}} \boldsymbol{\mu}_\alpha \cdot \mathbf{E}_{\mathbf{k}}^{cl*}(\mathbf{r}_\alpha). \tag{4.3}$$

The above coupling constant is only expressed as a function of the dipole moment of the QEs and the properties of the *classical* solutions to Maxwell eigenmode equations.

Specifically, $\mathbf{E}^{cl}_{\mathbf{k}}(\mathbf{r})$ represents the classical electric field profile associated to the mode $\mathbf{k}$, and U_{em} is the classical EM energy given by

$$U_{em}(\mathbf{k}) = \frac{\varepsilon_0}{2}\int d^3\mathbf{r}\left(\varepsilon(\omega)|\mathbf{E}^{cl}_{\mathbf{k}}(\mathbf{r})|^2 + c^2|\mathbf{B}^{cl}_{\mathbf{k}}(\mathbf{r})|^2\right), \tag{4.4}$$

where $\mathbf{B}^{cl}_{\mathbf{k}}(\mathbf{r})$ is the corresponding modal magnetic field and, as usual, we assume non-magnetic media ($\mu = 1$). Note that the coupling constant $g_\alpha(\mathbf{k})$ is independent on the normalization of the classical EM modes and thus physically consistent. Expressions 4.1 and 4.3 are the most important relations in both this chapter and chapter 5.

It is insightful to study some of the general properties of the above light-matter Hamiltonian in a very simple scenario, where an ensemble of N identical, non-interacting QEs with frequency ω_0 is coupled to a single EM mode of frequency ω_c. This can be achieved e.g. in a semiconductor microcavity, where any other EM modes can be artificially tuned away from the resonance frequency of the QEs [30]. In such situation, the Hamiltonian in Eq. 4.1 takes the well-known Tavis-Cummings form [18],

$$H_{TC} = \sum_\alpha \omega_0 \sigma^\dagger_\alpha \sigma_\alpha + \sum_\alpha \left(g_\alpha a^\dagger \sigma_\alpha + H.c.\right) + \omega_c a^\dagger a. \tag{4.5}$$

Although in the original work by Tavis and Cummings the exact diagonalization was presented for an arbitrary number of excitations, here we will remain within the single-excitation subspace for simplicity. In such situation, the Hamiltonian can be greatly simplified by defining the following collective spin operator,

$$B^\dagger = \frac{2}{\Omega_R}\sum_\alpha g^*_\alpha \sigma^\dagger_\alpha. \tag{4.6}$$

The constant $\Omega_R = 2\sum_\alpha |g_\alpha|^2$ receives the name of Rabi frequency, and plays a very relevant role in the system dynamics as we will see below. Interestingly, we can express the whole light-matter coupling in the Tavis-Cummings Hamiltonian by means of the above operator,

$$\sum_\alpha \left(g_\alpha a^\dagger \sigma_\alpha + H.c.\right) = \frac{\Omega_R}{2}\left(a^\dagger B + a B^\dagger\right). \tag{4.7}$$

Note that the Hilbert space for an ensemble of N QEs contains N states in the single excitation subspace, and yet we are able to express the light-matter coupling with only one collective state within such subspace. We thus conclude that it is possible to find a basis of the QEs Hilbert space in which only one state couples to the light mode, namely $B^\dagger|0\rangle$, where $|0\rangle = |g_1 g_2 ... g_N\rangle \otimes |\emptyset\rangle$ is the system vacuum state expressed in

terms of the ground states of the QEs, $|g_\alpha\rangle$, and the photonic vacuum $|\emptyset\rangle$. The state $B^\dagger|0\rangle$ is usually referred to as *bright state* $|B\rangle$. On the other hand, the remaining $N-1$ states remain completely uncoupled to the light, and are thus called *dark states* $|D_\alpha\rangle$ ($\alpha = 1, ...N-1$). Indeed, if we name $D_\alpha^\dagger$ the creation operator for each of those states, the Tavis-Cummings (TC) Hamiltonian in the bright-dark basis reads

$$H_{TC} = \sum_{\alpha=1}^{N-1} \omega_0 D_\alpha^\dagger D_\alpha + \omega_0 B^\dagger B + \frac{\Omega_R}{2}\left(a^\dagger B + a B^\dagger\right) + \omega_c a^\dagger a. \tag{4.8}$$

The dark states arise naturally when the number of QEs is larger than the number of EM modes. In the absence of EM modes, there is no privileged basis for the Hilbert space span by the non-interacting N QEs. In our single mode scenario, the coupling to an EM mode partially breaks that arbitrariness, and forces the eigenbasis to be defined by the bright state. This trend is generalized for an ensemble of M different modes, which would couple to M bright states, leaving an arbitrarily defined $N-M$-dimensional dark subspace consisting on purely matter states. Finally, when $M \geq N$, no dark states arise and the eigenbasis is completely defined.

Let us deepen in the study of the transformed Hamiltonian 4.8. As a first approach, it is insightful to consider the light-emitter coupling to be equal for all the QEs, i.e., $g_\alpha = g$. The resulting simplified Hamiltonian reads

$$H_{\text{Dicke}} = \sum_{\alpha=1}^{N-1} \omega_0 D_\alpha^\dagger D_\alpha + \omega_0 B^\dagger B + \sqrt{N} g\left(a^\dagger B + a B^\dagger\right) + \omega_c a^\dagger a. \tag{4.9}$$

The above expression is often referred to as the Dicke Hamiltonian, due to the pioneering studies carried out by Dicke in the weak coupling regime [6]. In this context, the dark and bright states are respectively called subradiant and superradiant states. The reason behind this notation is evident in terms of Purcell enhancement of the vacuum decay rates. Indeed, the decay rate or, equivalently, the coupling rate of the dark states to EM modes is much smaller than that of the bare QEs (in this particular case, it is strictly zero). In the weak coupling picture we have worked on in the previous chapters, this reduction results in the dark states decaying at a slower rate than the bare QEs, hence being subradiant. On the other hand, the decay rate of the bright state is increased by a factor $\sqrt{N}$, which induces a faster or superradiant decay. Aside from particular notations, the Dicke Hamiltonian is very illustrative since it explicitly shows how, by increasing the number of emitters coupled to the EM modes, the light-matter coupling rate is multiplied by a factor $\sim \sqrt{N}$. As we will see below, this general trend will be crucial for reaching the CSC regime.

Back to the general Tavis-Cummings Hamiltonian in Eq. 4.8, note that it is already diagonal on the $N-1$ dark states and, consequently, the diagonalization is reduced to a 2×2 problem in the subspace span by the bright state and the EM mode. The eigenenergies in this subspace are straightforward to calculate,

$$2\epsilon_{\pm} = \omega_0 + \omega_c \pm \sqrt{(\omega_0 - \omega_c)^2 + \Omega_R^2}. \tag{4.10}$$

This expression also provides insightful information. First, note how, if both EM mode and QEs are in resonance ($\omega_0 = \omega_c$) the eigenstates of the system, or polaritons, have energies $\epsilon_{\pm} = \omega_0 \pm \Omega_R/2$. This expression highlights the significance of the Rabi frequency, which can now be intuitively understood: apart from representing the energy difference between both polaritons (which originates its alternative name as Rabi splitting), it quantifies how much do the energies of such polaritons differ from the energy of the bare QEs, ω_0. For small Rabi splittings, the eigenstates will be very close to pure photons or pure QEs, and their hybrid character will not be appreciable. On the other hand, for large values of Ω_R the two polaritons are clearly different from any uncoupled subcomponent, and their hybrid properties will manifest. The above argument is the basis for the distinction between the weak and strong coupling regimes, although we will not give here a proper definition since a key ingredient is still missing in our description. As we will see in the following section, this ingredient is given by the system losses, which allow us to properly quantify a "large" and a "small" Rabi splitting.

Note that a large light-matter coupling rate Ω_R does not necessarily guarantee that the QEs and the EM mode hybridize appreciably. Indeed, from Eq. 4.10 it is clear that, if the EM mode is largely detuned with respect to the QEs, $|\omega_0 - \omega_c| \gg \Omega_R$, then the polariton energies are simply given by $\epsilon_+ \approx \omega_0$, $\epsilon_- \approx \omega_c$. Thus, as a result of the QEs and the EM mode having very different energies, the effective interaction is negligible and the eigenstates show no hybrid properties despite the coupling rate being large. This emphasizes the importance of adequately tuning the frequencies of light and matter components to resonance.

Finally, it is important to stress that the bright state is a delocalized excitation of the ensemble of QEs, and thus is distributed among all of them. Such extended character is directly inherited by the delocalized photonic excitation. Since the polaritons are superpositions of both the bright and the EM modes, they will also inherit this property, and their matter component will be delocalized. This is not necessarily the case for the dark states since their choice is arbitrary. Therefore, we can either select a very localized or a very delocalized basis for the dark subspace.

4.2.2. Introducing losses and external pumping in the system.

The light-matter Hamiltonian we are working with, Eq. 4.1, includes and properly quantizes only the relevant EM modes. In the usual setups for collective strong coupling (CSC), these modes represent the EM fields confined within a certain region of space, for instance a cavity or a waveguide. The energy stored in these fields, however, can leak from the confined region and abandon the system, either because of absorption in the materials forming the confinement volume, or by coupling to free-space EM modes [30]. Analogously, the population stored in the QEs can also suffer from losses because of nonradiative processes or direct emission into the above mentioned free space modes [22]. Losses are ubiquitous in these kind of systems, and a proper theoretical description of the light-matter interaction requires taking them into account.

From the point of view of quantum theory, the system under study is an open quantum system, in which the losses are associated with additional degrees of freedom not explicitly included in the Hamiltonian. The exclusion of the modes accounting for the losses is required in order to simplify an otherwise too complicated problem. However, even if we were able to explicitly include such degrees of freedom, it would not be a wise approach since their effect on the system is very small. Hence, the usual route in theory of open quantum systems is to first quantize explicitly the relevant modes for the system dynamics, and later include the losses only through their average action on the system dynamics. This is in general valid in our CSC problems, where the loss decay rates are usually much smaller than any other energy scale. In this section we will discuss two different ways to include losses, and show under which circumstances they are equivalent. This will be very helpful to reduce the computational cost of the many-particle Hamiltonians we solve in the following. We will also briefly comment on how to include intrinsically lossy EM excitations such as plasmons in our light-matter Hamiltonian. Finally, we study how to include different pumping sources in the system, and which of them are compatible with the descriptions of the losses presented previously.

Introducing losses.

Let us briefly discuss the two most employed methods for introducing losses into the system, both of which have already been introduced in chapters 2 and 3. The first and simplest approach for describing the losses consists in adding a small imaginary part to

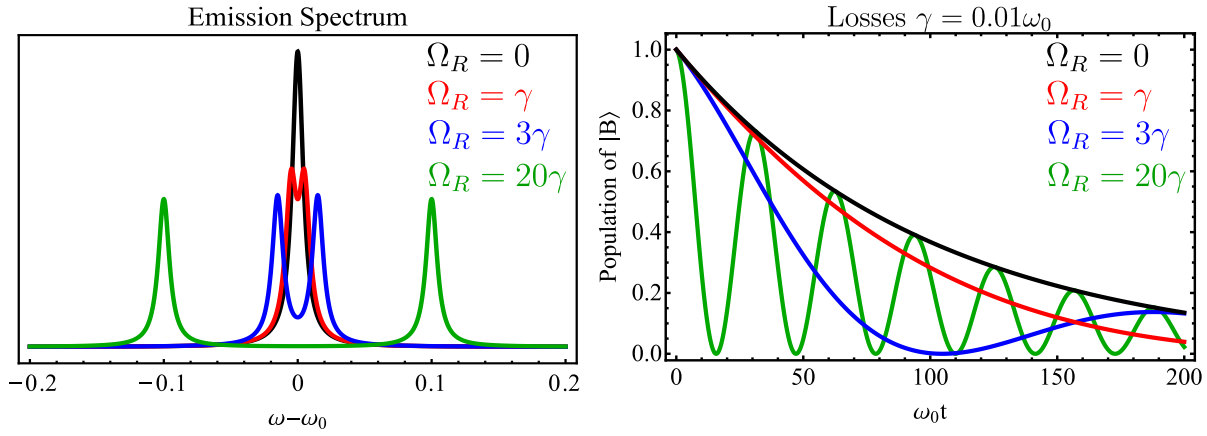

Figure 4.1: Simple example in which weak and strong coupling regimes are represented, for a loss rate $\gamma = 0.01\omega_0$. a) Energy distribution of the two polariton eigenstates of the TC Hamiltonian, for different values of the Rabi splitting. b) Decay of an initially excited bright state for different Rabi splittings. The transition between exponential decay and Rabi oscillations marks the weak-to-strong coupling crossover.

the self energies of the system components,

$$\omega_\alpha \rightarrow \omega_\alpha - i\gamma_\alpha/2 \qquad ; \qquad \omega(\mathbf{k}) \rightarrow \omega(\mathbf{k}) - i\kappa(\mathbf{k})/2, \tag{4.11}$$

(do not confuse γ_α with the weak coupling rates γ of chapters 2 and 3). The effect of including this non-Hermitian term is the addition of an effective linewidth to the system eigenenergies. As a consequence, the eigenstates of the system now decay in time at a rate given by the imaginary part of their energy. Let us study the effect of including such non-Hermitian components in the Tavis-Cummings Hamiltonian described in Eq. 4.8, where for simplicity we take the same frequency ω_0 and loss rate γ for both the QEs and the EM mode. For the sake of illustration, we will study the system dynamics for an initially excited bright state, i.e., $|\psi(t=0)\rangle = B^\dagger|0\rangle$. The relevant part of the Hamiltonian reads

$$H_{TC} - H_{\text{dark states}} = (\omega_0 - i\gamma/2)B^\dagger B + \frac{\Omega_R}{2}\left(a^\dagger B + aB^\dagger\right) + (\omega_0 - i\gamma/2)a^\dagger a. \tag{4.12}$$

Note that, due to the non-Hermitian component, the eigenmodes of the system are not proper eigenstates in the quantum mechanical sense, since the eigenenergies are complex. In the limit of low losses, however, the lossless eigenmodes, i.e., the polaritons, are approximately well defined [27]. By diagonalizing the above Hamiltonian, the eigenenergies are straightforward to determine,

$$\epsilon_\pm = \omega_0 - i\gamma/2 \pm \Omega_R/2. \tag{4.13}$$

As mentioned above, the imaginary components of the above energies prevent the polariton eigenstates from oscillating harmonically in time, instead acquiring a decaying character,

$$|\epsilon_{\pm}(t)\rangle = e^{-i\omega t}e^{-\gamma t/2}|\epsilon_{\pm}(0)\rangle. \tag{4.14}$$

As a result, the distribution in energies of a given polariton eigenstate is now spread with a Lorentzian profile, as one can certify by taking the Fourier transform of the above time dependence. In Fig. 4.1a, the energy spectrum of both polaritons is displayed for a loss rate $\gamma = \omega_0/100$, as a function of the Rabi splitting. The neighbouring panel (4.1b) shows the corresponding population of the bright state as a function of time. At zero splitting, both polariton states have the same energy and, since the bright state is thus uncoupled to the light mode, it decays only into the reservoir described by the loss rate γ. On the other hand, for finite Rabi splittings, the two peaks split away as the polaritons energies become increasingly different. If such splitting is small ($\Omega_R \lesssim 2\gamma$), the peaks are hardly distinguishable due to their overlapping profiles (red curves in Figs. 4.1a-b). This represents the so-called weak coupling regime, where the decay of an initially excited state (in this case, the bright state) still follows an exponential law, with a modified decay rate due to the Purcell effect. On the other hand, the system enters the strong coupling regime when Ω_R is large enough for both polaritons to be clearly distinguishable from each other (blue and green curves in Figs. 4.1a-b). In this regime, the eigenstates of the system are hybrid light-matter states, and the excitation of one subcomponent, in this case the pure matter state $B^{\dagger}|0\rangle$, results in a coherent exchange of population between it and the EM mode. The population dynamics of the bright state is thus characterized by the well-known Rabi oscillations [16].

Regardless of the simplicity of the problem and the accuracy of our simple description of the losses, the dynamics observed in Fig. 4.1b already captures the basic physics of the light-matter interaction. Importantly, by including the losses in the system we are able to properly identify the boundary between the weak and strong coupling regimes. Indeed, whereas Rabi oscillations always appear for lossless Hamiltonians, in a realistic system they arise only if the Rabi splitting overcomes the loss channels. A usual criterion for the onset of strong coupling is therefore given by

$$\Omega_R \gtrsim (\gamma + \kappa)/2, \tag{4.15}$$

where γ and κ represent the loss rates of QEs and EM modes, respectively. Note that in more complex systems the crossover between weak and strong coupling may become more complicated. Indeed, in the presence of multimode EM fields several bright states

arise, which can additionally couple to the dark states if the dipole-dipole interaction between the QEs is significant. In general, however, the CSC regime exists and can in principle be achieved in any system, provided that the light-matter coupling is large enough for some polariton eigenstates to be well resolved in energies [21].

The method of adding an imaginary part to the frequencies of the system can reproduce the relevant physics in many situations, but leads to flagrant inconsistencies in others. Indeed, although the decay of the bright state in Fig. 4.1b is accurately described, if we calculate the total population in that same system (i.e., bright state + EM mode + vacuum state) we find that it decays in time at a rate γ. In other words, the norm of the initial state is not conserved. Thus, if we were interested in some quantity involving, for instance, the population of the vacuum state, this formalism would lead to incorrect results, as it does not account for the decay-induced population increase of the state $|0\rangle$. This motivates an extension of the model in order to recover the missing probability, the simplest option for this purpose being the Lindblad Master Equation. As we have seen in chapter 2, this formalism is implemented as an *extended Schrödinger equation* for the density matrix $\rho = |\psi\rangle\langle\psi|$. In the single-mode TC model studied above, the dynamics of such density matrix reads

$$\dot{\rho} = -i[H, \rho] + \gamma \mathcal{L}_B[\rho] + \kappa \mathcal{L}_a[\rho], \tag{4.16}$$

where H is the Hermitian TC Hamiltonian Eq. 4.8, and the Lindblad superoperators are redefined for simplicity as

$$\mathcal{L}_A = -\frac{1}{2}\left(A^\dagger A \rho + \rho A^\dagger A\right) + A\rho A^\dagger \tag{4.17}$$

for a given operator A. The first two terms above are equivalent to the non-hermitian contribution to the energies, whereas the last contribution, usually referred to as the *quantum jump* term, compensates the loss of probability by repopulating the ground state. It can be checked that indeed this formalism conserves the total population in the simple problem studied in Fig. 4.1b. In the single-excitation subspace we are working on, the quantum jump term only affects the ground state, whose population is now $\rho_{gg} = 1 - \rho_{BB} - \rho_{aa}$ instead of 0. On the other hand, the occupations of both the bright and the EM mode, ρ_{BB} and ρ_{aa} respectively, are exactly the same as those obtained with the non-Hermitian component. Thus, the Lindblad master equation is physically consistent as it conserves the total population inside the system.

Along the rest of the thesis, we will alternatively use one of the two descriptions of the losses presented above. Despite the master equation formalism being more accurate,

many properties of the system are already recovered by a non-Hermitian Hamiltonian as we have seen above. If that is the case for the quantities we are interested in, the latter method is more advantageous for a theoretical study of large ensembles of $N \gg 1$ QEs coupled to many (M) EM modes. Indeed, the solution of the problem requires in one case the diagonalization of a $(N+M+1)\times(N+M+1)$ non-Hermitian Hamiltonian and, in the other, of a $(N+M+1)^2\times(N+M+1)^2$ Liouvillian [19]. Therefore, it will be very convenient to employ non-Hermitian Hamiltonians whenever is possible, i.e., when the excited states are so lowly populated that the norm is approximately conserved. We will briefly go back to this topic when we introduce the different pumping schemes.

Approximation for intrinsically lossy EM pseudomodes.

The two descriptions of the losses we have studied above assume that the bare light-matter Hamiltonian does not change in the presence of an additional loss mechanism. However, when the bosonic modes in the field Hamiltonian H_{em} do not correspond to pure EM resonances but to more complex matter excitations, some intrinsic losses arise which can affect the light-matter coupling. Specifically, along this thesis we will sometimes employ plasmonic resonances of metallic structures playing the role of the EM modes. Such metallic structures are characterized by a complex permittivity $\varepsilon(\omega)$, whose imaginary part introduces losses in the system associated to the damping of the electronic motion. As a consequence, the EM fields obtained from the Maxwell mode equation are not eigenmodes of the system in the physical sense, since the real eigenmodes of the nanostructure, i.e., the surface plasmons, are hybrid states of light and electronic oscillations, the latter of which are only accounted for macroscopically. The EM modes thus have imaginary frequencies, and decay in time instead of showing harmonic oscillations [290, 291]. An additional problem arises when calculating the light-matter coupling in Eq. 4.3, which becomes ill-defined since the classical electromagnetic energy in these systems, U_{em}, becomes imaginary (see Eq. 4.4).

The problem we have introduced with the example of surface plasmons is general for any lossy media where, unless the damping degrees of freedom are microscopically accounted for, the canonical quantization in Appendix C fails to fulfil fundamental constraints such as commutation relations or causality [292]. In order to solve this issue, a formalism of QED for lossy media was developed some time ago [19, 293], in which the resulting eigenmodes are physically consistent. This method has been successfully used in many plasmonic systems coupled to small numbers of QEs [187, 294–296], although when many emitters are present the formalism becomes increasingly difficult [297, 298].

Additionally, since in this picture the eigenmodes do not represent purely EM excitations, the light-matter Hamiltonian takes a much more involved expression as a function of the solutions to the classical Maxwell equations [106, 295].

In order to simplify the study of systems with many QEs, which would be challenging by means of the aforementioned exact formalism, in this thesis we will employ canonically quantized modes by assuming the losses are small, i.e., $\mathrm{Im}[\varepsilon] \ll \mathrm{Re}[\varepsilon]$ or, equivalently, $\mathrm{Im}[\omega(\mathbf{k})] \ll \mathrm{Re}[\omega(\mathbf{k})]$. Our approximation consists, first, on the substitution of the mode frequency in the Hamiltonian 4.1 by its real part, $\omega(\mathbf{k}) \to \mathrm{Re}[\omega(\mathbf{k})]$. The imaginary part of such eigenfrequencies can then be included a posteriori by one of the two procedures we have studied above [299]. The second and more important step is the substitution of the classical EM energy in Eq. 4.4 by the Landau approximation for lossy media [31, 300],

$$U_{em}(\mathbf{k}) \approx \tilde{U}_{em}(\mathbf{k}) = \frac{\varepsilon_0}{2}\int d^3\mathbf{r}\left[\mathrm{Re}\left(\frac{d}{d\omega'}\omega'\varepsilon(\omega')\right)\Big|_{\omega'=\omega}|\mathbf{E}^{cl}_{\mathbf{k}}(\mathbf{r})|^2 + c^2|\mathbf{B}^{cl}_{\mathbf{k}}(\mathbf{r})|^2\right]. \quad (4.18)$$

This expression has been widely employed in the study of e.g. Drude metals [301, 302], as it accurately predicts the correct results for small loss rates [303].

The two substitutions we carry out above approximate the complex quantities $\omega(\mathbf{k})$ and $U_{em}(\mathbf{k})$ by real numbers, and therefore allows us to use the canonical quantization scheme of appendix C. Both the resulting Hamiltonian and the light-matter coupling strength conserve their fundamental form, namely

$$H_{em} = \sum_{\mathbf{k}} \hbar\mathrm{Re}[\omega(\mathbf{k})]a^\dagger_{\mathbf{k}}a_{\mathbf{k}} \qquad ; \qquad g_\alpha(\mathbf{k}) = -\sqrt{\frac{\hbar\mathrm{Re}[\omega(\mathbf{k})]}{2\tilde{U}_{em}}}\boldsymbol{\mu}_\alpha \cdot \mathbf{E}^{cl*}_{\mathbf{k}}(\mathbf{r}_\alpha). \quad (4.19)$$

This simple approximation will be employed along this and the following chapters for the representation of plasmonic resonances in metallic nanostructures.

Pumping the system.

Usually, realistic problems are far from the simple decay dynamics we have studied in Fig. 4.1, where a given quantum state was excited at $t = 0$. Many of the usual experimental setups are based on an external control of the system by means of an adequate pump, for instance a laser beam [27]. Along this thesis, we will often encounter these kind of problems, where the initial state is the total ground state $|0\rangle$, and an external pump introduces population in the system. Therefore, we devote this section to a brief study of the different possible ways of describing the external pumping.

Two main types of excitation are of special interest, namely coherent and incoherent pumping. A coherent excitation scheme represents, for instance, a laser beam exciting a given transition between two states $|i\rangle$ and $|f\rangle$, and is usually represented by the following Hamiltonian [26],

$$H_p = \Omega_p \left(e^{i\omega_L t} |f\rangle\langle i| + H.c. \right). \tag{4.20}$$

The parameters ω_L and Ω_p represent, respectively, the frequency of the pump and its coupling strength to the corresponding transition. In our light-matter Hamiltonian, the operator $|f\rangle\langle i|$ would represent either a spin or a field operator, depending on whether we pump the QEs or the EM mode. The second possible kind of excitation is the incoherent pumping, which for instance occurs when a laser excites the transition from $|i\rangle$ to a vibrationally excited level of its excited electronic state, $|f'\rangle$. This short-lived state in turn quickly relaxes to the emitting state $|f\rangle$. Because it lives much longer than the vibronic state, $|f\rangle$ can accumulate population from several pumping interactions [78]. This makes incoherent pumping more efficient for populating a given state (in this case, $|f\rangle$), and thus it is employed in applications such as dye lasers [304]. However, the coherence of the source is lost during the nonradiative transition [305]. This kind of pumping is usually introduced through a reverse Lindblad term in the master equation, $\gamma_p \mathcal{L}_{A^\dagger}$, where γ_p represents the pump rate. The effect of such Lindblad term is exactly the opposite as the loss terms in Eq. 4.17, i.e., it incoherently transfers population from the ground state into the pumped state.

Let us briefly study the dynamics induced by these two types of pump. Along this thesis, we will be interested in weakly pumped systems, $\{\gamma_p, \Omega_p\} \ll 1$, where the initial state is the ground state $|0\rangle$. In this situation, the system should eventually reach a steady state where the loss is compensated by the pump. In Fig. 4.2a we show the bright state population for the TC Hamiltonian under coherent pumping of the state $|B\rangle$, for the same parameters of Fig. 4.1b and a Rabi splitting $\Omega_R = 0.2\omega_0$. The frequency of the pump is tuned to resonance with the bright state, $\omega_L = \omega_0$, and we calculate the same population for the two methods of considering the losses, namely imaginary frequencies (red curve) and Lindblad master equation (black line). For short times, the system oscillates at the frequency of the coherent pumping whereas, for longer times, these oscillations disappear and the population reaches a long-lived state. Although both curves are totally equivalent in the figure, for long enough times only the master equation results will stay constant, while the red curve will slowly decay as the probability abandons the system (inset of Fig. 4.2a). The absence of a true steady state is intrinsic to the non-conservation of the norm, since the system unavoidably loses population as time increases. Although this

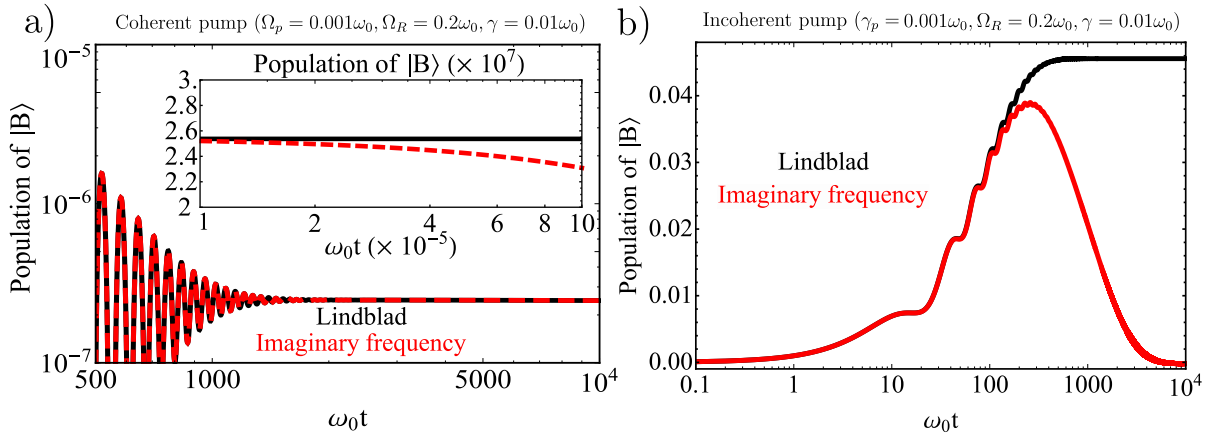

Figure 4.2: Population of the bright state for a TC Hamiltonian under resonant coherent (a) and incoherent (b) pumping of the bright state. The initial state is the total ground state. The red and black lines show the same results obtained with an imaginary frequency and with a Lindblad master equation, respectively. The inset in panel a shows the long time dynamics.

has to be considered when using non-Hermitian Hamiltonians, it is important to stress that an effective steady state is always achieved for low losses and weak pump. This is evident from the flat region in Fig. 4.2a, which extends to very large timescales before the decay is appreciable. In the limit of small γ and Ω_p, simple perturbation theory gives the following estimation for the lifetime of such quasi-steady state,

$$\tau_{ss} \approx \frac{\gamma}{4\Omega_p^2}\left(1 + \left[\frac{2\omega_0 \pm \Omega_R}{\gamma}\right]^2\right) \tag{4.21}$$

which can be made arbitrarily large by reducing the pump rate. For coherent pumpings, therefore, it is still possible to describe the losses via a non-Hermitian imaginary part in order to reduce the computational demand, as we have discussed above. For this approximation to be legitimate, we have to work with such a low pump rate Ω_p that the excited states remain practically unpopulated for all times. In such situation, the lifetime of the effective steady state increases well above any other timescale in the system.

The situation is very different when the pumping is incoherent, as we show in Fig. 4.2b. By looking at the black curve representing a Lindblad description of the losses, it is evident that an incoherent pumping is much more efficient at introducing probability into the system, since the steady state is more populated and arises faster than with a coherent pump. For this precise reason, the imaginary frequency description of the losses is highly inaccurate, as the probability is lost at a much faster rate. Note that in this case (red curve) the population decays even before reaching a long-lived state. In the

case of incoherent pumping, therefore, it is not possible to avoid a full description of the losses in terms of a Lindblad master equation.

To summarize this section, it is very important to properly choose which kind of pumping better suits our goal. If one is interested in an adequate probing of the frequency response of the system, or in keeping large coherences, a coherent pumping is the best choice. If, on the other hand, an efficient population of the excited states is sought, then the most adequate option is the incoherent pumping. The former will be employed in the next sections, whereas the latter is chosen in the next chapter. Note that, to correctly describe the system losses, the Lindblad description should be adopted, although, in the case of a weak coherent pumping, we can largely simplify the problem by describing the losses just as imaginary parts of the frequencies. This is only a good approximation if the pump is weak and the initial state is the total ground state, as in that case the probability is lost at a negligible rate.

4.3. Dark state localization in continuous systems.

Once we have established the basic definitions and methods we will employ throughout this and the following chapter, we can start analysing more complex systems in the CSC regime. As mentioned in the introduction, many works have been devoted to the properties and phenomenology of polaritons whereas, on the other hand, dark states have not attracted a lot of attention in the study of hybrid light-matter systems for obvious reasons: since they are by definition not coupled to light, they are purely matter states and therefore not expected to inherit any photonic property. The objective of this chapter is to challenge such view by demonstrating that, under the adequate circumstances, dark states can inherit the delocalization of the photonic modes. First, we will study in this section the CSC dynamics of ensembles of QEs coupled to continuous EM environments, with the particular example of a plasmonic nanowire. This study is motivated by the fact that the most commonly employed systems in polariton physics are large enough for the photonic modes to display a continuum dispersion relation [30, 53, 281]. As we will see below, the dark states in this situation will display a strongly localized character, a well-known behavior in polariton microcavities. The situation will be different in the next section, where the substitution of the nanowire by a nanoparticle showing a *discrete* spectrum will result in a spatial delocalization of the dark states.

4.3.1. Modelling of QEs coupled to an infinite plasmonic nanowire.

Although the results we extract will be of general character, we will illustrate them in a particular system for simplicity. The selected nanostructure will in this case be an infinite metallic nanowire (NW) with cylindrical cross section, as schematically illustrated in Fig. 4.3a. Such a structure can support propagating surface plasmon modes, which are coupled to an ensemble of QEs as shown in the figure. If the radius of the NW is small, some of these modes are largely confined in the vicinities of the metal-dielectric interface [31]. The consequently increased electric field intensity results in a large coupling rate for a QE placed in such region, thus facilitating the onset of the CSC regime. Note that the infinite length of such structure automatically confers it a continuous dispersion relation. Finally, an additional advantage of a nanowire is the possibility of obtaining its eigenmodes analytically [74].

Properties of the nanowire and the QEs.

The NW under study lies along the z axis, and has a radius $r_0 = 55$nm. For its permittivity ε_m, we choose the Drude-Lorentz expression in Eq. 6.6 now with silver coefficients taken from Ref. [306]. On the other hand, the surrounding dielectric is non dispersive and has a permittivity $\varepsilon_d = 2.4$, similar to that of the dielectric hosts in which molecular QEs are usually embedded, such as PMMA [307] or PVA [308]. The plasmon eigenmodes of the NW are calculated in many textbooks [309], and in cylindrical coordinates (r, ϕ, z) they can be expressed in terms of a parallel and a perpendicular wavevector, k_z and $k_\perp$, as

$$F_1(\mathbf{r}) \propto J_m(k_{\perp,1} r) e^{\pm i m \phi} e^{\pm i k_z z}, \tag{4.22}$$

$$F_2(\mathbf{r}) \propto H_m(k_{\perp,2} r) e^{\pm i m \phi} e^{\pm i k_z z}. \tag{4.23}$$

where the subindices $1, 2$ represent, respectively, the inside and outside regions of the nanowire. In the expression above, F represents any component (x, y, z) of the electric or magnetic field, and $J_m(x)$ and $H_m(x)$ are respectively the Bessel and Hankel functions of order m. The two mode indices in this case are m, which determines the azimuthal dependence of the fields, and the parallel wavevector k_z which is equal for both dielectric and metallic regions. Both the perpendicular and the total wavevector, $k_{\perp,i}$ and $k_i = \sqrt{\varepsilon_i}\omega/c = \sqrt{k_z^2 + k_{\perp,i}^2}$, are thus discontinuous, i.e., different for each medium $i = 1, 2$.

In this particular case, the radius r_0 of the NW lies well below the operation wavelength ($\sim$ 800nm). This allows us to neglect any mode with $|m| > 1$, since these modes only

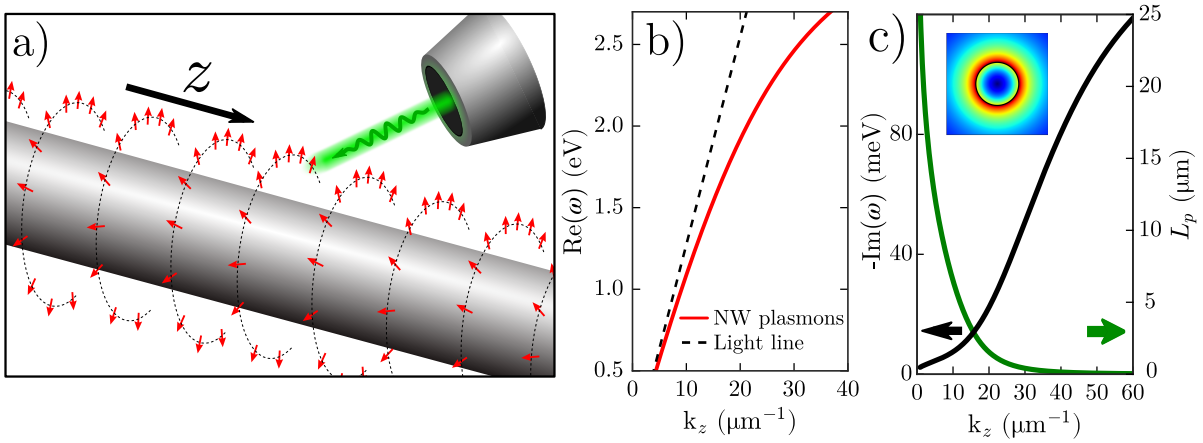

Figure 4.3: a) Scheme of the system under study. A coherent source pumps locally an infinite ensemble of QEs surrounding a plasmonic nanowire. b) Dispersion relation for the NW modes. c) Loss rate (green line) and propagation length (black line) of the plasmonic modes. The inset shows an electric field intensity map of the fundamental mode at $\omega = 1.4$eV.

appear above a cutoff radius $\sim 70 - 100$nm [23, 310]. Additionally, in the limit of small r_0, the EM fields for the modes with $m = 1$ become largely extended in space, and thus their electric field intensity becomes negligible as compared to that of the highly confined $m = 0$ modes [74]. Therefore, in our problem we can consider only the $m = 0$ plasmon eigenmodes. The EM fields for such modes has no azimuthal component, and their dispersion relation $\omega(k_z)$ is obtained by solving the following mode equation,

$$k_{\perp,2} J_1(k_{\perp,1} r_0) \varepsilon_m(\omega) H_0(k_{\perp,2} r_0) = k_{\perp,1} J_0(k_{\perp,1} r_0) \varepsilon_d H_1(k_{\perp,2} r_0). \tag{4.24}$$

The above equation cannot be analytically solved for our complex permittivity ε_m, and we must do so numerically. Note that in the conventional calculations of the nanowire eigenmodes, such modes are usually characterized by a real frequency ω and a complex parallel wavevector, k_z, whose imaginary part describes the decay of the plasmon as it propagates along the NW. In our quantum problem, however, this is not a suitable picture, since a decaying field intensity profile implies that the coupling of the plasmon to a given QE depends on its position along the NW, z_j. This in turn results in a light-matter Hamiltonian which does not fulfil the translational invariance of the system along the z axis. This apparent inconsistency is removed by solving the mode equation with a different constraint. Specifically, we allow the frequency to be complex and assume a real wavevector k_z, thus obtaining a family of eigenmodes which decay in time but are homogeneously distributed in space. Note that although this representation is more convenient for our quantum Hamiltonian, both pictures are equivalent, since decay in

time and decay in space are connected through the group velocity. Indeed, we can still calculate the mode propagation length in terms of the imaginary part of the frequency,

$$2L_p(k_z) = \mathrm{Im}[\omega(k_z)]\frac{d}{dk_z}\mathrm{Re}[\omega(k_z)]. \tag{4.25}$$

The real and imaginary part of $\omega(k_z)$ obtained from the mode equation 4.24 are displayed in Fig. 4.3b, whereas the propagation length calculated through the above expression is displayed in the adjacent panel, 4.3c.

Finally, for the QEs coupled to the NW, we choose as an example similar parameters than J-aggregated molecules at room temperature [311, 312]. J-aggregates are commonly used in plasmonic strong coupling experiments [313–316] because of their large dipole moments, in our case $|\boldsymbol{\mu}_\alpha| = 0.75\text{e}\cdot\text{nm}$. The frequency of the QEs will be imaginary to account for the losses, $\omega_\alpha \equiv \epsilon_0 - i\gamma_0/2$, with a frequency $\epsilon_0 = 1.378\text{eV}$ and a decay rate $\gamma_0 = 1\text{meV}$, which in this case represents mainly nonradiative dissipation [311, 312]. For simplicity, we assume the QEs are homogeneously distributed in a cylindrical layer 35nm above the metallic surface, with a first neighbour distance of 3nm and dipole moments oriented radially (see Fig. 4.3a).

Mapping of the Hamiltonian to an effective 1D chain.

With all the parameters set, we face the problem of calculating both the eigenstates of the system Hamiltonian H (Eq. 4.1) and their dynamics under a weak pump, whose particular form will be introduced later. In order to emulate the infinite system, we impose periodic boundary conditions over a 30μm long unit cell along the z axis, containing $N = 1.88 \times 10^6$ QEs. The Hamiltonian in this case is thus an enormous matrix ($\sim 10^6 \times 10^6$), whose numerical diagonalization is very demanding. In order to lower the computational requirements, we use a reduced Hamiltonian to represent the QE-NW system. We start by noticing that the QEs are regularly distributed in identical rings along the longitudinal coordinate of the cylinder, z, and thus their coupling to the $m = 0$ plasmon mode is independent on the azimuthal angle. Additionally, as we will work in the weak pumping regime, the system will never abandon the single-excitation subspace, and we can therefore replace the ensemble of QEs in the Hamiltonian by a single chain of sites along the z axis, each site describing a whole ring of QEs as schematically depicted in Fig. 4.3a. To do this, we define the ring operators

$$\tilde{\sigma}_r = \frac{1}{\sqrt{n_R}} \sum_{\alpha\in \text{ ring } r}^{n_R} \sigma_{(\alpha)r}, \tag{4.26}$$

which describe a collective excitation in the ring r with the same angular distribution as the plasmon field, i.e., $m = 0$. In the equation above, n_R is the total number of emitters per ring, and $\sigma_{(\alpha)r}$ describes the spin annihilation operator for the emitter α inside the ring r. If we assume all the QEs in a given ring are identical, the Hamiltonian of the QEs can be expressed as a sum over rings instead of individual emitters,

$$H_{qe} = \sum_{\alpha} \omega_\alpha \sigma_\alpha^\dagger \sigma_\alpha = \sum_{r} \omega_r \tilde{\sigma}_r^\dagger \tilde{\sigma}_r. \tag{4.27}$$

Additionally, the light-matter interaction term H_I is also straightforward to obtain since, as mentioned above, the QE-plasmon coupling is the same for all emitters in a given ring. We can therefore write

$$\sum_{\alpha\mathbf{k}} g_\alpha(\mathbf{k}) \sigma_\alpha^\dagger a_{\mathbf{k}} \equiv \sum_{r,\mathbf{k}} g_r(\mathbf{k}) a_{\mathbf{k}} \left(\sum_{\alpha\in \text{ ring } r}^{n_R} \sigma_{(\alpha)r}^\dagger \right) = \sum_{r,\mathbf{k}} \left(\sqrt{n_R} g_\alpha(\mathbf{k})\right) \tilde{\sigma}_r^\dagger a_{\mathbf{k}}, \tag{4.28}$$

i.e., this contribution to the Hamiltonian keeps its original form, with a new coupling intensity $\sqrt{n_R}$ times larger than the original. Finally, the total dipole-dipole interaction can also be expressed as a sum over rings as

$$\sum_{\alpha\beta} V_{\alpha\beta} \sigma_\alpha^\dagger \sigma_\beta = \sum_{r} \sum_{r'} \sum_{\alpha\in \text{ ring } r}^{n_R} \sum_{\beta\in \text{ ring } r'}^{n_R} \sigma_{(\alpha)r}^\dagger \sigma_{(\beta)r'} V_{rr'}^{\alpha\beta}. \tag{4.29}$$

We can now calculate the total dipole-dipole interaction between rings, $\tilde{V}_{rr'}$, through the following overlap,

$$\tilde{V}_{rr'} = \langle 0|\tilde{\sigma}_r H_{dd} \tilde{\sigma}_{r'}^\dagger|0\rangle = \frac{1}{n_R} \sum_{\alpha\in \text{ ring } r}^{n_R} \sum_{\beta\in \text{ ring } r'}^{n_R} V_{rr'}^{\alpha\beta} = \sum_{\beta\in \text{ ring } r'}^{n_R} V_{rr'}^{0\beta} \equiv \sum_{\beta\in \text{ ring } r'} V_{rr'}^{\beta}. \tag{4.30}$$

where in the last two steps we have used the fact that, due to the axial symmetry of the system, each sum in r gives exactly the same result. According to the above formula, the dipole-dipole interaction between rings r and r' is the sum of the dipole-dipole coupling between *one* emitter of ring i and each of the QEs inside ring j. The final expression for the Hamiltonian H_{dd} is therefore also expressed as a sum over rings,

$$\sum_{\alpha\beta} \left(V_{\alpha\beta} \sigma_\alpha^\dagger \sigma_\beta + H.c. \right) = \sum_{r,r'} \tilde{V}_{rr'} \tilde{\sigma}_r^\dagger \tilde{\sigma}_{r'} + H.c. \tag{4.31}$$

By performing the substitutions above in terms of ring operators, we recover a Hamiltonian with the same shape as the original one, H, in which both dipole-dipole interaction and QE-light couplings are modified such that every site in the Hamiltonian accounts for

a whole ring of QEs. This represents an enormous advantage since it allows for the solution of much larger systems. In the particular case of the NW under study, we are able to map the $N = 1.88 \times 10^6$ QEs onto an equivalent chain of only 10^4 sites (rings) separated by the nearest neighbour distance of 3nm. The number of entries in the resulting matrix is thus reduced in 99.997%, enormously accelerating the calculations.

4.3.2. Polariton dispersion and dark state dynamics.

Before studying the system dynamics under pumping, it is very informative to calculate the polariton eigenstates of the light-matter Hamiltonian. In Fig. 4.4a we show the polariton dispersion relation (blue line) as compared to the NW plasmon dispersion relation (red line). Note that the system is in the CSC regime, since the Rabi splitting at the anticrossing point ($k_z \approx 12\mu\text{m}^{-1}$), is much larger than the plasmon losses $\kappa \approx 5\text{meV}$. The polariton dispersion relation only deviates from the energies of both plasmons and QEs in the vicinities of the anticrossing point. The eigenstates in this region are propagating polaritons, whose group velocity can be extracted from the dispersion relation. On the other hand, for very small or very large values of k_z, the plasmons and the QEs do not hybridize, as their energies are largely detuned. In these regions, the eigenstates are either pure plasmons or pure QEs, the latter displaying a flat band structure. As we indicate in Fig. 4.4a, the eigenstates lying at such flat region of the dispersion are the dark states in this case since, although they are technically polaritons, their plasmonic component is negligible and they do not display any hybrid property.

Once the eigenstates of the Hamiltonian H in Eq. 4.1 have been determined, we intend to study their dynamics. In order to probe the behavior of the system at different frequencies within the dispersion relation (Fig. 4.4a), we add to our Hamiltonian the following additional pump term,

$$H_{tot} = H + V_p(t) = H + \Omega_p \cos(\omega_L t) f(t) \left(\sigma_1 + \sigma_1^\dagger\right), \tag{4.32}$$

where the weak pump strength Ω_p is much smaller than any other relevant energy scale. The modulation function, $f(t)$, is assumed to vary slowly in time such that the pulse is quasi-monochromatic. Notice that the coherent optical excitation as modelled by the above equation is only feasible in open EM cavities, where the QEs are coupled to both the cavity modes and free-space radiation. In this case, various possible ways exist to address the QEs locally, for instance, by near-field optical probes [317, 318], or by an external QE [201]. Finally, let us remark that, taking into account the aforementioned

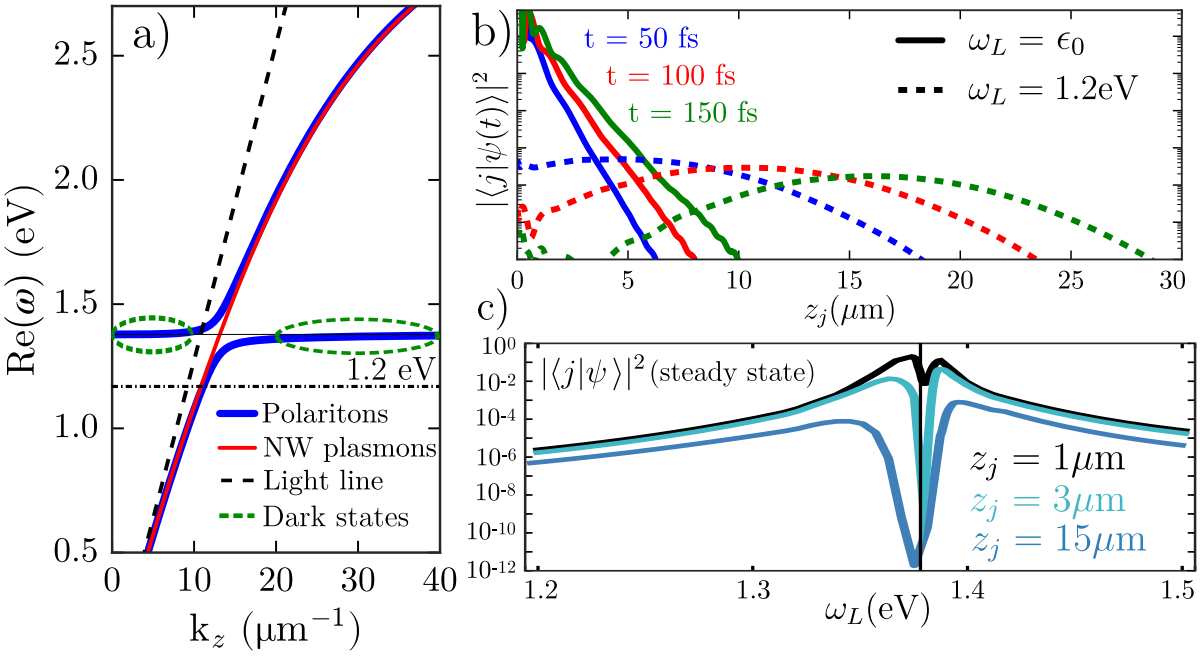

Figure 4.4: a) Polariton (blue) and plasmon (red) dispersion relations in the nanowire The circled flat band regions represent the dark states. The solid/dotted horizontal lines mark the energies ϵ_0 and 1.2 eV, respectively. b) Population of the QEs as a function of their position along the NW, z_j. Solid lines represent the diffusive behaviour when pumping the flat region of the band, $\omega_L = \epsilon_0$. Dashed lines show a polariton propagating along the system ($\omega_L = 1.2$eV). d) Steady-state population versus pump frequency, ω_L, evaluated at three QEs at different positions z_j. The vertical line indicates ϵ_0.

mapping of the Hamiltonian onto a chain of "ring" sites, the above pumping represents an excitation not of a single QE but of a whole ring.

In order to obtain the system wavefunction $|\psi(t)\rangle$ for the above pumping term, we can expand it to first order in the weak pump intensity Ω_p,

$$|\psi(t)\rangle = |\psi_0(t)\rangle + \Omega_p|\psi_1(t)\rangle + \mathcal{O}(\Omega_p^2), \tag{4.33}$$

where the first term in the expansion represents the evolution of the initial state, $|\psi(0)\rangle = |0\rangle$, by the unperturbed Hamiltonian.

$$|\psi_0(t)\rangle = e^{-iHt}|\psi(0)\rangle = e^{-iHt}|0\rangle = |0\rangle. \tag{4.34}$$

Note that, by assuming the initial state to be the ground state of the whole system, the losses are well described by means of an imaginary frequency. To obtain $|\psi_1(t)\rangle$, we introduce the wavefunction 4.33 into the time-dependent Schrödinger equation and, by

keeping only the linear terms in Ω_p, we obtain

$$i\frac{\partial}{\partial t}|\psi_1(t)\rangle = V_p(t)|\psi_0(t)\rangle + H|\psi_1(t)\rangle. \tag{4.35}$$

Finally, we can eliminate the second term above by transforming to the interaction picture [29]. There, the differential equation can be formally integrated and transformed back into the Schrödinger picture, where the following final expression for the total wavefunction is obtained,

$$|\psi(t)\rangle = |0\rangle - ie^{-iHt}\int_0^t dt' e^{iHt'}V_p(t')|0\rangle = |0\rangle - i\Omega_p\int_0^t dt' e^{iH(t'-t)}f(t')\cos(\omega_L t')\sigma_1^\dagger|0\rangle, \tag{4.36}$$

to first order in the perturbative parameter Ω_p. Since the Hamiltonian H has been previously diagonalized, it is straightforward to calculate the above wavefunction by numerical integration, once the pump function has been fixed.

Our first analysis consists on the propagation of polaritonic wavepackets along the chain. We choose for this study a finite duration pump pulse, $f(t) = e^{-(t/\tau)^2}$, where the pump is kept quasi-monochromatic by means of a very small frequency width, $\tau^{-1} = 0.01$ eV. In Fig. 4.4b, we show the spatial distribution of the QE populations, $|\langle j|\psi(t)\rangle|^2 \equiv |\langle 0|\sigma_j|\psi(t)\rangle|^2$, at three different times, when the pump frequency ω_L is tuned at the frequency of both a polariton (1.2 eV, dashed lines) and the dark states (solid lines). For the first case, we can clearly see the spatial propagation of a polaritonic wavepacket as time increases. Since the QE states have hybridized with a propagating plasmon, the population travels along the ensemble of QEs much faster than it would in the absence of the NW, where only nearest neighbour hopping will slowly spread the population. This is a clear example of an advantage brought about by the light-matter interaction, where excitonic wavepackets inherit the rapid propagating character of the EM modes.

When we pump at the dark state frequency, however, the resulting wavepacket in Fig. 4.4b is strongly localized at the origin $z = 0$. In this situation, the probability spreads along the system in a diffusive manner due to the natural widening of the initial distribution. Both the strong localization and the diffusive behavior of the wavepacket are expected since the pump frequency lies on a flat region of the dispersion relation, where the group velocity is practically zero, and the associated modes have a purely excitonic, i.e., localized character. Note that this is in apparent contrast with our previous claim that the basis for the dark subspace is arbitrary, and in principle nothing should favour a localized basis over a delocalized one. Even if we assume that the choice of a particular basis is imposed by the tiny coupling of the excitons to the detuned plasmon modes, that does not solve the problem of localization, since the resulting polaritons are labelled by

a well-defined parallel wavevector k_z, and therefore any eigenstate should in principle be fully delocalized. The solution to this apparent contradiction is provided by the system losses which, by adding a finite linewidth to any eigenstate, induce an overlap between it and the eigenstates with similar energies. For the dark states, this has a drastic effect, since a very large amount of states with very different wavevectors are compressed in the flat region of the band. As a consequence, by pumping at $\omega_L = \epsilon_0$ the combination of all these wavevectors always gives rise to a localized wavepacket, even for a monochromatic pump pulse. The localized behavior is therefore inherent to flat bands in lossy systems.

We can also explore this distinct spatial behaviour between polariton and dark states in a steady-state situation. For simulating this, we change the pump function by a purely monochromatic pulse, i.e., $f(t) = 1$, and take the long time limit. In Fig. 4.4c, we show the corresponding population $|\langle j|\psi\rangle|^2$ of three QEs placed at different positions z_j along the nanowire, as a function of the pump frequency ω_L. The three curves show a similar structure in which two maxima, associated with the delocalized polariton modes, are separated by a dip corresponding to the strongly localized dark states. Note how, despite decaying along the chain due to the losses, the polariton populations do not decrease as fast as that of the dark states, which drops by 9 orders of magnitude along a 1μm distance. This emphasizes the strongly localized character of such states, which remain concentrated around the pump region even for very long times. As a final comment, note that the two polariton maxima correspond to the most efficient excitation of polaritons we can achieve through a pumping of the QEs. Indeed, for ω_L closer to the dark state frequency, the bands flatten and such polaritons do not propagate. On the other hand, when the pump frequency grows apart from ϵ_0, the polaritons propagate more easily but their matter component is smaller, and thus the pumping is less efficient.

The diffusive, localized behavior observed for the dark states in this system is not specific of plasmonic NWs. Indeed, it is a general trend of any polaritonic system with a continuous dispersion relation for the reasons we have discussed above. Note how the inclusion of even the smallest losses is crucial in order to reproduce the realistic system dynamics. In the following section, we will consider a different type of system in which dark states show a strongly delocalized behavior.

4.4. Dark-state delocalization in discrete systems

In the previous section, the localized character of the dark states has been understood as a natural consequence of pumping a flat part of the polariton dispersion, i.e., a region with zero group velocity. The question naturally arises as to whether the same behavior is observed for systems in which such dispersion does not really form a continuum and, consequently, no group velocity can be defined. In this section, we study the same problem as above, but in a metallic nanoparticle which, as opposed to the NW, shows a discrete energy spectrum.

4.4.1. Modelling of QEs coupled to a plasmonic nanoparticle.

In order to better appreciate the differences between the discrete and the continuum spectrum, the system is chosen as similar as possible to the infinite NW. Specifically, we select a cylindrical nanoparticle (NP) with radius $r_0 = 55$nm and length 300nm, terminated by two additional hemispherical caps as depicted schematically in Fig. 4.5a. The permittivities of both the metal and the surrounding dielectric, as well as the parameters of the QEs, are the same as in the infinite NW case. The total number of QEs is now $N = 1.88 \times 10^4$, distributed regularly among 100 rings above the cylindrical surface of the metal. For this NP, the Maxwell eigenmode equation cannot be solved analytically and, hence, we have calculated the localized surface plasmon (LSP) eigenmodes by means of the FEM software used in the previous chapter (COMSOL Multiphysics). As in the continuum case, we only consider the modes with azimuthal number $m = 0$. In Fig. 4.5b we display the resulting real and imaginary parts of the frequencies for the first 9 eigenmodes, labelled by an arbitrary mode index n. The corresponding electric field intensities are displayed in Fig. 4.5c. Note that, due to the three dimensional confinement of the EM field, the dispersion relation of this structure is discrete. Additionally, by means of an adequate combination of parameters, the second EM mode, $n = 2$, is resonant with the QEs, i.e., $\omega_2 = \epsilon_0$ (see the solid dots in Fig. 4.5b).

The numerical calculation of the LSP eigenmodes can be carried out for low order modes, but becomes increasingly challenging for higher energies. In this limit, the eigenenergies grow closer to each other and, as their linewidth increases, tend to overlap forming the so-called pseudomode [297]. As a consequence, the identification of a particular re-

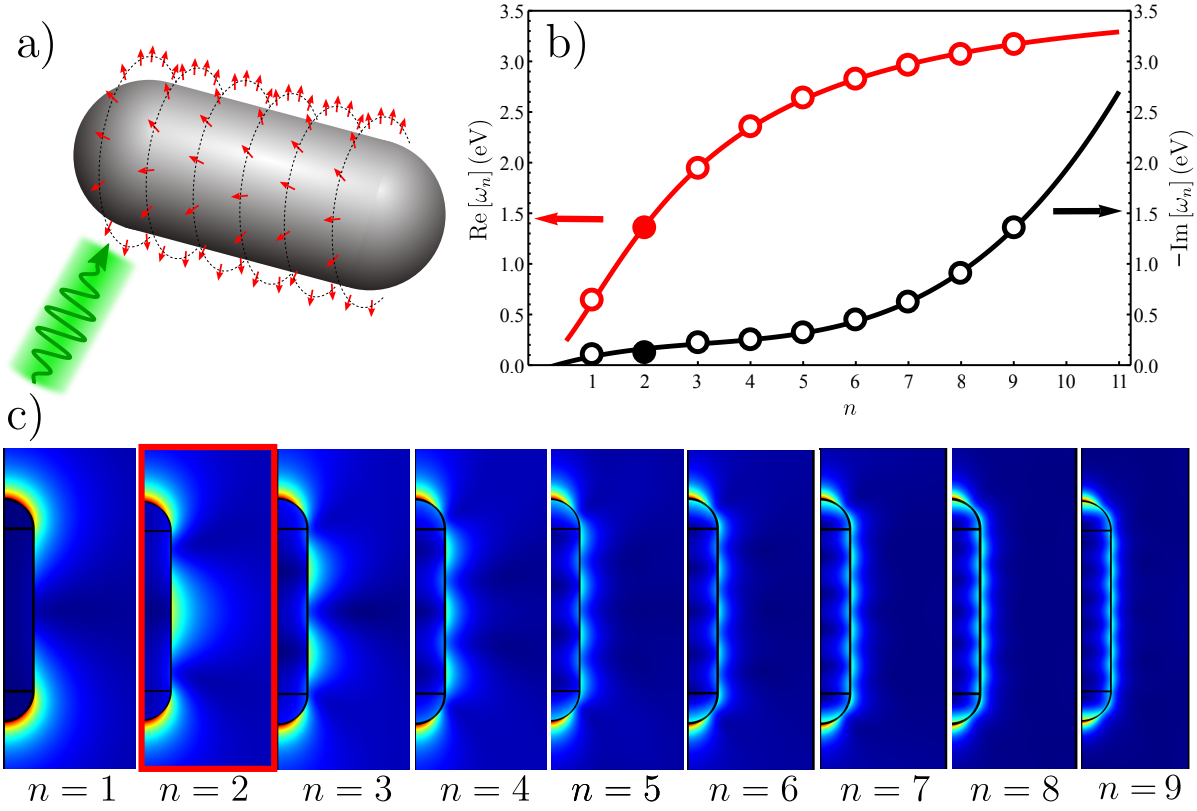

Figure 4.5: a) Schematic depiction of the system under study. The plasmon modes of a metallic nanoparticle are strongly coupled to an ensemble of QEs. b) Eigenfrequencies (red) and loss rates (black) of the lowest energy plasmon eigenmodes of the nanoparticle, versus the mode index n. c) Electric field intensity profile of the 9 plasmon modes of panel b. The mode $n = 2$ (filled circles in panel b, squared image in panel c) is in resonance with the QEs.

sonance becomes impossible in practical terms. However, note that we do not need to determine all the properties of the LSP modes but only those appearing in the system Hamiltonian, Eq. 4.1. Specifically, we are interested in the complex eigenfrequencies ω_α in the contribution of the EM modes, and in the electric field intensities at the positions of the QEs, which determine the coupling rate $g_\alpha(\mathbf{k})$. Fortunately, in the high energy limit, these relevant modal properties of the localized nanoparticle can be extracted by extrapolation of the modes of the infinite nanowire. This is demonstrated for the real part of the eigenfrequencies in Fig. 4.6a, which compares the dispersion relation of both NP and NW. In this panel, the allowed values of k_z for the nanoparticle have been extracted from the standing wave patterns of the electric field intensity shown in Fig. 4.5c. Since both curves converge to each other for large energies, we can extrapolate the first LSP modes by using the analytical solutions for the infinite nanowire. The fact that

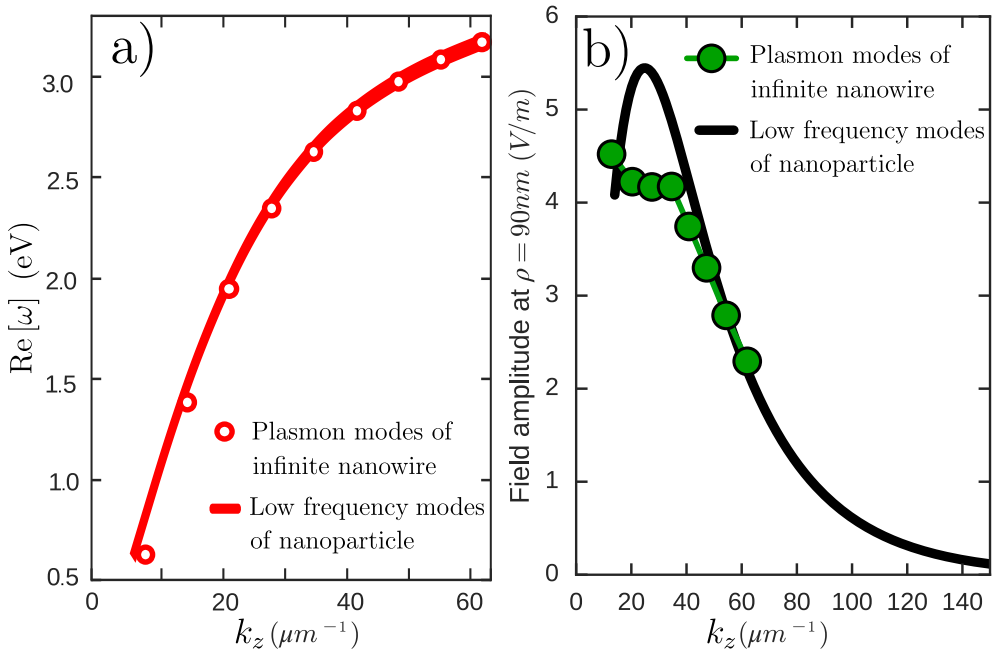

Figure 4.6: (colour online) Comparison of the eigenmodes of the nanoparticle and the infinite nanowire. a) dispersion relation. b) radial field amplitude 35 nm above the cylindrical surface.

both dispersion relations converge at high frequencies is related to the corresponding decrease in the wavelength of the LSPs, for which the NP appears increasingly larger and, eventually, indistinguishable from an infinite NW.

The calculation of the desired properties of the $n-$th mode of the nanoparticle starts by obtaining its parallel wavevector k_z, by a direct extrapolation of the corresponding low energy values. This is straightforward, as k_z displays a linear dependence on n for $n \leq 9$. We then insert this wavevector in the dispersion relation for the infinite nanowire in order to obtain the eigenfrequency of the mode, $\mathrm{Re}[\omega_n]$. The corresponding imaginary part of ω_n is not accurately described by the NW solution, since the field concentrated around the two hemispherical caps makes the nanoparticle modes much lossier than the NW plasmons [319]. However, we have checked that the particular values of $\mathrm{Im}[\omega_n]$ $(n \gg 1)$ do not affect the relevant physics of our system. This is due to the strong detuning of the high-energy modes with respect to the QEs, which reduces the corresponding light-matter coupling to a negligible value.

Once we determine the eigenfrequencies of the higher order modes, the only remaining modal property we are interested in is the electric field intensity at the position of the QEs. Since the dipole moments of the QEs are oriented radially, only the radial component of such electric field is needed, E_ρ. Assuming that the nanoparticle is centred

at the origin, the following extrapolation is an excellent approximation for every $n > 2$ mode in Fig. 4.5, in the region $-L/2 \leq z \leq L/2$,

$$E_\rho \approx \begin{cases} E_0(n)\cos(k_z(z - L/2)) & \text{for} \quad n \text{ odd}, \\ E_0(n)\sin(k_z(z - L/2)) & \text{for} \quad n \text{ even}. \end{cases} \tag{4.37}$$

Here, $E_0(n)$ is a field amplitude, dependent on the radial position ρ of the considered surface. For the particular coordinates of the QEs above the metallic surface ($\rho = r_0 + 35$ nm), the field amplitude $E_0(n)$ is very well approximated by the solutions of the infinite NW in the limit of large n, as we show in 4.6b. Hence, we can also extrapolate such field intensity in order to calculate the light-matter coupling rate.

It is important to emphasize that not all the modal properties of the nanoparticle are so easy to extract from the infinite NW. However, the relevant quantities of our particular problem, namely real part of the frequency and radial field at $\rho = r_0 + 35$nm, converge to the values of such NW in the high energy limit. Thanks to this fact, we are able to include as many LSP modes as we want in the Hamiltonian without calculating them explicitly. As a final remark, note that, as a consequence of the increasing confinement, the field intensity in Fig. 4.6b decays exponentially with n, and hence so does the QE-LSP coupling rate. In practical terms, this means that the inclusion of higher order modes does not significantly modify the system dynamics.

4.4.2. Dark state delocalization.

Once every parameter in the Hamiltonian 4.32 for the NP is calculated, we can study the population distribution along the ensemble of QEs. In this discrete situation, no continuous band builds up and, therefore, the concept of group velocity is ill-defined. Indeed, in this system the LSP modes distribute along all the nanoparticle in an instantaneous way (only limited by fundamental constraints). For this reason, a time propagation study such as the one in Fig. 4.4b does not make sense in this situation. We therefore calculate directly the steady-state distribution of the population in the same fashion as we have done for the infinite NW, i.e., by using a purely monochromatic pump function $f(t) = 1$. In order to include any possible effects that could arise in a realistic system, we will obtain the steady-state wavefunction in two different situations, namely without and with dipole-dipole interaction $V_{\alpha\beta}$ in the Hamiltonian. In the latter case, we also account by inhomogeneous broadening in the ensemble of QEs by including a random, site-dependent variation in their energies, $\epsilon_0 \to \epsilon_0 + \Delta_j$. The random numbers $\Delta_j \in [-\gamma_\phi, \gamma_\phi]$ are bound by the dephasing rate of J-aggregated molecules, i.e., $\gamma_\phi \approx 25$meV [311, 312]. When

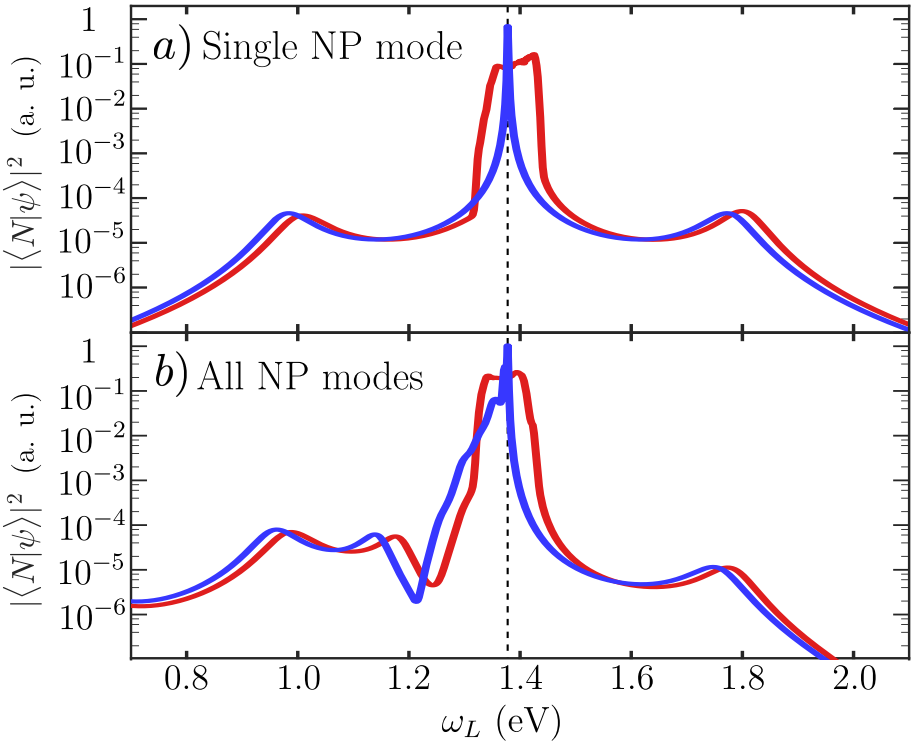

Figure 4.7: Steady-state population of the final emitters in the chain, as a function of the pump frequency ω_L. a) Situation in which only the resonant photonic mode $n = 2$ is taken into account. b) Same results when including all the modes. In both panels, the blue lines show the case where dipole-dipole interaction and disorder are neglected, while red lines show the more realistic situation with both included in the Hamiltonian. The dashed line marks the energy of the dark states, ϵ_0.

disorder is included, we perform an average over 10^4 realizations in order to obtain a statistically reliable prediction. Note that, in 1D systems, a physically consistent length scaling is obtained only if such average is logarithmic, $\langle A\rangle = \exp\langle \log A_i\rangle$ [320].

Steady-state delocalization of the dark states.

Let us consider first the case where only the resonant LSP mode, $n = 2$, is included in the Hamiltonian. For this situation and neglecting dipole-dipole coupling between the QEs, we render in Fig. 4.7a (blue curve) the steady-state population of the QEs lying farthest from the pump region, $|\langle N|\psi\rangle|^2$, as a function of the pump frequency ω_L. This emitter is chosen arbitrarily, since identical plots displaying a clear three-peak spectrum are obtained for the populations of every emitter in the ensemble. Therefore, the three maxima in the figure correspond to extended states, where the population

is largely delocalized across the system. The two peaks at higher and lower energies are associated with the two polaritons, which inherit the delocalized character of the photonic excitations thanks to their hybrid nature. However, the emergence of a peak located at the frequency of the dark states implies that the population of these modes also extends over the whole system. Notably, this population is several orders of magnitude larger than those of the two polaritons. This is in sharp contrast with the results obtained for an infinite NW (compare with Fig. 4.4c).

The peak in the population spectrum associated with the dark states remains when both dipole-dipole interaction and disorder are taken into account, as shown by the red curve in Fig. 4.7a. In such a situation, the dipole-dipole coupling tends to delocalize the system wavefunction, but this trend is compensated by the inhomogeneous broadening, which induces localization [321]. As a consequence, no qualitative changes are observed apart from the expected widening of the dark state peak caused by disorder. Moreover, the delocalized character also persists when all the EM modes of the nanoparticle are included in the Hamiltonian, as demonstrated in Fig. 4.7b. Here, the new LSP modes whose energy is close to ϵ_0 hybridize with the QEs to form new polaritons, which appear as additional peaks in the figure (for instance, at ~ 1.15eV). Conversely, the LSP modes which are very detuned with respect to the QEs couple poorly to them, and thus form eigenstates which are almost purely LSPs or purely QE states. The former are not displayed in the figure since they lie at higher energies, while the latter are very close in energies to the dark states and form the asymmetric sideband below 1.4eV in the figure. Although the population spectrum is modified due to the presence of several EM modes in the system, the larger population associated with the dark modes as compared to those of the polaritons is maintained when the full spectrum of the EM environment is taken into account. Figure 4.7 thus demonstrates a surprising finding, namely that dark states can inherit the delocalized character of the polaritons. Additionally, this feature is very robust against disorder, dipole-dipole interactions between the QEs, and light fields that support several discrete EM modes.

Fundamental explanation in terms of the Dicke Hamiltonian.

In order to understand the fundamental mechanism behind the dark state delocalization, we can elaborate a simple model that is able to capture the basic ingredients of the interaction of an ensemble of QEs with a photonic structure that displays a discrete EM spectrum. In this model, we neglect both dipole-dipole coupling and disorder since, as shown in Fig. 4.7, these two effects play a minor role. For the same reason, we also

consider only a single EM mode in resonance with the excitations within the QEs. Finally, we assume all the QEs to be coupled with such EM mode at the same rate, g. In this simple case, the unperturbed Hamiltonian H takes the form of the Dicke model studied in Eq. 4.9, now with complex energies whose imaginary parts, γ_0 and κ, describe the losses in the QEs and the EM mode, respectively. As we have already shown, the eigenstates of such Hamiltonian are formed, respectively, by the $(N-1)$ dark states $|D_\alpha\rangle$ with the same energy as the bare QEs, $\omega_j = \epsilon_0 - i\gamma_0/2$, and the upper and lower polaritons, $|\epsilon_+\rangle$ and $|\epsilon_-\rangle$ which, within the CSC regime, $\sqrt{N}g \equiv \Omega_R/2 \gg \gamma_0, \kappa$, have energies $\epsilon_\pm = \epsilon_0 - i(\gamma_0+\kappa)/2 \pm \sqrt{N}g$. All these eigenstates span the full single-excitation subspace of H, i.e.,

$$\sum_\epsilon |\epsilon\rangle\langle\epsilon| = |\epsilon_+\rangle\langle\epsilon_+| + |\epsilon_-\rangle\langle\epsilon_-| + \sum_\alpha |D_\alpha\rangle\langle D_\alpha| = \mathbb{1}_1, \tag{4.38}$$

$\mathbb{1}_1$ being the identity matrix within such subspace. In this simple model, when we introduce the pumping term in the Hamiltonian H, the time-evolved wavefunction $|\psi(t)\rangle$ can be analytically calculated from Eq. 4.36. Indeed, we can express the probability amplitude $p_j = \langle j|\psi\rangle$ as

$$p_j = -i\Omega_p \langle j|e^{-iHt} \int_0^t dt' e^{iHt'} \cos(\omega_L t')|1\rangle \tag{4.39}$$

and, after using the closure relation 4.38, integrate to obtain

$$p_j = -i\frac{\Omega_p}{2} \sum_\epsilon \langle j|\epsilon\rangle\langle\epsilon|1\rangle \left(\frac{e^{i\omega_L t} - e^{-i\epsilon t}}{\epsilon + \omega_L} + \frac{e^{-i\omega_L t} - e^{-i\epsilon t}}{\epsilon - \omega_L} \right). \tag{4.40}$$

Note that, since all the eigenstates of the Hamiltonian suffer from losses, in the steady state limit $t \to \infty$ the exponentials $e^{-i\epsilon t}$ vanish. In such steady state, we can additionally neglect the small off-resonant terms $\propto (\epsilon+\omega_L)^{-1}$, obtaining the following final expression,

$$\begin{aligned} p_j \approx -i\frac{\Omega_p}{2} e^{-i\omega_L t} \sum_\epsilon \frac{\langle j|\epsilon\rangle\langle\epsilon|1\rangle}{\epsilon - \omega_L} \propto \sum_\alpha \frac{\langle j|D_\alpha\rangle\langle D_\alpha|1\rangle}{\epsilon_0 - \omega_L - i\gamma_0/2} + \\ + \frac{\langle j|\epsilon_+\rangle\langle\epsilon_+|1\rangle}{\epsilon_0 - \omega_L + \sqrt{N}g - i(\gamma_0+\kappa)/4} + \frac{\langle j|\epsilon_-\rangle\langle\epsilon_-|1\rangle}{\epsilon_0 - \omega_L - \sqrt{N}g - i(\gamma_0+\kappa)/4}. \end{aligned} \tag{4.41}$$

According to the above equation, the population $|p_j|^2$ will display three well-separated Lorentzian peaks centred at ϵ_0 and $\epsilon_0 \pm \sqrt{N}g$, respectively. Equation 4.41 is thus able to account for the numerical results as displayed in Fig. 4.7a. It is also straightforward to calculate the ratio between the heights of the population peaks associated with the dark modes and with the two polaritons, respectively; this ratio is proportional to $(1+\kappa/\gamma_0)^2$.

In the case under study, the losses associated with the predominant EM mode of the NP ($\kappa \approx 100$ meV, see Fig. 4.5b) are much larger than the loss rate of the QEs ($\gamma_0 \approx 1$ meV). This explains why the population peak of the dark modes in Fig. 4.7a is four orders of magnitude higher than the heights of the polariton peaks. In general, whenever the photonic mode is more lossy than the QEs, the delocalized state existing at the dark state frequency will be much more robust against losses, as it only inherits the delocalization of the photons but not their loss rate. Interestingly, in the opposite limit $\gamma_0 \gg \kappa$, the dark state peak only decreases to half the height of the two polariton maxima. This certifies the general robustness of the dark state delocalization against any value of the losses.

It is possible to explore further inside our model to fully understand the process of dark-state delocalization. Let us consider the case $\omega_L \approx \epsilon_0$, a situation in which the two last terms of Eq. 4.41 are negligible if the system is in the CSC regime. In such limit, by using again Eq. 4.38 we can express p_j as

$$p_j\big|_{(\omega_L \approx \epsilon_0)} \propto \frac{\langle j|\Big(\mathbb{1}_1 - |\epsilon_+\rangle\langle\epsilon_+| - |\epsilon_-\rangle\langle\epsilon_-|\Big)|1\rangle}{\epsilon_0 - \omega_L - i\gamma_0/2}. \tag{4.42}$$

This expression shows that the dark-state population can be expressed as a function of the two polaritons only. Since both these polaritons are spatially extended, dark states are therefore constrained to display the same delocalized behavior. Note that this is not a property of any particular dark state but of the dark subspace as a whole, whose basis remains undetermined. This also implies that it is not possible to choose the basis of dark states in such a way that they are completely localized. According to Eq. 4.42, by strongly coupling the QEs to a discrete electromagnetic mode, one extended state is removed from the singly excited Hilbert space. This leaves an imprint on the remaining dark subspace, which hence inherits the delocalized character of the polaritons.

The explanation for the dark state delocalization also illustrates the generality of this fundamental property. In principle, the only three requirements are, first, a discrete EM mode, which can separate a single bright state from the dark subspace. Second, the onset of the CSC regime, which pushes the polaritons away in energies from the dark states. Finally, a local coherent pump which ensures $\langle j|1\rangle \approx 0$ in Eq. 4.42, for some QE j within the ensemble. Note that this pump must not necessarily have the form of Eq. 4.32, since the only constraint is to introduce excitations only in a fraction of the QEs and not in all of them. It is also important to stress that, although Eq. 4.42 is only valid in the limit of weak disorder and inhomogeneous broadening, our numerical results in Fig. 4.7 demonstrate that dark state delocalization survives even for significant disorder.

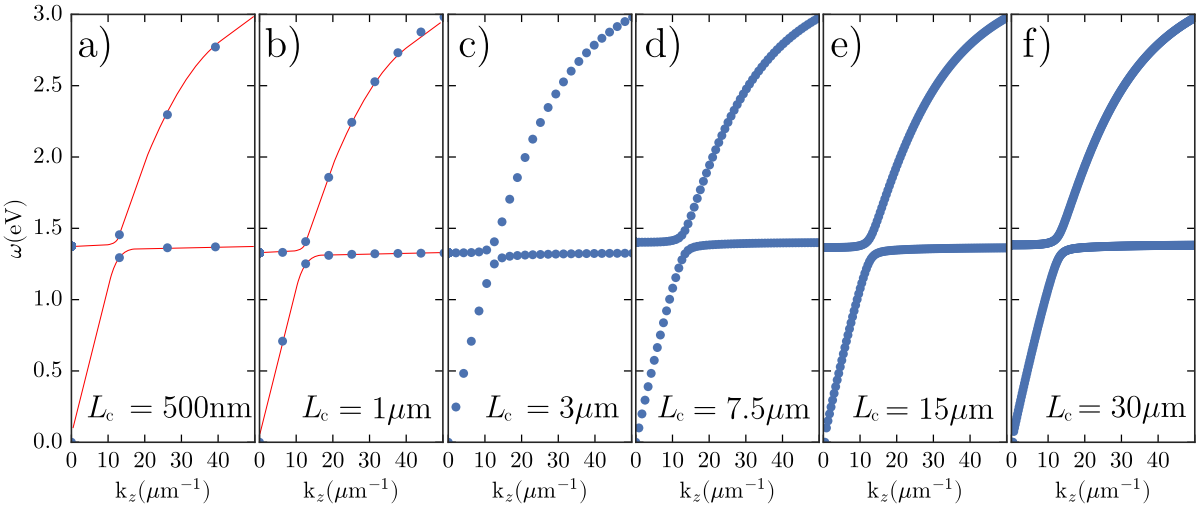

Figure 4.8: Polariton dispersion relation for QEs coupled to the plasmon modes of an infinite nanowire. The different panels show the results for increasing lengths of the periodic unit cell, L_c. The red lines in panels a) and b) is a guide to the eye.

Additionally, they also demonstrate that the presence of additional EM modes is not relevant as long as they form a discrete dispersion relation. The dark state delocalization thus constitutes a fundamental property of discrete light-matter systems.

4.4.3. Discrete to continuum transition.

In this chapter we have presented two situations in which the steady-state wavefunction displays a completely different behavior. On the one hand, when the cavity modes form a continuum, the dark states are strongly localized around the pump region, as shown by the dip in Fig. 4.4c. On the other hand, when the light modes are discrete the dark states become delocalized and such dip transforms into a maximum, as we illustrate in Fig. 4.7. In this section, we analyze how one regime evolves into the other as the system size increases.

As we have demonstrated above, the solutions for the nanoparticle are very similar to those of the infinite nanowire. Therefore, we simplify our study by analysing only the case of the nanowire, for varying lengths L_c of the periodic unit cell. In principle, for values of L_c close to the length of the nanoparticle ($\sim$ 300 nm) the modes, determined by the allowed wavevectors in the periodic unit cell, are well-separated in energy and thus should reproduce a discrete multimode scenario. This is confirmed in Fig. 4.8, where we display the NW polariton dispersion for different values of L_c. The parameters of the

NW are exactly the same as in the main text. To keep a constant Rabi splitting, the density of emitters has been kept constant at $n \sim (3\text{nm})^{-1}$ in every panel. Additionally, the energy of the QEs, ϵ_0, has been slightly tuned to be in resonance with the closest EM mode, in order to avoid small effects induced by detuning. According to Fig. 4.8a, for small L_c only a few modes are close to the bare QEs in energy, and hence we will obtain a similar behavior as in the nanoparticle. On the other hand, by gradually increasing the length L_c, the discrete dispersion evolves into a full continuum spectrum in panel 4.8f, which displays the same results as Fig. 4.4a.

The discrete-to-continuum transition observed in Fig. 4.8 can be tracked as well in the steady state wavefunction of the driven system, which we display in Fig. 4.9. Here, we plot the steady-state population at the centre of the unit cell, $|\langle N/2|\psi\rangle|^2$, as a function of $\epsilon_0 - \omega_L$, i.e., the detuning between the pump frequency and the energy of the QEs. The parameters in each panel of Fig. 4.9 are equal to those in the corresponding panels of Fig. 4.8. The discrete situation is recovered for $L_c = 500\text{nm}$, where a multi-peak structure arises due to the efficient pump of the different eigenstates of the system. In this panel only three peaks are present, the rest of them being out of the horizontal scale (compare for a better insight with the energies in panel 4.8a). As described above, the interaction of the QEs with strongly detuned high-n EM modes induces energy shifts leading to a sideband below the energy of the dark states, which in the case of Fig. 4.7b is clearly visible. In panel 4.9a, on the other hand, due to the smaller Rabi splitting the peaks induced by these polaritons and by the dark states overlap in a single maximum. As a consequence, the central peak in this figure displays a similar width as the two lateral maxima. Note that, despite the fact that only three peaks are resolved in panel 4.9a, we are not considering a single-mode situation. Indeed, this panel responds to a discrete multimode case, similar to the one displayed in Fig. 4.7b.

When the length of the unit cell is increased, the system undergoes a discrete-to-continuum transition, and the steady-state population drastically changes. Specifically, a dip starts to form at the dark state frequency, clearly indicating a localization of the dark states around the pump region. In the continuum limit (panel 4.9f), the steady-state population of the dark states is $\sim 10^8 - 10^9$ times smaller than that of the polaritons. It is interesting to point out that the absolute minimum in the curves of Fig. 4.9 is reached at a slightly lower energy than ϵ_0. This is a natural consequence of the finite linewidth of the dark states, which are able to overlap with other eigenstates of similar energy. When pumping exactly at the frequency of the QEs, propagating polaritons at similar energies are also slightly populated. In the particular case discussed here, the overlap with the lower polaritons is smaller since they have a smaller linewidth. Therefore, reducing the

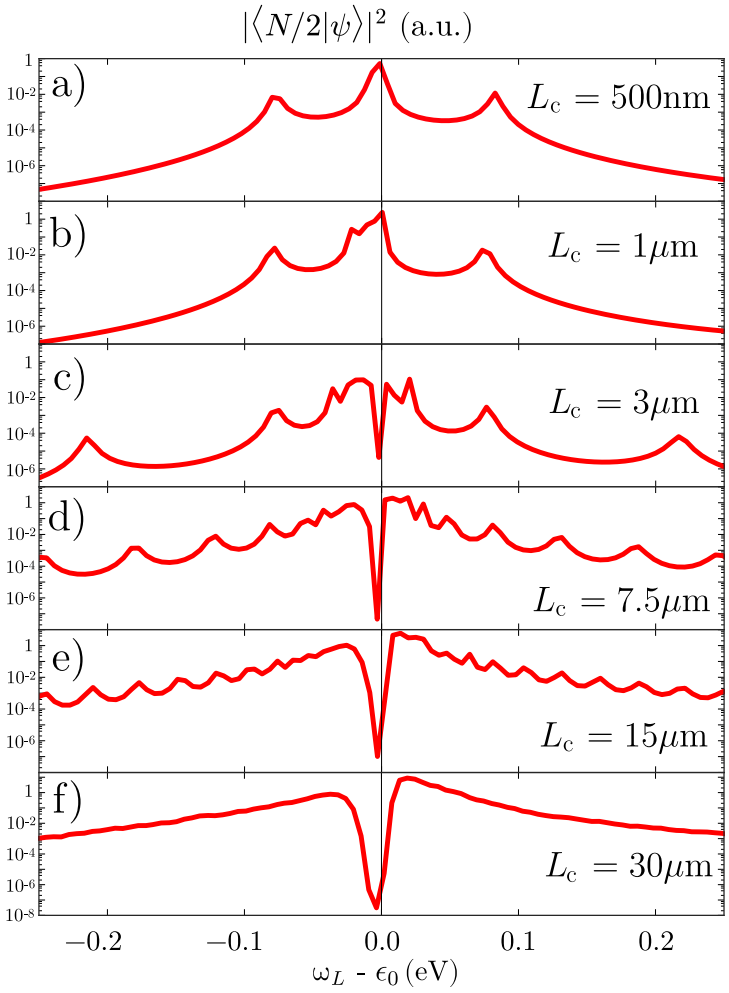

Figure 4.9: Steady-state population ($f(t) = 1$) of the QEs at the centre of the NW unit cell of length L_c. The horizontal axis displays the detuning between the pump frequency ω_L and the energy of the bare QEs, ϵ_0.

pump frequency a little below the energy of the bare QEs leads to a slightly smaller propagating component and a more localized state.

The discrete-to-continuum transition occurs roughly when the discrete modes start to spectrally overlap. Our particular examples consider plasmonic structures, in which the photonic modes are usually very lossy. Therefore, the typical length scale above which the discrete behaviour disappears is on the order of a few μm. However, for systems in which both the cavity modes and the QEs have a small linewidth, one can reasonably expect that the discrete regime will be extended to larger lengths. Even in plasmonic systems there is room for improvement in this sense, particularly for larger Rabi splittings. Indeed, either by increasing the density of emitters or by choosing a nanostructure with

stronger EM field confinement, the crossover length can be largely increased. Therefore, with the adequate improvements, dark-state delocalization could be achieved well within the micrometer scale.

4.5. Conclusion

In this chapter we have demonstrated how, in the CSC regime, not only the polaritons but also the dark states can feature a delocalized behavior across the system. This is a surprising result, since the dark states are uncoupled from the light modes. However, such result has a fundamental origin and therefore is of a very general nature, since it only requires the EM spectrum to be discrete. As a consequence, such effect might be observed in a wide variety of cavity systems as long as they allow for an external, local pump of the ensemble of QEs.

The dark state delocalization is understood as the effect of removing a set of bright delocalized states from the Hilbert space of the QEs. Although the resulting dark states are arbitrarily defined within the remaining subspace, such subspace as a whole displays a delocalized character due to the imprint left by the removed states. Importantly, the dark states remain uncoupled to the light modes, and hence acquire the extended nature of the photons while maintaining the loss rate of the QEs. This is very advantageous when the system decay is dominated by photon absorption, a situation where the delocalized dark states have a longer lifetime than the polaritons. Additionally, this property is shown to be robust against localization-inducing effects arising in realistic situations, such as inhomogeneous broadening.

While some usual polaritonic phenomena explicitly require the photonic component of the polaritons, such as Bose Einstein condensation or superfluidity, many other applications could benefit from the delocalized character of the dark states. For instance, this effect is very suggestive for quantum computation and quantum circuitry purposes, where the possibility of generating long-lived nonclassical states in an ensemble of qubits is of key importance [322, 323]. Other interesting example is the efficient distribution of excitons along the ensemble of QEs, with evident benefits in areas such as excitonic circuits or energy transport [110, 324]. Additionally, any application related to delocalization could in principle be attained in resonant structures with very low quality factors where, as opposed to the dark states, the polaritons are too lossy. Our result could thus enable the realization of some CSC physics in a wider family of photonic nanostructures.

5 | Harvesting excitons through plasmonic strong coupling.

5.1. Introduction

In the last decades, the collective strong coupling regime has been made available in a wide variety of physical systems such as atoms [325], ion Coulomb crystals [326], Bose-Einstein condensates [327, 328], and organic semiconductors [313, 329]. In all these systems, one of the most characteristic features introduced by the CSC is the presence of hybrid states, whose matter component inherits the delocalized character of the EM modes as we have discussed in the previous chapter. In the case of electronic transitions in QEs, this effect manifests as an extended excitonic wavepacket, distributed among the ensemble of QEs. Strongly coupled systems thus offer the possibility of manipulating the spatial extension of otherwise more localized excitons. This manipulation could have a strong impact in many fundamental areas in which excitons play a key role, such as Förster resonance energy transfer, energy conversion in light-harvesting complexes [140, 142, 147], and a wide range of processes related to heat transport [330]. Moreover, it could also improve the efficiency of various optoelectronic devices such as organic solar cells [331] and light-emitting diodes [332], or excitonic transistors [110]. Among these applications, those based on organic molecule systems could especially benefit from an increase of the exciton propagation length, since in these materials the combination of decoherence and recombination makes the exciton transport diffusive, and thus inefficient,

over long distances [333].

Recent works [138, 139] have demonstrated how the exciton transport along a 1D chain of organic molecules can be enhanced by several orders of magnitude if such QEs are strongly coupled to a cavity mode. This promising results offer many possibilities for all the aforementioned excitonic applications. However, the coupling to a homogeneous cavity mode fundamentally limits the efficiency of the exciton transport since, instead of physically propagating across the ensemble, the excitons spread homogeneously along the chain, thus most of the probability not being collected at the end. This motivates the search for improvements of such methods, in which the exciton can be efficiently extended from a region A to a region B of the ensemble of QEs without spreading into intermediate parts. Such a procedure would result in exciton funnelling into a narrow and, ideally, subwavelength region of space.

In order to achieve the aforementioned exciton harvesting, two principal ingredients should be present, namely EM fields confined in a subwavelength scale, and very large light-matter couplings at the single emitter level. Both these requirements would be met, among others, by organic molecules coupled to plasmonic resonances. The plasmons supported by metallic structures are particularly suitable for strong coupling applications due to their intense field confinement [334], as well as their known ability to improve exciton-related processes, such as Förster resonance energy transfer in weakly coupled systems [335–337]. Additionally, an intense research effort has been devoted to the study of strong coupling in these systems at the single and multiple emitter level, both theoretically [297–299, 338–340] and experimentally [313, 316, 341–348]. Many of these works achieve the CSC regime by means of organic molecular QEs with large dipole moments, such as J-aggregates. As mentioned in the previous chapter, these compounds are suited for many kinds of photon-exciton applications [349]. Moreover, in combination with the adequate cavities such as plasmonic nanostructures, they display Rabi splittings as large as 1eV [346, 350].

In this chapter, we demonstrate the possibility of exciton harvesting mediated by CSC. Although our results are in principle general, we illustrate our method in plasmonic nanoparticles coupled to J-aggregates, where excitons are shown to be efficiently funnelled into deep subwavelength spots. The first section (sec. 5.2) is devoted to describing the phenomenon of extraordinary exciton transport mediated by strong coupling, in terms of the original work by Feist and Garcia-Vidal (Ref. [138]). Here, we demonstrate that dark states are delocalized also in the case of incoherent pumping, thus extending the main result of the previous chapter to a much wider range of situations. In the following section (sec. 5.3), we demonstrate how the spatial profile of the exciton conductance

can be modified by coupling the molecular QEs to inhomogeneous field profiles, using as an example the dipolar resonance of a plasmonic nanosphere. A fast and spatially selective increase in the conductance is demonstrated when the system enters into the strong coupling regime. After deducing an analytical formula for general field profiles, we present in section 5.4 a modified nanostructure in which excitons can be funnelled into a deep subwavelength region of space. Finally, in section 5.5, we demonstrate how a more accurate description of the dephasing processes results in a richer phenomenology for the strong coupling exciton conductance. In this limit, dephasing can be harnessed to enhance exciton transport, as it induces a population transfer from the polaritons into the more efficient dark states. Finally, our conclusions are presented in section 5.6.

5.2. Enhancing exciton transport through coupling to cavity modes.

In this section, we illustrate the phenomenon of extraordinary exciton transport. We intend to summarize the results obtained in the recent work by Feist and Garcia-Vidal [138] as a starting point for our work in exciton harvesting. First, we will introduce the simple model for exciton transport, followed by the results showing a drastic increase of the exciton conductance in the strong coupling regime. We will then present the analytical model developed in the original work, where the excitonic transport is shown to be mediated by two independent channels, namely dipole-dipole interaction and cavity-assisted transport.

5.2.1. The model system.

In the original work in Ref. [138], the system is reduced to the simplest possible model which is able to capture the relevant physics. The authors consider an ensemble of QEs arranged in a 1D chain and placed inside a cavity, as schematically displayed in Fig. 5.1. For simplicity, a single-mode cavity with frequency ω_c is considered. The Hamiltonian of the system is thus a simpler version of Eq. 4.1,

$$H = \omega_c a^\dagger a + \sum_\alpha \omega_\alpha \sigma_\alpha^\dagger \sigma_\alpha + \sum_{\alpha\beta} V_{\alpha\beta} \left(\sigma_\alpha^\dagger \sigma_\beta + H.c.\right) + \sum_\alpha \left(g_\alpha a^\dagger \sigma_\alpha + H.c.\right), \tag{5.1}$$

where the coupling g_α and dipole-dipole interaction $V_{\alpha\beta}$ are given by Eqs. 4.3 and 4.2, respectively. In principle, the QEs are placed in the centre of the cavity as seen in Fig.

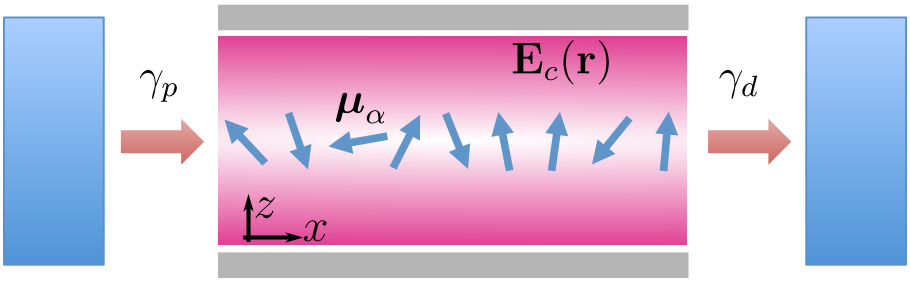

Figure 5.1: (Reproduced with permission from the authors) Schematic depiction of the model system. A single mode cavity with an electric field profile $\mathbf{E}_c(\mathbf{r})$ contains a 1D chain of QEs with dipole moments $\boldsymbol{\mu}_\alpha$. Excitons are introduced inside the first through an incoherent pump at a rate γ_p, and the exciton conductance is measured via the energy loss in the decay γ_d of the last QE in the chain.

5.1, and we assume their dipole moments are oriented along the (out-of-plane) z-axis. In this way, they couple only to the TE cavity modes [351], specifically to the fundamental TE mode in our simple picture. This results in an homogeneous coupling $g_\alpha = g$ for all the QEs.

Because the light-QE coupling is the same for all the QEs, the Hamiltonian is equivalent to the Dicke model in Eq. 4.9, apart from the dipole-dipole interaction. For the general situation of different loss rates of the QEs and the cavity, γ and κ respectively, an alternative convention for the onset of strong coupling is used, which is also often employed in the literature [299]. It is based on the polariton energies for the Dicke Hamiltonian at zero detuning ($\omega_c = \omega_0$),

$$\epsilon_\pm = \omega_0 - i\frac{\gamma+\kappa}{2} \pm \frac{1}{2}\sqrt{\Omega_R^2 - \frac{|\gamma-\kappa|^2}{4}}. \tag{5.2}$$

In the above expression, when the Rabi splitting is smaller than the difference of the loss rates, $\Omega_R < |\gamma - \kappa|/2$, the square root term is a pure imaginary number, thus adding an extra decay rate to the system eigenstates. A possible convention for the onset of the strong coupling regime can therefore be

$$\Omega_R > |\gamma - \kappa|/2. \tag{5.3}$$

In other words, strong coupling is reached when the Rabi splitting is large enough to produce a shift in the real part of the eigenenergies, by making the square root term in Eq. 5.2 a real positive number. This will be the convention used along this chapter.

As will be detailed below, the pumping scheme in this problem will be incoherent.

Thus, the equation of motion of this system is the Lindblad master equation,

$$\dot{\rho} = -i\,[H, \rho] + \kappa \mathcal{L}_a[\rho] + \sum_\alpha \gamma \mathcal{L}_{\sigma_\alpha}[\rho]. \tag{5.4}$$

The Lindblad terms $\mathcal{L}_a$ and $\mathcal{L}_{\sigma_\alpha}$, defined as in chapter 4, describe respectively the losses of the cavity mode and the QEs, with respective decay rates κ and γ. All the QEs are assumed to have the same decay rate, which is a combination of radiative decay, nonradiative decay, and dephasing processes, i.e., $\gamma = \gamma_\phi + \gamma_d = \gamma_\phi + \gamma_r + \gamma_{nr}$. The pure dephasing rate γ_ϕ describes an additional broadening of the spectral emission originating from exciton-photon interactions, usually a relevant process in organic compounds [352]. For simplicity, we now include the dephasing in the total rate γ, since the qualitative dependence of the exciton transport properties with the Rabi splitting Ω_R will remain unaltered. In the last section of this chapter (section 5.5), we analyze dephasing in more detail, focusing on its impact on the exciton transport in the strong coupling limit $\Omega_R \gg \gamma, \kappa$.

In order to study the transport of excitations along the chain of QEs, an exciton conductance is defined similar to the electrical conductance employed in charge transport problems. In order to do this, a pumping term will be added to introduce population into the system, eventually leading it to a steady state. Since in many cavities the most feasible situation is that of incoherent pumping [353–357], that will be the considered scenario. It is thus assumed that excitations are continuously pumped into the system through the first QE. As seen in the previous chapter, this incoherent pumping is represented by an additional Lindblad term $\gamma_p \mathcal{L}_{\sigma_1^\dagger}$, where γ_p represents the pump rate which will be considered weak along this chapter.

Once the pumping term is fixed, the steady state density matrix is calculated by setting $\dot{\rho} = 0$ in Eq. 5.4. In this situation, the rate of change of the total energy is also equal to zero [358],

$$\dot{E} = \frac{d}{dt}\langle H \rangle = \mathrm{Tr}\ [H\dot{\rho}] = 0. \tag{5.5}$$

This is a consequence of the fact that, in the steady state, the rate at which the system loses population due to the decay of both the cavity and the QEs is perfectly compensated by the excitation rate of the pump. This is evident when Eq. 5.4 together with the pumping term is introduced in the equation above, where the following relation for the steady-state density matrix ρ_{ss} is obtained,

$$\gamma_p \mathrm{Tr}\ H\mathcal{L}_{\sigma_1^\dagger}[\rho_{ss}] + \kappa \mathrm{Tr}\ H\mathcal{L}_a[\rho_{ss}] + \sum_\alpha \gamma \mathrm{Tr}\ H\mathcal{L}_{\sigma_\alpha}[\rho_{ss}] = 0. \tag{5.6}$$

Here, every term has a clear interpretation: the first Lindblad superoperator represents the population being introduced in the chain of QEs. The second and third terms can be identified with the loss of population due to cavity losses κ and decay rate γ in each emitter α. It is therefore possible to define the energy current between the last QE in the chain and its environment as the energy loss from such QE, i.e.,

$$J = \gamma \mathrm{Tr} H \mathcal{L}_{\sigma_N}[\rho_{ss}]. \tag{5.7}$$

The above quantity is related to the steady-state population of the $N-$th QE. Finally, the exciton conductance, σ_e (do not confuse with the spin operators σ_α) is defined as the above current normalized to the input power,

$$\sigma_e = J/\gamma_p. \tag{5.8}$$

This expression is very useful in the weak pumping limit, as the linear response of the system will be independent of γ_p.

5.2.2. Extraordinary exciton conductance.

So far, the system presented here is general since no assumptions have been made on the parameters of both cavity and QEs. In their original work, Feist and Garcia-Vidal now choose a specific physical system, by choosing the parameters of the QEs to match those of TDBC J-aggregates at room temperature, namely $\omega_m = 2.11$ eV, $\mu = 0.75e{\cdot}$nm, $\gamma_r = 1.32\mu$eV, $\gamma_{nr} = 1.1$meV, and $\gamma_\phi = 26.3$meV [311, 312, 315]. Note that in principle the coupling to the cavity could modify also the radiative decay rate into free space modes, γ_r. Here, however, this effect can be safely neglected since γ_r is extremely small, the main source of loss coming from non-radiative processes. The cavity frequency is left as a variable parameter for now, whereas its loss rate $\kappa = 13.2$meV is taken from the usual setups based on thin metallic mirrors [49]. Finally, the intermolecular distance between the QEs is set to $\delta x = 3$nm.

In order to obtain the steady state of the system, the open-source QuTiP package has been employed [359]. Since the interest is focused on the linear response of the system under weak pumping γ_p, the calculation is truncated to the zero- and single-excitation subspaces. Two different molecular configurations have been considered in the following results. First, a perfectly ordered distribution, where the molecule positions form a regular grid, and all the dipole moments are parallel to the cavity electric field. Second, a random arrangement in which Gaussian noise is added to both the positions and the

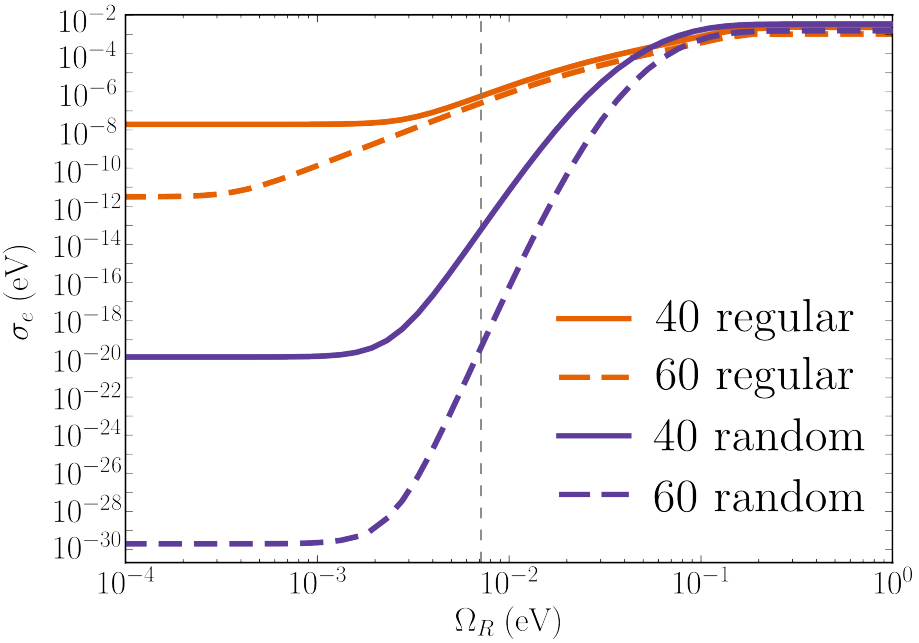

Figure 5.2: Exciton conductance for zero detuning ($\omega_c = \omega_m$), versus Rabi splitting Ω_R. The solid/dashed curves correspond to chains of $N = 40/N = 60$ QEs, in the regular (orange) and random (purple) configurations, respectively. The vertical dashed line indicates the onset of strong coupling according to Eq. 5.3, whereas the inset shows a zoom of the strong-coupling region.

dipole orientations of the QEs. Note that the latter is similar to an inhomogeneous broadening since, as no other cavity modes are considered, its only effect is to modify the ratio g_α/ω_α. As in the previous chapter, the calculations with the random configurations are repeated 10^4 times and averaged logarithmically.

The exciton conductance obtained for the case in which the cavity is in resonance with the QEs, $\omega_c = \omega_\alpha$, is displayed in Fig. 5.2 versus the total Rabi splitting. For this figure, the number of molecules has been fixed at either $N = 40$ (solid lines) or $N = 60$ (dashed lines), and Ω_R has been modified by changing the cavity electric field. This can be achieved in an experiment by, e.g., varying the separation between the cavity mirrors using a piezoelectric [360]. For all the curves in Fig. 5.2, the conductance has a constant value in the limit of small Rabi splittings, where the cavity mode does not play any role. In such scenario, the only conductance channel is provided by the dipole-dipole interactions. This is the reason behind the higher exciton conductance for the regular chains as opposed to the random arrangement, as the QE-QE hopping through dipole-dipole coupling is maximized when both dipoles are parallel. Another

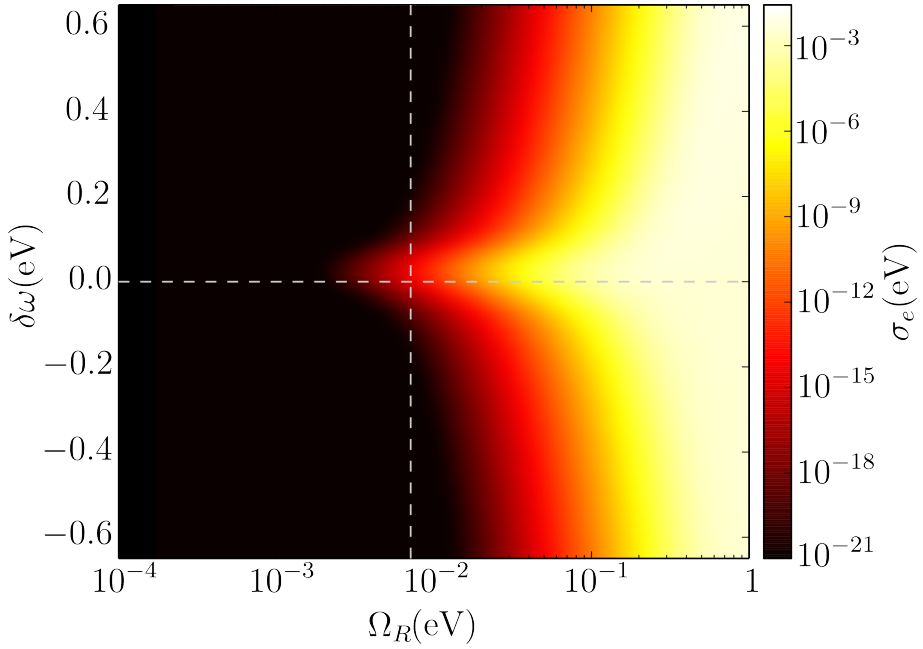

Figure 5.3: Exciton conductance as a function of the Rabi splitting Ω_R, and the detuning $\delta\omega$ between the cavity and the QEs. The dashed lines indicate $\delta\omega = 0$, and the onset of strong coupling.

factor contributing to this difference is the intrinsic Anderson delocalization induced in any disordered chain. Note that the exciton conductance in this limit decreases with the length of the chain N, as the excitons have to propagate along more QEs and, due to their lossy character, the probability of arriving to the end of the chain is reduced. This decrease in the conductance is very pronounced, making the transport largely inefficient over long distances. In fact, it can be easily demonstrated that the decrease of σ_e is exponential on the chain length. It can thus be concluded that in mesoscopic chains of $N \sim 10^3 - 10^6$ QEs the transport in the weak coupling regime is negligibly small.

The behavior of the conductance is very different in the strong coupling regime ($\Omega_R \gg \gamma, \kappa$). Here, the conductance increases significantly with respect to the weakly coupled case. Additionally, it becomes practicaly independent on Ω_R, indicating that dipole-dipole interactions play no role in the transport, which is in turn mediated by the well-formed delocalized system eigenstates. In the original work of Feist and Garcia-Vidal [138], the extraordinary increase in the exciton conductance was attributed to the formation of polaritons only but, as we will see below, the role of delocalized dark states could be relevant also in this system. However, even if the contribution of the dark states is important, the original argument is still valid in terms not only of polaritons

but of general delocalized eigenstates. The dependence with the number of molecules in the strong coupling case is polynomial ($\sim 1/N^2$), as the transport is due to the delocalization of the excitons along the chain. Before a full analytical deduction, we can intuitively understand this dependence by noting that, in strong coupling, the exciton does not have to jump along every QE to reach the end of the chain. Indeed, in this case there is a more efficient channel, namely to couple to the cavity mode at emitter 1, with probability $1/N$, and to couple back from the cavity mode to emitter N, with the same probability. Note also how the same argument can be used to explain why the strong coupling conductance in Fig. 5.2 is almost insensitive to disorder, since the cavity-mediated transport is independent of the configuration of the intermediate QEs.

In order to determine whether this conductance increase persists in the case of frequency mismatch between QEs and cavity, in Fig. 5.3 the exciton conductance is plotted versus the Rabi splitting and the detuning $\delta\omega = \omega_m - \omega_c$. As we have justified in the previous chapter, for large detunings the effective light-matter couplings decrease. Thus, as one would expect, the onset of strong coupling is achieved for larger Rabi splittings in the case of finite $|\delta\omega|$. Despite this fact, the final value of the exciton conductance remains independent on the detuning. This again indicates that the conduction proceeds through the delocalized eigenstates, which are only fully formed when the Rabi frequency Ω_R becomes large enough to not only overcome decoherence processes, but also the detuning. Once the polaritons and dark states are formed, their character does not strongly depend on the detuning. Note that a possible application as an exciton switch can be conceived from these results. Indeed, at some regions in Fig. 5.3, a small change of the detuning induces a strong decrease in the exciton conductance. This enables the control of the exciton transport properties through an external modification of the detuning, which can be achieved e.g. by dynamically varying the length of the cavity.

5.2.3. Analytical model.

In order to fully understand the phenomenon of extraordinary exciton conductance and demonstrate that it is due to the intrinsic delocalization of the eigenstates, a simple model has been developed. It is clear that only two possible channels exist for the propagation of excitations, namely the direct transport through dipole-dipole coupling, and the cavity-mediated transport. While the first one dominates in the weak coupling regime, the conductance through the delocalized channels should increase polynomially with the Rabi splitting and saturates in the strong coupling limit. The model thus simplifies the problem by isolating both effects and solving them independently. For the dipole-

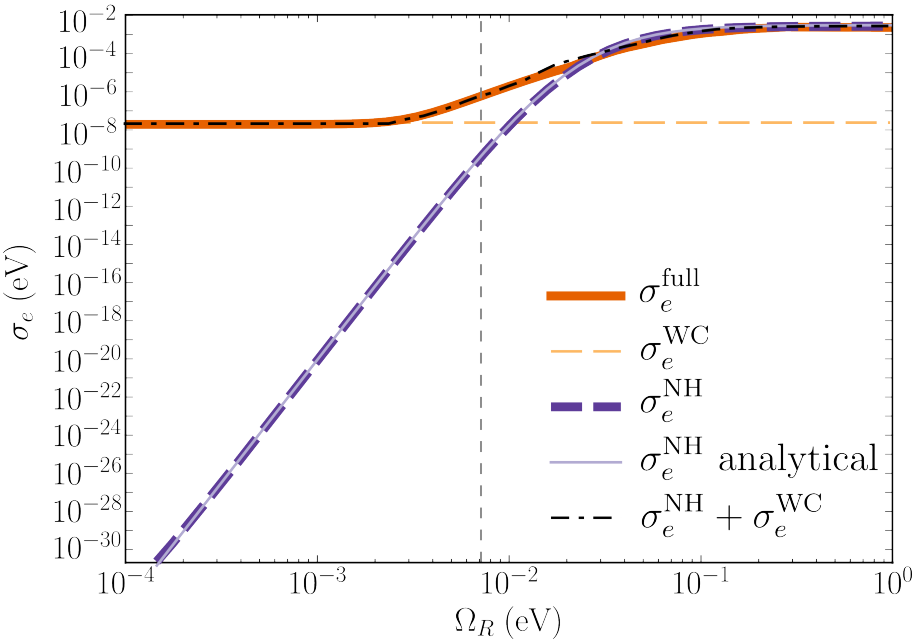

Figure 5.4: Exciton conductance ($N = 60$) calculated with the full model (solid orange line), and different approximations. The two purple lines are obtained in the absence of dipole-dipole interaction, both numerically (dashed) and analytically according to Eq. 5.10 (thin solid). The orange dashed line represents the solution only with dipole dipole interaction (i.e., $\Omega_R = 0$).

dipole channel, the Rabi splitting is set to 0 and the resulting conventional tight-binding problem is solved to determine the weak coupling conductance $\sigma_e^{\text{WC}}{=}\sigma_e(\Omega_R{=}0)$. On the other hand, for the cavity-mediated channel, an analytical solution is also achieved in the limiting case of a regular chain with zero dipole-dipole coupling. As mentioned above, in this case the Hamiltonian in Eq. 5.4 is that of the Dicke model. In such a simple situation, all the QEs except the one being pumped are indistinguishable and thus obey the exact same dynamics. This symmetry is extremely useful since it allows for writing the steady-state density matrix in a very simple way,

$$\rho_{ss} = \begin{pmatrix} \rho_{00} & 0 & 0 & 0 & 0 & 0 & 0 \\ 0 & \rho_{cc} & \rho_{c1} & \rho_{c2} & \cdots\cdots\cdots & & \rho_{c2} \\ 0 & \rho_{c1}^* & \rho_{11} & \rho_{12} & \cdots\cdots\cdots & & \rho_{12} \\ 0 & \rho_{c2}^* & \rho_{12}^* & \rho_{22} & \rho_{23} & \cdots & \rho_{23} \\ 0 & \vdots & \vdots & \rho_{23}^* & \ddots & \ddots & \vdots \\ 0 & \vdots & \vdots & \vdots & \ddots & \ddots & \rho_{23} \\ 0 & \rho_{c2}^* & \rho_{12}^* & \rho_{23}^* & \cdots & \rho_{23}^* & \rho_{22} \end{pmatrix}. \tag{5.9}$$

In the equation above, the coherences between the ground and any state are zero since no initial correlations are present. Note that the equivalence of all emitters reduces the problem to the calculation of 12 independent real variables. First, the four populations, namely ρ_{00} for the ground state (no photons or excitons), ρ_{cc} as the cavity occupation, and ρ_{ii} as the exciton population of molecule $i = 1, 2$. Second, the real and imaginary parts of the four relevant coherences $\{\rho_{c1}, \rho_{c2}, \rho_{12}, \rho_{23}\}$. The steady state density matrix is then obtained from $\dot{\rho}_{ss} = 0$, by solving for the null space of the Liouvillian and subsequently normalizing to $\mathrm{Tr}\rho_{ss} = 1$. Finally, the exciton conductance in the absence of hopping, σ_e^{NH}, is determined from Eq. 5.8 which, in the linear response limit of weak driving and for zero detuning $\omega_c = \omega_m$, reads

$$\sigma_e^{NH}\big|_{\delta\omega=0} = \frac{\gamma}{\gamma_p}\left(\frac{\Omega_R}{2\sqrt{N}}\mathrm{Re}(\rho_{c2}) + \omega_m\rho_{22}\right)\Bigg|_{\delta\omega=0} = \frac{(\gamma+\Gamma)\omega_m\Omega_R^4}{(2\Gamma\gamma+\Omega_R^2)\,\Gamma N^2\,(\kappa\gamma+\Omega_R^2)}, \quad (5.10)$$

where the total decoherence rate is defined as $\Gamma = \gamma + \kappa$.

Figure 5.4 shows the conductance calculated for the two different channels. In the weak coupling limit, the result obtained with the full model (orange curve) is extremely well approximated by the hopping channel only (orange dashed line). Additionally, the analytical formula Eq. 5.10 fits the strong coupling results but, due to the absence of dipole-dipole interaction, decreases polynomially for small Rabi splittings. The independence of the two transport channels is further verified by plotting the sum of both contributions (dash dotted black line). Since this quantity agrees excellently with the full result, the two different channels are demonstrated to be independent. The analytical expression Eq. 5.10 also contains very useful information about the system, since in the strong coupling limit it reproduces the numerical conductance profile. For small Rabi splittings the conductance increases as the fourth power of Ω_R, whereas for large Rabi splittings it saturates to $(\gamma+\Gamma)\omega_m/(\Gamma N^2)$. Notice how in this limit the decay of σ_e with the number of QEs is $\sim N^{-2}$, much better than the exponential decay displayed in the weak coupling regime.

5.2.4. Role of the dark states in the extraordinary exciton conductance.

The original work by Feist and Garcia-Vidal demonstrates that the onset of strong coupling can dramatically enhance exciton transport. When the Rabi splitting is large, the polaritons are able to avoid direct transport by hopping along the chain, by instead coupling to the delocalized eigenstates and *jumping* directly to the end of such chain. Although in principle this work associated the conductance enhancement to the polaritons

only, we know from chapter 4 that dark states can play a very relevant role in the exciton delocalization process, at least in the case of coherent pumping. The question naturally arises as to what is the relevance of such dark states in the present, incoherently pumped system.

To study the contribution of both polaritons and dark states to the exciton conductance, we make use of an alternative strategy to calculate their different contributions to the conductance in Eq. 5.10. We consider the strong coupling limit, where dipole-dipole interactions can be neglected. As we have already mentioned, in such regime only two states are completely defined, namely the upper and lower polaritons

$$|\epsilon_{\pm}\rangle = \frac{1}{\sqrt{2}}\left(|B\rangle \pm a^{\dagger}|0\rangle\right) = \frac{1}{\sqrt{2}}\left(\frac{1}{\sqrt{N}}\sum_{j}\sigma_{j}^{\dagger}|0\rangle \pm a^{\dagger}|0\rangle\right), \tag{5.11}$$

whereas the remaining dark subspace is degenerate and arbitrary, the only constraint being orthogonality with respect to the polaritons. Hence, by noting that the pumping is located in a single QE, we choose one of the dark states $|D\rangle$ such that it receives all the probability pumped into the dark subspace. It is simple to demonstrate that such state reads

$$|D\rangle = \sqrt{\frac{N-1}{N}}\left(\sigma_{1}^{\dagger} - \frac{1}{N-1}\sum_{\alpha=2}^{N}\sigma_{\alpha}^{\dagger}\right)|0\rangle. \tag{5.12}$$

The remaining $N-2$ dark states, $|D_k\rangle$ $(k = 1, ...N-2)$ remain arbitrarily defined aside from the orthogonality conditions $\langle D_k|B\rangle = \langle D_k|D\rangle = 0$.

By definition, the excited state of the first QE can be expressed as a sum of only $|D\rangle$ and the bright state $|B\rangle = \sum_j \sigma_j^{\dagger}|0\rangle/\sqrt{N}$, i.e.,

$$\sigma_{1}^{\dagger}|0\rangle = \frac{1}{\sqrt{N}}\left(|B\rangle + \sqrt{N-1}|D\rangle\right). \tag{5.13}$$

In other words, by choosing this convention, the pumping introduces population only in the above two states. As a consequence, the whole system dynamics will take place in the 4-dimensional subspace span by $\{|0\rangle, |\epsilon_+\rangle, |\epsilon_-\rangle, |D\rangle\}$, whereas the states $|D_k\rangle$ will remain unpopulated. In such situation, the contribution of the polaritonic and dark state channels can be determined by solving for the steady-state density matrix only in the populated subspace, which reads

$$\rho_{ss} = \begin{pmatrix} \rho_{00} & 0 & 0 & 0 \\ 0 & \rho_{DD} & \rho_{D+} & \rho_{D-} \\ 0 & \rho_{D+}^{*} & \rho_{++} & \rho_{+-} \\ 0 & \rho_{D-}^{*} & \rho_{+-}^{*} & \rho_{--} \end{pmatrix}. \tag{5.14}$$

Since in such basis no other state contributes to the dynamics, the problem is reduced to a 16×16 Liouvillian which can be analytically solved. The exciton conductance in this case is expressed as a sum of six contributions,

$$\begin{aligned}\sigma_e &= \sigma_{DD} + \sigma_{++} + \sigma_{--} + \sigma_{D+} + \sigma_{D-} + \sigma_{+-} = \\ &= \frac{\gamma_d \omega_0}{\gamma_p N}\left(\frac{1}{N-1}\rho_{DD} + \sum_{\alpha=\pm}\left[\frac{\rho_{\alpha\alpha}}{2} - \sqrt{\frac{2}{N-1}}\mathrm{Re}[\rho_{D\alpha}]\right] + \mathrm{Re}[\rho_{+-}]\right).\end{aligned} \tag{5.15}$$

It can be checked that the above relation is completely equivalent to the result obtained in Eq. 5.10. Here, the crossed terms associated with the coherences read

$$\sigma_{+-} = \frac{\gamma_d \kappa \omega_0}{2N^2(\gamma_d \kappa + \Omega_R^2)}, \tag{5.16}$$

$$\sigma_{D+} + \sigma_{D-} = -\frac{4\gamma_d \Gamma \omega_0}{N^2(2\gamma_d \Gamma + \Omega_R^2)}. \tag{5.17}$$

Interestingly, the coherence between both polaritons increases the conductance whereas that between dark state and polaritons tends to decrease it. Note that, in the intermediate and strong coupling regimes, $\Omega_R > \gamma_d, \kappa$, all the above terms become negligible as they decrease as Ω_R^{-2}. This is a very convenient result since, in such regime, it allows to write the conductance as a sum of three independent contributions,

$$\sigma_e(\Omega_R > \gamma_d, \kappa) \approx \sigma_{++} + \sigma_{--} + \sigma_{DD} \equiv \sigma_{pol} + \sigma_{DD}. \tag{5.18}$$

The different terms above are clearly independent and identifiable contributions, namely the conductance associated with the polaritonic channel $\sigma_{pol} = \sigma_{++} + \sigma_{--}$, and that associated with the dark states, σ_{DD}. These two contributions to the conductance read

$$\sigma_{DD} = \frac{\omega_0}{N^2}, \tag{5.19}$$

$$\sigma_{pol} = \frac{\gamma_d \omega_0 (\kappa\Gamma + 2\Omega_R^2)}{2N^2\Gamma(\gamma_d \kappa + \Omega_R^2)}. \tag{5.20}$$

Note how the conductance through the dark state channel is not affected by the cavity losses, as these states do not have a photonic component.

It is interesting to analyze the above two contributions to the exciton conductance in the strong coupling limit $\Omega_R \gg \kappa, \gamma_d$. Here, both terms reach a constant value given by

$$\sigma_{pol}(\Omega_R \gg \kappa, \gamma_d) = \frac{\omega_0}{N^2}\frac{\gamma_d}{\gamma_d + \kappa} \quad ; \quad \sigma_D(\Omega_R \gg \kappa, \gamma_d) = \frac{\omega_0}{N^2}. \tag{5.21}$$

This surprising result shows that the polaritonic contribution to the conductance is, in the best case scenario $\kappa \ll \gamma_d$, equal to that of the dark states. On the other hand, in the

opposite limit $\kappa \gg \gamma_d$, the transport is practically mediated by the dark states alone. This is a relevant result as it shows that, even in the incoherent pumping case, the dark states have a large contribution in the delocalization of the system eigenstates. For the specific parameters of the cavity setup chosen by Feist and Garcia-Vidal, $\gamma_d/(\gamma_d + \kappa) \approx 0.07$, roughly 93% of the conductance would be provided by the dark states. In the limit of lossy cavities such as e.g. plasmonic nanoparticles, this fraction would be much larger. The demonstration of the important contribution of the dark states generalizes the main result obtained in chapter 4 to the case of incoherent pumping. As we will discuss below, the contribution of the dark states will give rise to complex dynamics when molecular dephasing is introduced. It is important to emphasize that, regardless of the specific role of the dark states in the phenomenon of extraordinary exciton transport, the argument based on delocalized eigenstates in the original work by Feist and Garcia-Vidal remains valid.

5.3. Modifying the exciton conductance profile with inhomogeneous fields.

The phenomenon of exciton transport is of general character since the model Hamiltonian is applicable to many systems. This suggests that the extension of this principle to more complex nanostructures could improve the exciton transport properties. Specifically, it would be desirable to increase the exciton population at the two ends of the chain instead of distributing it homogeneously as we have shown in this section. A possible way of achieving such a modulation of the exciton population is by coupling the QEs to spatially inhomogeneous fields. This could in turn be advantageous from the point of view of exciton harvesting, provided one achieves a population increase in a very narrow region of space. Inspired by these ideas, we devote this section to a deeper study of the exciton transport phenomenon, this time in more complex nanostructures. First, we will illustrate our model nanostructure, namely a plasmonic nanoparticle, and determine the relevant parameters in the Hamiltonian. Second, the results for the exciton conductance will be shown, demonstrating how such conductance follows the field intensity profile. We then deduce an analytical expression which captures such dependence. Finally, by means of studying the time evolution of the system, we demonstrate how the onset of strong coupling also implies a much faster transport of excitons as the relevant timescale drastically changes.

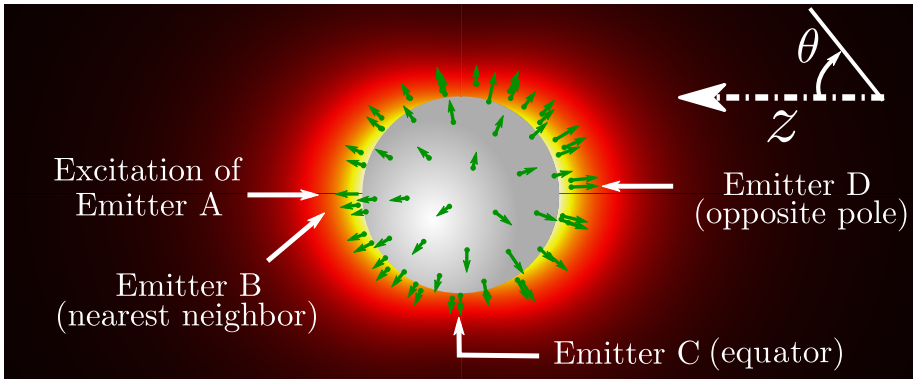

Figure 5.5: Sketch of the system under study. An ensemble of N QEs is coupled to a silver nanosphere with radius $R = 10$nm. One of the QEs, named A, is incoherently pumped. The background shows the electric field intensity profile for one of the three dipole plasmon modes coupled to the QEs. We will study the conductance as a function of the polar angle θ, defined from the pumping point.

5.3.1. The model system and methods.

Since ideally our objective is to tailor the exciton conductance at the subwavelength scale, plasmonic structures represent one of the best possibilities. We will therefore focus on plasmonic nanoparticles, although our results will be independent on the particular system. The first structure under study is a spherical plasmonic nanoparticle as shown in Fig. 5.5. The nanosphere (NS) has a radius $R = 10$nm, and is surrounded by a layer of N QEs placed at a distance $h = 1$nm above from the metallic surface. Note that in chapter 6 we have argued that at QE-metal distances smaller than ~ 10nm the emission into either plasmon or radiative modes is strongly quenched due to ohmic losses. In a nanoparticle, such fast nonradiative decay is associated with the higher multipole modes forming a wide band in the spectrum [361]. However, this has been demonstrated not to occur for the CSC of N QEs, where the dipolar plasmon resonance becomes the most relevant, and the higher multipoles merely add an effective detuning to the hybrid mode [297]. Therefore, we can approximate the nanosphere by the three degenerated dipolar LSP (Localized surface plasmon) modes (x, y, z), characterized by a frequency ω_p and a loss rate κ.

The quantum emitters surrounding the NS are modelled as point dipoles in the same fashion as in the previous chapter. For simplicity, they will be oriented along the radial direction and have the same transition frequency ω_0, dipole moment $\vec{\mu}$, and total decoherence rate $\gamma = \gamma_\phi + \gamma_d$, where γ_ϕ and $\gamma_d = \gamma_r + \gamma_{nr}$ have been defined in the previous

section. For the sake of illustration, we take the same parameters as in the previous section, corresponding to TDBC J-Aggregates at room temperature, i.e., $\omega_0 = 2.11$eV, $\mu = 0.75e{\cdot}$nm, $\gamma_r = 1.32\mu$eV, $\gamma_{nr} = 1.1$meV, and $\gamma_\phi = 26.3$meV. The system Hamiltonian is given by Eq. 4.1, which in this case reads

$$H = \omega_0 \sum_j \sigma_j^\dagger \sigma_j + \omega_{pl} \sum_{\alpha=x,y,z} a_\alpha^\dagger a_\alpha + \sum_{i\neq j} V_{ij}(\sigma_i^\dagger \sigma_j + H.c.) + \sum_{j,\alpha}(g_{j\alpha}\sigma_j^\dagger a_\alpha + H.c.), \quad (5.22)$$

where the coupling rate $g_{j\alpha}$ is proportional to the electric field profile of the corresponding LSP mode.

In order to work with the above Hamiltonian, we must determine the LSP mode properties, namely ω_p, κ, and the electric field profile which will allow us to calculate the coupling $g_{j\alpha}$. These modal properties can be extracted by means of the approximate quantization for lossy systems described in the previous chapter. However, here we will employ a more convenient analytical approach valid for the quantization of dipolar modes of small spherical nanoparticles. Such analytical deduction is based on comparing the classical and quantum values of the nanosphere polarizability α. For a small metallic sphere of permittivity $\varepsilon(\omega)$ and radius R, the classical static polarizability is given by [362]

$$\alpha_{cl} = 4\pi\varepsilon_0\varepsilon_d R^3 \frac{\varepsilon(\omega) - \varepsilon_d}{\varepsilon(\omega) + 2\varepsilon_d}, \quad (5.23)$$

being ε_d the permittivity of the surrounding dielectric. Here, we can approximate the permittivity of silver by a Drude model,

$$\varepsilon(\omega) \approx \varepsilon_\infty - \frac{\omega_p^2}{\omega(\omega + i\gamma_D)}, \quad (5.24)$$

where the parameters $\varepsilon_\infty = 3.91$, $\omega_p = 8.833$eV, and $\gamma_D = 0.0553$eV can be obtained from the literature [306]. By defining a resonance frequency $\omega_r = \omega_p/\sqrt{\varepsilon_\infty + 2\varepsilon_d}$ we can arrive after some algebra to the following expression [339],

$$\alpha_{cl} \approx -2\pi\varepsilon_0\varepsilon_d R^3 \frac{3\varepsilon_d}{\varepsilon_\infty + 2\varepsilon_d} \frac{\omega_r^2}{\omega(\omega - \omega_r + i\gamma_D/2)}, \quad (5.25)$$

which is valid in the vicinity of a narrow resonance, i.e., $\omega \approx \omega_r \ll \gamma_D$. This equation has the same form as the polarizability of a quantum two-level system with dipole moment μ, frequency ω_0 and linewidth γ_0, which close to a narrow resonance reads [21]

$$\alpha_q = \frac{\mu^2}{\hbar} \frac{2\omega_0}{\omega_0^2 - (\omega + i\gamma_0/2)^2} \approx -\frac{\mu^2}{\hbar} \frac{\omega_0}{\omega\,(\omega - \omega_0 + i\gamma_0/2)}. \quad (5.26)$$

By direct comparison of the two above expressions, we obtain the frequency and decay rate of the LSP modes as $\omega_\alpha = \omega_r \approx 0.16\sqrt{\varepsilon_d}$ and $\kappa = \gamma_D \approx 0.06$eV, respectively. In

our problem, we will choose the permittivity of the surrounding dielectric as $\varepsilon_d = 6.8$, so that the LSPs are in resonance with the QEs. Additionally, from the comparison of the polarizabilities we can deduce the following expression for the dipole moment of a nanosphere in a quantum model:

$$\mu_{pl} = \left(\hbar \omega_{pl} \frac{6\pi\varepsilon_0 \varepsilon_d^2 R^3}{\varepsilon_\infty + 2\varepsilon_d} \right)^{1/2} . \tag{5.27}$$

The classical electric field produced by the above dipole corresponds to the quantum field of the LSP mode, which allows us to calculate the LSP-QE couplings. This simple analytical approach can be checked to give the same results as the approximate quantization scheme employed for more complex plasmonic structures in the previous chapter.

Once the Hamiltonian is fully determined, we study the exciton transport by determining the steady state of the system, initially in its ground state, under incoherent pump of a single QE, which will be labelled A (see Fig. 5.5). The steady-state density matrix is obtained in an analogous way as in the previous section, namely by solving the Lindblad equation

$$\dot{\rho}_{ss} = 0 = -i[H, \rho_{ss}] + \sum_j \gamma \mathcal{L}_{\sigma_j} + \sum_\alpha \kappa \mathcal{L}_{a_\alpha} + \gamma_p \mathcal{L}_{\sigma_A^\dagger}. \tag{5.28}$$

Once the steady-state density matrix is calculated, we define a generalized exciton conductance from emitter A to any emitter j in the ensemble,

$$\sigma_e^j = \lim_{\gamma_p \to 0} \frac{\gamma}{\gamma_p} \mathrm{Tr}\left(H \mathcal{L}_{\sigma_j}[\rho_{ss}] \right) . \tag{5.29}$$

In the equation above, we have explicitly written the limit $\gamma_p \to 0$ to emphasize that, in an analogous way as in the problem of exciton transport, we work in the weak pump regime.

5.3.2. Steady-state results and exciton-plasmon dynamics.

Our results for the exciton conductance in the single nanosphere case are shown in Fig. 5.6, for QEs at three representative positions, B, C, and D, as depicted in Fig. 5.5. Such positions correspond respectively to the first neighbour of emitter A, a QE located at a polar angle $\theta = \pi/2$ away from A, and the farthest QE from A. The plot shows the evolution of the conductances versus the Rabi splitting which, for simplicity, is varied artificially here instead of e.g. by increasing the number of QEs. Clearly, the onset of strong coupling separates two distinct regimes. In the weak coupling limit, the spread of

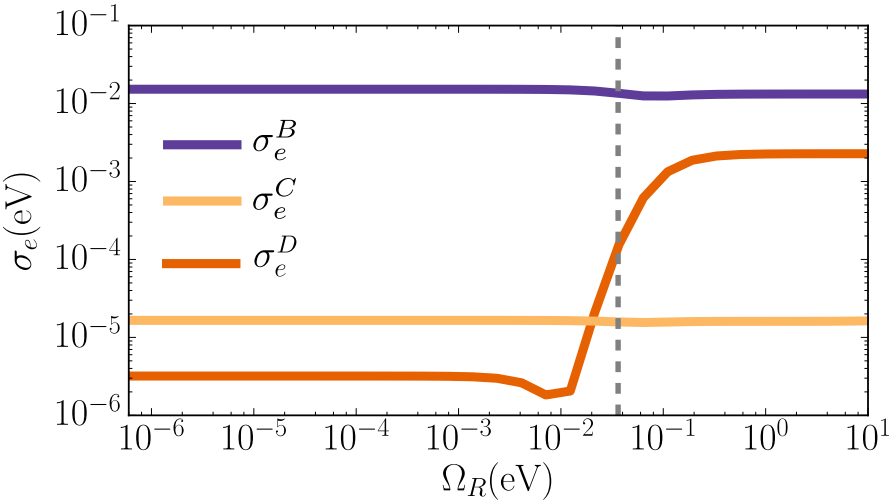

Figure 5.6: Exciton conductance at three different QEs ($N = 100$), placed at positions B (purple), C (light orange), and D (dark orange) as defined in Fig. 5.5, as a function of the total Rabi splitting. The dashed grey line marks the onset of strong coupling, $\Omega_R = |\gamma - \kappa|/2$.

the excitons among the ensemble of QEs is mediated by dipole-dipole interactions and thus diffusive, producing a rapid decrease of the conductance for QEs far away from the pump. The only factor determining the transport efficiency to an emitter j in this case is its distance to the pumped emitter, A. As a consequence, we have $\sigma_e^B > \sigma_e^C > \sigma_e^D$. However, when the strong coupling regime is accessed, the transport is mediated by the delocalized system eigenstates, which become the only relevant transport as we have already seen. In this particular case, the pumped QE (A) is able to couple only to one of the three dipolar LSP modes of the NS, since its dipole moment is oriented radially. The electric field intensity corresponding to such mode is displayed in the background of Fig. 5.5. Interestingly, since such field profile is very small at the position C, so is the coupling constant $g_{C\alpha}$. As a consequence, the conductance for emitters at these positions does not vary appreciably from weak to strong coupling. On the other hand, the pole-to-pole conductance σ_e^D increases by three orders of magnitude as the LSP field intensity is very large at the positions of both A and D. For an emitter at position B, the conductance slightly decreases with the onset of the strong coupling, as the exciton is more distributed among the ensemble of QEs than in the weak coupling case. Note, finally, that according to our simple model in the previous section, the strong coupling delocalization in this case is mainly mediated by the dark states, since the loss rate of the EM modes is very large.

The above results suggest that the exciton conductance profile mimics the field inten-

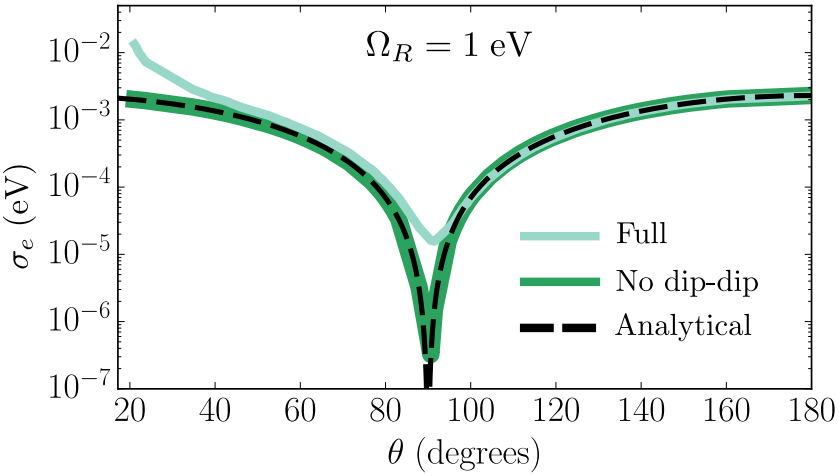

Figure 5.7: Angular dependence of the exciton conductance for the single NS ($N = 100$). The light green line shows the results obtained within the full model, whereas the dark green line has been obtained by neglecting dipole-dipole interactions. For comparison, we plot the analytical approximation obtained in Eq. 5.34 (dashed black line).

sity of the relevant mode, which in this case is the $z-$dipolar LSP mode coupling to the emitter A (see Fig. 5.5). The orthogonal modes x and y seem not to play a relevant role in the dynamics, since the emitter C is barely affected by the onset of strong coupling. These hypotheses are confirmed by the results in Fig. 5.7, which display the strong coupling exciton conductance ($\Omega_R = 1$eV) of all QEs, as a function of their angular position θ. Note how the full calculation (light green line) displays a cosine-like profile identical to that of the LSP dipole mode. The predominant role of the LSP-mediated transport is confirmed by the fact that the results without dipole-dipole interaction (dark green line) coincide very well with the full calculation, apart from a slight deviation at small angles caused by the extra diffusive channel. Both curves show a dip at $\theta = \pi/2$, evidencing that the orthogonal x and y LSP dipole modes do not play a relevant role in the dynamics. Our results confirm that, due to the inhomogeneous field profile, the exciton transport is position-dependent, mimicking the field intensity profile.

5.3.3. Analytical model for the steady-state conductance.

The above results show that, in the strong coupling regime, we can safely neglect both the dipole-dipole interaction and the two LSP modes orthogonal to the dipole moment of emitter A. In this limit, we can find an analytical expression for the exciton conductance. Since in the present case the electric field profile is not homogeneous, the QEs are not

identical and the density matrix cannot be written in the form of Eq. 5.9. Therefore, we employ the already discussed alternative approach based on an adequate election of the basis for the dark subspace. We start by writing the Hamiltonian in this simplified model as

$$H = \omega_0 \sum_j \sigma_j^\dagger \sigma_j + \omega_{pl} a^\dagger a + \sum_j (g_j \sigma_j^\dagger a + H.c.), \tag{5.30}$$

where the bosonic operator a refers to the main (z) dipole mode of the NS. The above expression has the form of the Tavis-Cummings Hamiltonian studied in the previous chapter (Eq. 4.5). We have demonstrated that, in this situation, the plasmonic mode only couples to a bright state given by Eq. 4.6,

$$|B\rangle = \frac{2}{\Omega_R} \sum_\alpha g_\alpha \sigma_\alpha^\dagger |0\rangle, \tag{5.31}$$

where the Rabi splitting is given by $\Omega_R = 2\sqrt{\sum_j |g_j|^2}$. The remaining $N-1$ dark states are in principle arbitrarily chosen, and we use this freedom to our advantage. As in our problem we pump the first molecule (state $\sigma_A^\dagger |0\rangle$), we choose the dark states such that this pumping only excites one of them, which we name $|D\rangle$. It is straightforward to prove that

$$|D\rangle = \frac{2}{\Omega_R} \left(G\sigma_A^\dagger - \sum_{j \neq A} \frac{g_1^* g_j}{G} \sigma_j^\dagger \right) |0\rangle \,, \tag{5.32}$$

where we have defined $G^2 = (\Omega_R/2)^2 - g_A^2$ for simplicity. Note that this state automatically fulfils $\langle D|B\rangle = 0$ and, for equal couplings ($g_j = g$) it is equivalent to Eq. 5.12. As in the case of homogeneous field profile studied above, the remaining dark states $\{|D_k\rangle ; k = 1, ...N-2\}$ are still arbitrary, provided that they fulfil the orthogonality conditions $\langle D_k|B\rangle = \langle D_k|D\rangle = 0$. Because of this partial choice of basis, the states $|D_k\rangle$ are not coupled to the pumped state, $\langle D_k|\sigma_A^\dagger|0\rangle = 0$, and hence do not take part in the dynamics. The time evolution of the system is thus restricted to the 4-dimensional subspace spanned by the states $\{|0\rangle, |B\rangle, |D\rangle, a^\dagger |0\rangle\}$, and the master equation reduces to a 16×16 linear system.

Thanks to the above simplification, we are able to calculate the steady-state density matrix analytically, from which it is straightforward to obtain the exciton conductance,

$$\begin{aligned} \sigma_e(j) = &-16|g_j|^2|g_A|^2 \times \\ &\times \frac{\gamma\delta(\kappa\Omega_R^2 + 4\gamma\Gamma^2) + \omega_0 \left(\Omega_R^2\Gamma(\Gamma+\gamma) - 2\gamma(2\gamma^3 + 5\kappa\gamma^2 - 4\delta^2\kappa + 4\gamma\kappa^2 + \kappa^3)\right)}{\left(-\Omega_R^4 + 4\gamma(4\delta^2 + \Gamma^2)\right)\left(\Omega_R^2\Gamma^2 + \gamma\kappa(4\delta^2 + \Gamma^2)\right)}, \end{aligned} \tag{5.33}$$

where we have defined the detuning $\delta = \omega_{pl} - \omega_0$. In our problem, the LSP dipole mode is resonant with the frequency of the QEs, and the above expression is reduced to

$$\sigma_e(j) = 16|g_j|^2|g_A|^2 \frac{\omega_0\,(\Gamma+\gamma)}{\Gamma\,(\Omega_R^2+\gamma\kappa)\,(\Omega_R^2+2\gamma\Gamma)}, \tag{5.34}$$

which is a generalization of the analytical result obtained for a homogeneous EM field profile, Eq. 5.10. In Figure 5.7 we show how the analytical expression 5.34 (black dashed line) is able to reproduce very well the exciton conductance profile. Note that the deduction of the above equation is completely analogous to the procedure followed in section 5.2.4 for an homogeneous field profile. It is thus straightforward to express the exciton conductance as a sum of independent contributions as in Eq. 5.18, demonstrating that dark states play a major role in the exciton dynamics also for inhomogeneous field distributions.

Additionally, we can easily generalize the above result for a more realistic scenario in which the pumping and collection are not realized at single QEs, but on several emitters located inside a pump region S_A and a collection region S_j, respectively. Assuming both pumping and collection areas do not overlap significantly, we obtain with an analogous method a conductance

$$\sigma_e(j) = \eta_A\eta_j \frac{\omega_0\,(\Gamma+\gamma)\,\Omega_R^4}{\Gamma\,(\Omega_R^2+\gamma\kappa)\,(\Omega_R^2+2\gamma\Gamma)}. \tag{5.35}$$

Here, the only position-dependent quantities are $\eta_X = 4\sum_{j\in S_X}|g_j|^2/\Omega_R^2$, which determine the contribution of the QEs involved in the pumping (η_A) or collection (η_D) processes to the total Rabi splitting. Both η_A and η_D are independent of N for uniform distributions of emitters.

The two analytic formulas we have obtained, Eqs. 5.34 and 5.35, clearly demonstrate that the steady-state exciton conductance mimics the field intensity profile through the couplings $g_j \propto \mathbf{E}(\mathbf{r}_j)$. Specifically, apart from a constant factor, a high conductance σ_e is achieved by optimizing two relevant values of the modal electric field. First, $\mathbf{E}$ has to be large in the pumped region, so that the population introduced through the pumping can efficiently couple to the EM modes. Second, it has to be large in the collection region, since otherwise the EM mode cannot deliver such population. In general, thus, the exciton population profile is inhomogeneous, as the excitons gather in the regions of larger field intensity. Note that again this is a consequence of the eigenstate delocalization, since the bright and dark states Eqs. 5.31 and 5.32 have larger contributions from QEs placed in the largely coupled areas.

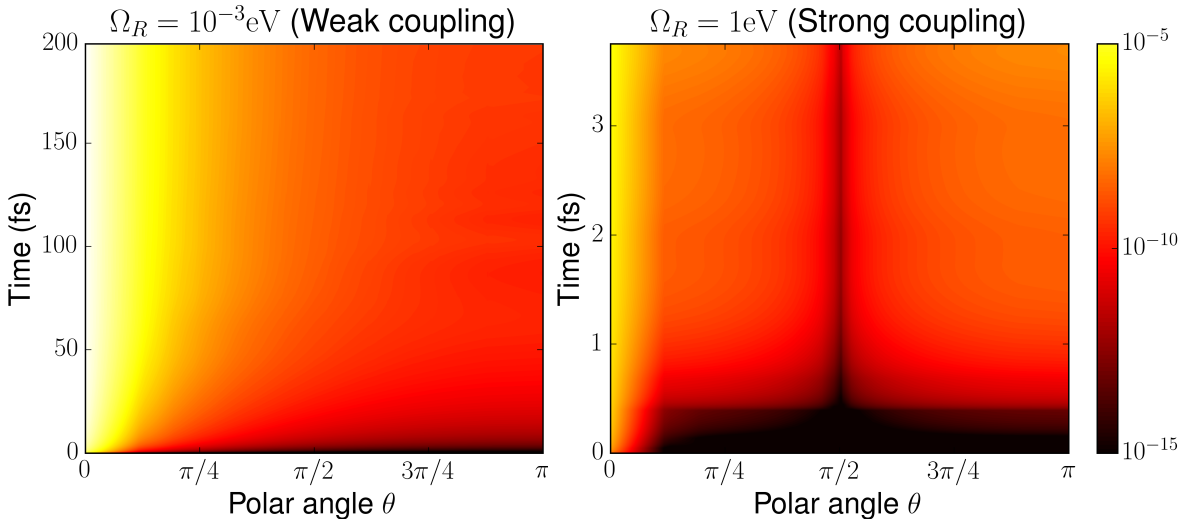

Figure 5.8: Time evolution of the incoherently pumped single-NS system, initially in the ground state $|0\rangle$. Left/right panels show the populations of all QEs as a function of time and their polar angle θ, on the weak/strong coupling regimes.

5.3.4. Time dynamics.

So far, along our search for an efficient nanostructure to achieve exciton harvesting, we have demonstrated how the steady-state exciton conductance mimics the field intensity profile. For most of the potential applications of an enhanced excitonic transport, not only the steady-state distribution of the population is important, but also the characteristic timescale in which such distribution builds up. It is thus convenient to perform a brief analysis on the time dynamics of the system under study.

In order to analyze the system dynamics, we can determine how the incoherently pumped system evolves into the steady-state. This is done by directly solving the time-dependent Schrödinger equation for the pumped system initially in the ground state, $|0\rangle$. Our results are displayed in Fig. 5.8, where the evolution of the system is studied in the weak and strong coupling regimes (left and right panels, respectively). Note how, in both cases, the plot does not change for long times as the steady-state is reached. Also, it is clear how in the weak coupling regime the exciton population is largely concentrated around the pump region, due to the diffusive character of the transport. On the other hand, in the strong coupling regime the population is more homogeneously distributed, with a characteristic dip at $\theta = \pi/2$ due to the cosine-like profile of the main LSP mode. Strikingly, the timescales associated with each regime are completely different. Whereas the steady-state in the weak coupling regime is formed on a timescale of $\kappa^{-1} \approx 50$ fs, in

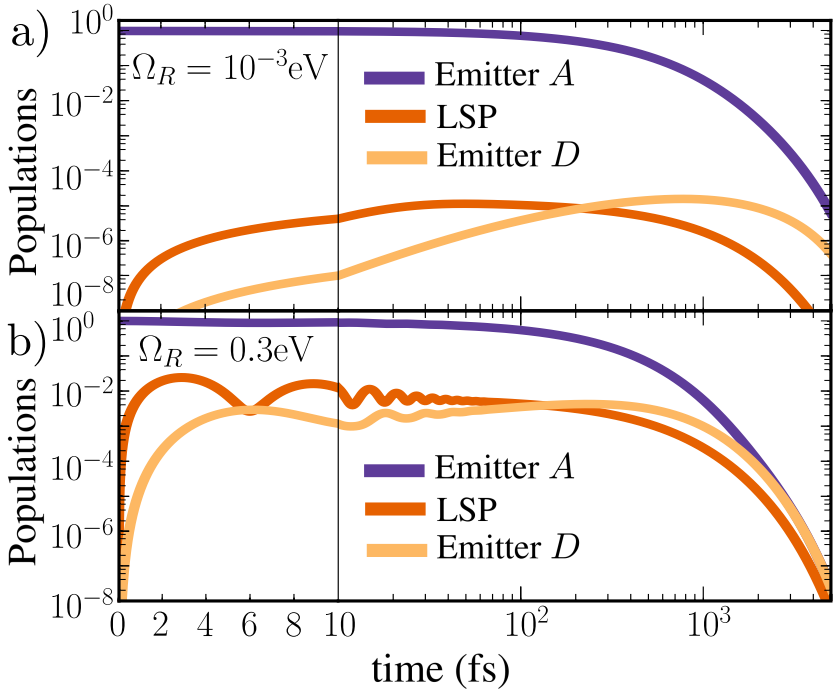

Figure 5.9: Time evolution of the populations in the single-NS system, for an initially excited emitter A in the absence of pumping. We render the population of emitters A and D (purple and light orange lines, respectively), and the main dipolar LSP mode (dark orange). Panels a and b show the case of weak and strong coupling, respectively.

the strong coupling time such timescale is reduced to $1/\Omega_R \sim 1$ fs.

To obtain a deeper insight on the short time dynamics of the system, we remove the pumping term and study the decay of an initially excited QE state, $\sigma_A^\dagger|0\rangle$. The resulting time evolution of emitters A and D, as well as the main dipolar LSP mode, is rendered in Fig. 5.9 for the weak and the strong coupling regimes (panels a and b, respectively). In the weak coupling regime, both the LSP and the population of emitter D only reach very small values, since the population transfer is determined by the dipole-dipole interaction. The weak effect of the QE-LSP interaction is only appreciable because such dipole-dipole transport is negligible for the emitter D. As the plasmon modes do not significantly participate in the dynamics, the decay of the populations is characterized by the lifetime of the bare QEs ($\sim$ 600fs). Since the light-matter coupling rate is even slower, the population of emitter D is cutoff at around that time, achieving a maximum value of $\sim 2\times10^{-5}$ during all the time evolution. On the other hand, in the strong coupling regime (panel 5.9b) the population is transferred much more efficiently to emitter D than in the previous case. First, note how the plasmon mode is populated almost instantaneously

due to the very large interaction rate Ω_R. Such excited plasmon in turn populates emitter D in a timescale given by the period of the Rabi oscillations, in this case $1/\Omega_R \sim 5$fs. The population of emitter D reaches significantly larger values as well, up to 4×10^{-3}. Note, finally, that for long times all the populations of the QEs decay at a larger rate than γ_d, showing that a collective state is determining the dynamics. Our results in this section thus demonstrate that the onset of strong coupling not only increases the probability of transferring an exciton from point A to point D, but additionally delivers the excitons orders of magnitude faster.

5.4. Exciton harvesting in engineered nanostructures.

The results obtained above for the nanosphere show a fast and efficient drag of excitons into the areas of large field intensity, both excellent properties regarding exciton transport and harvesting. However, the capacity of this system to efficiently transport the excitons over large distances, namely from one pole of the NS to the other, is limited. Indeed, in Fig. 5.6 we can see that, despite the large increase in the pole-to-pole conductance at the onset of the CSC regime, the population is still more efficiently transferred to the QEs close to A. In this particular case, the conductance ratio $\sigma_e^D \approx 0.1\sigma_e^B$ does not qualify the NS as an efficient platform for exciton harvesting. This ratio is a consequence of the EM field profile of such nanostructure being intense in a wide range of polar angles θ, as depicted in Fig. 5.7. Such a wide distribution makes the transport from emitter A to its nearest neighbours also efficient in the strong coupling regime.

Interestingly, our analytical expressions Eqs. 5.34 and 5.35 offer the solution for a more optimized harvesting of excitons at a particular spot. According to these expressions, when the EM field profile of the cavity mode is very confined around two QEs, say A and D, it is possible to boost the conductance exclusively between these two points. Note that, in such a configuration, the remaining QEs are still necessary, since the collective enhancement of the Rabi splitting produced by their coupling to the EM mode is the only way of achieving the CSC regime. This sets up the recipe for an efficient exciton harvesting. In this section, we will study a nanostructure optimized for this purpose, showing how the conductance between the two desired points can be boosted by appropriate nanostructure engineering.

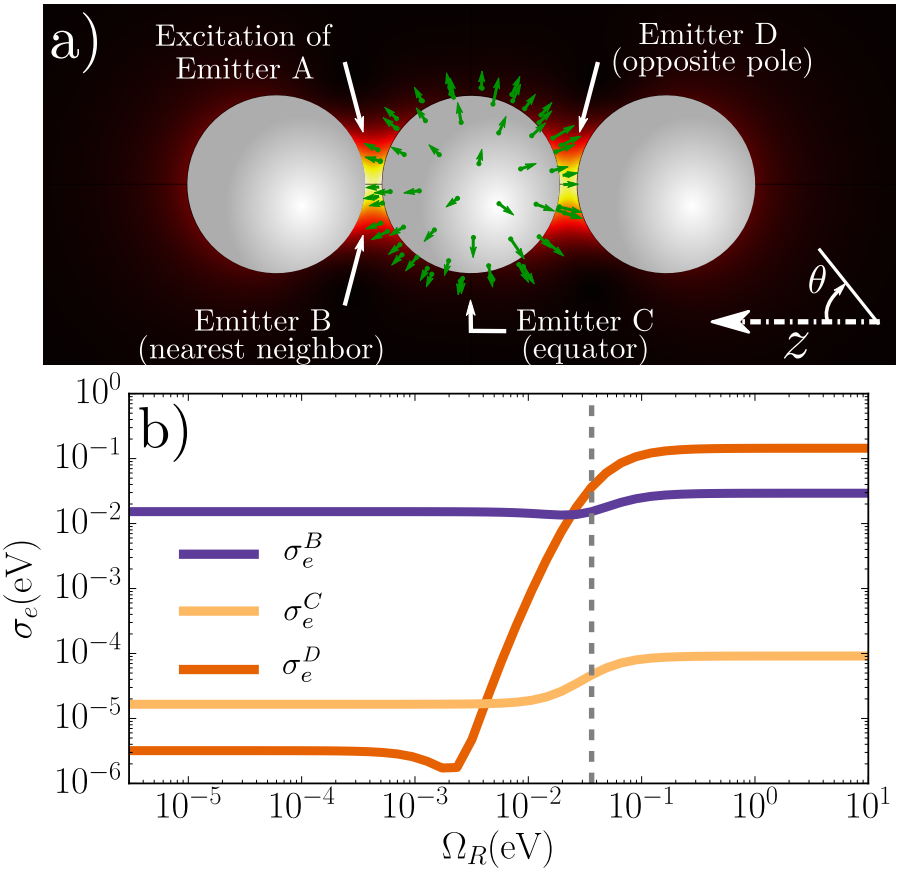

Figure 5.10: a) Illustration of the three-nanosphere structure devised for efficient exciton harvesting. The central sphere is surrounded by $N = 100$ QEs, and the emitter labelled A is incoherently pumped. The background shows the electric field intensity profile of the fundamental mode of the structure. b) Exciton conductance for the three emitters B, C, and D as described in panel a, versus total Rabi splitting. The grey dashed line indicates the onset of CSC.

5.4.1. Steady-state exciton conductance.

The nanostructure we study in this case is formed by placing two additional identical nanospheres at the two sides of the existing structure, as schematically depicted in Fig. 5.10a. Due to the breaking of the rotational symmetry, the fundamental mode of this three-sphere arrangement, whose field intensity profile is displayed in the background of the figure, is not degenerated. Note that the modal field is in this case extremely confined within the two gaps between the spheres. The extension of such gaps is set to 2nm, small enough to have a deep subwavelength confinement but too large for nonlocal effects to be relevant [363]. In order to facilitate the comparison with the single-NS case

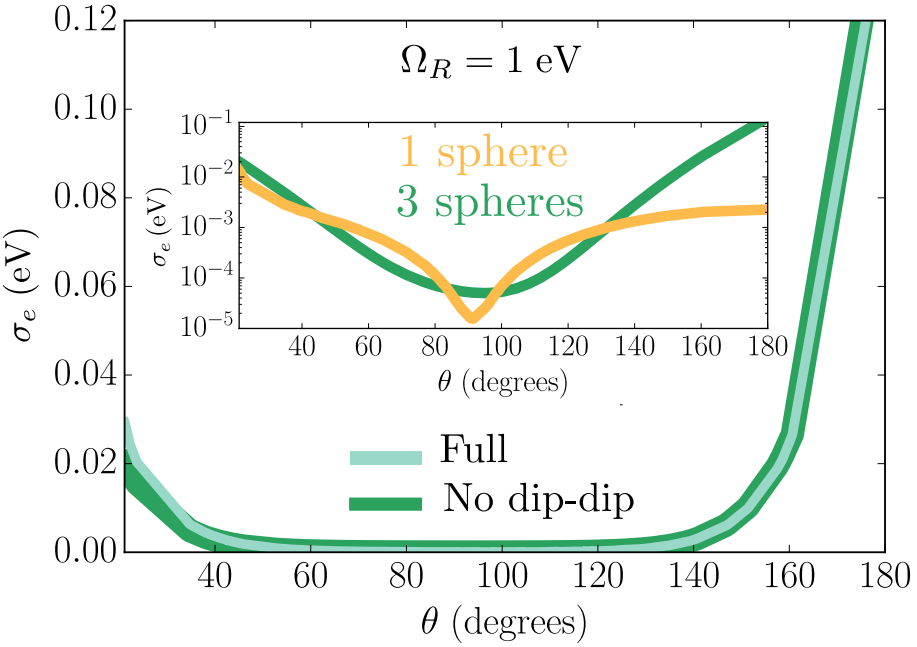

Figure 5.11: Angular distribution of the conductance in the three-nanosphere structure, for $\Omega_R = 1$eV and $N = 100$. The solution of the full model is shown by the light green line, and in the absence of dipole-dipole interaction by the dark green line. The inset shows the same profile in logarithmic scale, as compared to that of the single NS.

and focus on the effect of the different mode profile, the LSP frequency and losses as well as the QE properties and locations are kept unchanged. We also consider the pumping term to be concentrated exclusively on emitter A.

The exciton conductance for this nanostructure is displayed in Fig. 5.10b as a function of the Rabi splitting, for the same three QEs studied in the single-NS situation, namely B, C, and D. As the figure shows, the pole-to-pole conductance now displays a dramatic increase of 5 orders of magnitude at the onset of the CSC regime. This improves the value of the single-NS situation by a factor of ≈ 50. However, this is not the only sense in which this structure is more efficient than the single-NS case. Indeed, the most surprising feature of the three-NS arrangement is the fact that, in the strong coupling regime, the pole-to-pole exciton conductance σ_e^D is much more efficient than the conductance σ_e^B to the nearest neighbour of the pumped QE. Thus, with these particular parameters, we have achieved the conductance at point D, placed 22nm away from the pump, to be ≈ 10 times as large as that to point B, placed at 3nm. Note how the small increase in the conductance σ_e^C in the strong coupling certifies that the remaining QEs are still coupled to the main LSP mode, albeit weakly.

The angular dependence of the strong coupling exciton conductance in the 3-NS nanostructure is shown in Fig. 5.11. Here, we can observe how the excitons are strongly concentrated in the two *hot spots* of the structure, i.e., the two gaps between the nanospheres. Additionally, the coincidence of the full results (light green line) with those in the absence of dipole-dipole interaction (dark green line) certifies that, also in this case, such interaction plays a minor role in the system dynamics. The inset in Fig. 5.11 shows the comparison of the two setups studied in this chapter, namely the single NS and the 3-NS structures. It is clear how, by tailoring the electric field profile of the LSP mode, we are able to redistribute the excitonic population and, in case of the three nanospheres, focus it within a deep subwavelength region. We have therefore demonstrated how to efficiently harvest excitons by an adequate selection of the appropriate nanostructures. Note how, again, our result stems from the delocalization of the system eigenstates and, consequently, is not particular to plasmonic structures or organic molecular emitters. The possibility of an efficient and fast addressing of excitons to a narrow region of space is the main result of this chapter and illustrates one of the many applications of strongly coupled systems.

5.5. Effect of dephasing on the exciton transport.

In our above studies of plasmonic structures, we have treated the dephasing as a simple decay rate in order to understand the fundamental phenomena behind the exciton harvesting. However, in the particular case of organic QEs, dephasing is usually not negligible, and a more detailed description of this mechanism could be relevant for an accurate estimation of the SC exciton conductance. Additionally, recent works [147] have shown how dephasing can be an important resource for exciton transport in organic compounds. The last section of this chapter is thus devoted to a more detailed study of the impact of dephasing on the strong coupling exciton transport.

We introduce a more precise description of the dephasing in our formalism by means of population-conserving Lindblad superoperators [355], i.e., we perform the following substitution inside the master equation, Eq. 5.28:

$$\gamma \mathcal{L}_{\sigma_j} \rightarrow \gamma_d \mathcal{L}_{\sigma_j} + \gamma_\phi \mathcal{L}_{\sigma_j^\dagger \sigma_j}. \tag{5.36}$$

Note that, in general, the above description is accurate for moderate values of the dephasing rate γ_ϕ [288]. However, it can be checked that more elaborate methods like

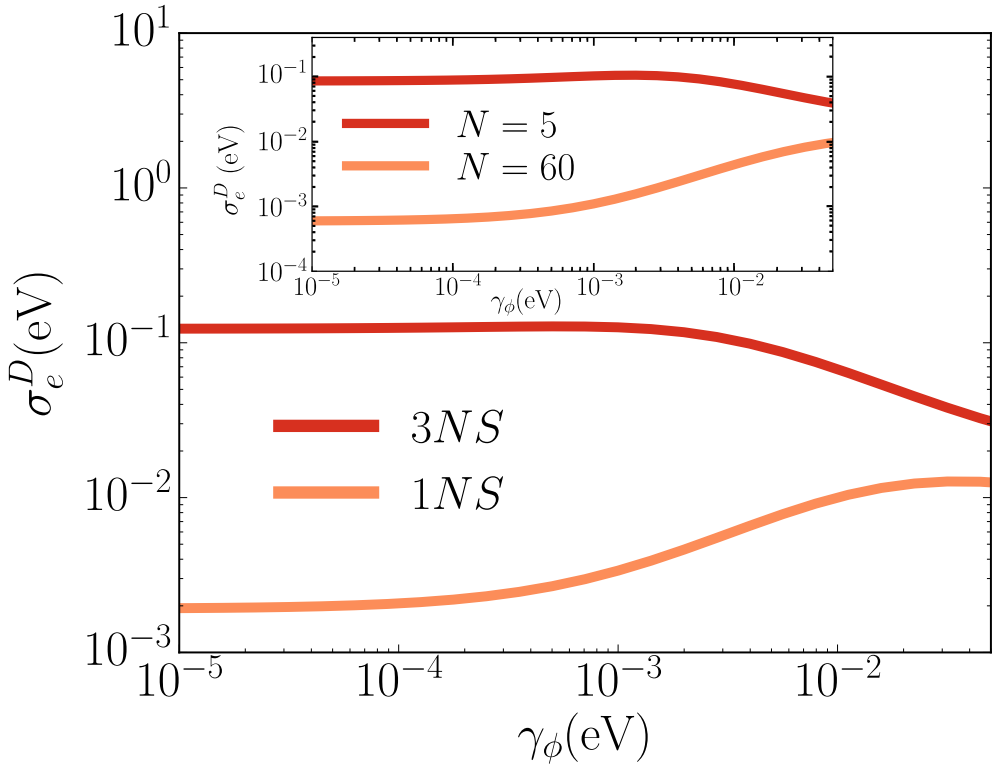

Figure 5.12: Exciton conductance from point A to point D in the SC regime ($\Omega_R = 1$eV), as a function of the dephasing rate. The single-NS case (light orange line) is compared with the three-NS structure (dark orange line). The inset displays the conductance for QEs placed inside a cavity mode displaying a homogeneous field profile, for $N = 60$ (light orange line) and $N = 5$ (dark orange line).

the Bloch-Redfield-Wangsness formalism give the same results in the present case [20]. The dephasing as described by the above equation is known to effectively couple all the eigenstates of the system, namely polaritons and dark states, by inducing an incoherent population transfer between them [288]. This will be a key mechanism determining the effect of the dephasing in our system, as we will see below.

The pole-to-pole exciton conductance in the SC regime is shown in Fig. 5.12 as a function of the dephasing rate, for both the single-NS and the three-NS cases. Except for the value of γ_ϕ, the parameters of the nanospheres and the QEs are the same as in the previous calculations. Surprisingly, the dependence of the strong coupling conductance with dephasing is different for the two considered nanostructures. As dephasing is increased, the conductance decreases monotonically for the three-NS structure, but counterintuitively increases for the single NS. Since we purposely have chosen every parameter to be identical in both situations, it is evident that the fundamental discrepancy

between these cases must be related to the different electric field profile or, equivalently, to the *effective* number of QEs coupled to the main EM mode. Such number is smaller for the three-NS case, since the electric field is more confined and, as a consequence, the main dynamics is played by the smaller amount of largely coupled QEs. This hypothesis is confirmed by the inset in Fig. 5.12. Here, we display the exciton conductance in the simplest possible scenario, where all the QEs are homogeneously coupled to the EM field, i.e., $g_j = g$. This corresponds to the single-mode cavity setup in the exciton transport model we have discussed in the first section of this chapter. Note how in this simplified system, the distinct dependence on the dephasing rate is maintained, and associated with a different number of molecules participating in the dynamics.

The analogy observed in Fig. 5.12 is very useful for elaborating a theoretical argument, since we can explain the effect of dephasing in terms of a simplified model of homogeneously coupled QEs. We have already studied this problem analytically in the limit of zero dephasing, $\gamma_\phi = 0$, in section 5.2.4. In such case, the dynamics of the system was restricted to the reduced Hilbert subspace populated by the pumping term, namely the subspace spanned by the vacuum state $|0\rangle$, the two polaritons $|\epsilon_\pm\rangle$ defined in Eq. 5.11, and an adequately chosen dark state $|D\rangle$ determined in Eq. 5.12. However, in the presence of dephasing, $\gamma_\phi > 0$, this model breaks down since, as mentioned above, the Lindblad terms in Eq. 5.36 introduce an incoherent coupling between all the system eigenstates. Therefore, the population initialized in either $|\epsilon_\pm\rangle$ or $|D\rangle$ can now be transferred to the remaining dark states $|D_k\rangle$ ($k = 1, ...N-2$), and the exciton conductance σ_e is not simply the sum of two independent contributions, σ_{pol} and σ_D. Note that this does not necessarily imply a decrease in the exciton conductance, but only that the states $|D_k\rangle$ can now represent a significant contribution to σ_e. Indeed, whereas the pumping term at emitter 1 privileges the state $|D\rangle$, the orthogonal dark subspace $\{|D_k\rangle\}$ remains arbitrary and, as a whole, fully delocalized among the QEs $j = 2, ...N$ as we know from the previous chapter. We can therefore expect that any population introduced in this subspace is very efficiently transported along the chain. In the presence of dephasing, therefore, the system behavior is determined by an intricate interplay between three components, namely the polaritons, the state $|D\rangle$, and the whole ensemble of remaining dark states $\{|D_k\rangle\}$.

In this simple system of homogeneously coupled QEs, the exciton conductance can be analytically calculated even in the presence of dephasing. Indeed, since all the QEs are identical, the density matrix of the system can be written in the form of Eq. 5.9. A similar argument as the one employed in section 5.2.3 allows us to determine the total

exciton conductance, for weak pumping and at zero detuning, as [138]

$$\sigma_e = \frac{\gamma_d}{\gamma_p}\omega_0\rho_{22} = \frac{\gamma\gamma_d(\gamma+\Gamma)\omega_m\Omega_R^4}{(2\gamma\gamma_d\Gamma N + (2\gamma_\phi+\gamma_d N)\Omega_R^2)\,(\kappa\gamma\gamma_d\Gamma N + (\kappa\gamma_\phi+\gamma_d\Gamma N)\Omega_R^2)}, \tag{5.37}$$

where $\rho_{22} = \langle 0|\sigma_2\rho_{ss}\sigma_2^\dagger|0\rangle$ is the only element of the density matrix contributing to the conductance in this limit. In order to split the above expression into contributions from the different system eigenstates, we can express such element in the basis $\{|\epsilon_\pm\rangle, |D\rangle, |D_k\rangle\}$ to write

$$\rho_{22} = \frac{1}{N(N-1)}\rho_{DD} + \frac{1}{2N}\sum_{\alpha=\pm}\left(\sum_{\beta=\pm}\rho_{\alpha\beta} - \sqrt{\frac{2}{N-1}}(\rho_{\alpha D}+\rho_{D\alpha})\right) + \delta\rho. \tag{5.38}$$

Here, the first terms have a similar form as the different contributions in Eq. 5.15. On the other hand, we have grouped under $\delta\rho$ all the matrix elements containing a contribution from the dark states $\{|D_k\rangle\}$. This is a sensible choice since, due to the fact that all these states are equivalent, they will contribute equally to the conductance. Each of the above terms can be explicitly calculated although, as in the zero dephasing case studied above, only a few are important in the strong coupling limit. Specifically, for $\Omega_R \gg \gamma, \kappa$, any coherence between the states $\{|\epsilon_\pm\rangle, |D\rangle\}$ decays as Ω_R^{-2} and can thus be neglected. Then, by introducing the above expression for ρ_{22} into Eq. 5.37, we can write in the strong coupling limit

$$\sigma_e^{SC} \equiv \sigma_e(\Omega_R \gg \gamma, \kappa) = \sigma_{pol} + \sigma_D + \sigma_\delta. \tag{5.39}$$

Here, we define $\sigma_{\rm pol} = \gamma_d\omega_0(\rho_{++}+\rho_{--})/\gamma_p$, $\sigma_D = \gamma_d\omega_0\rho_{DD}/\gamma_p$, and $\sigma_\delta = \gamma_d\omega_0\delta\rho/\gamma_p$. According to the above equation, the conductance can be now split into three independent contributions, one from the polaritons, a second one from the dark state $|D\rangle$, and a third one associated with the remaining dark subspace. The analytical expressions of these terms are calculated as

$$\sigma_D = \frac{\omega_0\gamma_d(\gamma(2\gamma_\phi+\gamma_d N(N-1)) + \kappa N(\gamma_\phi+\gamma_d(N-1)))}{N(N-1)(N\gamma_d+2\gamma_\phi)(\gamma_\phi\kappa+N\gamma_d\Gamma)}, \tag{5.40}$$

$$\sigma_{pol} = \frac{\omega_0\gamma_d\gamma}{N(\gamma_\phi\kappa+N\gamma_d\Gamma)}, \tag{5.41}$$

$$\sigma_\delta = \sigma_e^{SC} - \sigma_D - \sigma_{pol}, \tag{5.42}$$

where the total conductance $\sigma_e^{SC} = \sigma_e(\Omega_R \gg \gamma, \kappa)$ is determined by taking the strong coupling limit of Eq. 5.37, .

The contributions of both the polaritons and the dark state $|D\rangle$ to the total conductance are shown in Figs. 5.13a-b for a chain of $N = 5$ and $N = 60$ QEs, respectively.

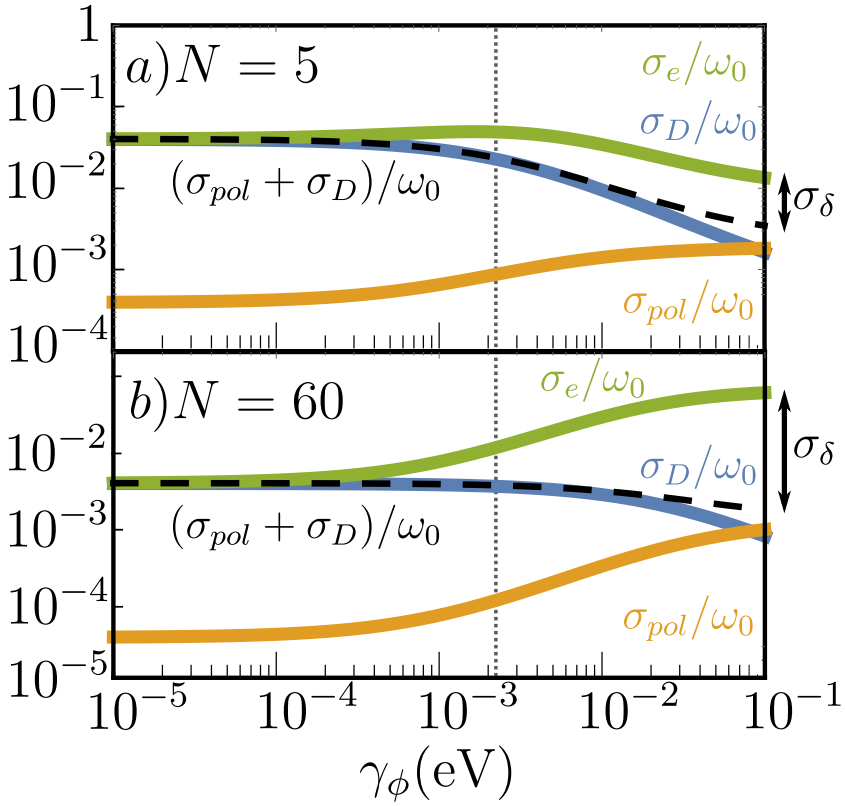

Figure 5.13: Exciton conductance in units of ω_0 as a function of the dephasing rate, for a chain of $N = 5$ (panel a) and $N = 60$ (panel b) QEs homogeneously coupled to a cavity mode. The total conductance (green line) is compared to the contributions of the polaritons (orange) and the dark state $|D\rangle$ (blue). The sum of both these contributions is shown in the black dashed line. The vertical line marks the dephasing rate for TDBC aggregates, $\gamma_\phi = 26.3$meV. Note how the curves start to deviate from their zero dephasing values around $\gamma_\phi \approx \gamma_d = 1$meV.

Here, we render the conductances σ_e, σ_{pol}, and σ_D as a function of the dephasing rate. Interestingly, the qualitative behavior of σ_{pol}, and σ_D is the same regardless of the number of QEs. First, the conductance through the dark state $|D\rangle$, which for small γ_ϕ is the most efficient channel as we have shown in previous sections, tends to decrease for larger values of the dephasing rate, as the population is transferred to other eigenstates. On the other hand, the polaritonic channel becomes more efficient for large dephasings, since due to their lossy character ($\kappa \gg \gamma_d$), polaritons act as exciton sinks with respect to the dark states. Indeed, when an exciton from any eigenstate is transferred to a dark state via dephasing, it is possible for such exciton to live for a long time, undergo further jumps and eventually make its way to the end of the chain, since the loss rate of the dark states, γ_d, is small. However, for an excitation transferred into the polaritons, a

second "jump" back into the dark subspace is much more unlikely since the probability of being lost through the cavity mode is large. This explains the increase in the polariton population observed in Fig. 5.13a-b, as for large dephasing rates it receives an incoming exciton flux that partially compensates for the one exiting through the cavity modes. Note that, in any case, the conductance σ_{pol} always remains a very reduced contribution to the total conductance. This indicates that the decrease of σ_D can not be compensated by the small increase in σ_{pol}, and explains why the sum $\sigma_D + \sigma_{pol}$ decreases with γ_ϕ.

The total exciton conductance, however, can increase for large dephasings, if such decrease in $\sigma_{pol} + \sigma_D$ is compensated by the injection of population into the delocalized dark subspace. Such a compensation can occur if two conditions are met, namely a small role of the lossy polaritons, and a large amount of orthogonal dark states to which the excitons can be transferred. These requirements are clearly not met when N is small (Fig. 5.13a), where a large amount of population is initialized in the polaritons through the bright state, in this case $1/N = 0.2$. Due to the above discussed behavior of the polaritons as exciton sinks, 20% of the initial population is thus not likely to reach the dark subspace. Consequently, the dephasing-induced depletion of the dark state population, ρ_{DD}, is not capable of populating the dark subspace $\{|D_k\rangle\}$ enough to compensate for the polariton losses. This results in the overall decrease in the conductance observed in Fig. 5.13a.

On the other hand, when the number of QEs N is increased (Fig. 5.13b) two effects combine to maximize the conductance. First of all, the dark state $|D\rangle$ contains the majority of the population, as the initial contribution of the polaritons is much smaller (for $N = 60$, it amounts to $1/60 \lesssim 2\%$). Additionally, the larger number of QEs increases the amount of dark states $|D_k\rangle$, and thus the transfer rate to the orthogonal subspace is multiplied by a large factor, $N - 2$. Hence, even if the incoherent coupling rate between the states $|D\rangle$ and $|D_k\rangle$ is small, upon increasing N the decay into the dark subspace will become the most relevant channel, eventually compensating for the polaritonic losses. Indeed, it is interesting to check that, in the hypothetical limit $\gamma_\phi \gg \gamma_d N$, the conductances read

$$\left.\begin{pmatrix} \sigma_e \\ \sigma_{pol} \\ \sigma_D \end{pmatrix}\right|_{\gamma_\phi \gg \gamma_d N} = \frac{\omega_0 \gamma_d}{\gamma_\phi \kappa + \gamma_d N(\gamma_\phi + \kappa)} \begin{pmatrix} \gamma_\phi + \kappa/2 \\ \gamma_\phi / N \\ (\gamma_\phi + N\kappa/2)/2N(N-1) \end{pmatrix}. \tag{5.43}$$

Here, while we recover the dependence $\sim 1/N^2$ for the single eigenstates $|\epsilon_\pm\rangle$ and $|D\rangle$, the total conductance containing the contribution of the orthogonal dark subspace decreases only as $1/N$, becoming the most relevant channel for large ensembles of QEs. This different dependence is a result of the delocalized orthogonal dark subspace containing

$N-2$ states, each of them decreasing as $1/N^2$.

To summarize, dephasing in this system introduces an incoherent population transfer between the three initially populated states, $|\epsilon_\pm\rangle$ and $|D\rangle$, and a *delocalized* orthogonal dark subspace, which is extremely efficient as a whole in transporting the excitons along the chain. As N grows larger, the excitation transfer to this subspace is enhanced by a factor $N-1$ as more and more dark states are coupled to $|D\rangle$. Eventually the transfer rate to the orthogonal dark subspace is able to overcome the population transfer to the lossy polaritons. By this mechanism, the presence of a large reservoir of delocalized dark states is capable of generating a dephasing-induced enhancement of the exciton conductance. Note that this behavior is strongly dependent on the system parameters, as different physics would arise if, for instance, polaritons were not as lossy as the QEs.

The results introduced in this section are intrinsic to the CSC regime, and rely on the delocalization of the dark subspace introduced in chapter 4. They illustrate how, by an adequate nanostructure engineering, it is possible to use dephasing as a resource for exciton transport and harvesting. Note that, although this specific mechanism has not been presented before, alternative forms in which decoherence enhances excitonic transport have been studied in the absence of EM modes. Specifically, dephasing has been shown to allow the excitons either to bypass Anderson impurities in 1D tight-binding chains [364, 365], or to cancel coherent destructive interferences in light-harvesting complexes [147]. Finally, it is important to remark that a full microscopical description of the effect of dephasing for any range of light-matter interaction is still lacking, due to the enormous difficulties from the theoretical point of view. Some works have tackled the problem in the limits of small [288] and large Rabi splitting [366], predicting a variety of phenomena from incoherent coupling between the system eigenstates to absolute decoupling of the polaritons [367]. Recently, advanced numerical techniques have been developed which offer promising perspectives in this regard [148], paving the way towards dissipative engineering at the molecular level.

5.6. Conclusion

In this chapter, two main results have been presented, based on the previously reported phenomenon of extraordinary exciton transport mediated by CSC [138, 139]. First, we have demonstrated how, since such effect is based on the photon-induced delocalization of the system eigenstates, it is possible to tune the spatial profile of the exciton conductance by means of an inhomogeneous EM field. Based on this idea, we have shown

how excitons can be very efficiently harvested even into deep subwavelength spatial regions. Second, we have demonstrated the fundamental role of the dark states in this process, whose complex interplay with the polaritons allows for a rich phenomenology in the presence of dephasing. Specifically, the possibility of dephasing-assisted, dark-state based extraordinary exciton conductance has been shown.

As we have mentioned in the introduction, the ability of enhancing the exciton transport on demand is very important for devices whose efficiency would increase for larger exciton propagation lengths, such as solar cells [331] or excitonic circuits [110]. Additionally, the possibility of finely tuning the spatial distribution of the polaritons could have an impact in many applications of CSC, especially those which could benefit from a local manipulation of the light-matter interaction. Among others, possible candidates are the control of chemical reactions [368, 369], work functions [370], or energy transfer [324, 371], or the modification of charge transport properties [49]. The deep role of both the dark states and the dephasing in the transport of excitons mediated by strong coupling also shines new light on the fundamental structure of strongly coupled systems, which in turn facilitates the improvement of all the above applications by means of an adequate system engineering.

Finally, let us emphasize that, although we have illustrated the principle by means of particular examples, all the results presented in this chapter are of general character. Indeed, they can be applied not only to organic molecules but to other kinds of QEs such as quantum dots, or trapped ions, which offer a high degree of controllability [372, 373]. Additionally, it can be extended in principle to any kind of nanostructure as long as the CSC regime is reached and, in the case of exciton harvesting, the EM modes display an inhomogeneous spatial dependence.

6 | Coupling single nitrogen-vacancy centres to channel plasmons.

6.1. Introduction

This final chapter of the thesis is devoted to the study and characterization of a realistic light-matter interface for quantum nanophotonics. So far the thesis has been devoted to a theoretical exploration of systems of quantum emitters coupled to nanostructures. All of this work relies on the possibility of efficiently coupling single quantum emitters to nanophotonic structures, and addressing them in a controlled fashion. Whereas such achievement is not a big obstacle in microwave devices due to their intrinsically larger length scale [93, 212, 374], in the optical range, and particularly in systems where light is confined in a subwavelength scale, such coupling represents a challenge that researchers have only started to overcome in recent years [375]. Here, we demonstrate the coupling of a single quantum emitter, specifically a nitrogen-vacancy centre, to a one-dimensional plasmonic structure. This chapter aims to demonstrate the possibility of devising efficient platforms for quantum nanophotonics in realistic situations. For this reason, we will also briefly describe the experimental realization of the proposed device. Such an experiment was undertaken by our collaborators, specifically prof. Sergey Bozhevolnyi's group at the University of Southern Denmark, who fabricated the plasmonic waveguides, and prof. Romain Quidant's group at ICFO, who assembled the device and demonstrated the efficient light-matter coupling.

6. Coupling single nitrogen- vacancy centres to channel plasmons.

In order to devise an efficient light-QE interface, a careful selection of the nanophotonic structure is of utmost importance. Among the different waveguide setups available nowadays, plasmonic waveguides (PW) were chosen for this device, since they operate in the optical range and show deep subwavelength confinement of the electric field [22]. These remarkable properties make plasmonic systems optimum candidates for highly integrated photonic circuitry [112, 376, 377]. As we have mentioned in chapter 1, PWs represent excellent quantum light-matter interfaces, since the small mode volumes associated with the strong field confinement allow for large couplings between plasmons and quantum emitters. Hybrid systems consisting of QEs coupled to PWs have been extensively studied in the context of quantum circuitry [59, 115, 123, 124, 211, 258, 378]. On the other hand, however, plasmonic systems are usually more influenced by losses than other nanophotonic structures such as photonic crystal waveguides [31]. For this reason, it is important for our purpose to choose the most adequate PW among the wide variety available.

Considering possible PW configurations, the most common setups are metallic nanowires, since they can be fabricated in a precise way by chemical synthesis [379]. As a result, strong mode confinement and large propagation lengths have been reported in such systems [380, 381]. Nanowires fabricated in this way, however, are not good candidates as circuitry elements, since a precise control over their positions and orientations on top of the substrate is usually challenging. Although this issue can be circumvented by means of lithography techniques on a bulk sample (the so-called top-down techniques), the resulting nanowires are more prone to contain defects and therefore the propagation length, a critical parameter in plasmonic structures, significantly decreases [382]. Among the family of PWs directly fabricated on a metallic surface, one of the most promising alternatives to nanowires is formed by the plasmonic V-grooves (VGs) [383]. The VG-PWs are characterized by hollow V-shaped channels, which can be directly carved on top of the metallic substrate by means of a focused ion beam [384]. Such a fabrication method is highly controllable and makes VGs very promising candidates for developing planar plasmonic circuitry [337, 385, 386]. VG waveguides can support the propagation of channel plasmon polaritons (CPPs), which combine a strong field confinement with relatively long propagation lengths [387, 388], and low losses at sharp bends [389]. Furthermore, it is possible to devise an efficient route for the local coupling of the VG-CPP to free-space modes, for instance by integrating nanomirror tapers at the ends of the waveguide [390]. This enables an external control of the system by means of the natural input-output ports characteristic of waveguide systems, and facilitates the implementation of photon-based techniques such as those developed in the previous chapter.

An experimental observation of efficient single emitter-CPP coupling does not only rely on the choice of an optimum PW. A second key ingredient is the involved quantum emitter, for which a careful selection is also necessary. In previous works on hybrid QE-PW systems, the most employed emitters were quantum dots [59, 378, 391] and NV centres [392–396] due to their stable character and high controllability [55, 84]. Specifically, NV centres are usually chosen for room temperature experiments because of their brightness and stability, two aspects which make these emitters exceptional solid-state single-photon sources [84]. An additional advantage of these QEs is the possibility of optically controlling their internal state, which can be initialized, manipulated, and read out with high precision [397, 398]. Such degree of control has been extended into more complex operations such as the creation of spin-photon entangled states [399] and the increase of their spin coherence time, achieved by decoupling such spin from the surrounding nuclear spin bath [400]. All these applications show the enormous potential of NV centres as the basic matter components of quantum circuitry [87], and have motivated our election of these emitters for our hybrid device.

This chapter is mainly devoted to the theoretical study and characterization of a system composed by a single NV centre coupled to a VG-plasmonic waveguide. First, we introduce the system in section 6.2, together with the figure of merit quantifying its efficiency as a hybrid light-matter interface. Here, we also define the relevant properties of the NVs and theoretically estimate the propagation length of the modes supported by the VG. We then devote section 6.3 to the numerical analysis of the hybrid device. The optimal position and orientation of the NV centre are determined by considering a simplified system, in which the NV is simply modelled as a suspended electric dipole. After predicting that a high figure of merit is achievable in such scenario, in section 6.4 we address the more complicated problem of including the diamond host surrounding the cipolar emitter. A new formula for the coupling efficiency is deduced for this case, allowing for an estimation of the figure of merit in the realistic experimental conditions. In the following section (section 6.5), we briefly outline the work undertaken by our experimental collaborators confirming our theoretical predictions. Finally, we present our conclusions in section 6.6.

6.2. The system, figure of merit, and characterization of the components.

The configuration investigated consists on a nanodiamond hosting a single NV centre inside a gold VG-PW, as schematically depicted in Fig. 6.1. The NV centre can be excited through the aperture of the VG by means of a laser beam, which in the experiments has a wavelength of $\lambda = 532$ nm. If the NV is positioned in such a way as to be significantly coupled to the modes supported by the VG, a fraction of its emission will be directed into such CPP modes. The guided light propagating through the VG in this manner will arrive at the two ends of the waveguide and out-couple at the two tapered nanomirrors. By analysing the light scattered into free-space at the two ends of the VG, the ability of such system to achieve long-range energy transfer can be determined. We can quantify this energy transfer efficiency by defining a figure of merit (FOM) as a function of the critical parameters of the system,

$$\mathrm{FOM} = \frac{L_p P_F \beta}{\lambda_0}. \tag{6.1}$$

In the equation above, L_p represents the propagation length of the CPP modes. Similarly, P_F and β represent, respectively, the Purcell and beta factors already defined in previous chapters. Finally, in order to work with an adimensional FOM, we normalize the product of the above three quantities to the central wavelength in the NV emission spectrum. Practically, achieving a large FOM is exceedingly challenging in plasmonic systems, as this requires combining an appropriate VG configuration with low propagation losses, and a large Purcell enhancement with near-unity coupling efficiency.

Before studying the hybrid device as a whole, let us describe the properties of the components involved and determine the relevant parameters describing them. First, we will analyze our QEs and adapt the definition of the Purcell factor to a quantity that can be both predicted theoretically and measured in an experiment. We continue by studying the VG-PWs and theoretically estimate their most relevant intrinsic parameter, namely the propagation length.

6.2.1. Properties and characterization of the NV centres

The emitters chosen for this experiment are NV centres. As described in chapter 1, such systems consist on a double impurity in a diamond crystal lattice, in which two adjacent carbon atoms are substituted by a vacant and a nitrogen atom, respectively. Naturally,

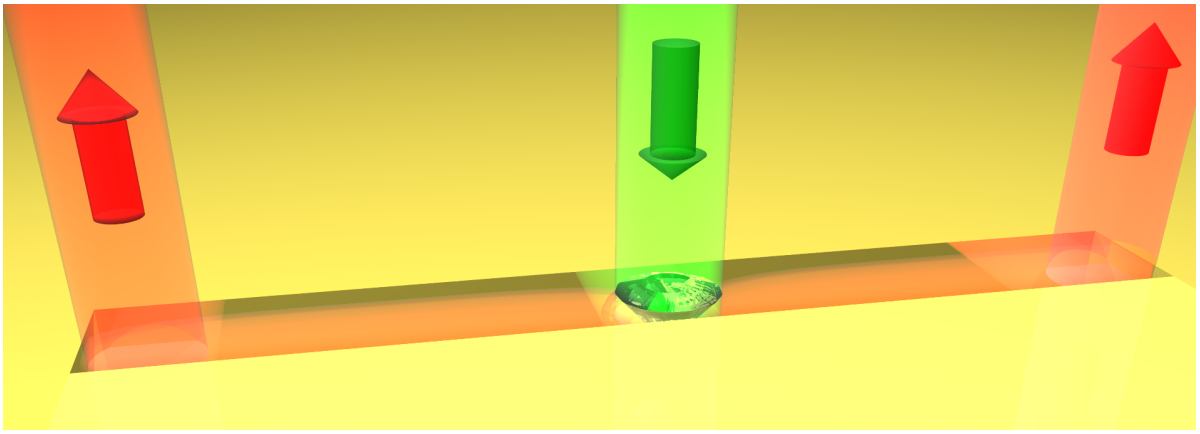

Figure 6.1: Schematic illustration of the system under consideration. A nanodiamond containing a single NV centre is introduced inside a VG waveguide carved on a gold substrate. When pumping the NV centre with external laser light, the emitted photons couple to channel plasmon polaritons which propagate away, and can out-couple from the waveguide through the tapered nanomirrors at both ends.

an NV centre cannot exist in the absence of a bulk diamond host. In our case, since we aim to introduce the NV centre inside the VG, such hosts must be nanometric in size. In the experimental setup, this can be achieved by means of high-purity monocrystalline nanodiamonds (NDs). These NDs contain a small, variable number of NV centres, and oscillate in size between 80 and 160 nm.

For a later calculation of the FOM, it is necessary to determine the decay rate γ of the NV centres or, equivalently, their mean lifetime τ, before placing them in the vicinities of the VG. Indeed, if the NV centres were first deposited over the metallic surface close to the VG, their intrinsic lifetime could be largely modified by the presence of surface plasmon modes [22]. The measurement of the NV centres mean lifetime completely characterizes our QEs, and is very important for two reasons. First, the fact that the NV centres are hosted inside nanometric diamonds implies that we cannot rely on theoretical or experimental values for their lifetime in macroscopic bulk diamond. Indeed, such value, namely $\tau_{\text{bulk}} \sim 11.6\text{ns}$ [84], will turn out to be very different from the lifetime measured in the experiment (see section 6.5). The slower decay in our nanometre-sized NDs is associated to the variation of the refractive index of the surrounding medium [401]. This effect is especially noticeable for nanoparticles smaller than the emission wavelength, which in these NVs lies in the range $\lambda \approx 650 - 750\text{nm}$ with a central value $\lambda_0 = 690\text{nm}$.

The second reason why we need a measurement of the lifetime is to properly define a

Purcell factor for the NV centres, which is susceptible to be determined both theoretically and experimentally. The usual definition of the Purcell factor for a general emitter is given by τ_0/τ, where τ is the lifetime of the QE in the vicinities of a certain nanostructure (in this case, the VG), and τ_0 represents the lifetime in a 3D, infinite vacuum. Clearly, the above definition does not make sense in the case of the NV centres, since they exist only inside a diamond crystal lattice and thus can never be isolated in free space. As a consequence, it is necessary in this case to choose a different reference lifetime than τ_0. Although at a first glance the lifetime τ_{bulk} seems an appropriate choice, it is not valid to define a proper Purcell factor, since the enhancement of the decay rate measured experimentally will refer to the lifetime of the NVs inside the nanodiamonds. Therefore, the appropriate reference in our case is the lifetime of the emitter inside the ND, but in the absence of any other photonic nanostructure. The Purcell factor is then defined in this experiment as

$$P_F = \frac{\tau_{\text{ND}}}{\tau} = \frac{\gamma}{\gamma_{\text{ND}}}, \tag{6.2}$$

where the right-hand term is expressed in terms of the corresponding decay rates.

We consider necessary to clearly differentiate between two very similar quantities that will appear repeatedly along the chapter. The first of these magnitudes is the ratio γ/γ_0, i.e., the theoretical definition of the Purcell factor. Since this ratio assumes the NV can exist as a stand-alone QE in vacuum (or, equivalently, in an infinite and homogeneous diamond lattice), it determines the modification of the decay rate caused by *both* the finite character of the ND host and the plasmonic nanostructure. Hence, along this chapter we will avoid referring to this quantity as Purcell factor. Instead, we will name this ratio the *Decay rate enhancement* (DRE) of the QE, as a reminiscence of its definition. On the other hand, we will employ the notation *Purcell factor* P_F for the enhancement induced by the plasmonic structure alone on the decay rate, defined in Eq. 6.2. In the following sections it will be important to properly differentiate between the theoretical-only DRE, and the experimentally measurable Purcell factor. Finally, note that, since P_F also represents a certain modification of the decay rate, the notation we have chosen for both quantities is somewhat arbitrary, and the respective labels could arguably be exchanged. However, we have purposely chosen the present notation for the Purcell factor in order to be consistent with the definitions in the previous chapters. In the following sections we will detail the theoretical and experimental determination of both the Purcell factor and the DRE.

6.2.2. Properties and characterization of the V Groove

The VG waveguide under consideration will have the same properties as that employed in the experiment (see section 6.5). Specifically, it will be 10μm long, with a depth of 510nm, a width of 315nm at the top, and an aperture angle 24° at the bottom. Such PW is fabricated directly by milling a 1.2μm thick gold layer with a focused ion beam. This procedure is aimed to produce narrow and deep VGs which, as in the present case, can be terminated in tapered nanomirrors for efficient CPP out-coupling [390]. The inset 6.2a shows a scanning electron microscopy image of the VG, accompanied by a transverse cut, and the close picture of one of the two tapered ends.

The main parameter characterizing a stand-alone VG is its propagation length, for which a large value is desirable in order to have a large FOM. In order to calculate such length, we devote the first theoretical calculation of this system to a characterization of the CPP modes supported by the VGs. In principle, our calculations can confirm beforehand if the fabricated VGs are adequate for the experiment, by determining that they enable sub-diffraction confinement with a long propagation length at the natural emission frequency of the NV centres. Additionally, they provide a theoretical estimation of the propagation length, which will be used later on to theoretically calculate the FOM.

The electromagnetic (EM) eigenmodes of any nanostructure are the solutions of the Maxwell eigenvalue equations, which for a non-magnetic material ($\mu = 1$) read [309]

$$\nabla^2 F + \frac{\varepsilon \omega^2}{c^2} F = 0. \tag{6.3}$$

Here, F represents any component (x, y, z) of the electric or magnetic fields E, B. The permittivity of the considered medium is represented by ε, and c and ω account for the vacuum speed of light and the field frequency, respectively. In the case of long structures such as our VG, the length along the main axis is much larger than the typical emission wavelength of the NV centres and, consequently, we can approximate our system by an infinitely long VG. Our waveguide is thus characterized by a translational symmetry along the main axis, which we choose along the y Cartesian coordinate. This allows to write any solution of the mode equation as

$$F(x, y, z) = F_{\perp}(x, z) e^{\pm i k_y y}. \tag{6.4}$$

The above expression describes a channel plasmon propagating along the VG with a wavevector k_y, which is generally complex. According to Eq. 6.4, the light intensity, given by the square of the EM fields, decays as $\sim \exp(-2\mathrm{Im}\,[k_y]\, y)$, and therefore the imaginary part of k_y determines the propagation length of the CPP modes through

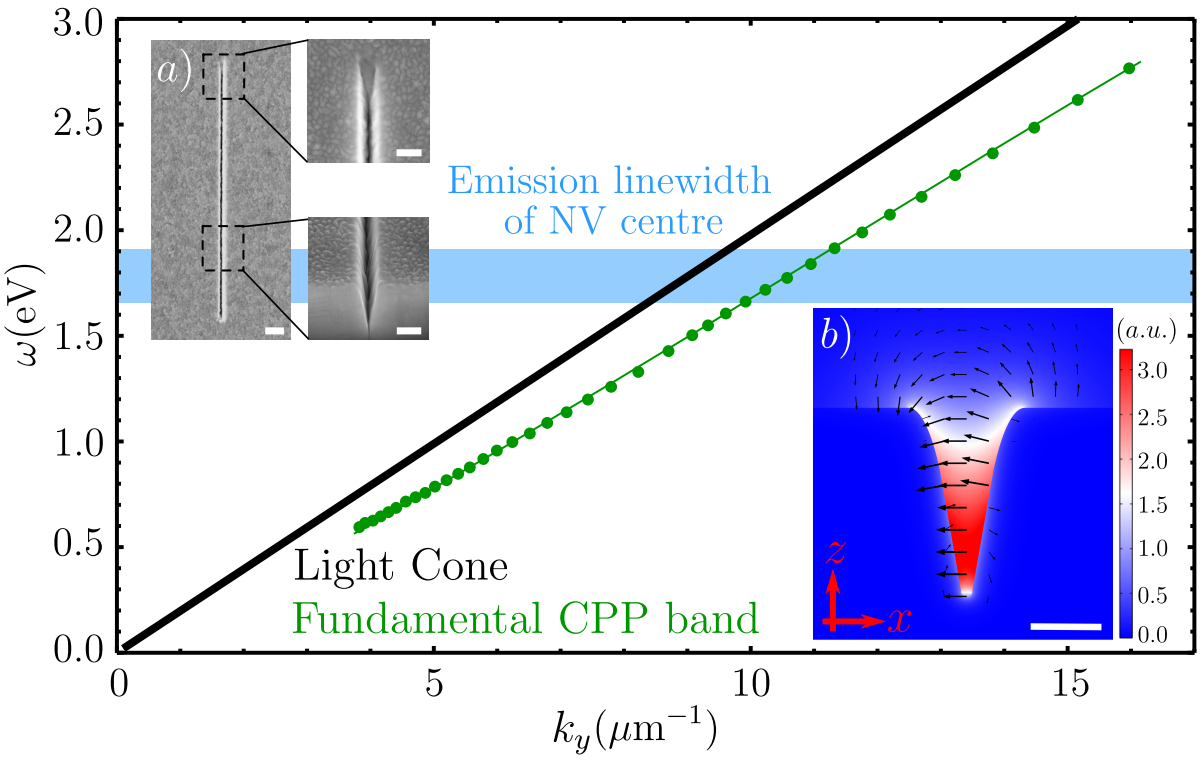

Figure 6.2: Dispersion relation of the fundamental band of the VG structure. The results of our simulations (green dots) are compared to the emission range of the considered NV centres, 650nm$< \lambda_0 <$ 750nm (shaded sky blue area). The black line displays the free space dispersion relation $\omega = ck_y$ (black line). Inset a) Scanning electron microscopy image of a 10μm long V-Groove equivalent to the one under consideration. The scale bar is 1μm. the top/bottom zoomed frames show the tapered nanomirror at the VG end and a transverse cut of the VG, respectively. Inset b) Norm of the transverse electric field of the fundamental CPP mode at $\lambda_0 = 650$nm. The black arrows indicate the electric field lines, their respective length being proportional to the logarithm of the field intensity. The scale bar in this panel is 200nm.

$L_p = (2\mathrm{Im}\,[k_y])^{-1}$. On the other hand, the transverse field profile $F_\perp(x,z)$ fulfils the equivalent two-dimensional mode equations

$$\nabla_\perp^2 F_\perp + \left(\frac{\varepsilon\omega^2}{c^2} - k_y^2\right) F_\perp = 0, \tag{6.5}$$

which determine the remaining properties of the CPP mode.

Since the transverse shape of the VG structure does not have enough symmetries, a solution of Eq. 6.5 can be obtained only by means of numerical simulations. Such calculations are performed using a Finite Element Method (FEM) software (COMSOL Multiphysics), a widely used approach in nanophotonics [337]. In order to solve the two-

dimensional problem at hand, we reproduce the experimental profile of the VG displayed in the inset 6.2a. In our reproduced profile, to avoid an unrealistic extreme concentration of the EM fields at the bottom of the VG, we round the lower edge with a curvature radius of 15nm (inset 6.2b). We assume the dielectric above the gold surface is air ($\varepsilon = 1$), and use the following Drude-Lorentz formula for the permittivity of the gold substrate,

$$\varepsilon_{\text{gold}}(\omega) = \varepsilon_r - \frac{\omega_p^2}{\omega(\omega - i\gamma_p)} - \Delta\frac{\omega_L^2}{(\omega^2 - \omega_L^2) - i\gamma_L\omega}, \tag{6.6}$$

where the phenomenological parameters above are experimentally fitted [402] to $\varepsilon_r = 5.967$, $\omega_p = 8.729$ eV, $\gamma_p = 0.065$ eV, $\Delta = 1.09$, $\omega_L = 2.684$ eV, and $\gamma_L = 0.433$ eV.

The 2D problem is solved for various mode frequencies $\omega = 2\pi c/\lambda$ in the vicinities of the optical spectrum. The dispersion $\omega(k_y)$ for the fundamental band of the VG is shown in Fig. 6.2, together with the emission linewidth of the NV centre, $\lambda_0 = 650 - 750$nm (shaded light blue area). In principle, higher energy bands do appear in this structure above a certain cutoff frequency that depends on the waveguide geometry [23]. In this case, we have checked that the reduced size of the structure displaces the cutoff frequency of the second band above ~ 4.5eV. The resulting modes are therefore far detuned with respect to the NV emission frequency, and will not play any relevant role. We will thus consider only the lowest energy CPP band from now on. In the inset 6.2b we show the norm of the transverse electric field for such fundamental band at $\lambda_0 = 650$nm. The simulations indicate a considerable field confinement of the electric field, peaking up close to the VG bottom while being practically constant across the VG. Note that the maximum field intensity is achieved at $\sim 200 - 300$nm above the bottom of the VG, a fact that will be beneficial for the coupling of the NV centres as we will see below. The electric field lines (black arrows) show the mode to be TE polarized, a common characteristic of VG waveguides [390].

In order to estimate the propagation length that will be measured experimentally, we consider the VG eigenmodes for three different values of the frequency, corresponding to $\lambda_0 = 650$nm, 690nm, and 750nm, respectively. The resulting values for the propagation lengths are averaged by weighting the contribution of each wavelength to the NV emission spectrum. As a result, we obtain a value of

$$L_p|_{\text{theory}} = 4.6\mu\text{m}. \tag{6.7}$$

The above result is in good agreement with other theoretically calculated values [387] and experimental measurements in similar devices [390]. Such agreement suggests that the model for the VG employed in our simulations is accurate, a fact that will be certified

in section 6.5 via an experimental determination of the propagation length in our VG waveguides.

6.3. Numerical characterization of dipole emission inside the VG.

After the characterization of both the VG waveguide and the NV centres, we are in a position to study the combined system, where the quantum emitter is coupled to the VG. In this section, we present a first theoretical analysis of such hybrid device which will provide preliminary information. Specifically, we will be able to determine the optimum experimental arrangement of the NV centre inside the VG in terms of position and dipole orientation. Additionally, our results will provide a first estimation for Purcell and beta factors, as well as for the FOM of this hybrid light-matter interface.

Since we have already determined the propagation length of the CPP modes, only two unknowns remain for the estimation of the FOM, namely the Purcell and the beta factor. Both these quantities are defined as the ratio between two decay rates,

$$P_F = \gamma/\gamma_{\mathrm{ND}} \qquad ; \qquad \beta = \gamma_{\mathrm{CPP}}/\gamma, \tag{6.8}$$

where γ and γ_{ND} are respectively the decay rate of the single NV centre in the vicinities of the nanostructure and inside the ND only. Similarly, γ_{CPP} represents the decay rate into the CPP modes.

Normally, the intrinsic decay rate γ of any quantum emitter does not describe only radiative processes, but also contains a nonradiative contribution which is usually due to internal losses [403, 404]. The proportion of the total decay rate corresponding to radiative emission is quantified by the so-called *intrinsic quantum yield* of a quantum emitter, q_i. In this work, we assume the ideal situation in which any nonradiative contribution is absent, corresponding to a quantum yield of $q_i = 1$. This is not a too restrictive approximation, as NV centres in NDs have been reported to have rather large quantum yields [401, 405]. Additionally, the experiment will be carried out with specifically selected NVs fulfilling $q_i \approx 1$. [125]. The assumption of maximum quantum yield is extremely advantageous since, for $q_i = 1$, the following relation can be demonstrated for the DRE [22]:

$$\frac{\gamma}{\gamma_0} = \frac{W}{W_0}. \tag{6.9}$$

In the above equation, W represents the total power radiated by a *classical* dipole in the vicinities of the nanostructure, whereas W_0 is the equivalent quantity in vacuum. The corresponding electric point dipole has the same properties as the original emitter, namely frequency of oscillation and dipole moment.

Thanks to the result in Eq. 6.9, we can determine the Purcell and beta factors of the system in terms of emission properties of a classical oscillating dipole. Indeed, since we can express the Purcell factor as a function of two different DREs, the following equality is straightforward to obtain,

$$P_F = \frac{\gamma}{\gamma_{\mathrm{ND}}} = \left(\frac{\gamma}{\gamma_0}\right)\left(\frac{\gamma_{\mathrm{ND}}}{\gamma_0}\right)^{-1} = \left(\frac{W}{W_0}\right)\left(\frac{W_{\mathrm{ND}}}{W_0}\right)^{-1} = \frac{W}{W_{\mathrm{ND}}}. \tag{6.10}$$

An analogous argument can be employed to find a similar relation for the beta factor,

$$\beta = W_{\mathrm{CPP}}/W. \tag{6.11}$$

In this fashion, we have expressed the relevant quantities of our system in terms of classical radiated powers. Therefore, our theoretical approach to this system will consist on solving Maxwell equations for an oscillating dipole in the presence of the appropriate nanostructure, in our case, the VG. The problem of an oscillating dipole has been extensively studied in the literature, and the following closed expressions for the DRE and the beta factors are well known (see appendix D):

$$\frac{\gamma}{\gamma_0} = \frac{6\pi\varepsilon_0 c^3}{\omega^3}\frac{\mathrm{Im}\{\boldsymbol{\mu}\cdot\mathbf{E}(\mathbf{r}_0,\omega)\}}{|\boldsymbol{\mu}|^2}, \tag{6.12}$$

$$\beta = \left(\frac{\gamma}{\gamma_0}\right)^{-1}\frac{3\pi c^3\varepsilon_0}{\omega^2}\frac{|\mathbf{u}_\mu\cdot\mathbf{e}|^2}{\mathrm{Re}\int dxdz\mathbf{u}_y\left(\mathbf{e}\times\mathbf{h}^*\right)} \tag{6.13}$$

Here, $\mathbf{u}_y$ and $\mathbf{u}_\mu$ are the unit vectors parallel to the waveguide axis y and the dipole moment $\boldsymbol{\mu}$, respectively. The total electric field is given by $\mathbf{E}(\mathbf{r},\omega)$ and evaluated at the position of the dipole, $\mathbf{r}=\mathbf{r}_0$, whereas the vectors $\mathbf{e}$ and $\mathbf{h}$ represent the respective electric and magnetic fields of the guided plasmon mode. Note that, whereas expression 6.12 is valid for any problem in which an oscillating dipole is the only source, the β factor in Eq. 6.13 is not. Indeed, such expression assumes that the dipole moment $\boldsymbol{\mu}$ lies within the xz plane, the CPP mode has low losses, and the nanostructure is translationally invariant along the y axis. We therefore cannot apply such expression to the VG+ND system where translational symmetry is broken, and a refined formula will have to be deduced. For now, however, we can employ the above simple equalities to extract preliminary information about the system.

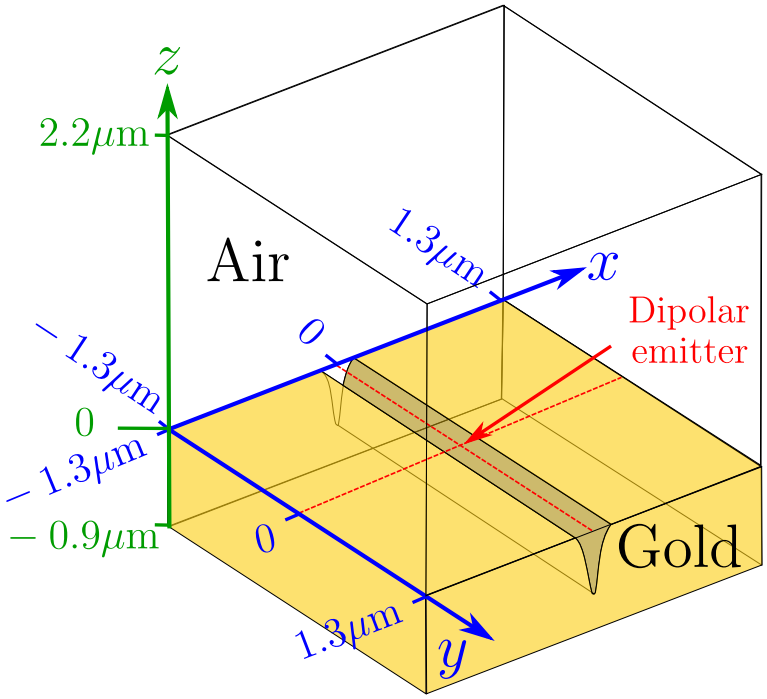

Figure 6.3: Schematic depiction of the simulation domain for the FEM calculations.

6.3.1. Modelling the NV centre as a suspended dipole emitter without the diamond host

The expressions deduced above allow for a first estimation of the properties of our hybrid QE-VG system. In this section, we theoretically calculate the Purcell and beta factors of a dipole emitter with the properties of the NV centre, placed in the vicinities of the VG under consideration. Since we are neglecting the diamond host in a first approximation, we can consider this a way of theoretically probing the modes of the VG by means of a fictitious emitter, in order to estimate the optimum configuration for a later placement of the ND. These simulations will provide very useful estimations of the emission properties, and represent a first step towards the refinement of the model in the following section.

Despite the translational invariance of the VG, the whole VG+dipole system does not have enough symmetries for an analytical solution. We thus perform a numerical analysis with the FEM software employed in the previous section. For a 3D simulation, the system has been confined inside a box of dimensions $2.6 \times 2.6 \times 3.1\mu$m (Fig. 6.3) where two main domains are defined, namely the metallic substrate with permittivity ε_m (Eq. 6.6) and the surrounding dielectric with $\varepsilon = 1$. In order to emulate an infinite system, all the walls of the simulation domain are terminated in perfectly matched layers

[406], designed to absorb any incident plane wave with wavevector perpendicular to the surface. The emitter is modelled as a current I_0 oscillating at a frequency $\omega = 2\pi c/\lambda_0$ along a segment of length $l \ll \lambda_0$, whose centre and orientation mark, respectively, the position and the direction of the dipole moment $\boldsymbol{\mu}$. The magnitude of such dipole moment is given by $|\boldsymbol{\mu}| = iI_0 l/\omega$ [407], where the arbitrary values for I_0 and l are chosen as $I_0 = 1\text{A}$ and $l = 2\text{nm}$ respectively. In our simulations, the emitter will be placed in a maximally symmetric position. Indeed, it will lie at the intersection between the two mirror symmetry planes of the VG, namely the vertical line given by $x = y = 0$ (see Fig. 6.3). We will perform FEM calculations for different heights of the QE, z_0, and dipole moments oriented along the three orthogonal directions x, y, and z.

After computing the radiated EM fields in this system, we can directly calculate the decay rate enhancement of the dipolar emitter through Eq. 6.12. We display such enhancement in Fig. 6.4 for three different wavelengths within the emission spectrum of the NV centre, namely 650nm, 690nm, and 750nm. Some general features arise regardless of the dipole orientation. First, when the emitter is close to the bottom of the VG, the DRE largely increases. This is a consequence of the dipole being too close to the metallic surface, where non-radiative ohmic losses arise due to absorption [22, 356, 361]. This region of the VG is not adequate for an efficient excitation of CPP modes, since the decay of the QE is dominated by these nonradiative processes. The second feature common to all the dipole orientations is the behavior for large values of z_0. Although the limiting value is not shown in panels 6.4a-c, it can be checked that, when the QE is so far from the bottom of the waveguide as to be outside of the VG ($z_0 > 510\text{nm}$), the Purcell factor tends to unity when increasing z_0, since the vacuum dipole emission is gradually less affected by the presence of the metal.

Apart from this common features, the DRE clearly shows a distinct behavior for a dipole oriented along the x axis, as shown in panel 6.4a. In this case, the regions of intermediate height $z_0 \sim 250 - 400\text{nm}$ are characterized by a large DRE, $\gamma/\gamma_0 \sim 5$, which can not be caused by ohmic losses since the QE is at a distance $\gtrsim 50\text{nm}$ from the metal [22]. Therefore, the faster emission is directed either into free-space modes or into CPPs. A comparison with the results for the $y-$ and $z-$oriented dipoles (panels 6.4b-c) strongly suggests that in this region the emission into CPP modes is the main decay channel, since the DRE reaches large values only when the dipole is parallel to the polarization of the CPP mode, namely x. On the other hand, when such dipole orientation is orthogonal to the x axis, the decay rate is strongly suppressed, and the QE decays much slower than in vacuum. This seems to indicate that, when the QE cannot couple to the main CPP mode due to an unfavourable dipole orientation, the

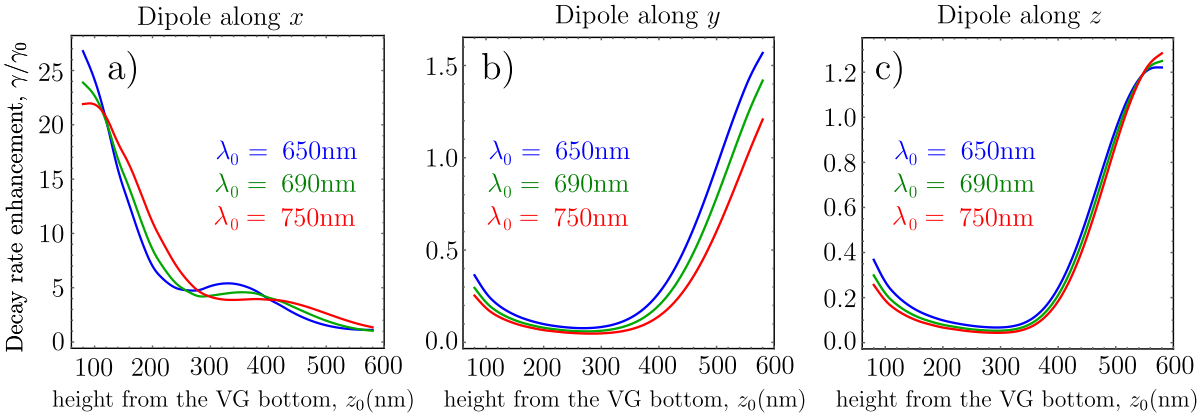

Figure 6.4: Decay rate enhancement for a dipole emitter in the presence of the VG, for three different emission wavelengths within the spectrum of the NV centre. The panels a,b, and c correspond to a dipole moment oriented along the x, y, and z axis, respectively.

coupling to other decay channels (in this case, only free-space modes) is not very efficient.

In order to determine if the above physical argument is correct, we calculate the β factor by means of Eq. 6.13. The result is displayed in Fig. 6.5a, for a dipole oriented along the x direction. For $z_0 \sim 200 - 350$nm, the coupling to the CPP mode is very large, reaching values of $\sim 70\%$. Such region of heights above the bottom of the VG is therefore very convenient for the design of our hybrid device. Note that, for smaller values of z_0, the beta factor largely decreases despite the field intensity of the CPP mode being still large (see inset 6.2b), a signature of the aforementioned ohmic losses in the metal. The beta factor also decreases for $z_0 \gtrsim 350$nm, not only because the modal field of the CPP is less intense, but also because the QE is closer to the top of the VG and thus the coupling to free-space modes increases.

In Fig. 6.5a, the results for the $z-$orientation have been disregarded since the associated β factor is extremely small, even if the DRE appearing in the denominator of Eq. 6.13 is very low (see Fig. 6.4c). This poor coupling efficiency is a natural consequence of the tiny component of the electric field along the z direction, which is close to our numerical resolution. Note that such a small electric field indicates not only the absence of significant coupling to the CPP, but also the extremely low emission into radiative modes, which remain as the only possible decay channel. The inability of the dipole emitter to couple to free-space modes can be understood by noting that the aperture of the VG at the top, namely 315nm, is smaller than $\lambda_0/2$, and therefore the radiation leakage is severely hindered by the diffraction limit. On the one hand, this condition facilitates the large beta factors for dipoles oriented along the x axis. On the other hand,

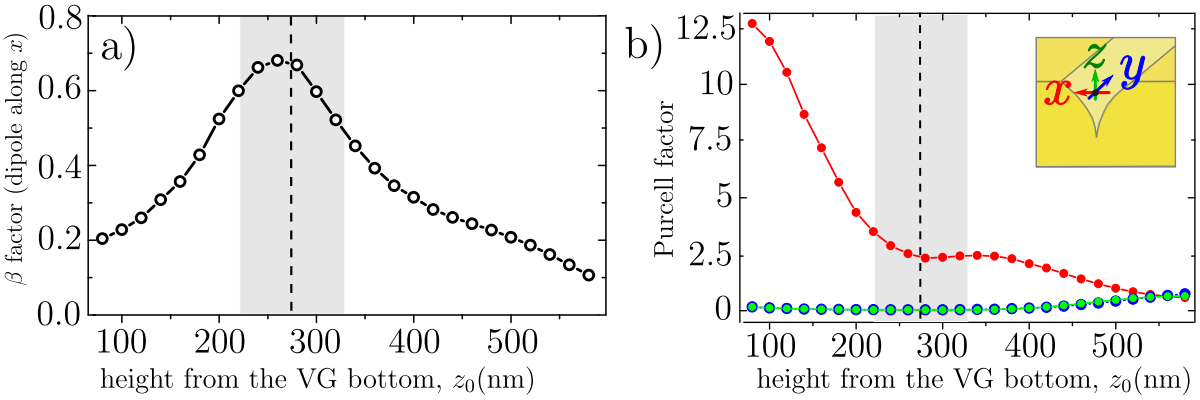

Figure 6.5: a) Beta factor for the QE dipole moment aligned with the x axis. The corresponding factor for both y and z orientations is practically zero (see main text). b) Averaged estimation of the Purcell factor for the dipolar QE oriented along he three Cartesian axis. In both panels, the grey area represents the possible positions of the NV if it was embedded in a 60-nm-radius nanodiamond host lying inside the VG.

it strongly suppresses the decay rate of the other two orientations for intermediate values of z_0, since the QE cannot efficiently couple to any of the three possible decay channels, namely free-space modes, CPP modes, or ohmic losses. As a final remark, note that although the β factor can not be easily calculated for the dipole oriented along y, both the above argument and the tiny value of E_y obtained in our simulations suggest that the beta factor is also negligible in this situation.

So far we have determined the optimum configuration of our hybrid QE-PW device, namely a position 200nm$\lesssim z_0 \lesssim$ 350nm above the VG, and a dipole moment aligned along the x axis. When such conditions are fulfilled, the system is characterized by a large beta factor and DRE. However, in order to properly estimate both the experimentally observed enhancement of the decay rate and the FOM, we need to compute the Purcell factor through

$$P_F = \frac{\gamma}{\gamma_{\mathrm{ND}}} = \frac{\gamma}{\gamma_0}\left(\frac{\gamma_{\mathrm{ND}}}{\gamma_0}\right)^{-1}. \tag{6.14}$$

The first quotient in the above formula is the DRE displayed in Fig. 6.4. In order to obtain an estimation for an experimental measurement of this quantity, we average the values of γ/γ_0 for the three different values of λ_0 in the figure, by weighting the contribution of each wavelength to the NV emission spectrum. The second component of the Purcell factor, $\gamma_0/\gamma_{\mathrm{ND}}$, represents the DRE of the same dipolar emitter when it is placed inside a ND. We estimate this quantity through a new series of FEM calculations, in which

the VG is absent, and the dipole emitter is surrounded by a diamond sphere ($\varepsilon = 5.737$) suspended in vacuum. We average the results obtained for different sphere radii in the interval given by the experimental size of the nanodiamonds, i.e., $r \in (40, 80)$nm. Finally, we carry out the same simulations for $\lambda_0 = 650$nm, $\lambda_0 = 690$nm, and $\lambda_0 = 750$nm, and perform the average as detailed above to obtain a final value of $\gamma_{\mathrm{ND}} = 1.93\gamma_0$. At this point we are able to calculate the Purcell factor according to Eq. 6.14, which we display in Fig. 6.5b. In the region of interest, the Purcell factor remains approximately constant at $P_F \approx 3$, yielding an estimated FOM of ~ 11.5.

The particular value of our estimated FOM is not the main point of this section, since in the following section we will refine such estimation by including the ND host in all our simulations. Indeed, the relevant conclusion of our calculations in the absence of the diamond host is the importance of controlling the position of a single QE inside the VG structure. Whereas in nanowire PWs the optimal distance between the QE and the metallic surface is approximately 10nm [59, 76, 211, 395], our VG devices are favourable to QEs located $\sim$ 50nm away from the metallic surfaces. This allows for high Purcell and beta factors while maintaining a low nonradiative decay rate. Additionally, the apparent difficulty of suspending a given QE at the optimum height within the VG is already solved in the case of our NV centres. Indeed, the NVs are contained inside a nanodiamond host of $40 - 80$nm radius, which acts as a natural spacer between the emitter and the metallic surfaces. By letting a spherical ND with a radius $\sim$ 60nm fall into the VG, the position of the single NV will automatically lie within the optimum coupling region (see the shaded areas in Fig. 6.5). This makes our NV-ND very interesting as a hybrid device, and motivates a theoretical approach to the complete system in which the ND is explicitly included.

6.4. Numerical simulation of the complete NV-VG hybrid device.

The results obtained above suggest that the NV-VG hybrid device can display a FOM as large as $\sim$ 11. Motivated by these estimations, we devote this section to the study of the full system including the ND host, in order to predict the experimental measurements of Purcell and β factors in a more accurate way. The problem we intend to solve is very similar to the one analyzed above, albeit the estimation of some quantities, namely the beta factor, are more involved. The simulation box employed for the FEM calculations is

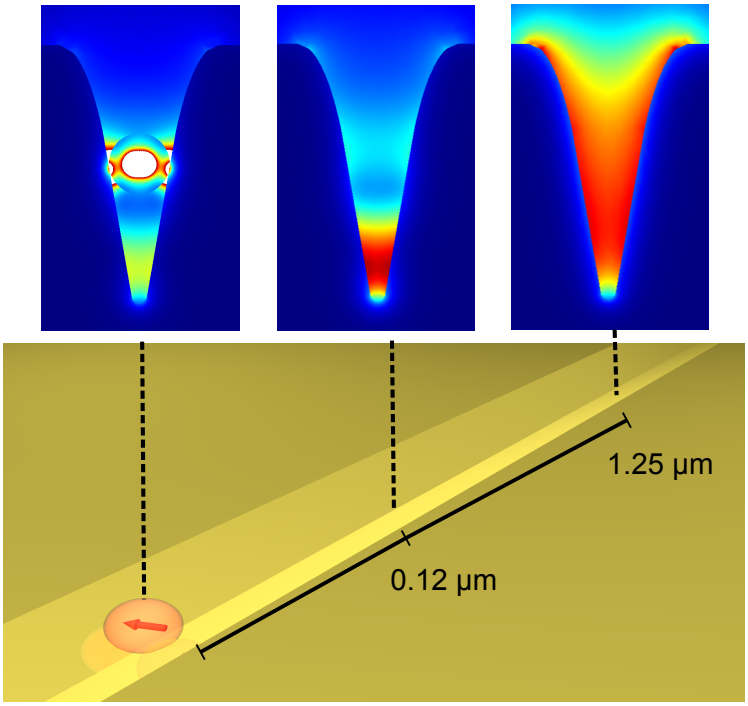

Figure 6.6: Normalized electric field maps for three different transversal cuts of the VG (dipole oriented along the x axis). Already at a distance 1.25μm away from the QE, the electric field profile resembles that of the VG-supported CPP mode. The colour scale in each panel has been adjusted for a better view.

identical to the one of Fig. 6.3. In this case, we add a nanodiamond host around the QE, modelled as a dielectric sphere with permittivity $\varepsilon = 5.737$ [408] and radius 60nm. The sphere is allowed to fall inside the VG, such that its centre lies 276nm above the bottom of the VG. Both the centre of the ND and the dipole representing the NV are placed at $x = y = 0$, and we perform simulations for different heights z_0 of the dipole inside the nanosphere. In this situation, the emitted field intensity at the position of the dipole is modified by the presence of the host, as the left panel of Fig. 6.6 shows. Remarkably, however, the 2D CPP mode profile of Fig. 6.2b is recovered at a short distance from the QE, as illustrated in Fig. 6.6 (right panel). This evidences that the ND only represents a small perturbation of the modal structure, and that the possibility of QE-CPP coupling remains regardless of the host.

In order to quantify the properties of this QE-PW device, it is necessary to calculate both the Purcell and the beta factors. The former is determined directly from the EM fields calculated in our FEM simulation, exactly in the same way as in the previous section. However, the calculation of the β factor is more involved, since the presence of

the ND host breaks the translational symmetry of the nanostructure in which the dipole emitter is embedded. Therefore, the useful relation 6.13 is no more valid, and a different method has to be employed. We start by rewriting Eq. 6.11 in the following way,

$$\beta = \frac{W_{\mathrm{CPP}}}{W} = \frac{W_{\mathrm{CPP}}}{W_0\,(\gamma/\gamma_0)}. \tag{6.15}$$

The denominator on the right-hand side of the above equation can be determined by means of the DRE in Eq. 6.12, and the power emitted by a dipole in vacuum (see appendix D),

$$W_0 = \frac{|\boldsymbol{\mu}|^2}{4\pi\varepsilon_0}\frac{\omega^4}{3c^3}. \tag{6.16}$$

For the calculation of W_{CPP}, on the other hand, we would in principle need to obtain the eigenmodes of the 3D structure. Since the calculation of such modes is exceedingly involved, it is very convenient to find an expression of W_{CPP} in terms of the CPPs of the bare VG, calculated in previous sections (see Fig. 6.2). Such modes are the solution of the two-dimensional mode equation 6.5 and, due to their translational symmetry along the y axis, they can be expressed as [409]

$$|n\rangle \equiv |n(\mathbf{r}_\perp)\rangle = \{\mathbf{e}_n(\mathbf{r}_\perp), \mathbf{h}_n(\mathbf{r}_\perp)\}, \tag{6.17}$$

where $n = \pm1, \pm2, \pm3, ...$ We only consider the fundamental CPP band, $|\mathrm{CPP}_{2D}\rangle$, which corresponds to $n = \pm1$, the negative indices describing modes propagating in the negative z direction. The vectors $\{\mathbf{e}_n, \mathbf{h}_n\}$ stand for the electric and magnetic modal fields, respectively, and $\mathbf{r}_\perp = (x, z)$ represents the coordinate vector in the transverse plane. The overlap between two different modes of the bare VG is related to the total power transferred from one to the other, and can be employed to write the following orthogonality relation [197]

$$\langle n|m\rangle = \int d\mathbf{r}_\perp \mathbf{u}_y \cdot [\mathbf{e}_n(\mathbf{r}_\perp) \times \mathbf{h}_m^*(\mathbf{r}_\perp)] = \mathrm{sgn}(m)\delta_{nm}. \tag{6.18}$$

Here, sgn represents the sign function, and δ_{nm} the Kronecker delta.

In the more complex structure under consideration, namely VG+ND, the translational symmetry is broken, and the eigenstates of the system generally depend also on the longitudinal coordinate, $|n(y)\rangle$. Fortunately, in the case of the CPP modes, $|\mathrm{CPP}_{3D}(y)\rangle$, we know from Fig. 6.6 that, aside from a small region in the close vicinities of the ND, they are practically identical to the 2D CPP mode described above. In other words, at a distance y_0 far enough from the origin, the following relation holds,

$$|\mathrm{CPP}_{3D}(y_0)\rangle\Big|_{\text{large } y_0} \approx |\mathrm{CPP}_{2D}\rangle. \tag{6.19}$$

This relation is key to obtain a simple expression for the power W_{CPP}.

Let us now consider the total EM field emitted by the dipole, $|f(\mathbf{r}_\perp, y)\rangle$, which we have calculated in our FEM simulations. This field contains contributions from both radiative modes and from the main CPP mode, $|\mathrm{CPP}_{3D}(y)\rangle$. The power radiated into the latter modes can be formally expressed as [197, 409]

$$W_{\mathrm{CPP}} = |\langle f(\mathbf{r}_\perp, 0)|CPP_{3D}(0)\rangle|^2. \tag{6.20}$$

Our objective is to determine the overlap above in terms of the already obtained 2D CPP modes. To do this, we can calculate it at a distance $y_0 > 0$ away from the origin, where due to the relation 6.19 we can write

$$\langle f(\mathbf{r}_\perp, y_0)|\mathrm{CPP}_{3D}(y_0)\rangle \approx \langle f(\mathbf{r}_\perp, y_0)|\mathrm{CPP}_{2D}\rangle = \frac{\int d\mathbf{r}_\perp \mathbf{u}_y \cdot [\mathbf{E}(\mathbf{r}_\perp, y_0) \times \mathbf{h}^*(\mathbf{r}_\perp)]}{\left(\int d\mathbf{r}_\perp \mathbf{u}_y \cdot [\mathbf{e}(\mathbf{r}_\perp) \times \mathbf{h}^*(\mathbf{r}_\perp)]\right)^{1/2}}. \tag{6.21}$$

In the equation above, $\mathbf{E}(\mathbf{r}_\perp)$ is the total electric field obtained in our 3D simulations, and $\mathbf{e} \equiv \mathbf{e}_1$ and $\mathbf{h} \equiv \mathbf{h}_1$ are the electric and magnetic fields of the 2D CPP mode, respectively. The denominator of Eq. 6.21 is the normalization required for the modal fields to satisfy the orthogonality relation Eq. 6.18. Note that the square modulus of the overlap 6.21 has units of power, and therefore we can write

$$|\langle f(\mathbf{r}_\perp, y_0)|\mathrm{CPP}_{3D}(y_0)\rangle|^2 = \frac{\left|\int d\mathbf{r}_\perp \mathbf{u}_y \cdot [\mathbf{E}(\mathbf{r}_\perp, y_0) \times \mathbf{h}^*(\mathbf{r}_\perp)]\right|^2}{\int d\mathbf{r}_\perp \mathbf{u}_y \cdot [\mathbf{e}(\mathbf{r}_\perp) \times \mathbf{h}^*(\mathbf{r}_\perp)]} = W_{\mathrm{CPP}}(y_0). \tag{6.22}$$

The notation $W_{\mathrm{CPP}}(y_0)$ stems from the interpretation of the above equation, which is clear in terms of EM powers. Indeed, the above expression represents the contribution of the CPP mode to the total power carried by the electric field at the position y_0 along the waveguide [197]. The final step is to relate the above quantity with the overlap at $y = 0$, which appears in Eq. 6.20. Naturally, the power emitted into the 3D-CPP modes decays exponentially with the coordinate y_0, at a rate inversely proportional to the propagation length of such CPP, $\sim e^{-y_0/L_p}$. Additionally, in our system the presence of the ND only slightly perturbs the mode structure of the infinite VG, an argument supported by the results displayed in Fig. 6.6. As a consequence, we can approximate the propagation length of the 3D CPP mode as that of the 2D CPP, calculated in Eq. 6.7. In this approximation, the power radiated into the 3D-CPP mode at $y = 0$ is simply given by

$$W_{\mathrm{CPP}} = W_{\mathrm{CPP}}(0) = W_{\mathrm{CPP}}(y_0)e^{y_0/L_p} = e^{y_0/L_p}\frac{\left|\int d\mathbf{r}_\perp \mathbf{u}_y \cdot [\mathbf{E}(\mathbf{r}_\perp, y_0) \times \mathbf{h}^*(\mathbf{r}_\perp)]\right|^2}{\int d\mathbf{r}_\perp \mathbf{u}_y \cdot [\mathbf{e}(\mathbf{r}_\perp) \times \mathbf{h}^*(\mathbf{r}_\perp)]}, \tag{6.23}$$

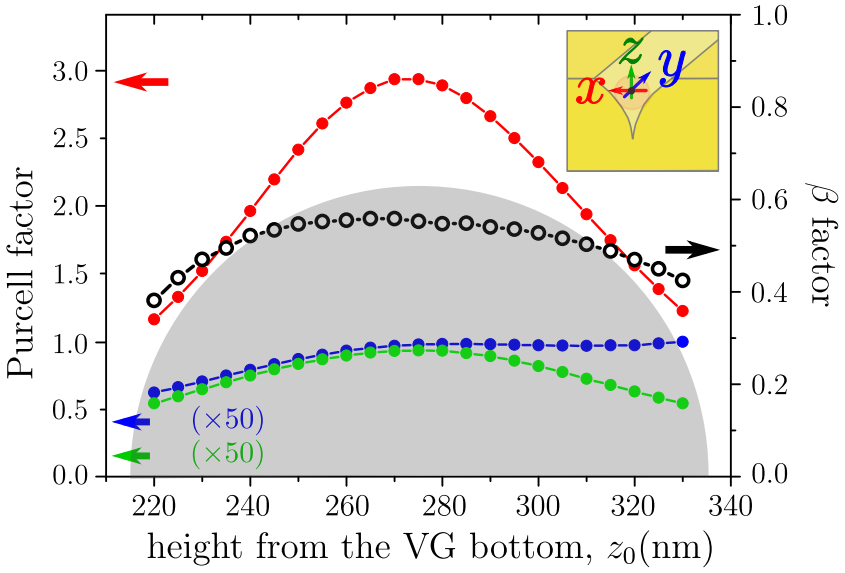

Figure 6.7: Purcell factor for an NV-ND system inside the VG, for a dipole oriented along x (red), y (blue), and z axis (green), and beta factor (back line) for a dipole oriented parallel to the x axis. The shaded region shows the spherical contour of the nanodiamond.

which is a function only of the calculated 3D field and the properties of the 2D CPP mode of the VG. The above equation, combined with the definition 6.15, allows for the calculation of the beta factor in this system. We have checked that the above equation is correct by reproducing the beta factors in the absence of the diamond host.

The final results obtained for the Purcell and beta factor in this case are shown in Fig. 6.7, where the NV emission displays a similar behavior as the one shown in previous sections. Again, the Purcell factor is extremely low for dipole orientations along y and z, indicating a very inefficient coupling to both CPPs and free-space modes. Indeed, the beta factors for y and z directions are not displayed in the figure since their values are practically zero. On the other hand, for a dipole oriented along the x axis, the coupling efficiency between the QE and the CPP mode is still very large, only decreasing slightly as compared to the bare dipole case. For a QE placed in the centre of the ND sphere, the beta factor rises up to $\beta = 0.56$, while the Purcell factor remains at a moderate value of $P_F = 3.0$. The resulting FOM, 11.1, is also very similar to the previously obtained result, and significantly larger in comparison with other proposed implementations based on colloidal nanowires [59]. The simulations carried out in this section show that the presence of the ND host does not modify the efficiency of the hybrid QE-PW system in a drastic way. Moreover, our results unambiguously demonstrate how the NV-VG system can display efficient emitter-CPP coupling in a realistic situation, therefore motivating

an experimental implementation.

6.5. Overview of the experimental realization

This section is devoted to a brief description of the experimental realization of the NV+VG system studied in this chapter. The experiment was carried by Esteban Bermúdez and other members of Romain Quidant's group at ICFO. We will describe here the three main steps along such experiment, namely characterization of the NV centres and the VG waveguide, assembly of the hybrid device, and demonstration of NV-CPP coupling and measurement of the FOM. Since we present here only the key points, we address the reader to ref. [125] for a detailed description of the full experimental procedure.

The first step towards the calculation of the FOM relies on the separate characterization of the two components of the hybrid device, namely NV centres and VG. In the case of the NVs, it is necessary to measure their intrinsic lifetime τ since, as we have discussed above, such lifetime depends strongly on the size of the ND host and is in general very different from the bulk lifetime $\tau_{\text{bulk}} \sim 11.6\text{ns}$. In order to determine this value, the NV in solution were deposited onto a glass substrate, which can be considered optically inert in terms of lifetime enhancement. This allows for an optical probing of individual NDs, yielding an average experimental lifetime

$$\tau_{ND} \approx \tau_{\text{glass}} = 24.2 \pm 7.2\text{ns}. \tag{6.24}$$

Regarding the characterization of the plasmonic VG, only the measurement of the propagation length is necessary. This parameter was determined in the experiments by placing multiply occupied NDs inside similar VGs and measuring the out-coupled light intensity at the tapered nanomirrors. Such measurement yielded a propagation length

$$L_p = (4.6 \pm 0.5)\,\mu\text{m}, \tag{6.25}$$

very close to our theoretical predictions in Eq. 6.7.

Once both components are characterized, the experiment goes on with the assembly of the NV+VG device. First, several NDs are positioned in an ordered array in the close vicinities of the VG (Fig. 6.8a). Then, a ND hosting a single NV is identified by measuring second order correlations in the fluorescence emission [26, 410]. Finally, by means of an AFM tip the chosen ND is displaced along the surface until it falls inside the

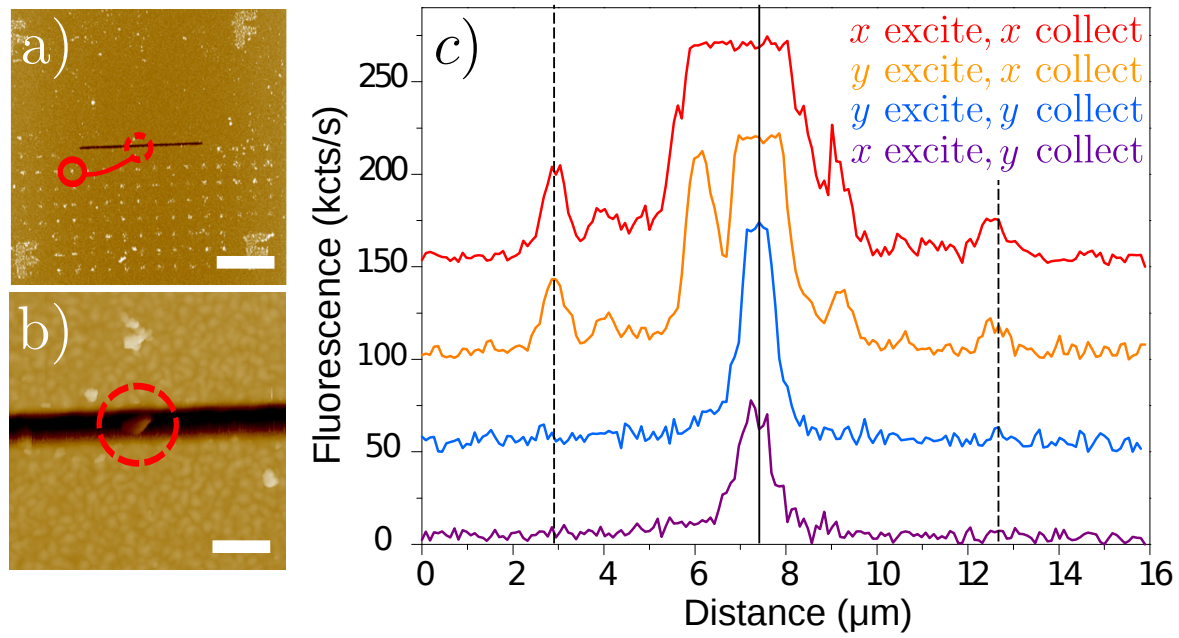

Figure 6.8: (reproduced with permission from the authors) a) AFM image of NDs positioned in the vicinity of the VG. The solid and dashed lines indicate, respectively, the position of the chosen ND containing a single NV centre and the position of the VG where it will be positioned. The scale bar is 5μm. b) Image of the positioned ND. The scale bar is 500nm c) Fluorescence counts along the VG axis. The solid and dashed vertical lines mark the centre and the two ends of the VG, respectively. Results are shown for four different combinations of excitation and collection polarization.

VG. The same tip can be employed to image the resulting device, confirming that the ND is placed within the plasmonic structure (Fig. 6.8b). The device is now assembled and ready for the study of NV-CPP coupling.

The final part of the experiment consists on demonstrating the emission of the NV centre to CPP guided modes, as well as measuring the FOM. The emission properties of the coupled NV are determined by fluorescence measurements, where additional precautions have to be taken in order to account for undesired processes such as the excitation of gap or wedge modes at the edges of the VG and, more importantly, the effect of gold autofluorescence [125]. By means of the fluorescence measurements, the lifetime of the NV centre once it is coupled to the VG is determined. By comparing the result to the bare lifetime measured above, Eq. 6.24, the following experimental value for the Purcell factor is obtained,

$$P_F = 2.3 \pm 0.7. \tag{6.26}$$

The increase in the decay rate of the NV centre evidences the coupling to the VG nanostructure. Additionally, the experimental P_F is close to the theoretical prediction for the optimal dipole orientation ($P_F \sim 3$), suggesting that the dipole moment is at least partially oriented along the beneficial axis (labelled x in previous sections) for coupling to the CPP.

The only remaining measurement is that of the coupling efficiency or β factor. First, the coupling of the NV emission to CPP modes is demonstrated by the bright fluorescence spots arising at the two ends of the VG, as displayed in Fig. 6.8c. The fact that these out-coupled photons are transversely polarized indicates that the fundamental CPP plays the main role in the transport of energy across the PW. Once the NV-CPP coupling has been experimentally demonstrated, it is possible to determine the β factor by comparing the photon counts detected at the two ends of the VG and those detected right above the ND, which arise from emission to free space. Since, during the assembly process, an NV centre showing a low nonradiative decay rate has been explicitly chosen [125], this decay channel can be neglected. Therefore, the photon count measurements described above completely determine the coupling efficiency as

$$\beta = 0.42 \pm 0.03. \tag{6.27}$$

This is a remarkably large value taking into account that the experimentalists did not have control over the dipole orientation of the NVs inside the VG and, according to our simulations, for both y and z orientations the beta factor would be extremely small. The above experimental measurement is thus consistent with the transverse component of the NV dipole moment being very large, and indicates an efficient NV-CPP coupling.

By combining the values obtained for the Purcell and beta factors, Eqs 6.26 and 6.27, with the propagation length in Eq. 6.25, the following value for the figure of merit is obtained for this device,

$$\text{FOM} = 6.6 \pm 1.5. \tag{6.28}$$

Despite being small as compared to the theoretical prediction, it is $\sim 50\%$ larger than the value 4.2 ± 1.9 extracted from similar devices based in colloidal quantum dot-silver nanowire systems [59]. Additionally, the experimental team checked that the ND-VG device was highly reproducible by preparing a second analogous device and measuring a very similar performance, namely $P_F = 2.1 \pm 0.6$ and $\beta = 0.41 \pm 0.05$. This experiment therefore demonstrates the possibility of efficiently and deterministically coupling single quantum emitters to channel plasmons, in a configuration that is able to outperform similar hybrid devices with respect to the proposed FOM.

6.6. Conclusions

In this chapter we have introduced a hybrid QE-PW device in which the efficient coupling of an NV centre to propagating plasmons has been demonstrated. We have achieved this by means of a plasmonic VG waveguide, a good candidate for integrated circuitry since it combines relatively low losses with subwavelength confinement of the EM field, as well as flexible and realistic circuit designs. The choice of ND-NV centres as suitable QEs is very appropriate, since the ND acts as a natural spacer which prevents nonradiative decay. The device thus combines the very large field enhancement of the VG with the stable and bright character of the NV as a single photon source.

Our theoretical results demonstrate the efficiency of this hybrid device quantified through a figure of merit (FOM) combining propagation length, Purcell factor, and beta factor. According to our predictions, the system is able to achieve a good tradeoff between these values, being able to outperform previous implementations in colloidal nanowires. This has been experimentally demonstrated by our collaborators at ICFO. Regarding such experimental implementation, the device presented in this chapter benefits from a top-down fabrication technique that can enable functional and highly controllable plasmonic circuitry. Additionally, our simulations leave room for a twofold improvement in terms of achievable FOM, provided that a larger degree of control is achieved over the critical parameters such as defects along the VG and the dipole orientation of the NV centre.

Since usually the realization of quantum protocols, such as the ones presented in chapters 2 and 3, requires larger beta factors, other systems like photonic crystal waveguides are often chosen for this purpose [411–413]. However, as illustrated in chapters 4 and 5, the attractive properties of plasmonic systems make them also unique platforms which could bring significant advantages in this field [124, 414]. Only few works have been devoted to the improvement of plasmonic devices for quantum applications [59, 392, 415–417] and, therefore, the demonstration of such an efficient device as the one achieved in this chapter represents an advance along a promising path. The reproducibility of the experiment makes this system a secure platform over which present plasmonic devices can be improved and, potentially, basic quantum circuitry could be implemented.

7 | General conclusions and outlook

7.1. English

The research activity we have carried out in this thesis covers different areas related to quantum nanophotonics. The first two chapters (2 and 3) are devoted to the growing field of waveguide QED, which aims to develop a platform for quantum optics and quantum networks able to exploit the advantages of waveguide systems. On the other hand, in chapters 4 and 5, we study plasmonic systems in the collective strong coupling regime, where light and matter hybridize into superposition states which inherit properties of both constituents. Finally, chapter 6 lies between both the above disciplines, since it is devoted to the study of a realistic waveguide platform for quantum plasmonics. In this last chapter we present the general conclusions of the thesis, together with a brief overview of both the current status and the prospects of the different lines of research.

7.1.1. Waveguide QED

As we discussed in the introductory chapter 1, the possibility of generating entangled states between qubits is an essential resource for quantum computation and modern quantum simulation. One of the possible ways of entangling qubits is to couple them to a common environment which, by mediating the interaction, can lead to the spontaneous formation of entanglement from an initial product state. Due to their potential as basic components of quantum networks, waveguides are especially appealing candidates for implementing this kind of protocols [62], a proposal that previous studies have already demonstrated [106, 107]. Based on these works, in chapter 2 we have focused on the study of dissipative entanglement generation between two qubits coupled to a waveguide. In the first part of the chapter, we have applied to this problem the waveguide QED

Hamiltonian developed by Fan et al. [196], in order to determine the adequacy for the case of waveguides of the Markovian master equation, usually employed in cavity QED. We have shown how such master equation fails to predict non-Markovian dynamics that arise either for large qubit-photon coupling or for very separated qubits. Our results demonstrate that, in order to capture the rich phenomenology arising in waveguide systems, a description of the photonic modes beyond the Markovian approximation is required.

The main advantage of the above scheme for entanglement generation is the long lifetime of the resulting entangled state when the qubit-qubit separation is a half-integer multiple of the emission wavelength, as such state becomes a dark state with respect to the waveguide. However, this mechanism intrinsically sets an upper bound of 0.5 for the generated concurrence, thus limiting the achievable amount of entanglement. Another drawback of this protocol is the extreme sensitivity to small perturbations in both the qubit-qubit separation and the detuning between the qubits transition frequencies. These limitations can be overcome when the waveguide-qubit coupling is chiral, as we demonstrate in the second part of chapter 2. In this case, the maximum achievable concurrence is shown to increase by 50%, a value that is also very robust against variation of the system parameters. Although the dark resonance disappears in this case, making the entanglement lifetime shorter than in the previous situation, such lifetime can in principle be controlled through the waveguide-qubit coupling. We believe that our chiral protocol relaxes some strict requirements in terms of an experimental realization of waveguide-mediated entanglement generation. Note that, aside from a fundamental insight on the generation of two-qubit entanglement, our results shed light to the dynamics of the basic unit of chiral quantum networks [214] which, according to recent predictions, could have a strong impact in quantum optics [109, 418]. Furthermore, during the development of this thesis, the waveguide-mediated entanglement generation has been extended from the two-qubit case to a system of N emitters, where efficient methods of generating mesoscopic entanglement have been proposed in both non-chiral [419] and chiral systems [420]. These promising works already demonstrate a platform for basic quantum simulation, and represent a further step toward waveguide-based quantum computing.

The schemes for entanglement generation studied above do not fully exploit the built-in input/output ports of waveguides, which in principle allow for a modification of the state of coupled qubits by means of photon scattering. Therefore, in chapter 3, we have studied the generation, manipulation, and detection of entanglement in waveguide QED by means of few-photon inputs. We have demonstrated how an impinging guided photon is able to generate entanglement between two qubits initially in their ground state, and

how a two-photon wavepacket can reshape the generated entanglement pulse by means of the so-called sudden death and revival of entanglement. Finally, we have demonstrated that the scattering output of a single-photon probe contains information about the entanglement between the qubits, initialized in an arbitrary single-excitation state. Based on this correspondence, we have devised a method for entanglement detection that is independent on the particular parameters of the waveguide or the QEs, therefore easing the demanding requirements associated to other schemes such as full state tomography [228]. Note that our work is by no means the only recent research demonstrating interesting physics based on few-photon scattering in waveguide QED. Starting from the early results on full inversion of qubits [190] or perfect reflection of single photons [199], many different phenomena have been uncovered in scattering problems such as multi-photon bound states [198, 265] and the presence of quantum beats [77]. Such fundamental understanding of the processes governing the interaction between matter and guided light has been also complemented by realistic proposals for waveguide-based quantum computations on four level systems [271]. As of today, all of this research lines are still being developed and extended but, although promising, these works still remain somehow disconnected from each other. It is not unrealistic to think, however, that in the forthcoming years we will witness a unification effort, aimed toward the integration of all the different relevant results in the field into a scattering-based platform for complex quantum operations at a larger scale.

The final topic related to waveguide QED systems goes further along the way to fully exploit the flexibility of such setups, this time using matter to modify the state of photonic inputs. In the second part of chapter 3, we have employed a chirally coupled three-level system to perform nonreciprocal operations on guided photonic qubits. In the single-photon regime, a simple rectifier or router has been devised, in which a photon is completely transferred to a second waveguide. Based on such principle, we have been able to implement a single-photon diode and a two-photon transistor, both of which display large efficiencies for realistic parameters. Our results demonstrate true nonreciprocity at the single-photon level, a property that usually remains elusive at such scale. As in the case of scattering-based applications, our work represents just a small fraction of the research in the field of few-photon quantum gates, which has largely increased in the last years. Indeed, the design of devices specifically adapted to waveguides has been advancing in parallel to the evolution of waveguide QED, from the early proposals of basic plasmonic transistors [75] to almost any imaginable gate in the few photon regime, such as nonlinear operations for single [421] and two photon inputs [422], phase shifters [120], and many more. In the last years, the implementation of efficient chiral coupling

schemes has represented a final breakthrough, since it has opened the way toward the design of otherwise involved devices such as our diode/transistor in chapter 3, isolators [121] or optical circulators [423]. Regarding quantum photonic devices it is clear that, in the next years, interfacing the enormous available variety of few-photon gates within compact and functional complex photonic chips is a path not only worth pursuing, but necessary in order to take the next step toward the realization of nanophotonic quantum technologies.

As for the prospects of waveguide QED, I think it is not realistic to assume that future research will bring exclusively waveguide-based complex quantum devices. On the other hand, waveguides are becoming more and more sophisticated as standalone light-matter interfaces, and it seems evident that forthcoming quantum technologies will incorporate such systems in combination with cavities. From the theoretical point of view, this is a challenging goal as it surely requires the improvement of state of the art problem solving methods. During the last years, the analysis of waveguide QED problems has largely evolved from the first input-output [195] or cavity array formalisms [424], into very complex models such as the Lehmann-Symanzik-Zimmermann reduction [194]. Despite such undeniable improvements of the analytical toolbox for waveguide QED, all these fully analytical approaches seem to have already reached their limit as the problems become impracticably difficult in the presence of, among others, more than 2 photons, external pumping, waveguides with complex dispersion relations, or significant photon propagation losses. Fortunately, recent works have been able to successfully study some of these otherwise intractable problems with advanced numerical techniques such as Matrix Product States [425], a very promising method that represents one of the main theoretical resources for waveguide QED in the next decade. The combination of these advanced numerical tools, the wide variety of waveguides available experimentally, and their intrinsic potential for quantum applications suggest that the research in waveguide QED will continue to increase in the years to come.

7.1.2. Collective strong coupling in quantum nanophotonics.

The second main topic of this thesis concerns the collective phenomena arising when an ensemble of QEs is strongly coupled to the EM field. First, in chapter 4, we have studied the spatial distribution of the excitonic population under weak and coherent pumping of one QE in the ensemble. Our main result in that chapter is the demonstration of dark state delocalization, where states uncoupled to the light modes can inherit their spatially extended character, as long as such modes are discrete. Interestingly, in the

case of plasmonic structures, the high loss rates of the surface plasmon modes make the polaritons very lossy, and hence dark states become much more efficient at spreading excitations across the ensemble of QEs. After, we have continued in chapter 5 by studying a related problem, namely that of exciton transport under incoherent excitation. Based on previous results demonstrating an increase in the exciton conductance for an ensemble of QEs strongly coupled to a homogeneous cavity mode, we have devised a strategy to tune such conductance increase by means of inhomogeneous field profiles. Moreover, using a plasmonic nanostructure with highly confined eigenmodes, we have demonstrated how excitons can be efficiently harvested in subwavelength spatial regions. We have also shown that dark states play a relevant role also in the case of incoherent pumping. Finally, we have studied how, under certain conditions, the intricate interplay between dark states and polaritons allows for a dephasing-assisted exciton transport, a potential advantage in organic molecules with high dephasing rates.

The delocalized character of the system eigenstates is the fundamental mechanism in which all the above results are based. It is worth noting that the requirement of a local and coherent pumping of the ensemble of QEs hinders the experimental observation of this effect in conventional microcavities, where the QEs are only indirectly coupled to the environment, and thus only the cavity modes can be efficiently populated [30]. In order to observe our results in such systems, the only remaining option would be electrical pumping schemes [426] which, however, are limited by material properties and can only provide incoherent excitation. In this regard, quantum nanophotonic structures can make a difference not only due to the wide variety of available resonators, but also because most of such resonators are *open cavities*, where QEs can be addressed directly by means of external sources. Combined with the excellent available tools for single-molecule excitation such as near-field optical probes [317] and excitation-reemission of an external probe emitter [201], nanophotonic resonators reveal as ideal candidates to observe many phenomena related to dark states and, specifically, their delocalized character.

One of the interesting features of the dark state delocalization and the associated exciton transport enhancement is their weak dependence on the cavity losses. Indeed, most of the phenomena studied in chapters 4 and 5 are observable in very lossy cavities. This is a particular advantage in plasmonic structures, whose main drawback for usual quantum nanophotonics is their large loss rate. Thus, for the particular applications where such loss rate is irrelevant, plasmonic resonators become excellent quantum nanophotonics platforms. First, their large field confinement allows for very large Rabi splittings, and thus they easily reach the CSC regime [334]. Second, they allow for a subwavelength tailoring of the electric field intensity and, consequently, of the light-matter interaction.

This enables not only highly-efficient exciton harvesting as studied in chapter 5, but also the realization of extremely compact excitonic devices. I believe these features should be exploited in future research, especially since there is still room for optimization of such systems. Some of the future challenges along this path are to increase the harvesting distances or to tailor the field profiles to design excitonic circuits based on EM hot-spots. The careful engineering of plasmonic nanostructures could also significantly improve the present designs, for instance in terms of miniaturization of excitonic devices. Even some structures already available in classical plasmonics could be readapted to this purpose. For instance, the multiresonant arrangement of nanoantennas in Ref. [427] may be employed to efficiently harvest excitons from molecules of different transition energies, or for frequency multiplexing in a photon-exciton circuit. Although exciton-plasmon circuits and devices seem not able to compete with state of the art nanophotonic circuitry, it is likely that they will find a niche within future integrated hybrid devices, especially whenever organic molecular QEs are involved.

As a final comment, it is worth noting that, from a fundamental point of view, the phenomenon of dark-state delocalization is not exclusive of an EM environment. Thus, a second interesting line for future research consists on applying the same principle to other environments, for instance a collective phonon bath. Since strong coupling to single or multiple phononic modes can be achieved in some systems even at room temperature [428], it is in principle conceivable that a delocalized "dark" phononic state can be employed to transport excitations across molecular ensembles or other systems. A deeper study of phononic environments would also be particularly interesting regarding the dephasing-assisted transport we demonstrate in chapter 5. Specifically, by means of tailoring the properties of the phonon bath, one could in principle modify the effect of dephasing on the system, adding a further degree of tunability to exciton transport. It is still uncertain whether this could have an impact in excitonic applications, but the answer to such question is closer than ever due to the recent works studying photon-exciton-phonon dynamics [148, 288, 367, 369, 429].

In general, the CSC regime recently achieved in nanophotonic structures seems a powerful asset for tailoring the light-matter interaction at the nanoscale. Moreover, when complex QEs such as organic molecules come into play, quantum nanophotonics starts to overlap with photochemistry, molecular physics and, in some cases, molecular biology. The ever increasing number of works lying in these boundaries [348, 349, 369] suggests that a deeper understanding of these systems may be at reach within the following decades, an achievement that could have a tremendous impact in a wide range of areas, from the fundamental insight on photosynthetic processes to promising applications in

photovoltaics, nanoscale energy transfer, and many more.

7.1.3. Realistic platforms for quantum plasmonics

The last part of this conclusion chapter is devoted to the analysis of realistic implementations of quantum nanophotonic platforms. The potential of photonic nanostructures for quantum applications has been evidenced by the vast amount of theoretical works on the subject, including those within this thesis. Such works have motivated the research on implementation and optimization of hybrid light-matter devices at the nanoscale. In terms of photon-emitter coupling efficiency, or β factors, photonic crystal structures have achieved an outstanding performance [66], and have therefore consolidated as excellent quantum circuitry platforms [70]. Moreover, the decades of extensive research in semiconductor devices have recently lead to an increased interest in such dielectric systems, which according to some researchers will mark the future of quantum computing [430]. On the other hand, plasmonic structures have not reached such efficiency levels, and hence most of them do not perform at the level required for many quantum applications. Therefore, a large research effort has been undertaken in the last years to enhance plasmon-based light-matter platforms. Such effort is not only motivated by the realization of purely quantum plasmonic devices, but additionally by the potential of plasmonic systems to overcome the intrinsic drawbacks of dielectric-based structures (including photonic crystals), e.g. diffraction-limited field confinement. This promising idea leads me to think that the development of efficient hybrid platforms, able to exploit the advantages of each subcomponent, will be essential for improving present quantum nanophotonics devices. In this regard, although some ideas have already been proposed [77, 122], researchers still have a long way to cover in order to achieve highly efficient hybrid light-matter platforms.

The above mentioned potential capabilities of plasmonic nanostructures rely on increasing the state of the art efficiencies of plasmon-emitter structures. Hence, in chapter 6 of this thesis, we propose a platform formed by a plasmonic V-Groove waveguide coupled to a single NV centre. By exhaustive numerical simulations we have been able to demonstrate the high efficiency of our device, as measured through a usual figure of merit (FOM). Thanks to a particularly chosen geometry, both nonradiative decay and emission to free space modes are significantly suppressed and, as a consequence, our device can show a relatively large β factor. Our theoretical predictions, as well as the experimental verification carried out by our collaborators at ICFO [125], confirm a larger FOM than that obtained by previous studies of plasmonic nanowires. Our value

is still not large enough for high-fidelity quantum applications but, nevertheless, the proposed setup leaves room for improvement, particularly in terms of plasmon propagation losses. In this regard, it is in principle possible to achieve much higher figures of merit, for instance, by using more complex structures [431], or by exploiting the new generation of fabrication techniques with atomic resolution [67]. Although the research field devoted to optimizing plasmonic structures for quantum applications is relatively young, the progress achieved in the last years demonstrates that, in the next decades, such structures will become an even more valuable resource in quantum nanophotonics.

To summarize the whole chapter, all the main areas in which this thesis is divided have experienced a significant advance in the last years. Promising new lines are currently unfolding, led by new and powerful theoretical techniques which are able to tackle very complex problems in quantum nanophotonics. In this way, a fundamental understanding of systems which were considered intractable some years ago is starting to be achieved, a fact which, combined with the increasing experimental optimization of light-matter platforms, evidences that complex quantum devices based on engineered light-matter interaction are closer to reality than ever before. Our research addresses some hot topics in the field, offering not only fundamental insight and proposals for particular implementations but, additionally, raising new questions to be answered by forthcoming research. In the next years, it is justified to expect a flourishing of quantum nanophotonics, as well as an expansion into many different scientific areas. It is therefore not daring to assert that, in quantum nanophotonics, there is still plenty of room at the bottom.

7.2. Castellano

La investigación llevada a cabo en esta tesis abarca diferentes areas relacionadas con la nanofotónica cuántica. Los primeros dos capítulos (2 y 3) se centran en el creciente campo de la electrodinámica cuántica (QED) en guías de onda, cuyo objetivo es el desarrollo de plataformas para óptica cuántica y redes cuánticas que aprovechen las ventajas de sistemas de guía de onda. Por otro lado, en los capítulos 4 y 5, estudiamos sistemas plasmónicos en el régimen de acoplo fuerte, en el que luz y materia forman estados híbridos que presentan propiedades de ambos componentes. Finalmente, el capítulo 6 ocupa un lugar intermedio entre estas dos disciplinas, ya que está dedicado al estudio de sistemas de guía de onda realistas para aplicaciones en plasmónica cuántica. En este último capítulo presentamos las conclusiones generales de la tesis, acmpañadas de una breve descripción tanto del estado actual como de las perspectivas de futuro de las diferentes líneas de investigación.

7.2.1. QED en guías de onda

Tal como discutimos en el capítulo 1, la posibilidad de generar estados entrelazados entre qubits es un recurso esencial tanto para computación cuántica como para la simulación cuántica moderna. Una de las posibles formas de entrelazar qubits consiste en acoplar ambos a un entorno común que, mediando la interacción, lleve a la generación espontánea de entrelazamiento a partir de un estado producto inicial. Dado su potencial como componentes fundamentales de redes cuánticas, las guías de onda son candidatos especialmente interesantes para implementar este tipo de protocolos [62], una idea que ya ha sido demostrada por estudios previos [106, 107]. En base a dichos trabajos, en el capítulo 2 nos hemos centrado en el estudio de la generación disipativa de entrelazamiento entre dos qubits acoplados a una guía de ondas. En la primera parte del capítulo, hemos aplicado a este problema el Hamiltoniano de guías desarrollado por Fan et al. [196], con el objetivo de determinar la adecuación al caso de guías de onda de la ecuación maestra Markoviana, normalmente empleada en cavidades. Hemos demostrado cómo dicha ecuación maestra no es capaz de predecir la dinámica no Markoviana que surge tanto para grandes acoplos entre qubit y fotones como para qubits muy separados espacialmente. Nuestros resultados demuestran que, para capturar la rica fenomenología que emerge en sistemas de guía de onda, se requiere una descripción de los modos fotónicos más allá de la aproximación de Markov.

La mayor ventaja del protocolo de generación de entrelazamiento arriba mencionado

es la gran vida media del estado entrelazado resultante cuando la separación entre los qubits es un múltiplo semientero de la longitud de onda de emisión, ya que entonces dicho estado se transforma además en un "estado oscuro" con respecto a la guía. Sin embargo, en este mecanismo la concurrencia generada está superiormente acotada por 0.5, lo que limita la cantidad de entrelazamiento realizable. Otra desventaja de este protocolo es su extrema sensibilidad a pequeñas perturbaciones en la separación entre los qubits o en sus frecuencias de transición. Dichas limitaciones pueden superarse si el acoplo entre qubits y guía es quiral, tal y como mostramos en la segunda parte del capítulo 2. En ese caso, demostramos que la máxima concurrencia realizable aumenta un 50%, un valor que además es muy robusto con respecto a variaciones en los parámetros del sistema. Aunque el estado oscuro desaparece en dicha situación, reduciendo la vida media del estado entrelazado con respecto al caso no quiral, dicha vida media puede en principio ser controlada a través del acoplo guía-qubit. Creemos que nuestro protocolo quiral reduce los obstáculos para la realización experimental de generación de entrelazamiento en guías de onda. Nótese que, aparte de ofrecer un estudio fundamental sobre la generación de entrelazamiento entre dos qubits, nuestros resultados dan información sobre la dinámica de la unidad básica de las llamadas redes cuánticas quirales [214] que, de acuerdo con recientes predicciones, podrían tener un profundo impacto en óptica cuántica [109, 418]. Además, durante el desarrollo de esta tesis, la generación de entrelazamiento en guías de onda ha sido extendida a un sistema de N emisores, donde métodos para generar entrelazamiento mesoscópico han sido propuestos tanto en sistemas no quirales [419] como en sistemas quirales [420]. Estos prometedores trabajos ya componen una plataforma básica para simulación cuántica, y representan un paso adelante hacia la computación cuántica basada en guías de onda.

Los protocolos de generación de entrelazamiento arriba estudiados no explotan todas las capacidades ofrecidas por los puertos de entrada y salida de las guías de onda, que en principio permiten modificar el estado de qubits acoplados a dichas guías a través de dispersión (scattering) de fotones. Por esta razón, en el capítulo 3, hemos estudiado la generación, manipulación y detección de entrelazamiento en guías de onda basados en dispersión fotónica. Hemos demostrado cómo un fotón incidente puede generar entrelazamiento entre dos qubits inicialmente en su estado fundamental, y cómo un paquete de dos fotones puede modificar el perfil temporal de entrelazamiento generado, a través de procesos llamados muerte súbita y renacimiento del entrelazamiento. Finalmente, hemos demostrado que el estado fotónico resultante de la dispersión de un fotón contiene información sobre el entrelazamiento de los dos qubits, cuando estos son inicializados en un estado arbitrario de una excitación. Haciendo uso de esta correspondencia, hemos

diseñado un método para detección de entrelazamiento que es independiente de los parámetros particulares de la guía o los emisores, reduciendo por tanto los exigentes requisitos asociados a otros protocolos como la tomografía completa [228]. Nótese que nuestro trabajo no es en absoluto la única investigación reciente que demuestra física interesante basada en dispersión fotónica en guías de onda. Comenzando por los primeros resultados en inversión completa de qubits [190] o reflexión perfecta de un fotón [199], muchos fenómenos diferentes han sido descubiertos en problemas de dispersión como por ejemplo estados ligados de varios fotones [198, 265] y la presencia de pulsos cuánticos [77]. La comprensión fundamental de los procesos que gobiernan la interacción entre materia y luz guiada ha sido además complementada por propuestas realistas de computación cuántica basada en guías acopladas con sistemas de cuatro niveles [271]. A día de hoy, todas estas líneas de investigación están aún siendo desarrolladas y extendidas pero, a pesar de su carácter prometedor, todavía se encuentran relativamente aisladas una de otra. Es realista pensar, sin embargo, que en los próximos años presenciaremos un esfuerzo unificador, orientado hacia la integración de todos los resultados relevantes en el campo en una plataforma basada en scattering capaz de realizar operaciones cuánticas complejas a una escala mayor.

El último tema relacionado con QED en guías de onda explora una posibilidad adicional ofrecida por estos flexibles sistemas, en este caso utilizar materia para modificar el estado de fotones entrantes. En la segunda parte del capítulo 3, hemos utilizado un sistema de tres niveles con acoplo quiral para realizar operaciones no recíprocas sobre qubits fotónicos en la guía de ondas. En el régimen de un sólo fotón, hemos diseñado un rectificador simple, en el que un fotón es completamente transferido a una segunda guía. En base a dicho principio, hemos implementado un diodo de un sólo fotón y un transistor de dos fotones, ambos con altas eficiencias para valores realistas de los parámetros. Nuestros resultados demuestran auténtica no-reciprocidad a nivel de un sólo fotón, una propiedad difícil de obtener a esa escala. Análogamente al caso de aplicaciones basadas en dispersion fotónica, nuestro trabajo representa sólo una pequeña fracción de la investigación en el área de puertas cuánticas para pocos fotones, que se ha visto incrementada enormemente en los últimos años. El diseño de dispositivos específicamente adpatados a guías de onda ha avanzado en paralelo a la evolución de la QED en guías, desde las primeras propuestas de transistores plasmónicos básicos [75] hasta prácticamente cualquier puerta imaginable en el régimen de pocos fotones, como operaciones no lineales para uno [421] y dos fotones [422], desplazadores de fase [120], y muchos más. En los últimos años, la implementación de esquemas eficientes de acoplo quiral ha supuesto el avance definitivo, ya que ha abierto las puertas hacia el diseño de dispositivos que

de otra forma serían difícilmente alcanzables, por ejemplo, nuestro diodo/transistor, aisladores [121] o circuladores ópticos [423]. En lo que respecta a los dispositivos fotónicos cuánticos está claro que, en los próximos años, la capacidad de integrar la gran variedad de puertas disponibles para pocos fotones en chips fotónicos compactos y funcionales es un objetivo no sólo merecedor de atención, sino necesario para dar el siguiente paso hacia la realización de tecnologías cuánticas basadas en nanofotónica.

Respecto a las perspectivas de la QED en guías de onda, creo que no es realista pensar que las investigaciones futuras traerán consigo dispositivos cuánticos complejos excusivamente basados en guías de onda. Por otro lado, los sistemas de luz guiada están haciéndose más y más sofisticados como plataformas aptas para interacción luz-materia, y parece evidente que las tecnologías cuánticas del futuro incorporarán dichos sistemas en combinación con cavidades. Desde el punto de vista teórico, este objetivo representa un desafío, ya que requerirá una mejora de los métodos actuales de resolución de problemas. En los últimos años, el análisis de problemas en QED en guías de onda ha evolucionado significativamente, desde los precursores formalismos de input-output [195] o cadenas de cavidades [424], hasta modelos altamente complejos como la reducción de Lehmann-Symanzik-Zimmermann [194]. A pesar de los innegables refinamientos de las herramientas analíticas en QED en guías de onda, parece evidente que todas estas aproximaciones analíticas han alcanzado ya su límite, dado que los problemas se vuelven excesivamente complejos en presencia de, entre otros, más de dos fotones, bombeo externo, guías con relaciones de dispersión complicadas, o pérdidas en la propagación de los fotones guiados. Afortunadamente, trabajos recientes han conseguido estudiar con éxito algunos de estos problemas mediante técnicas numéricas avanzadas como Matrix Product States [425], un método muy prometedor que representa uno de los recursos teóricos más importantes para la QED en guías de la próxima década. La combinación de estas técnicas numéricas avanzadas, la gran variedad de guías de onda disponibles experimentalmente, y su gran potencial para aplicaciones cuánticas sugieren que la investigación en QED en guías de onda continuará creciendo en los próximos años.

7.2.2. Acoplo fuerte colectivo en nanofotónica cuántica.

El segundo tema abordado en esta tesis concierne a los fenomenos colectivos que surgen cuando un conjunto de emisores cuánticos (QEs) está fuertemente acoplado al campo electromagnético. Primero, en el capítulo 4, hemos estudiado la distribución espacial de la población excitónica cuando un emisor en el conjunto es bombeado coherentemente. Nuestro resultado más importante en dicho capítulo es la demostración de la deslocal-

ización de los estados oscuros, que a pesar de estar desacoplados de la luz pueden adquirir su carácter extendido siempre que los modos electromagnéticos formen un conjunto discreto. En el caso de estructuras plasmónicas, las altas pérdidas características de los plasmones son heredadas por los polaritones y, por tanto, los estados oscuros son mucho más eficientes propagando las excitaciones a lo largo del conjunto de QEs. En el capítulo 5 hemos continuado estudiando un problema similar, particularmente el del transporte excitónico para bombeo incoherente. En base a resultados previos que demostraban un aumento en la conductancia excitónica de un conjunto de QEs fuertemente acoplado al modo homogéneo de una cavidad, hemos diseñado una estrategia para modificar dicho aumento de la conductancia a través un perfil inhomogéneo de campo. Además, usando una estructura plasmónica con modos muy confinados, hemos demostrado cómo los excitones pueden ser canalizados eficientemente hacia regiones espaciales mucho menores que la longitud de onda. Asimismo, hemos mostrado que los estados oscuros también juegan un papel muy importante en el caso de bombeo incoherente. Finalmente, hemos estudiado cómo, bajo ciertas condiciones, la compleja interacción entre polaritones y estados oscuros permite que el "dephasing" favorezca el transporte de excitones, una ventaja potencial en conjuntos de moléculas orgánicas donde este efecto es relevante.

El carácter deslocalizado de los autoestados del sistema es el mecanismo fundamental en el que se basan todos los resultados arriba mencionados. Es importante notar que el requisito de un bombeo local y coherente del conjunto de QEs dificulta la observación experimental de dicho efecto en microcavidades convencionales, donde los QEs sólo están acoplados con el entorno externo de forma indirecta, y por tanto sólo los modos de cavidad pueden ser poblados eficientemente [30]. Para observar nuestros resultados en estos sistemas, la única opción sería a través de bombeo eléctrico [426] que, no obstante, está limitado por las propiedades del material y sólo puede proporcionar excitación incoherente. En este sentido, las estructuras nanofotónicas marcan la diferencia no sólo debido a la gran variedad de resonadores disponibles, sino porque la mayoría de dichos resonadores son *cavidades abiertas*, en las que los QEs son accesibles directamente a través de fuentes externas. Combinados con las excelentes herramientas disponibles para excitar moléculas individuales, como sondas de campo cercano [317] y excitación-reemisión de un emisor externo [201], los resonadores nanofotónicos se revelan como excelentes candidatos para la observación de muchos fenómenos relacionados con los estados oscuros y, en particular, su carácter deslocalizado.

Una de las propiedades más interesantes de la deslocalización de los estados oscuros y el incremento asociado de la conductancia excitónica es su leve dependencia con las pérdidas de la cavidad. En efecto, la mayoría de los fenómenos estudiados en los capítulos

4 y 5 son observables en cavidades con muchas pérdidas. Esta es una ventaja particularmente importante en estructuras plasmónicas, cuya mayor desventaja en cuanto a nanofotónica cuántica se refiere son sus altas pérdidas. Por tanto, para las aplicaciones en las que dichas pérdidas son irrelevantes, los resonadores plasmónicos se convierten en excelentes plataformas en nanofotónica cuántica. En primer lugar, ofrecen un gran confinamiento del campo que resulta en grandes acoplos luz-materia [334]. En segundo lugar, son capaces de conseguir una modulación del campo eléctrico, y en consecuencia de la interacción plasmón-emisor, a escalas menores que la longitud de onda. Esto permite no sólo canalizar eficientemente excitones como mostramos en el capítulo 5, sino también realizar dispositivos excitónicos muy compactos. Creo que estas propiedades deberían ser aprovechadas en el futuro, especialmente dado que aún hay mucho por optimizar en dichos sistemas. Algunos de los obstáculos a superar en esta línea son incrementar las distancias de canalización o modular el perfil del campo para diseñar circuitos excitónicos basados en puntos de alta intensidad. Una cuidadosa manipulación de las nanoestructuras plasmónicas podría también mejorar los diseños actuales, por ejemplo en cuanto a miniaturización de dispositivos excitónicos. Incluso algunas estructuras ya disponibles en plasmónica clásica podrían ser readaptadas a este objetivo. Por ejemplo, el conjunto multirresonante de nanoantenas en la Ref. [427] podría ser empleado para canalizar eficientemente excitones de moléculas con diferentes energías de transición, o para multiplexar frecuencias en un circuito excitónico-fotónico. Aunque los circuitos y dispositivos excitónicos-plasmónicos no parecen capaces de competir con la circuitería nanofotónica actual, es probable que encuentren un nicho en futuros dispositivos integrados, especialmente aquellos en los que estén presentes QEs moleculares orgánicos.

Como comentario final, merece la pena destacar que, desde un punto de vista fundamental, el fenómeno de la deslocalización de los estados oscuros no es exclusivo de un entorno electromagnético. Por tanto, otra línea interesante para la investigación futura consiste en aplicar el mismo principio a otros entornos, por ejemplo un baño colectivo de fonones. Dado que el régimen de acoplo fuerte con uno o varios modos fonónicos puede ser conseguido incluso a temperatura ambiente [428], es en principio concebible utilizar un estado "oscuro" fonónico deslocalizado para transportar excitaciones a través de conjuntos de moléculas u otros sistemas. Un estudio detallado de entornos fonónicos sería particularmente interesante también por lo que respecta al transporte asistido por dephasing que demostramos en el capítulo 5. En particular, modificando las propiedades del baño fonónico, se podría en principio alterar el efecto del dephasing en el sistema, añadiendo un grado adicional de control al transporte excitónico. Es aún incierto si esto podría tener un impacto en aplicaciones excitónicas, pero la respuesta a esta pregunta

está más cerca que nunca debido a los recientes trabajos estudiando la dinámica de sistemas de fotones-excitones-fonones [148, 288, 367, 369, 429].

En general, el régimen de acoplo fuerte colectivo en estructuras nanofotónicas promete ser una herramienta poderosa para modificar la interacción luz-materia en la nanoescala. Además, cuando emisores complejos como moléculas orgánicas entran en juego, la nanofotónica cuántica comienza a solapar con la fotoquímica, la física molecular y, en algunos casos, la biología molecular. La creciente cantidad de trabajos explorando dichas fronteras [348, 349, 369] sugiere que una comprensión más profunda de estos sistemas puede estar a nuestro alcance en las próximas décadas, un logro que podría tener un enorme impacto en una gran variedad de áreas, desde el estudio fundamental de procesos fotosintéticos hasta prometedoras aplicaciones en sistemas fotovoltaicos, transporte de energía en la nanoescala, y muchos más.

7.2.3. Plataformas realistas para plasmónica cuántica

La última parte de este capítulo de conclusión está dedicada al análisis de implementaciones realistas de plataformas para nanofotónica cuántica. El potencial de las estructuras nanofotónicas para aplicaciones cuánticas ha sido evidenciado por una enorme cantidad de trabajos teóricos, incluídos los desarrollados en esta tesis. Dichos trabajos han motivado la investigación en implementaciones y optimización de dispositivos híbridos luz-materia en la nanoescala. En términos de eficiencia en el acoplo fotón-emisor, o factor β, las estructuras de cristal fotónico han alcanzado cotas excelentes [66], lo que las ha consolidado como extraordinarias plataformas para circuitos cuánticos [70]. Adicionalmente, las décadas de investigación en dispositivos semiconductores han dado lugar recientemente a un creciente interés en dichos sistemas dieléctricos, que de acuerdo a algunos investigadores representan el futuro de la computación cuántica [430]. Por otro lado, las estructuras plasmónicas no han alcanzado dichas cotas de eficiencia, y por tanto la mayoría de ellas no operan al nivel requerido para la mayoría de aplicaciones cuánticas. En consecuencia, en los últimos años una gran actividad investigadora ha estado orientada a la mejora de plataformas de luz-materia basadas en plasmones. Dicha actividad no ha sido sólo motivada por la posibilidad de realizar dispositivos puramente plasmónicos, sino adicionalmente por el potencial de los sistemas plasmónicos para solventar las desventajas intrínsecas de las estructuras basadas en dieléctricos (incluyendo cristales fotónicos), por ejemplo el confinamiento del campo limitado por difracción. Esta prometedora idea me lleva a pensar que el desarrollo de plataformas híbridas eficientes, capaces de aprovechar las ventajas de cada componente, serán esenciales de cara a mejo-

rar los dispositivos cuánticos nanofotónicos actuales. En esta línea, aunque algunas ideas han sido propuestas, [77, 122], los investigadores aún tienen un largo camino por delante en el desarrollo de plataformas luz-materia altamente eficientes.

Las potenciales ventajas de las estructuras plasmónicas mencionadas arriba requieren un incremento de las eficiencias actuales de las estructuras plasmón-emisor. Por tanto, en el capítulo 6 de esta tesis, proponemos una plataforma formada por una guía de onda plasmónica en forma de V acoplada con un centro vacante-nitrógeno individual. A través de simulaciones numéricas exhaustivas hemos sido capaces de demostrar la alta eficiencia de nuestro dispositivo, cuantificada a través de un factor de calidad. Gracias a una geometría elegida adecuadamente, tanto el decaimiento no radiativo como la emisión a modos de espacio vacío son suprimidos significativamente y, como consecuencia, nuestro dispositivo puede mostrar un factor β relativamente alto. Nuestras predicciones teóricas, así como la verificación experimental llevada a cabo por nuestros colaboradores en el ICFO [125], confirman un factor de calidad más grande que el obtenido por previos estudios en nanocables plasmónicos. El valor obtenido no es aún suficiente para apicaciones cuánticas de alta fidelidad pero, no obstante, el sistema propuesto aún puede ser mejorado, particularmente en cuanto a las pérdidas de propagación se refiere. En este sentido, es en principio posible obtener factores de calidad mucho más altos, por ejemplo, utilizando estructuras más complejas [431], o aprovechando la nueva generación de técnicas de fabricación con resolución atómica [67]. Aunque el campo de investigación dedicado a optimizar estructuras plasmónicas para aplicaciones cuánticas es relativamente joven, el progreso conseguido en los últimos años demuestra que, en las próximas décadas, dichas estructuras se convertirán en un recurso aún más valioso para nanofotónica cuántica.

Para concluir el presente capítulo, todas las áreas en las que esta tesis está dividida han experimentado un avance significativo en los últimos años. Nuevas y prometedoras líneas de investigación están siendo actualmente desarrolladas, lideradas por nuevas y poderosas técnicas capaces de afrontar problemas muy complejos en nanofotónica cuántica. De este modo, se está comenzando a conseguir una comprensión fundamental de sistemas considerados intratables hace algunos años, un hecho que, combinado con la creciente optimización experimental de las plataformas de luz-materia, evidencia que los dispositivos cuánticos complejos basados en interacción de luz y materia están más cerca que nunca de ser una realidad. Nuestra investigación aborda algunos temas relevantes en el campo, no sólo ofreciendo un punto de vista fundamental y propuestas para implementaciones experimentales, sino además planteando nuevas cuestiones para la investigación venidera. En los próximos años, es justificado esperar un florecimiento de la nanofotónica cuántica, así como una expansión hacia muchas otras áreas científicas.

No es por tanto atrevido afirmar que, en nanofotónica cuántica, sigue habiendo mucho espacio al fondo.

A | Decay of a two-level system coupled to a waveguide.

In this Appendix I explicitly solve the problem of the decay of an initially excited qubit coupled to a waveguide. This calculation has a triple purpose. First, it illustrates the required steps to determine the dynamics of a waveguide QED system by using the time evolution operator, something we have repeatedly undertaken along chapters 2 and 3. Second, it allows for the explicit calculation of the photonic wavepacket emitted by a two-level system, which appears in the first sections of chapter 3. Finally, it demonstrates the definition we use for the directionality in chapters 2 and 3 is equivalent to the homonymous magnitude measured by experimentalists.

For the sake of simplicity we will study the simple situation depicted in Fig. A.1, which is fully solvable analytically. A single qubit of frequency ω_0 is coupled to a waveguide with unit efficiency $\beta \approx 1$, i.e., we neglect any free space losses. In principle we let the right and left coupling strengths to be different. The Hamiltonian of the system is similar to Eq. 2.23,

$$\begin{aligned} H = &- iv_g \int dx \left(c_R^\dagger(x) \frac{\partial}{\partial x} c_R(x) - c_L^\dagger(x) \frac{\partial}{\partial x} c_L(x) \right) + \omega_0 \sigma^\dagger \sigma + \\ &+ \int dx \delta(x) \left(V_R c_R^\dagger(x) + V_L c_L^\dagger(x) \right) \sigma + H.c., \end{aligned} \tag{A.1}$$

where v_g is the group velocity, and we assume the couplings V_α to be real for simplicity. The right and left decay rates are given by $\gamma_\alpha = V_\alpha^2 / v_g$.

The diagonalization of the above Hamiltonian in the single-excitation subspace follows an analogous procedure as we have detailed in chapter 2, therefore we will only briefly summarize it here. We start with the following general expression for the single-excitation eigenstate of the system,

$$|\epsilon\rangle = \alpha \sigma^\dagger |0\rangle + \int dx \left(\phi_R(x) c_R^\dagger(x) + \phi_L(x) c_L^\dagger(x) \right) |0\rangle, \tag{A.2}$$

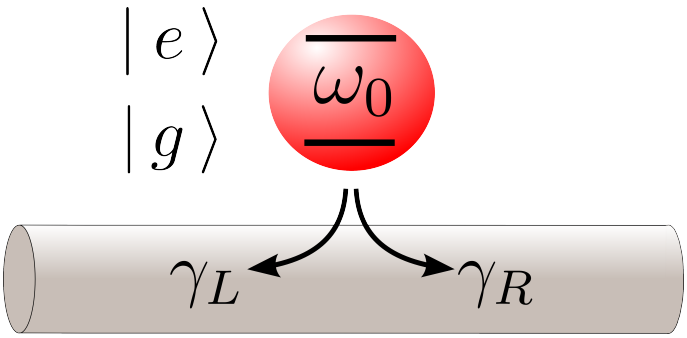

Figure A.1: Schematic depiction of the simple waveguide QED system under study. A qubit decays into right(left) propagating modes of the waveguide at a rate $\gamma_R(\gamma_L)$.

and solve the time-independent Schrödinger equation for the system coefficients. Two different branches of eigenstates will arise in this case, corresponding to the scattering of single photons introduced from the left and the right ports of the waveguide. These two branches are labelled $|\epsilon_a\rangle$ and $|\epsilon_b\rangle$, respectively, and their scattering coefficients are given by

1. Rightward propagating photonic input, $|\epsilon_a\rangle$:

$$\phi_R^{(a)} = e^{i\epsilon x/v_g}\begin{cases} 1 & \text{for} \quad x<0 \\ t_a & \text{for} \quad x>0 \end{cases} \quad ; \quad \phi_L^{(a)} = e^{-i\epsilon x/v_g}\begin{cases} 0 & \text{for} \quad x<0 \\ r_a & \text{for} \quad x>0, \end{cases} \tag{A.3}$$

with the atomic, transmission, and reflection coefficients given by

$$\begin{pmatrix} \alpha_a \\ t_a \\ r_a \end{pmatrix} = \frac{1}{\epsilon-\omega_0+i\gamma/2}\begin{pmatrix} V_R \\ \epsilon-\omega_0+i(\gamma_L-\gamma_R)/2 \\ -i\sqrt{\gamma_R\gamma_L} \end{pmatrix}. \tag{A.4}$$

where $\gamma = \gamma_R + \gamma_L$.

1. Leftward propagating photonic input, $|\epsilon_b\rangle$:

$$\phi_R^{(b)} = e^{i\epsilon x/v_g}\begin{cases} 0 & \text{for} \quad x<0 \\ r_b & \text{for} \quad x>0 \end{cases} \quad ; \quad \phi_L^{(b)} = e^{-i\epsilon x/v_g}\begin{cases} t_b & \text{for} \quad x<0 \\ 1 & \text{for} \quad x>0, \end{cases} \tag{A.5}$$

with the atomic, transmission, and reflection coefficients given by

$$\begin{pmatrix} \alpha_b \\ t_b \\ r_b \end{pmatrix} = \frac{1}{\epsilon-\omega_0+i\gamma/2}\begin{pmatrix} V_L \\ \epsilon-\omega_0+i(\gamma_R-\gamma_L)/2 \\ -i\sqrt{\gamma_R\gamma_L} \end{pmatrix}. \tag{A.6}$$

The two branches of eigenstates above can be shown to be orthogonal to each other, and the eigenstates $|\epsilon_a\rangle$ and $|\epsilon_b\rangle$ to be normalized to $2L$, where $L \to \infty$ is the total length of the waveguide. Note from the expression of the scattering coefficients of both branches how in the non-chiral case, $\gamma_R = \gamma_L$, a photon in resonance has zero transmission probability. On the other hand, for maximum positive directionalities $\gamma_L = 0$, the transmission probabilities are maximal (and non-reciprocal) since $t_a = -t_b = -1$.

A.1. Dynamics of the qubit decay

A.1.1. Population of the qubit

Once the two branches are calculated, the time-evolution operator is determined in the same fashion as in chapter 2,

$$U(t) = \frac{1}{2\pi v_g} \sum_{m=a,b} \int d\epsilon |\epsilon_m\rangle\langle\epsilon_m| e^{-i\epsilon t}. \tag{A.7}$$

Let us now study how the qubit decays. For an initial state $|\psi(0)\rangle = |e\rangle \equiv \sigma^\dagger|0\rangle$, the time evolution is given by

$$|\psi(t)\rangle = \frac{1}{2\pi v_g} \sum_{m} \int d\epsilon |\epsilon_m\rangle \alpha_m^*(\epsilon) e^{-i\epsilon t}. \tag{A.8}$$

The simplest quantity we can obtain with the above state is the expected value of the qubit population, given by the square modulus of the overlap

$$\langle e|\psi(t)\rangle = \frac{1}{2\pi v_g} \sum_{m} \int d\epsilon |\alpha_m|^2 e^{-i\epsilon t} = \frac{\gamma}{2\pi} \int d\epsilon \frac{e^{-i\epsilon t}}{[\epsilon - (\omega_0 + i\gamma/2)]\,[\epsilon - (\omega_0 - i\gamma/2)]}. \tag{A.9}$$

For $t > 0$, we can integrate the above expression by taking an integration contour encircling the lower complex semiplane. We then apply the residue theorem to obtain

$$\langle e|\psi(t)\rangle = \frac{\gamma}{2\pi}(-2\pi i)\frac{1}{-i\gamma} e^{-i(\omega_0 - i\gamma/2)t} = e^{-i(\omega_0 - i\gamma/2)t}, \tag{A.10}$$

which recovers the simple exponential law for the decay of a weakly coupled qubit,

$$\left|\langle e|\psi(t)\rangle\right|^2 = e^{-\gamma t}. \tag{A.11}$$

A.1.2. Distribution of the emitted photons.

The photonic wavepacket emitted during the qubit decay is more involved to obtain. We have to calculate separately the distribution of right- and left-propagating photons. For the former, the position probability amplitude is given by the overlap $\langle 0|c_R(x)|\psi(t)\rangle$, which has different values depending on the sign of x. Specifically,

$$\langle 0|c_R(x)|\psi(t)\rangle\Big|_{x<0} = \frac{1}{2\pi v_g}\int d\epsilon \frac{V_R}{\epsilon-(\omega_0+i\gamma/2)} e^{i\epsilon(-|x|-v_g t)/v_g}. \tag{A.12}$$

It is straightforward to demonstrate that the above integral is equal to 0. Indeed, the sign of the exponential factor allows for an integration only in the lower complex semiplane, but in this region the integrand does not have any singularities. The integral thus vanishes according to the residue theorem. A similar argument for the left-propagating component allows us to write the following two relations for the emitted photons (at any time $t>0$),

$$\langle 0|c_R(x)|\psi(t)\rangle \propto \theta(x) \qquad ; \qquad \langle 0|c_L(x)|\psi(t)\rangle \propto \theta(-x). \tag{A.13}$$

The above is an intuitive result, since the photons resulting from the decay of the emitter must propagate away from the qubit and not towards it.

Let us now calculate the overlap A.12 for positive values of x. The integrand can be expressed as a sum of two terms corresponding respectively to the contribution of the two branches of eigenstates,

$$\begin{aligned}\langle 0|c_R(x)|\psi(t)\rangle\Big|_{x>0} =& \frac{1}{2\pi v_g}\int d\epsilon \frac{e^{i\epsilon(x-v_g t)/v_g}}{[\epsilon-(\omega_0+i\gamma/2)]\,[\epsilon-(\omega_0-i\gamma/2)]}\times \\ &\times\Big(V_R\,[\epsilon-\omega_0+i(\gamma_L-\gamma_R)/2]-iV_L\sqrt{\gamma_R\gamma_L}\Big).\end{aligned} \tag{A.14}$$

The above integral is solved in a different way depending on the sign of the argument $x-v_g t$ in the exponential. First, for $x>v_g t$, the integration contour must be taken in the upper complex semiplane. Then, we can use the residue theorem again to obtain

$$\langle 0|c_R(x)|\psi(t)\rangle\Big|_{x>v_g t>0} = \frac{2\pi i}{2\pi v_g}\frac{e^{i(\omega_0+i\gamma/2)(x-v_g t)/v_g}}{i\gamma}\left(V_R(i\gamma_L)-iV_L\sqrt{\gamma_R\gamma_L}\right)=0, \tag{A.15}$$

since $V_R\gamma_L - V_L\sqrt{\gamma_R\gamma_L} = \left(V_R V_L^2 - V_L V_R V_L\right)/v_g = 0$. The cancellation of the integral for $x>v_g t$ is a logical consequence of the finite group velocity of the guided photons, which prevents any excitation to propagate faster than v_g.

When $x<v_g t$, on the other hand, the integration contour in A.14 encloses the lower complex semiplane, and the application of the residue theorem yields

$$\begin{aligned}\langle 0|c_R(x)|\psi(t)\rangle\Big|_{v_g t>x>0} &= \frac{-2\pi i}{2\pi v_g}\frac{e^{i(\omega_0-i\gamma/2)(x-v_g t)/v_g}}{-i\gamma}\left(-iV_R\gamma_R - iV_L\sqrt{\gamma_R\gamma_L}\right) \\ &= \frac{-iV_R}{v_g}e^{i(\omega_0-i\gamma/2)(x-v_g t)/v_g}.\end{aligned} \tag{A.16}$$

An analogous procedure can be undertaken to demonstrate that, for left-propagating photons,

$$\langle 0|c_L(x)|\psi(t)\rangle = \frac{-iV_L}{v_g} e^{-i(\omega_0 - i\gamma/2)(x+v_g t)/v_g} \theta(-x)\theta(x+v_g t). \tag{A.17}$$

This expression justifies the general shape for the photon wavefunction employed in chapter 3. Finally, the total photonic position probability density, $P(x,t)$, can be obtained as

$$\begin{aligned} P(x,t) =& \Big| \sum_{\alpha=R,L} \langle 0|c_\alpha(x)|\psi(t)\rangle \Big|^2 \\ =& e^{-\gamma t} \left[\theta(x)\theta(v_g t - x) \frac{\gamma_R}{v_g} e^{\gamma x/v_g} + \theta(-x)\theta(v_g t + x) \frac{\gamma_L}{v_g} e^{-\gamma x/v_g} \right] \end{aligned} \tag{A.18}$$

Note that, despite the exponential decay $e^{-\gamma t}$ above, the total probability stored in the photonic degrees of freedom does not decrease with time, since such exponential is compensated by the increasing length of the photonic state (i.e., the space delimited by the two Heaviside functions). Indeed, we can calculate the total population stored in the photonic modes through

$$P_{tot}(t) = \int_{-\infty}^{\infty} dx P(x,t) = 1 - e^{-\gamma t}, \tag{A.19}$$

which is consistent with the qubit decay in Eq. A.11. Additionally, thanks to the outgoing character of the photons (Eq. A.13), it is straightforward to calculate the amount of population emitted toward the right and left ends of the waveguide independently. In the long time limit, when the qubit has completely decayed, the total photonic population in each arm of the waveguide reads

$$P_R = \lim_{t\to\infty} \int_0^{\infty} dx P(x,t) = \frac{\gamma_R}{\gamma}, \tag{A.20}$$

$$P_L = \lim_{t\to\infty} \int_{-\infty}^{0} dx P(x,t) = \frac{\gamma_L}{\gamma}. \tag{A.21}$$

The above expressions allow us to retrieve the concept of directionality we have employed in Chapters 2 and 3. Originally, this quantity was defined in experimental works [72, 108] as

$$D_j = \frac{p_R - p_L}{p_R + p_L}, \tag{A.22}$$

where p_R and p_L represent the total probabilities of detecting a photon in each arm of the waveguide[1]. Since the probability of detection in a given arm, p_j, is proportional to

[1] In a laboratory, this directionality is estimated by repeating the experiment a statistically significant amount of times. Then, the ratio of probabilities is determined through the number of photons detected at each arm, i.e., $D_j = (N_R - N_L)/(N_R + N_L)$.

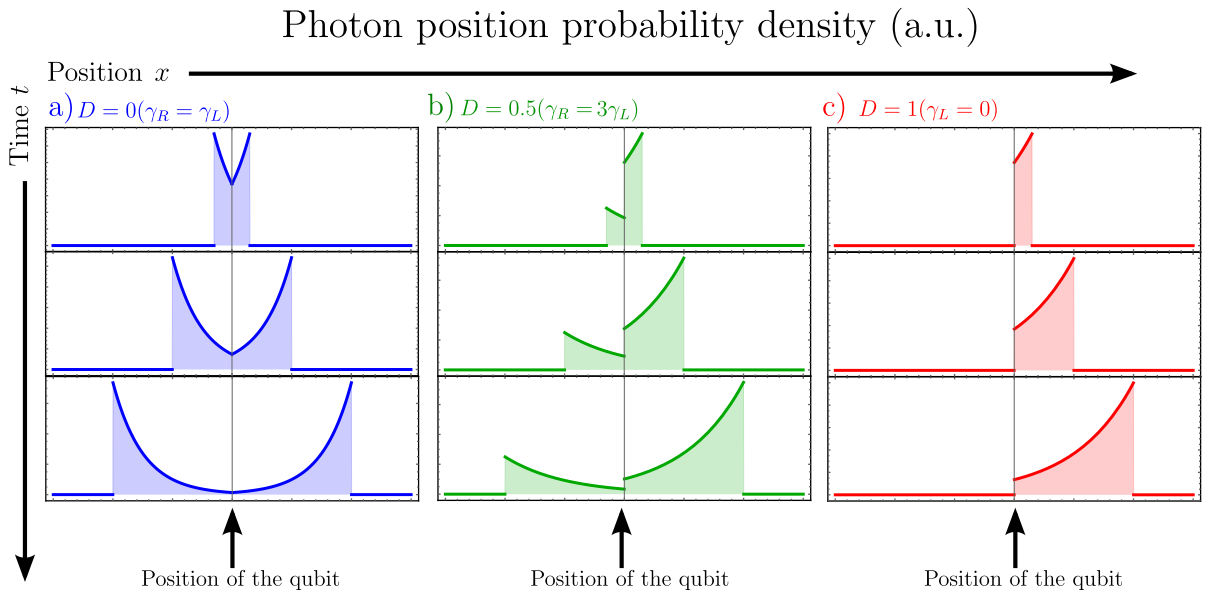

Figure A.2: Photon position probability density emitted during the decay of a non-chirally coupled qubit (left panel), a chirally coupled qubit with directionality 0.5 (medium panel), and a maximally directional situation (right panel).

the photon occupation in such region, P_j, we can use our results in Eqs. A.20 and A.21 to express

$$D_j = \frac{\gamma_R - \gamma_L}{\gamma_R + \gamma_L}. \tag{A.23}$$

In this way we justify rigorously the *ad hoc* definition we employ in the main text.

As a final comment, note that in this appendix we solve the simplest possible problem in waveguide QED. However, in most of the calculations in the main text, the poles of the integrands are given by a transcendental equation and therefore no analytical solution exists. As a consequence, the results presented in Chapters 2 and 3 have been integrated numerically even if the diagonalization is analytical.

B | Diagonalization of the four-port device Hamiltonian.

In this Appendix we diagonalize the Hamiltonian Eq. 3.49, both in the single- and two-excitation subspace. Then, we explicitly calculate the two-photon detection probabilities P_{mn} and demonstrate that they describe all the possible scattering outputs in our system.

B.1. Diagonalization in the single-excitation subspace.

Since we have detailed the diagonalization of a very similar Hamiltonian in chapter 2, here we will only briefly summarize the key steps. First, we define the general form for our single-excitation eigenstate as in Eq. 3.53,

$$|\epsilon\rangle = \alpha_e|e\rangle + \sum_{\alpha=R,L}\int dx\phi_\alpha(x)c_\alpha^\dagger(x)|g\rangle + \int dy\psi_\alpha(y)b_\alpha^\dagger(y)|s\rangle, \tag{B.1}$$

where the coefficients $\alpha, \phi_\alpha(x), \psi_\beta(y)$ are unknown functions to determine. In order to do so, we solve the time-independent Schrödinger equation $H|\epsilon\rangle = \epsilon|\epsilon\rangle$ by directly applying the Hamiltonian H in Eq. (3.49) to the eigenstate above. In this way, we obtain the following system of equations,

$$(\epsilon - \omega_e + i\Gamma/2)\alpha = \sum_{\beta=R,L} V_\beta\phi_\beta(0) + W_\beta\psi_\beta(0), \tag{B.2}$$

$$(\epsilon - \omega_g + iv_g\partial_x)\phi_R(x) = \alpha V_R\delta(x), \tag{B.3}$$

$$(\epsilon - \omega_g - iv_g\partial_x)\phi_L(x) = \alpha V_L\delta(x), \tag{B.4}$$

$$(\epsilon + iv_g\partial_y)\psi_R(y) = \alpha W_R\delta(y), \tag{B.5}$$

$$(\epsilon - iv_g\partial_y)\psi_L(y) = \alpha W_L\delta(y), \tag{B.6}$$

where we use the short-hand notation $\partial_x \equiv \partial/\partial x$. We now proceed to make the usual Ansatz for the photonic wavefunctions in terms of the scattering coefficients defined in Fig. 3.10,

$$\phi_R(x) = e^{i(\epsilon-\omega_g)x/v_g}\big(\theta(-x) + t\theta(x)\big), \tag{B.7}$$

$$\phi_L(x) = e^{-i(\epsilon-\omega_g)x/v_g} r\theta(-x), \tag{B.8}$$

$$\psi_R(y) = e^{i\epsilon y/v_g}\tilde{t}\theta(y), \tag{B.9}$$

$$\psi_L(y) = e^{-i\epsilon y/v_g}\tilde{r}\theta(-y), \tag{B.10}$$

which allows for an integration of the system of equations (B.3-B.6) around $x = y = 0$ in order to get rid of the delta functions. After such integration, the problem is reduced to a 5×5 system of algebraic equations. The solutions to this system, after the trivial substitution $\omega = \epsilon - \omega_g$, are the scattering coefficients Eqs. (3.54-3.57) in the main text.

B.1.1. Inputs through other ports.

Our four port device naturally displays four branches of single-excitation scattering eigenstates, corresponding to the incoming single photon being introduced by each of the four ports. In this set we are ignoring the four additional eigenstates in which the 3LS is in a state which does not interact with the photonic input, as the solution for this situation is trivial. Let us label the nontrivial eigenstate branches as $|\epsilon_{(j)}\rangle$ $(j = 1, 2, 3, 4)$, where the subindex j indicates which port is chosen for the single-photon input. The eigenstates calculated right above represent the branch $|\epsilon_{(1)}\rangle$. Interestingly, in order to obtain the remaining three branches no more calculations are needed, since they are related through symmetry operators as we illustrate in Fig. B.1. The corresponding symmetry operators are mirror inversions which exchange either R and L modes or u and d waveguides,

$$\mathcal{P}_{RL}: \text{ Substitutes every label } R \text{ by } L \text{ and vice versa,} \tag{B.11}$$

$$\mathcal{P}_{ud}: \text{ Substitutes every label } u \text{ by } d \text{ and vice versa.} \tag{B.12}$$

The operator $\mathcal{P}_{ud}$ also exchanges the couplings according to $V \leftrightarrow W$. It is evident from the definition of the system and the images in Fig. B.1 that the different branches of eigenstates are related through these symmetry operations[1]. Note, however, that these

[1] An example of these symmetries in the simpler system of a qubit chirally coupled to a single waveguide can be easily checked for the single-photon scattering coefficients in Appendix A.

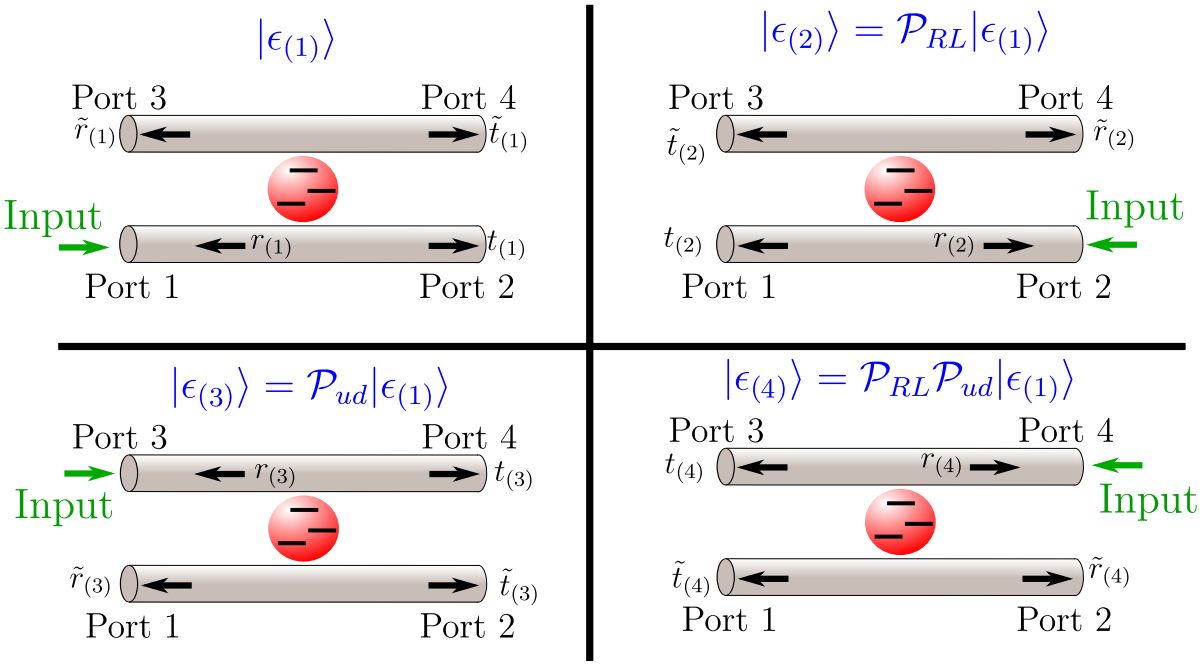

Figure B.1: Single-photon reflection probability versus directionality of the bottom waveguide. This is the only parameter determining the performance of a single-photon diode.

are not symmetries of the Hamiltonian, and these operators cannot be straightforwardly applied. Indeed, we need to redefine the scattering coefficients $t, r, \tilde{t}$, and $\tilde{r}$ for each case as depicted in the figure, with a corresponding definition of the involved wavefunctions B.7-B.10. If we do that correctly, the 5×5 algebraic system of equations we obtained when solving branch 1 is transformed into the corresponding system of equations for branch j by applying the appropriate symmetry operator. Specifically, it can be checked that

$$\begin{pmatrix} t_{(4)} \\ r_{(4)} \\ \tilde{t}_{(4)} \\ \tilde{r}_{(4)} \end{pmatrix} = \mathcal{P}_{RL} \begin{pmatrix} t_{(3)} \\ r_{(3)} \\ \tilde{t}_{(3)} \\ \tilde{r}_{(3)} \end{pmatrix} = \mathcal{P}_{ud} \begin{pmatrix} t_{(2)} \\ r_{(2)} \\ \tilde{t}_{(2)} \\ \tilde{r}_{(2)} \end{pmatrix} = \mathcal{P}_{RL}\mathcal{P}_{ud} \begin{pmatrix} t_{(1)} \\ r_{(1)} \\ \tilde{t}_{(1)} \\ \tilde{r}_{(1)} \end{pmatrix}. \tag{B.13}$$

In this way we can calculate the scattering amplitudes associated with every input in a straightforward way. We have employed this to determine the scattering coefficients for a photon introduced through port 2 in the case of the single-photon diode in chapter 3.

B.2. Diagonalization in the two-excitation subspace.

The basic steps for the diagonalization in this case are the same as in the single-excitation problem, starting by the general form of the two-excitation eigenstate Eq.(3.70). By directly applying the Hamiltonian (3.49) to the eigenstate $|\epsilon\rangle$ we obtain a system of differential equations relating all the coefficients. For the sake of compactness, let us first define the variable

$$\eta_\alpha = \begin{cases} 1 & \text{for} \quad \alpha = R \\ -1 & \text{for} \quad \alpha = L \end{cases}, \tag{B.14}$$

as well as the function

$$G_\alpha(x_1, x_2) = \varphi_\alpha(x_1)\delta(x_2). \tag{B.15}$$

With these useful definitions at hand, we can express the system of equations in the following form,

$$\left[\epsilon - \omega_g + iv_g\left(\eta_\alpha\partial_1 + \eta_\beta\partial_2\right)\right]\phi_{\alpha\beta} = \left(V_\alpha G_\beta(x_2, x_1) + V_\beta G_\alpha(x_1, x_2)\right)\frac{2-\delta_{\alpha\beta}}{2}, \tag{B.16}$$

$$\left[\epsilon + iv_g\left(\eta_\alpha\partial_x + \eta_\beta\partial_y\right)\right]\psi_{\alpha\beta} = W_\beta G_\alpha(x, y), \tag{B.17}$$

$$\begin{aligned}\left[\epsilon - \omega_e + iv_g\partial_x\right]\varphi_R(x) = \\ = 2V_R\phi_{RR}(x,0) + V_L\phi_{RL}(x,0) + W_R\psi_{RR}(x,0) + W_L\psi_{RL}(x,0),\end{aligned} \tag{B.18}$$

$$\begin{aligned}\left[\epsilon - \omega_e - iv_g\partial_x\right]\varphi_L(x) = \\ = 2V_L\phi_{LL}(x,0) + V_R\phi_{RL}(0,x) + W_L\psi_{LL}(x,0) + W_R\psi_{LR}(x,0),\end{aligned} \tag{B.19}$$

where $\partial_j \equiv \partial/\partial x_j$ and $\delta_{\alpha\beta}$ represents the Kronecker delta. In a general case the losses are included as an imaginary part in ω_e, i.e., $\omega_e \to \omega_e - i\Gamma/2$.

The homogeneous solutions to the above differential equations are two-variable plane waves. The only difficulty is posed by the delta functions, which account for the matching conditions for these waves at the position of the 3LS, $x = y = 0$. It is then necessary to carefully define the different domains in which the functions ψ, ϕ are well defined,

- Region (i): $x_1, x_2 < 0$, or $x, y < 0$.
- Region (ii): $x_1 < 0 < x_2$, or $x < 0 < y$.
- Region (iii): $0 < x_1, x_2$, or $0 < x < y$.

- Region (iv): $x_2 < 0 < x_1$, or $y < 0 < x$.

We can do the same for the one-variable functions $\varphi_\alpha(x)$,

$$\varphi_\alpha(x) = \varphi_\alpha^<(x)\theta(-x) + \varphi_\alpha^>(x)\theta(x). \tag{B.20}$$

Once the different regions are defined, it is possible to simplify the problem by imposing physical restrictions. In particular, as we are interested in the scattering of two photons incoming through port 1, we can impose as a constraint that no photons are introduced through other ports. This condition applies as a series of restrictions in our wavefunctions, in particular

$$\begin{aligned}
\phi_{LL}^{(iii)} &= \phi_{LL}^{(ii)} = \phi_{RL}^{(iii)} = \phi_{RL}^{(ii)} = 0,\\
\psi_{RR}^{(i)} &= \psi_{RR}^{(iv)} = 0,\\
\psi_{RL}^{(ii)} &= \psi_{RL}^{(iii)} = 0,\\
\psi_{LR}^{(i)} &= \psi_{LR}^{(iii)} = \psi_{LR}^{(iv)} = 0,\\
\psi_{LL}^{(ii)} &= \psi_{LL}^{(iii)} = \psi_{LL}^{(iv)} = 0,\\
\varphi_L^> &= 0.
\end{aligned} \tag{B.21}$$

Finally, we can integrate Eqs. (B.16-B.17) around $x, y = 0$ to get rid of the delta functions, obtaining the following system of equations and boundary conditions:

$$\left[\omega + iv_g\left(\eta_\alpha\partial_1 + \eta_\beta\partial_2\right)\right]\phi_{\alpha\beta}^{(j)} = 0, \tag{B.22}$$

$$iv_g\left(\phi_{RR}^{(ii)}(x,0) - \phi_{RR}^{(i)}(x,0)\right) = \tfrac{V_R}{2}\varphi_R^<(x), \tag{B.23}$$

$$iv_g\left(\phi_{RR}^{(iii)}(0,x) - \phi_{RR}^{(ii)}(0,x)\right) = \tfrac{V_R}{2}\varphi_R^>(x) \tag{B.24}$$

$$iv_g\phi_{LL}^{(i)}(x,0) = \tfrac{V_L}{2}\varphi_L^<(x), \tag{B.25}$$

$$iv_g\phi_{RL}^{(i)}(x,0) = V_L\varphi_R^<(x), \tag{B.26}$$

$$iv_g\phi_{RL}^{(iv)}(x,0) = V_L\varphi_R^>(x), \tag{B.27}$$

$$iv_g\left(\phi_{RL}^{(iv)}(0,x) - \phi_{RL}^{(i)}(0,x)\right) = V_R\varphi_L^<(x). \tag{B.28}$$

B. Diagonalization of the four-port device Hamiltonian.

$$\left[\omega + \omega_g + iv_g\left(\eta_\alpha\partial_x + \eta_\beta\partial_y\right)\right]\psi^{(j)}_{\alpha\beta} = 0, \tag{B.29}$$

$$iv_g\begin{pmatrix}\psi^{(ii)}_{RR}(x,0)\\ \psi^{(iii)}_{RR}(x,0)\end{pmatrix} = W_R\begin{pmatrix}\varphi^{<}_R(x)\\ \varphi^{>}_R(x)\end{pmatrix}, \tag{B.30}$$

$$\psi^{(iii)}_{RR}(0,y) = \psi^{(ii)}_{RR}(0,y), \tag{B.31}$$

$$iv_g\begin{pmatrix}\psi^{(i)}_{RL}(x,0)\\ \psi^{(iv)}_{RL}(x,0)\end{pmatrix} = W_L\begin{pmatrix}\varphi^{<}_R(x)\\ \varphi^{>}_R(x)\end{pmatrix}, \tag{B.32}$$

$$\psi^{(iv)}_{RL}(0,y) = \psi^{(i)}_{RL}(0,y), \tag{B.33}$$

$$iv_g\begin{pmatrix}\psi^{(i)}_{LL}(x,0)\\ \psi^{(ii)}_{LR}(x,0)\end{pmatrix} = \begin{pmatrix}W_L\varphi^{<}_L(x)\\ W_R\varphi^{<}_L(x)\end{pmatrix}, \tag{B.34}$$

$$\psi^{(ii)}_{LR}(0,y) = \psi^{(i)}_{LL}(0,y) = 0. \tag{B.35}$$

$$\begin{aligned}&2\left[\omega - \omega_{eg} + iv_g\partial_x\right]\varphi^{>}_R(x) =\\ &= 2V_R\left(\phi^{(iii)}_{RR}(0,x) + \phi^{(ii)}_{RR}(0,x)\right) + V_L\phi^{(iv)}_{RL}(x,0) + W_R\psi^{(iii)}_{RR}(x,0) + W_L\psi^{(iv)}_{RL}(x,0).\end{aligned} \tag{B.36}$$

$$\begin{aligned}&2\left[\omega - \omega_{eg} + iv_g\partial_x\right]\varphi^{<}_R(x) =\\ &= 2V_R\left(\phi^{(ii)}_{RR}(x,0) + \phi^{(i)}_{RR}(x,0)\right) + V_L\phi^{(i)}_{RL}(x,0) + W_R\psi^{(ii)}_{RR}(x,0) + W_L\psi^{(i)}_{RL}(x,0).\end{aligned} \tag{B.37}$$

$$\begin{aligned}&2\left[\omega - \omega_{eg} - iv_g\partial_x\right]\varphi^{<}_L(x) =\\ &= 2V_L\phi^{(i)}_{LL}(x,0) + V_R\left(\phi^{(iv)}_{RL}(0,x) + \phi^{(i)}_{RL}(0,x)\right) + W_R\psi^{(ii)}_{LR}(x,0) + W_L\psi^{(i)}_{LL}(x,0).\end{aligned} \tag{B.38}$$

In the above equations, we define the total energy of the two-photon wavepacket, $\omega = v_g k = v_g\left(k_1 + k_2\right) = \omega_1 + \omega_2$, where k_1 and k_2 are the wavevectors of the two photons.

The following step is to make an ansatz for the input state, i.e., the two photon wavefunction introduced through port 1. We assume the following plane wave structure,

$$\phi^{(i)}_{RR}(x_1,x_2) = A\left(e^{ik_1x_1}e^{ik_2x_2} + e^{ik_2x_1}e^{ik_1x_2}\right), \tag{B.39}$$

which fulfils the required bosonic symmetry. The normalization constant A is in principle arbitrary. By inserting the above ansatz into the equations, it is possible to compute the rest of the unknowns following a similar procedure as in Ref. [198]. In order to express the final solutions in a more compact way, let us define the general two-photon plane wave function as

$$f_{p,q} = e^{ipx_1}e^{iqx_2}, \tag{B.40}$$

where the variables may switch from x_1, x_2 to x, y when necessary. In terms of these functions, the eigenstate coefficients normalized to A are given by

$$\varphi^{<}_R(x) = 2V_R\left(\frac{e^{ik_1x}}{\omega_2 - \omega_{eg} + i\gamma/2} + \frac{e^{ik_2x}}{\omega_1 - \omega_{eg} + i\gamma/2}\right), \tag{B.41}$$

$$\varphi_R^{>}(x) =2V_R\Bigg(e^{ik_1x}\frac{t_1}{\omega_2-\omega_{eg}+i\gamma/2}+e^{ik_2x}\frac{t_2}{\omega_1-\omega_{eg}+i\gamma/2}+ \\ +\frac{2i\gamma_{dR}}{(\omega_1-\omega_{eg}+i\gamma/2)(\omega_2-\omega_{eg}+i\gamma/2)}e^{i(k-\omega_{eg})x}e^{-\gamma x/2}\Bigg), \tag{B.42}$$

$$\varphi_L^{<}(x) = 2V_R\frac{r_1}{\omega_2-\omega_{eg}+i\gamma/2}\left(e^{-ik_1x}+e^{-ik_2x}-2e^{\gamma x/2}e^{-i(k-\omega_{eg})x}\right), \tag{B.43}$$

$$\phi_{RR}^{(ii)}(x_1,x_2) = t_2f_{k_1,k_2}+t_1f_{k_2,k_1}, \tag{B.44}$$

$$\phi_{RR}^{(iii)}(x_1,x_2) = t_1t_2\left(f_{k_1,k_2}+f_{k_2,k_1}\right)- \\ 2(t_1-1)(t_2-1)e^{-\gamma|x_2-x_1|/2}\left(f_{\omega_{eg},k-\omega_{eg}}\theta(x_2-x_1)+f_{k-\omega_{eg},\omega_{eg}}\theta(x_1-x_2)\right), \tag{B.45}$$

$$\phi_{RL}^{(ii)}(x_1,x_2) = 2\left(r_2f_{k_1,-k_2}+r_1f_{k_2,-k_1}\right), \tag{B.46}$$

$$\phi_{RL}^{(iv)}(x_1,x_2) = 2\Bigg(r_2t_1f_{k_1,-k_2}+r_1t_2f_{k_2,-k_1}- \\ 2r_1(t_2-1)e^{-\gamma|x_1+x_2|/2}\left[f_{k-\omega_{eg},-\omega_{eg}}\theta(x_1+x_2)+f_{\omega_{eg},-k+\omega_{eg}}\theta(-x_1-x_2)\right]\Bigg), \tag{B.47}$$

$$\phi_{LL}^{(i)}(x_1,x_2) =r_1r_2\Bigg(f_{-k_1,-k_2}+f_{-k_2,-k_1}- \\ 2e^{-\gamma|x_2-x_1|/2}\left[f_{-k+\omega_{eg},k-\omega_{eg}}\theta(x_2-x_1)+f_{-\omega_{eg},-k+\omega_{eg}}\theta(x_1-x_2)\right]\Bigg), \tag{B.48}$$

$$\psi_{RR}^{(ii)}(x,y) = 2\tilde{t}_2f_{k_1,k_2+\omega_g}+2\tilde{t}_1f_{k_2,k_1+\omega_g}, \tag{B.49}$$

$$\psi_{RR}^{(iii)}(x,y) = \psi_{RR}^{(ii)}(x,y)\theta(y-x)+ \\ 2\Bigg(\tilde{t}_2t_1f_{k_1,k_2+\omega_g}+\tilde{t}_1t_2f_{k_2,k_1+\omega_g}-2\tilde{t}_1(t_2-1)f_{k-\omega_{eg},\omega_{eg}+\omega_g}e^{\gamma(y-x)/2}\Bigg)\theta(x-y), \tag{B.50}$$

$$\psi_{RL}^{(i)}(x,y) = 2\tilde{r}_2f_{k_1,-k_2-\omega_g}+2\tilde{r}_1f_{k_2,-k_1-\omega_g}, \tag{B.51}$$

$$\psi_{RL}^{(iv)}(x,y) = \psi_{RL}^{(i)}(x,y)\theta(-x-y)+ \\ 2\Bigg(\tilde{r}_2t_1f_{k_1,-k_2-\omega_g}+\tilde{r}_1t_2f_{k_2,-k_1-\omega_g}-2\tilde{r}_1(t_2-1)f_{k-\omega_{eg},-\omega_{eg}-\omega_g}e^{-\gamma(y+x)/2}\Bigg)\theta(x+y), \tag{B.52}$$

$$\psi_{LL}^{(i)}(x,y) = 2\tilde{r}_1r_2\left(f_{-k_1,-k_2-\omega_g}+f_{-k_2,-k_1-\omega_g}-2e^{\gamma(y-x)/2}f_{-k+\omega_{eg},-\omega_{eg}-\omega_g}\right)\theta(y-x), \tag{B.53}$$

$$\psi_{LR}^{(ii)}(x,y) = 2\tilde{t}_1r_2\left(f_{-k_1,k_2+\omega_g}+f_{-k_2,k_1+\omega_g}-2e^{\gamma(y+x)/2}f_{-k+\omega_{eg},\omega_{eg}+\omega_g}\right)\theta(-y-x), \tag{B.54}$$

where $\gamma = \gamma_{dR}+\gamma_{dL}+\gamma_{uR}+\gamma_{uL}$, and the coefficients t_j stand for $t(v_gk_j)$ (and the same for $r_j, \tilde{t}_j, \tilde{r}_j$). In the above equations, whenever the energies γ, ω_{eg} or ω_g appear in the argument of exponential functions, they represent a short-hand notation for their corresponding wavevectors, γ/v_g, ω_{eg}/v_g, and ω_g/v_g respectively. Finally, note that in

general all the wavefunctions have two different possible components, namely a plane wave component and a two-photon *bound state* proportional to $\exp(-\gamma|x_2 - x_1|)$. This nonlinear term is related to the 3LS's saturable absorber properties, as we discuss in chapter 3.

B.3. Calculation of the detection probabilities.

We devote this section to the calculation of the detection probabilities P_{mn}, as well as to demonstrate that any contribution from the wavefunctions φ_α vanishes. We start by noticing that the two-photon components of the eigenstate calculated above split into contributions of three different types, which arise naturally from the separation between the regions i, ii, iii, iv imposed by the boundary conditions. First, the state corresponding to the incoming two-photon wavepacket is given by $\phi^{(i)}_{RR}$ as defined in Eq. B.39. Secondly, the two-photon wavefunctions $\phi^{(ii)}_{RR}, \phi^{(i)}_{RL}, \psi^{(ii)}_{RR}$, and $\psi^{(i)}_{RL}$ represent transient states, in which one of the two photons has interacted with the 3LS and the other has not. Finally, the rest of the two-photon contributions, namely $\phi^{(iii)}_{RR}, \phi^{(i)}_{LL}, \phi^{(iv)}_{RL}, \psi^{(iii)}_{RR}, \psi^{(iv)}_{RL}, \psi^{(ii)}_{LR}$, and $\psi^{(i)}_{LL}$, describe the asymptotic limit in which both photons have interacted with the 3LS, and travel towards the exit ports of our system. This is a general structure for the eigenstates of any system calculated using the same method (see e.g. Ref [198, 220]).

Once the different contributions are isolated, we can properly define the so-called input state, $|\epsilon_i\rangle$, which contains only the parts of $|\epsilon\rangle$ for which a right-propagating photon is present in the region $x < 0$. In other words, it is the fraction of the two-photon eigenstate $|\epsilon\rangle$ containing both the input and the transient contributions described above. From this definition, the state $|\epsilon_i\rangle$ can be obtained directly from the general two-photon eigenstate $|\epsilon\rangle$ in Eq. 3.70, by making the substitution $\phi^{(i)}_{RR}, \phi^{(ii)}_{RR}, \phi^{(i)}_{RL}, \psi^{(ii)}_{RR}, \psi^{(i)}_{RL}, \varphi^{<}_{R} \to 0$. Finally, we can use the input state defined above to calculate the output state as $|\epsilon_o\rangle = |\epsilon\rangle - |\epsilon_i\rangle$. Such state contains only the asymptotic contributions to the eigenstate, as well as the functions $\varphi^{<}_{R}$ and $\varphi^{>}_{R}$ which, however, do not contribute to any detection probability as we will see below. The reason behind this definition of the output state will become clear in the following.

Once the output state is properly determined, we can calculate the detection probabilities P_{mn} according to their definition in the main text (Eq. 3.77),

$$P_{mn} = \frac{1}{1+\delta_{mn}} \int_{-L/2}^{L/2} dz_m \int_{-L/2}^{L/2} dz_n \frac{\langle \epsilon_o | a^\dagger_m(z_m) a^\dagger_n(z_n) a_n(z_n) a_m(z_m) | \epsilon_o \rangle}{\langle \epsilon_o | \epsilon_o \rangle|_{\Gamma=0}}. \tag{B.55}$$

The first step in the calculation of the probabilities P_{mn} is to prove that the norm of the output state $|\epsilon_o\rangle|_{\Gamma=0}$ is proportional to L^2, where $L \to \infty$ is the length of the waveguide. Note that this result would be trivial in the case of a bare waveguide, as it is the natural norm of a two-variable plane wave. We start by directly calculating the norm of such state as

$$\begin{aligned}\langle\epsilon_o|\epsilon_o\rangle = &\int dx_1 \int dx_2 \left(2|\phi_{LL}^{(i)}|^2 + 2|\phi_{RR}^{(iii)}|^2 + |\phi_{RL}^{(iv)}|^2\right) + \int dx \left(|\varphi_L^{(<)}|^2 + |\varphi_R^{>}|^2\right) + \\ &+ \int dx \int dy \left(|\psi_{RR}^{(iii)}|^2 + |\psi_{RL}^{(iv)}|^2 + |\psi_{LR}^{(ii)}|^2 + |\psi_{LL}^{(i)}|^2\right),\end{aligned} \tag{B.56}$$

which is valid for any value of Γ. In principle, we could expand the wavefunctions by using their expressions above, but we can greatly simplify the calculation in advance. Indeed, note that apart from external factors, the overlap (B.56) can be expressed as a sum of simple integrals, all of them with one of the following general shapes (or equivalent after a change of variables),

$$I_a = \int_0^{L/2} dx \int_0^{L/2} dy 1 = L^2/4, \tag{B.57}$$

$$I_b = \int_0^{L/2} dx \int_{0 \text{ or } x}^{L/2} dy e^{ipx} e^{iqy} \qquad \text{where } p, q \in \mathbb{R}, \tag{B.58}$$

$$I_c = \int_0^{L/2} dx \int_x^{L/2} dy e^{ipx} e^{iqy} e^{-\kappa|y-x|} \qquad \text{where } p, q, \kappa \in \mathbb{R}, \text{ and } \kappa > 0. \tag{B.59}$$

It is straightforward to demonstrate that

$$I_b \propto \delta_{pq} L^2/4, \tag{B.60}$$

$$I_c \propto \delta_{p0} L/2, \tag{B.61}$$

which means that only the pure plane wave terms contribute to the norm, the bound states adding a negligible contribution of order $1/L \to 0$. In other words, the norm fulfils

$$\langle\epsilon_o|\epsilon_o\rangle \propto L^2 + \mathcal{O}(L) \tag{B.62}$$

for any Γ, which is the first important result of this section. Note that, additionally, the largest contributions of the wavefunctions φ_α are only proportional to L, therefore in the limit $L \to \infty$ they do not have any weight in the norm.

The two-photon detection probabilities P_{mn} as defined above can be split into elementary integrals exactly in the same way as we have done with the norm $\langle\epsilon_o|\epsilon_o\rangle$. An analogous treatment allows us to also demonstrate that

$$P_{mn} \propto \frac{1}{\langle\epsilon_o|\epsilon_o\rangle|_{\Gamma=0}} \left(L^2 + \mathcal{O}(L)\right) \to \text{constant}, \tag{B.63}$$

where we have made use of Eq. B.62. This apparently trivial result is extremely helpful when calculating the probabilities P_{mn}. Indeed, from Eq. B.63 it is clear that the eigenstate norm will cancel out any contribution of order $\mathcal{O}(L)$ or lower, hence we only need to compute a fraction of the integrals appearing in P_{mn}. By explicitly introducing the eigenstate wavefunctions in the definition of P_{mn} and using the above simplification, we obtain the following expressions for two photons of wavevectors k_1, k_2 in the $L \to \infty$ limit,

$$P_{11} = R_1 R_2, \tag{B.64}$$

$$P_{12} = \left(R_1 T_2 + R_2 T_1\right), \tag{B.65}$$

$$P_{22} = T_1 T_2, \tag{B.66}$$

$$P_{13} = \frac{\tilde{T}_1 R_2 + \tilde{T}_2 R_1}{2}, \tag{B.67}$$

$$P_{14} = \frac{\tilde{R}_1 R_2 + \tilde{R}_2 R_1}{2}, \tag{B.68}$$

$$P_{23} = \frac{\tilde{T}_2 \left(T_1 + 1\right) + \tilde{T}_1 \left(T_2 + 1\right)}{2}, \tag{B.69}$$

$$P_{24} = \frac{\tilde{R}_2 \left(T_1 + 1\right) + \tilde{R}_1 \left(T_2 + 1\right)}{2}, \tag{B.70}$$

$$P_{33} = P_{34} = P_{44} = 0. \tag{B.71}$$

where $\{T_j, R_j, \tilde{T}_j, \tilde{R}_j\} = \{|t_j|^2, |r_j|^2, |\tilde{t}_j|^2, |\tilde{r}_j|^2\}$. Importantly, it can be shown that in the lossless case the above probabilities add up to one,

$$\sum_{m=1}^{4} \sum_{n=m}^{4} P_{mn}\Big|_{\Gamma=0} = 1. \tag{B.72}$$

This implies that the two-photon processes whose probabilities we calculate above are the only output possibilities, and completely describe the scattering in the two-photon case. In other words, such probabilities have the same role as the square modulus of the single-photon scattering amplitudes defined in Eqs. (3.54-3.57). This is the reason behind the definition of the probability densities in Eq. 3.76 in terms of the output state $|\epsilon_o\rangle$. By removing the contributions in which part or all the interaction has not yet occurred, we obtain consistent two-photon probabilities which, additionally, can be proven to coincide with the results obtained within the S-matrix formalism [275]. Finally, note that when we particularize the expressions of P_{mn} for two equivalent photons, $k_1 = k_2$, we recover Eqs. (3.86-3.89) of the main text for $t = 0$.

A final argument can be easily made as to why the contribution of the states $\propto \varphi_\alpha(x)c_\alpha^\dagger(x)|e\rangle$ is negligible in the scattering output, which represents an additional demonstration of the complete character of the set $\{P_{mn}\}$ for describing the two-photon scattering. In principle, we could extend the definition of P_{mn} and associate a detection probability to these states,

$$P(\varphi_R^>) = \frac{1}{\langle\epsilon_o|\epsilon_o\rangle|_{\Gamma=0}} \int_{-L/2}^{L/2} dx \Big| c_R(x)\sigma_{ge}|\epsilon_o\rangle \Big|^2, \tag{B.73}$$

$$P(\varphi_L^<) = \frac{1}{\langle\epsilon_o|\epsilon_o\rangle|_{\Gamma=0}} \int_{-L/2}^{L/2} dx \Big| c_L(x)\sigma_{ge}|\epsilon_o\rangle \Big|^2, \tag{B.74}$$

where $\sigma_{ge} = |g\rangle\langle e|$, and $P(\varphi_L^>) = 0$ by definition as $\varphi_L^>(x) = 0$ (see previous section). Now, it is straightforward to see that the largest contribution to these integrals has the form

$$\int_{-L/2}^{L/2} dx e^{ipx} \propto L, \tag{B.75}$$

i.e., even the largest term in the numerator of Eqs. (B.73-B.74) is cancelled by the denominator $\langle\epsilon_o|\epsilon_o\rangle|_{\Gamma=0} \propto L^2$. Any possible contribution of these states to the scattering output will then be of order $\sim 1/L \to 0$ as compared to the two-photon probabilities of Eq. (B.63). As a consequence, as we mentioned above, the detection probabilities P_{mn} are the only relevant scattering variables in this case.

C | Extraction of the quantum light-matter Hamiltonian.

In this Appendix, we obtain the light-matter Hamiltonian employed throughout this thesis from fundamental principles. First, we introduce the Lagrangian formulation of the EM field and the canonical quantization procedure. Then, we extract the fundamental interaction Hamiltonian, often referred to as minimal coupling Hamiltonian. We then deviate slightly from the usual quantization schemes in order to explicitly express the quantum EM field operators as a function of classical EM fields obtained from Maxwell equations. Finally, we devote the last part of the appendix to introduce the necessary approximations in order to reduce the minimal coupling Hamiltonian to the most usual form, which we will employ in this thesis. Since this only represents a brief summary, we address the reader for additional information to the book of Cohen-Tannoudji [16] or the excellent compilation of notes from Daniel Steck [432].

C.1. Canonical quantization of arbitrary EM fields.

The process of canonical quantization was introduced by Paul Dirac in his PhD thesis and, later on, detailed in his classic text [2]. Unlike other routes to obtain quantum mechanics from classical principles, canonical quantization has taken lead in more advanced field theories due to its simplicity and elegance. The crucial step of the canonical quantization for a particle of position x and momentum p consists in imposing quantum commutation relations to the canonical Poisson brackets,

$$\{x, p\} \mapsto \frac{1}{i\hbar}\left[\hat{x}, \hat{p}\right]. \tag{C.1}$$

It is straightforward to extend the above quantization rule to any general coordinate system in which the relevant coordinates, Q_i, and their respective canonical momenta, P_i,

are identified. This is the route we will follow for the quantization of the electromagnetic field.

C.1.1. Lagrangian formulation of the field-matter interaction.

In order to properly define a canonical momentum, it is necessary that both the coordinate variable Q_i and its time derivative $\dot{Q}_i$ appear in the Lagrangian. We will name such the *relevant* variables in our system. Our first goal, therefore, will be to express the Lagrangian of the EM field only in terms of relevant variables. Let us start by the classical equations describing a general system of particles with charges q_α and position vectors $\mathbf{r}_\alpha$ ($\alpha = 1, 2, ...N$) interacting with the EM field, namely Maxwell Equations and the Lorentz force equation [309],

$$\nabla \times \mathbf{B} = \mu_0 \mathbf{J} + \mu_0 \varepsilon_0 \varepsilon \dot{\mathbf{E}}, \tag{C.2}$$

$$\nabla \cdot \mathbf{E} = \rho / \varepsilon_0 \varepsilon, \tag{C.3}$$

$$\nabla \times \mathbf{E} = -\dot{\mathbf{B}} \quad ; \quad \nabla \cdot \mathbf{B} = 0, \tag{C.4}$$

$$m_\alpha \ddot{\mathbf{r}}_\alpha = q_\alpha \left[\mathbf{E}(\mathbf{r}_\alpha) + \dot{\mathbf{r}}_\alpha \times \mathbf{B}(\mathbf{r}_\alpha) \right]. \tag{C.5}$$

In the above expressions, we have assumed the system is non-magnetic ($\mu = 1$) and has a real dielectric permittivity ε which may depend on the frequency. The charge and current densities are related to the positions and velocities of the particles through

$$\mathbf{J} = \sum_\alpha q_\alpha \dot{\mathbf{r}}_\alpha \delta(\mathbf{r} - \mathbf{r}_\alpha) \quad ; \quad \rho = \sum_\alpha q_\alpha \delta(\mathbf{r} - \mathbf{r}_\alpha). \tag{C.6}$$

The most important variable in this problem, as we will see below, is the vector potential of the EM field, $\mathbf{A}$. This vector potential is the fundamental field characterizing the EM interaction since, as opposed to the electric and magnetic fields, the only EM interaction which always preserves locality is that of a particle with the vector potential field [432] [1]. For this reason it is usually very convenient to express both electric and magnetic fields in terms of a vector potential $\mathbf{A}$ and a scalar potential ϕ, as

$$\mathbf{B} = \nabla \times \mathbf{A} \quad ; \quad \mathbf{E} = -\nabla \phi - \dot{\mathbf{A}}. \tag{C.7}$$

It is straightforward to check that the fields satisfying the above equations automatically satisfy two of the Maxwell's equations above, namely Eqs. C.4. For the the remaining

[1] The most celebrated example of a non local particle-field interaction arises in the Aharonov-Bohm effect [433], specifically for the magnetic field.

three equations, C.2, C.3, and C.5, a possible Lagrangian is given by [16]

$$L = \frac{1}{2}\sum_\alpha m_\alpha \dot{\mathbf{r}}_\alpha^2 + \frac{\varepsilon_0}{2}\int dV\left(\varepsilon \mathbf{E}^2 - c^2\mathbf{B}^2\right) + \sum_\alpha q_\alpha\left[\dot{\mathbf{r}}_\alpha \cdot \mathbf{A}(\mathbf{r}_\alpha) - \phi(\mathbf{r}_\alpha)\right], \tag{C.8}$$

where the electric and magnetic fields should be interpreted as functionals of the scalar and vector potentials. The above Lagrangian can be shown to recover these three independent equations by applying the Euler-Lagrange equation to the three different independent coordinates and time derivatives in the above expression, namely $\{\mathbf{r}_\alpha, \dot{\mathbf{r}}_\alpha\}$, $\{\mathbf{A}, \dot{\mathbf{A}}\}$, and $\{\phi, \dot{\phi}\}$. Within the latter pair, corresponding to the scalar potential, only the variable ϕ appears in the Lagrangian, but not its time derivative. We must therefore get rid of such scalar potential if we want to express our Lagrangian in terms of relevant variables for a posterior canonical quantization.

The elimination of the variable ϕ is somewhat involved [16], and we will only briefly outline the key steps here. First, we transform into Fourier space both Eq. C.3 and the second equation in C.7, and combine them to obtain

$$\phi(\mathbf{k}) = \frac{1}{k^2}\left(\rho(\mathbf{k})/\varepsilon\varepsilon_0 + i\mathbf{k}\cdot\dot{\mathbf{A}}\right). \tag{C.9}$$

We now introduce the above expression for the scalar potential inside the definition of the electric field (right equation in C.7) to obtain the following relevant expression for the components of the electric field,

$$E_j(\mathbf{k}) = -i\frac{k_j}{\varepsilon\varepsilon_0 k^2}\rho(\mathbf{k}) + \left(\delta_{jk} - \frac{k_j k_k}{k^2}\right)\dot{A}_k(\mathbf{k}) \equiv -i\frac{k_j}{\varepsilon\varepsilon_0 k^2}\rho(\mathbf{k}) + \dot{A}_j^\perp(\mathbf{k}). \tag{C.10}$$

In the above equality, we have defined the *transverse* vector potential $\mathbf{A}^\perp$, which is by definition orthogonal to the wavevector $\mathbf{k}$. The above relation shows that the total electric field can be decomposed into two orthogonal vectors, a manifestation of the well-known Helmholtz theorem. The longitudinal component is only originated by the presence of charged particles, whereas the free-space field is purely transverse and will be the only one requiring a proper quantization [432]. As it turns out, the absence of any magnetic monopoles makes the magnetic field always transverse, and therefore dependent exclusively on such transverse vector potential. Once we have expressed both EM fields in terms of either ρ and $\mathbf{A}^\perp$, we introduce them in the Lagrangian and simplify the result by fixing the gauge. A particularly convenient choice is the Coulomb gauge $\nabla\cdot\mathbf{A} = 0$, for which the final Lagrangian reads

$$\begin{aligned} L = \frac{1}{2}\sum_\alpha m_\alpha \dot{\mathbf{r}}_\alpha^2 - V_{\text{Coulomb}} + \frac{\varepsilon_0}{2}\int d^3\mathbf{k}\left(\varepsilon|\dot{\mathbf{A}}^\perp(\mathbf{k})|^2 - c^2k^2|\mathbf{A}^\perp(\mathbf{k})|^2\right) + \\ + \varepsilon_0\int d^3\mathbf{k}\,\text{Re}\left[\mathbf{J}^\perp(\mathbf{k})\cdot\mathbf{A}^{\perp *}(\mathbf{k})\right]. \end{aligned} \tag{C.11}$$

The first two terms correspond to the Lagrangian of the ensemble of particles, where the Coulomb potential is given by

$$V_{\text{Coulomb}} = \frac{1}{2\varepsilon\varepsilon_0}\int d^3\mathbf{k}\frac{|\rho(\mathbf{k})|^2}{k^2} = \frac{1}{2}\sum_{\alpha\neq\beta}\frac{q_\alpha q_\beta}{4\pi\varepsilon\varepsilon_0|\mathbf{r}_\alpha-\mathbf{r}_\beta|}. \tag{C.12}$$

The second term in the Lagrangian is the contribution from the free EM field, and the third and last term describes the light-matter coupling.

C.1.2. Hamiltonian and canonical quantization.

With the Lagrangian expressed in terms of the relevant variables $\mathbf{r}_\alpha$ and $\mathbf{A}^\perp$ in Eq. C.11, it is now possible to undertake the canonical quantization procedure. Since only the transverse part of the vector potential appears in the following, we will drop the label " $\perp$ " from now on. The first step is to identify the canonical momenta through their classical definition,

$$\mathbf{p}_\alpha = \frac{\partial L}{\partial\dot{\mathbf{r}}_\alpha} = m\dot{\mathbf{r}}_\alpha + q_\alpha\mathbf{A}(\mathbf{r}_\alpha), \tag{C.13}$$

$$\mathbf{\Pi}(\mathbf{k}) = \frac{\partial L}{\partial\dot{\mathbf{A}}^*(\mathbf{k})} = \varepsilon\varepsilon_0\dot{\mathbf{A}}(\mathbf{k}). \tag{C.14}$$

In terms of the above canonical variables and momenta, $\{Q_i, P_i\}$, the Hamiltonian is immediately constructed as $H = \sum_i \dot{Q}_i P_i - L$, which in this case reads

$$H = \sum_\alpha \frac{1}{2m_\alpha}\left[\mathbf{p}_\alpha - q_\alpha\mathbf{A}(\mathbf{r}_\alpha)\right]^2 + V_{\text{Coulomb}} + \frac{\varepsilon_0}{2}\int d^3\mathbf{k}\left(\frac{|\mathbf{\Pi}(\mathbf{k})|^2}{\varepsilon\varepsilon_0^2} + c^2k^2|\mathbf{A}(\mathbf{k})|^2\right). \tag{C.15}$$

Finally, in order to quantize the above Hamiltonian, we transform the coordinates and momenta into operators and impose canonical commutation relations. Noting that $\mathbf{A}$ has only two independent components, because it is transverse, it is easiest to write its commutation relations in reciprocal space, introducing directions $\mathbf{e}_{\mathbf{k},n}(\mathbf{r})$ orthogonal to $\mathbf{k}$ with $n = 1, 2$. These vector functions describe the vector potential field profile associated with the mode $\{\mathbf{k}, n\}$, which in a general case is given by the boundary conditions imposed by the geometry and configuration of a given problem. They display a harmonic time dependence, and satisfy the Maxwell eigenmode equation for the electric and magnetic fields, Eq. 6.3,

$$\mathbf{e}_{\mathbf{k},n}(\mathbf{r},t) = \mathbf{e}_{\mathbf{k},n}(\mathbf{r})e^{-i\omega(\mathbf{k})t} \quad ; \quad \left(\nabla^2 + k^2\right)\mathbf{e}_{\mathbf{k},n}(\mathbf{r}) = 0. \tag{C.16}$$

By definition, the eigenmodes obtained from the above equation are orthogonal, and then we can express the total vector potential as a linear combination,

$$\mathbf{A}(\mathbf{r}) = \sum_{\mathbf{e}_{\mathbf{k},n}} \mathbf{A}_{\mathbf{e}_{\mathbf{k},n}}(\mathbf{k})\mathbf{e}_{\mathbf{k},n}(\mathbf{r}) \equiv \sum_{\mathbf{k},n} \mathbf{A}_{\mathbf{e}_{\mathbf{k},n}}(\mathbf{k})\mathbf{e}_{\mathbf{k},n}, \tag{C.17}$$

where we assume the eigenmodes are normalized. Then, the commutation relations can be expressed in terms of each component of the vector potential,

$$[\hat{r}_{\alpha i}, \hat{p}_{\beta j}] = i\hbar\delta_{\alpha\beta}\delta_{ij}, \tag{C.18}$$

$$\left[\hat{\mathbf{A}}_{\mathbf{e}_{\mathbf{k}n}}(\mathbf{k}), \hat{\mathbf{\Pi}}_{\mathbf{e}_{\mathbf{k}'m}}(\mathbf{k}')\right] = i\hbar\delta_{nm}\delta(\mathbf{k}-\mathbf{k}'). \tag{C.19}$$

This step concludes the canonical quantization procedure.

It is usually convenient to rewrite the Hamiltonian C.15 in terms of the normal modes of the vector potential. The commutation relation C.19 has a clear similarity to that of usual position and momentum operators, and therefore the field contribution in the Hamiltonian C.15 clearly resembles a harmonic oscillator, with a separate oscillator for each polarisation and momentum. Rewriting in normal modes thus means introducing the ladder operators

$$\hat{a}_{\mathbf{k}n} = \sqrt{\frac{\varepsilon\varepsilon_0}{2\hbar\omega(\mathbf{k})}}\left(\omega(\mathbf{k})\hat{A}_{\mathbf{e}_{\mathbf{k},n}}(\mathbf{k}) + \frac{i}{\varepsilon\varepsilon_0}\hat{\Pi}_{\mathbf{e}_{\mathbf{k},n}}(\mathbf{k})\right). \tag{C.20}$$

These operators can be shown to satisfy bosonic commutation relations,

$$[\hat{a}_{\mathbf{k}n}, \hat{a}_{\mathbf{k}'m}] = [\hat{a}^\dagger_{\mathbf{k}n}, \hat{a}^\dagger_{\mathbf{k}'m}] = 0 \qquad ; \qquad [\hat{a}_{\mathbf{k}n}, \hat{a}^\dagger_{\mathbf{k}'m}] = \delta_{mn}\delta(\mathbf{k}-\mathbf{k}'). \tag{C.21}$$

It is straightforward to combine them into

$$\hat{a}_{\mathbf{k}n}\mathbf{e}_{\mathbf{k},n} + \hat{a}^\dagger_{\mathbf{k}n}\mathbf{e}^*_{\mathbf{k},n} = \sqrt{\frac{\varepsilon\varepsilon_0\omega}{2\hbar}}\left(\hat{A}_{\mathbf{k}n}\mathbf{e}_{\mathbf{k},n} + \hat{A}^*_{\mathbf{k}n}\mathbf{e}^*_{\mathbf{k},n}\right) = \sqrt{\frac{2\varepsilon\varepsilon_0\omega}{\hbar}}\hat{A}_{\mathbf{k}n}\mathbf{e}_{\mathbf{k},n}, \tag{C.22}$$

where in the last step we have employed the hermitian character of the operator $\hat{\mathbf{A}}$ and the decomposition Eq. C.17. From the above equation we obtain the following expression for the transverse vector potential in the position basis,

$$\hat{\mathbf{A}}(\mathbf{r}) = \sum_{\mathbf{k}}\sum_{n=1,2}\sqrt{\frac{\hbar}{2\varepsilon\varepsilon_0\omega(\mathbf{k})}}\left(\hat{a}_{\mathbf{k}n}\mathbf{e}_{\mathbf{k},n} + H.c.\right). \tag{C.23}$$

The usual expressions for the electric and magnetic fields are immediately recovered from their definition in terms of the vector potential,

$$\hat{\mathbf{B}}(\mathbf{r}) = \sum_{\mathbf{k}}\sum_{n=1,2}\sqrt{\frac{\hbar}{2\varepsilon\varepsilon_0\omega(\mathbf{k})}}\left([\nabla\times\mathbf{e}_{\mathbf{k},n}]\,\hat{a}_{\mathbf{k}n} + H.c.\right). \tag{C.24}$$

$$\hat{\mathbf{E}}(\mathbf{r}) = -i \sum_{\mathbf{k}} \sum_{n=1,2} \sqrt{\frac{\hbar\omega(\mathbf{k})}{2\varepsilon\varepsilon_0}} \left(\hat{a}_{\mathbf{k}n}\mathbf{e}_{\mathbf{k},n} - H.c.\right). \tag{C.25}$$

Note that the above expression is valid for the transverse field, which corresponds to the free space radiation as commented above. In the case of the electric field, such expression has been obtained by transforming to the Heisenberg picture in order to perform the time derivative.

Let us finally obtain the Hamiltonian of the EM field as a function of these operators. It is usually convenient to rewrite the energy of the EM fields in Eq. C.15 as a function of the electric and magnetic field operators. By expressing $\hat{\mathbf{A}}(\mathbf{k})$ and $\hat{\mathbf{\Pi}}(\mathbf{k})$ as a function of $\hat{\mathbf{E}}(\mathbf{k})$ and $\hat{\mathbf{B}}(\mathbf{k})$, we arrive to the following equivalent expression,

$$\frac{\varepsilon_0}{2}\int d^3\mathbf{k}\left(\frac{|\hat{\mathbf{\Pi}}(\mathbf{k})|^2}{\varepsilon\varepsilon_0^2} + c^2k^2|\hat{\mathbf{A}}(\mathbf{k})|^2\right) = \frac{\varepsilon_0}{2}\int d^3\mathbf{r}\left(\varepsilon|\hat{\mathbf{E}}(\mathbf{r})|^2 + c^2|\hat{\mathbf{B}}(\mathbf{r})|^2\right). \tag{C.26}$$

By introducing the expressions for the field operators, Eqs. C.24 and C.25, the Hamiltonian of the EM field reads

$$\begin{aligned}\frac{\varepsilon_0}{2}\int d^3\mathbf{r}\left(\varepsilon|\hat{\mathbf{E}}(\mathbf{r})|^2 + c^2|\hat{\mathbf{B}}(\mathbf{r})|^2\right) = \\ \sum_{\mathbf{k}n}\frac{\hbar\omega(\mathbf{k})}{2\varepsilon_0}\left(\hat{a}^\dagger_{\mathbf{k}n}\hat{a}_{\mathbf{k}n} + \hat{a}_{\mathbf{k}n}\hat{a}^\dagger_{\mathbf{k}n}\right)\frac{\varepsilon_0}{2}\int d^3\mathbf{r}\left(\varepsilon|\mathbf{e}_{\mathbf{k},n}|^2 + c^2\frac{|\nabla\times\mathbf{e}_{\mathbf{k},n}|^2}{\omega(\mathbf{k})^2}\right).\end{aligned} \tag{C.27}$$

Now, the modes $\mathbf{e}_{\mathbf{k},n}$ above are determined by the eigenmode equation Eq. C.16 up to an arbitrary normalization constant. In practical situations, one usually solves the classical Maxwell Equations for the electric and magnetic fields $\mathbf{E}^{cl}_{\mathbf{k},n}$ and $\mathbf{B}^{cl}_{\mathbf{k},n}$, since the boundary conditions for the vector potential eigenmodes are involved and depend on the chosen gauge [434]. Hence, it is convenient to express the system eigenmodes as a function of the more available electric and magnetic fields. Since both $\mathbf{e}_{\mathbf{k},n}$ and, for instance, $\mathbf{E}^{cl}_{\mathbf{k},n}$ are solutions of the same eigenmode equation, they must be proportional to each other,

$$\mathbf{e}_{\mathbf{k},n} = C\mathbf{E}^{cl}_{\mathbf{k},n}. \tag{C.28}$$

Additionally, since each mode oscillates harmonically, we can apply the first equation in C.4 to obtain the following relation for the magnetic field,

$$\nabla\times\mathbf{e}_{\mathbf{k},n} = C\nabla\times\mathbf{E}^{cl}_{\mathbf{k},n} = i\omega(\mathbf{k})C\mathbf{B}^{cl}_{\mathbf{k},n}. \tag{C.29}$$

By introducing Eqs. C.28 and C.29 in the Hamiltonian of the EM field, Eq. C.27, we obtain

$$\frac{\varepsilon_0}{2}\int d^3\mathbf{r}\left(\varepsilon|\hat{\mathbf{E}}(\mathbf{r})|^2 + c^2k^2|\hat{\mathbf{B}}(\mathbf{r})|^2\right) = \sum_{\mathbf{k}n}\frac{\hbar\omega(\mathbf{k})}{2\varepsilon\varepsilon_0}\left(\hat{a}^\dagger_{\mathbf{k}n}\hat{a}_{\mathbf{k}n} + \hat{a}_{\mathbf{k}n}\hat{a}^\dagger_{\mathbf{k}n}\right)|C|^2U_{em}(\mathbf{k}), \tag{C.30}$$

where the expression for the classical EM energy of a mode with wavevector $\mathbf{k}$ is given by

$$U_{em}(\mathbf{k}) = \frac{\varepsilon_0}{2}\int d^3\mathbf{r}\left(\varepsilon|\mathbf{E}^{cl}_{\mathbf{k},n}(\mathbf{r})|^2 + c^2|\mathbf{B}^{cl}_{\mathbf{k},n}(\mathbf{r})|^2\right). \tag{C.31}$$

It is now evident that the Hamiltonian of the EM field has the form of a set of independent harmonic oscillators. By employing the commutation relation for the bosonic operators, and rescaling our origin of energies to get rid of the factor 1/2, we arrive to

$$\frac{\varepsilon_0}{2}\int d^3\mathbf{r}\left(\varepsilon|\hat{\mathbf{E}}(\mathbf{r})|^2 + c^2k^2|\hat{\mathbf{B}}(\mathbf{r})|^2\right) = \sum_{\mathbf{k}n}\hbar\omega(\mathbf{k})\hat{a}^\dagger_{\mathbf{k}n}\hat{a}_{\mathbf{k}n}\frac{|C|^2U_{em}(\mathbf{k})}{\varepsilon\varepsilon_0}. \tag{C.32}$$

Now, since the constant C is an arbitrary normalization of the electric and magnetic field operators, the energy of the harmonic oscillators cannot depend on it. Additionally, we know that the natural oscillation frequency of the mode $\{\mathbf{k}, n\}$ is $\omega(\mathbf{k})$, and thus the whole fraction in the above equation must be equal to 1. This implies

$$C = i\sqrt{\frac{\varepsilon\varepsilon_0}{U_{em}(\mathbf{k})}}, \tag{C.33}$$

where we have chosen the arbitrary phase factor as i for a simpler expression of the EM fields. The total Hamiltonian of the system now takes the compact form

$$\hat{H} = \sum_\alpha \frac{1}{2m_\alpha}\left[\hat{\mathbf{p}}_\alpha - q_\alpha\hat{\mathbf{A}}(\mathbf{r}_\alpha)\right]^2 + V_{\text{Coulomb}} + \sum_{\mathbf{k}}\sum_{n=1,2}\hbar\omega(\mathbf{k})\hat{a}^\dagger_{\mathbf{k}n}\hat{a}_{\mathbf{k}n}. \tag{C.34}$$

The advantage of this method is that now we can express the electric and magnetic fields in terms not of arbitrary modes $\mathbf{e}_{\mathbf{k},n}$, but of the classical solution of the Maxwell eigenmode equations, $\mathbf{E}^{cl}_{\mathbf{k},n}$ and $\mathbf{B}^{cl}_{\mathbf{k},n}$. This is very convenient for a fast quantization of any classical solution we can obtain, either analytically or numerically. Indeed, by combining the expression of C with Eqs. C.28 and C.29, we can reexpress the EM fields in Eqs. C.24 and C.25 as

$$\hat{\mathbf{B}}(\mathbf{r}) = -\sum_{\mathbf{k}}\sum_{n=1,2}\sqrt{\frac{\hbar\omega(\mathbf{k})}{2U_{em}(\mathbf{k})}}\left(\hat{a}_{\mathbf{k}n}\mathbf{B}^{cl}_{\mathbf{k},n} + H.c.\right), \tag{C.35}$$

$$\hat{\mathbf{E}}(\mathbf{r}) = \sum_{\mathbf{k}}\sum_{n=1,2}\sqrt{\frac{\hbar\omega(\mathbf{k})}{2U_{em}(\mathbf{k})}}\left(\hat{a}_{\mathbf{k}n}\mathbf{E}^{cl}_{\mathbf{k},n} + H.c.\right). \tag{C.36}$$

C.2. Transformation into dipole coupling Hamiltonian and rotating wave approximation.

Once the Hamiltonian of the EM field has been expressed in a compact form as a sum of harmonic oscillator modes, we turn our attention to the interaction term in Eq. C.34. Such interaction is expressed in terms of the vector potential operator but, however, for calculations in usual light-matter systems it is more convenient to express it as a function of the electric field $\hat{\mathbf{E}}$ and, consequently, of the classical electric field, in the same way as we have done in the previous section. Although not necessary, it is convenient for simplicity to take at this point the dipole approximation [432]. We thus consider that the particles labelled by an index α are organized in pairs, formed by two opposite charges very close to each other. In other words, the EM field is interacting with electric dipoles. This is the usual depiction of QEs in hybrid light-matter systems. Now, consider the first term of the Hamiltonian for one of these dipoles,

$$\sum_{\alpha=1,2} \frac{1}{2m_\alpha}\left[\hat{\mathbf{p}}_\alpha - q_\alpha \hat{\mathbf{A}}(\mathbf{r}_\alpha)\right]^2 = \frac{1}{2m_1}\left[\hat{\mathbf{p}}_1 - q\hat{\mathbf{A}}(\mathbf{r}_1)\right]^2 + \frac{1}{2m_2}\left[\hat{\mathbf{p}}_2 + q\hat{\mathbf{A}}(\mathbf{r}_2)\right]^2. \tag{C.37}$$

If the two charges above are very close to each other, the separation between them, $|\mathbf{r}_1 - \mathbf{r_2}|$, is very small as compared with the typical length in which the vector potential varies, namely the wavelength of the mode. In such long wavelength limit, we can assume that both charges are affected approximately by the same vector potential, i.e.,

$$\hat{\mathbf{A}}(\mathbf{r}_1) \approx \hat{\mathbf{A}}(\mathbf{r}_2) \approx \hat{\mathbf{A}}(\mathbf{R}), \tag{C.38}$$

where $\mathbf{R}$ is the the centre of mass position of the dipole. We can therefore rewrite the above Hamiltonian for the dipole in terms of the centre of mass coordinates, $\mathbf{R}$ and $\hat{\mathbf{P}}$, the reduced mass, $m = m_1 m_2/M$, and the relative momentum $\hat{\mathbf{p}} = (\hat{\mathbf{p}}_1 m_2 - \hat{\mathbf{p}}_2 m_1)/M$, where $M = m_1 + m_2$ is the total mass of the system [27]. The result is

$$\sum_{\alpha=1,2} \frac{1}{2m_\alpha}\left[\hat{\mathbf{p}}_\alpha - q_\alpha \hat{\mathbf{A}}(\mathbf{r}_\alpha)\right]^2 = \frac{\hat{\mathbf{P}}^2}{2M} + \frac{1}{2m}\left[\hat{\mathbf{p}} - q\hat{\mathbf{A}}(\mathbf{R})\right]^2. \tag{C.39}$$

The first term only adds a self-energy to the dipoles and can thus be disregarded, especially taking into account that, in the systems we study in this thesis, the QEs are fixed in space and thus this terms vanishes. We then obtain an analogous Hamiltonian for the

system of emitters,

$$\hat{H} = \sum_{\alpha} \frac{1}{2m_\alpha} \left[\hat{\mathbf{p}}_\alpha - q_\alpha \hat{\mathbf{A}}(\hat{\mathbf{R}}_\alpha)\right]^2 + V_{\text{Coulomb}} + \sum_{\mathbf{k}} \sum_{n=1,2} \hbar\omega(\mathbf{k}) \hat{a}^\dagger_{\mathbf{k}n} \hat{a}_{\mathbf{k}n} \tag{C.40}$$

where now each "particle" α represents a dipole emitter with relative momentum $\hat{\mathbf{p}}_\alpha$, reduced mass m_α and position $\hat{\mathbf{R}}_\alpha$. The term V_{Coulomb} in this case represents bth the dipole-dipole interactions and the electrostatic energy of each dipole.

From this Hamiltonian in the dipole approximation, we can easily express the couplings in terms of the electric field. Two analogous and equivalent procedures are possible for this purpose. First, the addition of a convenient time derivative to the Lagrangian, which by definition does not change the observable physics of the system. This method was the first to be employed, in the doctoral thesis of Maria Goeppert-Mayer [435]. The second method is more intuitive, and consists on applying the following unitary transformation to the above Hamiltonian,

$$\tilde{H} = e^{-i\sum_\alpha q_\alpha \hat{\mathbf{r}}_\alpha \cdot \hat{\mathbf{A}}(\mathbf{R}_\alpha)/\hbar} \hat{H} e^{i\sum_\alpha q_\alpha \hat{\mathbf{r}}_\alpha \cdot \hat{\mathbf{A}}(\mathbf{R}_\alpha)/\hbar}, \tag{C.41}$$

where $\hat{\mathbf{r}}_\alpha = \hat{\mathbf{r}}_{\alpha,2} - \hat{\mathbf{r}}_{\alpha,1}$ is the relative position of the two charges within each dipolar emitter. This is called the Power-Zienau transformation in the literature [436]. It is straightforward to determine how each term of the Hamiltonian is transformed, by means of the useful relation [432]

$$e^A B e^{-A} = B + [A, B] + \frac{1}{2!}[A, [A, B]] + ... \tag{C.42}$$

The final expression in terms of the untransformed operators reads

$$\tilde{H} = \sum_{\alpha} \left[\frac{\hat{\mathbf{p}}_\alpha^2}{2m_\alpha} - q_\alpha \hat{\mathbf{r}}_\alpha \cdot \hat{\mathbf{E}}(\mathbf{R}_\alpha)\right] + V_{\text{Coulomb}} + \sum_{\mathbf{k}} \sum_{n=1,2} \hbar\omega(\mathbf{k}) \hat{a}^\dagger_{\mathbf{k}n} \hat{a}_{\mathbf{k}n}. \tag{C.43}$$

Note that, if we had not neglected the vacuum energy of each harmonic oscillator, an extra shift Δ_P would appear in the self-energy of the dipoles, related to the polarization density of the QE. Usually such corrections, related to the Lamb shift, are dropped or reabsorbed at this point in the energy of the QEs. Finally, by introducing the dipole operator $q_\alpha \hat{\mathbf{r}}_\alpha \equiv \hat{\boldsymbol{\mu}}_\alpha$, we obtain the final Hamiltonian, represented now in terms of the electric field operator (we drop the tilde above H for simplicity),

$$H = H_{qe} + H_I + H_{em} = \sum_{\alpha} \left[\hat{H}_{0\alpha} - \hat{\boldsymbol{\mu}}_\alpha \cdot \hat{\mathbf{E}}(\mathbf{r}_\alpha)\right] + \sum_{\mathbf{k}} \sum_{n=1,2} \hbar\omega(\mathbf{k}) \hat{a}^\dagger_{\mathbf{k}n} \hat{a}_{\mathbf{k}n}. \tag{C.44}$$

Here, we have regrouped all terms acting on the quantum emitter α, including the dipole-dipole interaction, inside the operator $\hat{H}_{0\alpha}$. Additionally, since the relative position operator does not appear anymore within the Hamiltonian, we change the notation

of the centre of mass position $\mathbf{R}_\alpha$ to $\mathbf{r}_\alpha$, which now indicates the position of the dipolar emitter. Usually, the QEs have an optical transition which is more relevant than any other, and thus are approximated as two-level systems [432]. In this approximation, each of the dipoles $\alpha = 1, 2, 3...N$ is fully characterized only by two states, which we label $|g_\alpha\rangle$ and $|e_\alpha\rangle$. By choosing their energies as $\omega_{g\alpha} = 0$ and $\omega_{e\alpha} = \omega_\alpha$, we can immediately express the Hamiltonian of the QEs as a function of these states,

$$\begin{aligned} H_{qe} = \sum_\alpha H_{0\alpha} = \sum_\alpha \hbar\omega_\alpha |e_\alpha\rangle\langle e_\alpha| + \sum_{\alpha\beta} \hbar \left(V_{\alpha\beta} |e_\alpha\rangle \otimes |g_\beta\rangle\langle g_\alpha| \otimes \langle e_\beta| + H.c. \right) = \\ = \sum_\alpha \hbar\omega_\alpha \sigma_\alpha^\dagger \sigma_\alpha + \sum_{\alpha\beta} \hbar \left(V_{\alpha\beta} \sigma_\alpha^\dagger \sigma_\beta + H.c. \right). \end{aligned} \tag{C.45}$$

In the last step, we have rewritten the Hamiltonian in the second quantization picture by means of the spin creation and annihilation operators $\sigma_\alpha^\dagger = |e_\alpha\rangle\langle g_\alpha|$ and $\sigma_\alpha = (\sigma_\alpha^\dagger)^\dagger$. The hopping term $V_{\alpha\beta}$ arises from the Coulomb potential in the Hamiltonian, and describes the dipole-dipole interaction between the QEs,

$$\hbar V_{\alpha\beta} = \frac{1}{2} \frac{1}{4\pi\varepsilon\varepsilon_0 |\mathbf{r}_\alpha - \mathbf{r}_\beta|^3} \left(\boldsymbol{\mu}_\alpha \cdot \boldsymbol{\mu}_\beta - 3 \frac{(\boldsymbol{\mu}_\alpha \cdot [\mathbf{r}_\alpha - \mathbf{r}_\beta]) (\boldsymbol{\mu}_\beta \cdot [\mathbf{r}_\alpha - \mathbf{r}_\beta])}{|\mathbf{r}_\alpha - \mathbf{r}_\beta|^2} \right). \tag{C.46}$$

Once the Hamiltonian of both the QEs and the EM field, namely H_{qe} and H_{em}, have been expressed in terms of creation and annihilation operators, we can do the same with light-matter interaction Hamiltonian, H_I. Let us first consider the most general form for the dipole operator $\hat{\boldsymbol{\mu}}_\alpha$, obtained by expanding it in the complete basis formed by the operators $\{\sigma_\alpha, \sigma_\alpha^\dagger, \sigma_\alpha^\dagger\sigma_\alpha, \sigma_\alpha\sigma_\alpha^\dagger\}$,

$$\hat{\boldsymbol{\mu}}_\alpha = c\sigma_\alpha + c^*\sigma_\alpha^\dagger + \tilde{c}\sigma_\alpha^\dagger\sigma_\alpha + \tilde{c}'\sigma_\alpha\sigma_\alpha^\dagger. \tag{C.47}$$

In principle, we will work with QEs displaying no permanent dipole moment. This is usual in many emitters such as atoms, where it can be strictly demonstrated by arguments of parity [432]. Mathematically, this condition is expressed as $\langle g_\alpha|\hat{\boldsymbol{\mu}}_\alpha|g_\alpha\rangle = \langle e_\alpha|\hat{\boldsymbol{\mu}}_\alpha|e_\alpha\rangle = 0$, and automatically implies $\tilde{c} = \tilde{c}' = 0$. If we then identify the transition dipole moment as $\boldsymbol{\mu}_\alpha = \langle g_\alpha|\hat{\boldsymbol{\mu}}_\alpha|e_\alpha\rangle$, the final expression for the dipole moment operator reads

$$\hat{\boldsymbol{\mu}}_\alpha = \boldsymbol{\mu}_\alpha \left(\sigma_\alpha + \sigma_\alpha^\dagger \right). \tag{C.48}$$

By introducing the above equation together with Eq. C.36 inside the interaction Hamiltonian H_I, we finally obtain

$$H_I = -\sum_\alpha \sum_{\mathbf{k},n} \sqrt{\frac{\hbar\omega(\mathbf{k})}{2U_{em}(\mathbf{k})}} \left(\sigma_\alpha + \sigma_\alpha^\dagger \right) \boldsymbol{\mu}_\alpha \cdot \left(\hat{a}_{\mathbf{k}n} \mathbf{E}_{\mathbf{k},n}^{cl}(\mathbf{r}_\alpha) + \hat{a}_{\mathbf{k}n}^\dagger \mathbf{E}_{\mathbf{k},n}^{cl*}(\mathbf{r}_\alpha) \right). \tag{C.49}$$

The above equation is still not suitable for a simple theoretical treatment, since the terms $\sigma_\alpha^\dagger \hat{a}^\dagger$ and $\sigma_\alpha \hat{a}_\alpha$ do not conserve the number of excitations. It is usually very convenient to invoke the celebrated Rotating Wave Approximation (RWA) to get rid of those terms. The usual approach is to transform the total Hamiltonian into the interaction picture [29],

$$H^{(i)} = e^{-i(H_{qe}+H_{em})t/\hbar} H e^{i(H_{qe}+H_{em})t/\hbar}. \tag{C.50}$$

Both H_{qe} and H_{em} remain unaltered by this transformation whereas, on the other hand, the interaction term becomes

$$\hat{H}_I^{(i)} = -\sum_\alpha \sum_{\mathbf{k},n} \sqrt{\frac{\hbar\omega(\mathbf{k})}{2U_{em}}} \Big[\boldsymbol{\mu}_\alpha \cdot \mathbf{E}^{cl*}_{\mathbf{k},n}(\mathbf{r}_\alpha) \hat{a}^\dagger_{\mathbf{k}n} \left(\sigma_\alpha e^{it(\omega(\mathbf{k})-\omega_\alpha)} + \sigma_\alpha^\dagger e^{it(\omega(\mathbf{k})+\omega_\alpha)} \right) + \\ + \boldsymbol{\mu}_\alpha \cdot \mathbf{E}^{cl}_{\mathbf{k},n}(\mathbf{r}_\alpha) \hat{a}_{\mathbf{k}n} \left(\sigma_\alpha e^{it(-\omega(\mathbf{k})-\omega_\alpha)} + \sigma_\alpha^\dagger e^{it(-\omega(\mathbf{k})+\omega_\alpha)} \right) \Big]. \tag{C.51}$$

In the above equation, the two terms which do not conserve the number of excitations oscillate at a much faster pace than the other two. The RWA consists on neglecting such contributions since their dynamics is too fast to be relevant, and averages out to zero. In principle, this approximation is valid for light-emitter couplings inferior to $\sim 0.1\omega_\alpha$ [26]. By dropping these terms and transforming back into the Schrödinger picture, the following final expression for the Hamiltonian is obtained,

$$H = H_{qe} + H_I + H_{em} = \\ \sum_\alpha \omega_\alpha \sigma_\alpha^\dagger \sigma_\alpha + \sum_{\alpha\beta} \left(V_{\alpha\beta} \sigma_\alpha^\dagger \sigma_\beta + H.c. \right) + \sum_{\alpha,\mathbf{k}} \left(g_\alpha(\mathbf{k}) \hat{a}^\dagger_{\mathbf{k}} \sigma_\alpha + H.c. \right) + \sum_{\mathbf{k}} \omega(\mathbf{k}) \hat{a}^\dagger_{\mathbf{k}} \hat{a}_{\mathbf{k}}. \tag{C.52}$$

where for simplicity we have regrouped the field mode indices $\{\mathbf{k}, n\}$ into a single one, namely $\mathbf{k}$, and we have taken $\hbar = 1$. The exciton-photon coupling strength above is defined as

$$\hbar g_\alpha(\mathbf{k}) = -\sqrt{\frac{\hbar\omega(\mathbf{k})}{2U_{em}}} \boldsymbol{\mu}_\alpha \cdot \mathbf{E}^{cl*}_{\mathbf{k},n}(\mathbf{r}_\alpha). \tag{C.53}$$

This is the general Hamiltonian employed in the basic theory of light-matter interaction. As a detail, note how in the absence of dipole-dipole interaction, the above expression is equivalent to the waveguide QED Hamiltonian in Eq. 2.2.

D | The oscillating electric dipole.

In this short Appendix, we briefly detail the calculation of both the Purcell and the beta factor for a dipole emitter in the vicinities of an arbitrary nanostructure. The description of the system as a classical radiating dipole has been widely employed to estimate the emission properties of quantum emitters coupled to nanostructures [337, 437, 438]. Usually, the dipole is the only field source of the problem and it oscillates harmonically. In such situation, it is more convenient to express Maxwell Equations in the frequency domain [309],

$$\nabla \times \mathbf{E}(\mathbf{r},\omega) = i\omega\mu_0 \mathbf{H}(\mathbf{r},\omega), \tag{D.1}$$

$$\nabla \times \mathbf{H}(\mathbf{r},\omega) = -i\frac{\omega\varepsilon(\omega)}{\mu_0 c^2}\mathbf{E}(\mathbf{r},\omega) + \mathbf{j}_N(\mathbf{r},\omega), \tag{D.2}$$

$$\omega\nabla \cdot \mathbf{E}(\mathbf{r},\omega) = -\frac{i}{\varepsilon_0\varepsilon(\omega)}\nabla \cdot \mathbf{j}_N(\mathbf{r},\omega), \tag{D.3}$$

$$\nabla \cdot \mathbf{H}(\mathbf{r},\omega) = 0, \tag{D.4}$$

where $\mathbf{E}$ and $\mathbf{H}$ represent, respectively, the electric and magnetic field, and ε_0, μ_0 are the vacuum permittivity and permeability, respectively. In the equations above, we have assumed a non-magnetic material ($\mu = 1$) and an homogeneous and isotropic relative permittivity $\varepsilon(\omega)$ for all domains. The term $\mathbf{j}_N$ represents the so-called noise current density [290], and accounts for the field sources of this problem, in our case the radiating dipole. This quantity is related to the permanent polarization vector $\mathbf{P}_N = \mathbf{P} - \mathbf{P}_{\text{ind}}$ through $\mathbf{j}_N = -i\omega\mathbf{P}_N$, where $\mathbf{P}$ and $\mathbf{P}_{\text{ind}}$ represent the total and field-induced polarization vectors, respectively. The above relation between the current density and the permanent polarization in the frequency space indicates that, in the time domain, $\mathbf{j}_N$ is the time derivative of $\mathbf{P}_N$, and therefore represents any electric current in the system that is not induced by the EM fields.

As we have already mentioned, the only source of radiation in this problem is a point dipole of moment $\boldsymbol{\mu}$. This dipole can be considered as an oscillating current placed at the emitter position, $\mathbf{r}_0$, for which the corresponding current density is given by $\mathbf{j}_N(\mathbf{r},\omega) = -i\omega\boldsymbol{\mu}\delta(\mathbf{r}-\mathbf{r}_0)$ [22]. Once the source terms are fixed, the Maxwell equations D.1-D.4 can be solved either analytically or numerically to obtain the EM fields. From here, it is straightforward to calculate the DRE as given by Eq. 6.10. Indeed, in a linear medium the total dissipated power W of any current distribution with a harmonic time dependence is given by the following simple expression [22],

$$W = -\frac{1}{2}\int_V \mathrm{Re}\{\mathbf{j}_N^*(\mathbf{r},\omega)\cdot\mathbf{E}(\mathbf{r},\omega)\}dV, \tag{D.5}$$

V being the volume of the source. By introducing the explicit form of the dipole current density in the above equation, we determine the total power as

$$W = \frac{\omega}{2}\mathrm{Im}\{\boldsymbol{\mu}\cdot\mathbf{E}(\mathbf{r}_0,\omega)\}, \tag{D.6}$$

which is a function of the frequency and dipole moment of the emitter, as well as the electric field obtained upon solving Maxwell equations. Finally, the above quantity can be normalized to the well-known expression for the radiated power of a dipole in vacuum,

$$W_0 = \frac{|\boldsymbol{\mu}|^2}{4\pi\varepsilon_0}\frac{\omega^4}{3c^3}, \tag{D.7}$$

to obtain a general definition for the DRE,

$$\frac{\gamma}{\gamma_0} = \frac{W}{W_0} = \frac{6\pi\varepsilon_0 c^3}{\omega^3}\frac{\mathrm{Im}\{\boldsymbol{\mu}\cdot\mathbf{E}(\mathbf{r}_0,\omega)\}}{|\boldsymbol{\mu}|^2}. \tag{D.8}$$

Note that, since the electric field produced by a radiating dipole is proportional to the dipole moment itself, the DRE remains independent on the absolute value of $\boldsymbol{\mu}$.This standard definition is a relevant expression, since it is valid for any EM environment in which the oscillating dipole moment $\boldsymbol{\mu}$ is the only source. In a given problem, if the QE can exist in vacuum, then we can define a vacuum decay rate γ_0, and the above expression is automatically equal to the Purcell factor. On the other hand, in the case of our NV centre, the DRE has to be properly normalized as we will see below.

While Eq. D.8 is valid for any general EM environment, further particularizations have to be assumed in order to calculate the β factor. Specifically, we consider that our nanostructure is an infinite waveguide set along the y axis, and that losses in the metal are small, i.e., $\mathrm{Im}\,[\varepsilon_m] \ll \mathrm{Re}\,[\varepsilon_m]$. This approximation is legitimate in the specific case of our VG, since its propagation length fulfils $L_p \gg \lambda_0$. We also assume that the

dipole moment $\boldsymbol{\mu}$ lies in the transverse plane of the waveguide, namely the xz plane. In this situation, a simple expression for the normalized decay rate γ_{CPP}/γ_0 can be obtained when the waveguide is translationally invariant along the y direction. Since a detailed extraction of such equality is quite involved, we address the reader for further information to Ref. [407], where a step by step deduction is presented in a clear way. The final expression reads [337, 439]

$$\frac{\gamma_{\mathrm{CPP}}}{\gamma_0} \equiv \frac{W}{W_0} = \frac{3\pi c^3 \varepsilon_0}{\omega^2} \frac{|\mathbf{u}_\mu \cdot \mathbf{e}|^2}{\mathrm{Re} \int dS \mathbf{u}_y \left(\mathbf{e} \times \mathbf{h}^*\right)}. \tag{D.9}$$

Here, $\mathbf{u}_y$ and $\mathbf{u}_\mu$ are the unit vectors parallel to the waveguide axis y and the dipole moment $\boldsymbol{\mu}$, respectively. The vectors $\mathbf{e}$ and $\mathbf{h}$ are the respective electric and magnetic fields of the guided plasmon mode. In the case of the plasmonic VG under consideration, such EM fields correspond to the CPP modes, and have been calculated numerically in section 6.2. The dot product in the numerator of Eq. D.9 indicates that the coupling to CPPs is maximized when the dipole orientation is parallel to the CPP modal field. Finally, the integral in the denominator is a normalization constant for the CPP mode. For convention, such normalization is chosen in the plane transverse to the waveguide axis [409, 440], i.e., in the above equation $dS \equiv dxdz$. Once the decay rate to the guided modes is determined, the β factor is straightforward to calculate through

$$\beta = \left(\frac{\gamma}{\gamma_0}\right)^{-1} \frac{\gamma_{\mathrm{CPP}}}{\gamma_0}, \tag{D.10}$$

as a function of the decay rate enhancement in Eq. D.8. This expression will be helpful to calculate the beta factor in a first approximation although, as we discuss in the main text, it has to be substituted by a more general formula for an accurate description of our experimental setup.

Bibliography

[1] N. Bohr. *The Theory of Spectra and Atomic Constitution: Three Essays* (Cambridge University Press, 2011). (cited on p. 1)

[2] P. A. M. Dirac. *The principles of quantum mechanics*. 27 (Oxford university press, 1981). (cited on pages 1, 3, 112, and 239)

[3] F. J. Dyson. The radiation theories of tomonaga, schwinger, and feynman. Phys. Rev. **75**, 486 (1949). (cited on p. 1)

[4] E. M. Purcell. Spontaneous emission probabilities at radio frequencies. Physical Review **69**, 681 (1946). (cited on pages 1 and 4)

[5] K. Drexhage. Influence of a dielectric interface on fluorescence decay time. Journal of Luminescence **1**, 693 (1970). (cited on p. 2)

[6] R. H. Dicke. Coherence in spontaneous radiation processes. Phys. Rev. **93**, 99 (1954). (cited on pages 2, 3, 30, and 114)

[7] T. H. Maiman. Stimulated optical radiation in ruby (1960). (cited on p. 2)

[8] B. Liedberg, C. Nylander, and I. Lunström. Surface plasmon resonance for gas detection and biosensing. Sensors and Actuators **4**, 299 (1983). (cited on p. 2)

[9] D. W. Pohl, W. Denk, and M. Lanz. Optical stethoscopy: Image recording with resolution $\lambda/20$. Applied Physics Letters **44** (1984). (cited on p. 2)

[10] D. R. Smith, W. J. Padilla, D. C. Vier, S. C. Nemat-Nasser, and S. Schultz. Composite medium with simultaneously negative permeability and permittivity. Phys. Rev. Lett. **84**, 4184 (2000). (cited on p. 2)

[11] E. Yablonovitch. Inhibited spontaneous emission in solid-state physics and electronics. Phys. Rev. Lett. **58**, 2059 (1987). (cited on pages 2 and 9)

[12] J. S. Bell. On the einstein podolsky rosen paradox. Physics **1 (3)**, 195 (1964). (cited on pages 2 and 66)

[13] J. F. Clauser. Experimental distinction between the quantum and classical field-theoretic predictions for the photoelectric effect. Phys. Rev. D **9**, 853 (1974). (cited on p. 2)

[14] D. Walls *et al.* Squeezed states of light. nature **306**, 141 (1983). (cited on p. 2)

[15] J. I. Cirac and P. Zoller. Quantum computations with cold trapped ions. Phys. Rev. Lett. **74**, 4091 (1995). (cited on pages 2 and 15)

[16] C. Cohen-Tannoudji, J. Dupont-Roc, and G. Grynberg. *Photons and Atoms: Introduction to Quantum Electrodynamics* (Wiley, 1997). (cited on pages 3, 110, 118, 239, and 241)

[17] E. T. Jaynes and F. W. Cummings. Comparison of quantum and semiclassical radiation theories with application to the beam maser. Proceedings of the IEEE **51**, 89 (1963). (cited on p. 3)

[18] M. Tavis and F. W. Cummings. Exact solution for an n-molecule—radiation-field hamiltonian. Physical Review **170**, 379 (1968). (cited on pages 3, 110, and 113)

[19] W. Louisell. *Quantum statistical properties of radiation.* Wiley Series in Pure and Applied Optics Series (John Wiley & Sons Canada, Limited, 1973). (cited on pages 3, 7, 26, 27, 32, and 120)

[20] H.-P. Breuer and F. Petruccione. *The theory of open quantum systems* (Oxford University Press on Demand, 2002). (cited on pages 3, 27, and 172)

[21] R. Loudon. *The Quantum Theory of Light* (OUP Oxford, 2000). (cited on pages 3, 119, and 160)

[22] L. Novotny and B. Hecht. *Principles of nano-optics* (Cambridge university press, 2012). (cited on pages 3, 4, 13, 28, 50, 56, 116, 180, 183, 188, 191, and 252)

[23] A. Maradudin, J. Sambles, and W. Barnes. *Modern Plasmonics.* Handbook of Surface Science (Elsevier Science, 2014). (cited on pages 4, 126, and 187)

[24] K. H. Madsen, S. Ates, T. Lund-Hansen, A. Löffler, S. Reitzenstein, A. Forchel, and P. Lodahl. Observation of non-markovian dynamics of a single quantum dot in a micropillar cavity. Physical review letters **106**, 233601 (2011). (cited on p. 4)

[25] K. V. Nerkararyan and S. I. Bozhevolnyi. Relaxation dynamics of a quantum emitter resonantly coupled to a coherent state of a localized surface plasmon. Faraday discussions **178**, 295 (2015). (cited on p. 4)

[26] C. Gerry and P. Knight. *Introductory Quantum Optics* (Cambridge University Press, 2005). (cited on pages 5, 24, 26, 27, 29, 84, 122, 199, and 249)

[27] W. Vogel and D. Welsch. *Quantum Optics* (Wiley, 2006). (cited on pages 5, 117, 121, and 246)

[28] Y. Kaluzny, P. Goy, M. Gross, J. M. Raimond, and S. Haroche. Observation of self-induced rabi oscillations in two-level atoms excited inside a resonant cavity: The ringing regime of superradiance. Phys. Rev. Lett. **51**, 1175 (1983). (cited on pages 5, 8, and 110)

[29] C. Cohen-Tannoudji, B. Diu, and F. Laloe. *Quantum Mechanics*. Number v. 1 in Quantum Mechanics (Wiley, 1991). (cited on pages 5, 45, 131, and 249)

[30] A. Kavokin, J. Baumberg, G. Malpuech, and F. Laussy. *Microcavities*. Series on Semiconductor Science and Technology (OUP Oxford, 2007). (cited on pages 5, 9, 110, 113, 116, 124, 207, and 215)

[31] S. Maier. *Plasmonics: Fundamentals and Applications* (Springer US, 2010). (cited on pages 5, 10, 121, 125, and 180)

[32] D. Porras, C. Ciuti, J. J. Baumberg, and C. Tejedor. Polariton dynamics and bose-einstein condensation in semiconductor microcavities. Phys. Rev. B **66**, 085304 (2002). (cited on p. 5)

[33] J. Kasprzak, M. Richard, S. Kundermann, A. Baas, P. Jeambrun, J. Keeling, F. Marchetti, M. Szymańska, R. Andre, J. Staehli, *et al.* Bose–einstein condensation of exciton polaritons. Nature **443**, 409 (2006). (cited on pages 5 and 110)

[34] A. Amo, J. Lefrère, S. Pigeon, C. Adrados, C. Ciuti, I. Carusotto, R. Houdré, E. Giacobino, and A. Bramati. Superfluidity of polaritons in semiconductor microcavities. Nature Physics **5**, 805 (2009). (cited on pages 5 and 110)

[35] E. Ahmadi, H. Chalabi, A. Arab, and S. Khorasani. Cavity quantum electrodynamics in the ultrastrong coupling regime. Scientia Iranica **18**, 820 (2011). (cited on p. 6)

[36] A. A. Anappara, S. De Liberato, A. Tredicucci, C. Ciuti, G. Biasiol, L. Sorba, and F. Beltram. Signatures of the ultrastrong light-matter coupling regime. Phys. Rev. B

79, 201303 (2009). (cited on p. 6)

[37] B. Peropadre, D. Zueco, D. Porras, and J. J. García-Ripoll. Nonequilibrium and nonperturbative dynamics of ultrastrong coupling in open lines. Phys. Rev. Lett. **111**, 243602 (2013). (cited on p. 6)

[38] C. Ciuti and I. Carusotto. Input-output theory of cavities in the ultrastrong coupling regime: The case of time-independent cavity parameters. Phys. Rev. A **74**, 033811 (2006). (cited on p. 6)

[39] T. Niemczyk, F. Deppe, H. Huebl, E. Menzel, F. Hocke, M. Schwarz, J. Garcia-Ripoll, D. Zueco, T. Hümmer, E. Solano, *et al.* Circuit quantum electrodynamics in the ultrastrong-coupling regime. Nature Physics **6**, 772 (2010). (cited on pages 6 and 8)

[40] D. Hagenmüller, S. De Liberato, and C. Ciuti. Ultrastrong coupling between a cavity resonator and the cyclotron transition of a two-dimensional electron gas in the case of an integer filling factor. Phys. Rev. B **81**, 235303 (2010). (cited on p. 6)

[41] S. Gambino, M. Mazzeo, A. Genco, O. Di Stefano, S. Savasta, S. Patané, D. Ballarini, F. Mangione, G. Lerario, D. Sanvitto, *et al.* Exploring light–matter interaction phenomena under ultrastrong coupling regime. ACS Photonics **1**, 1042 (2014). (cited on p. 6)

[42] Y. Wang, J. Zhang, C. Wu, J. Q. You, and G. Romero. Holonomic quantum computation in the ultrastrong-coupling regime of circuit qed. Phys. Rev. A **94**, 012328 (2016). (cited on p. 6)

[43] J. Casanova, G. Romero, I. Lizuain, J. J. García-Ripoll, and E. Solano. Deep strong coupling regime of the jaynes-cummings model. Phys. Rev. Lett. **105**, 263603 (2010). (cited on p. 6)

[44] S. De Liberato. Light-matter decoupling in the deep strong coupling regime: The breakdown of the purcell effect. Physical review letters **112**, 016401 (2014). (cited on p. 6)

[45] G. Khitrova, H. Gibbs, M. Kira, S. W. Koch, and A. Scherer. Vacuum rabi splitting in semiconductors. Nature Physics **2**, 81 (2006). (cited on pages 8, 9, and 295)

[46] K. Santhosh, O. Bitton, L. Chuntonov, and G. Haran. Vacuum rabi splitting in a plasmonic cavity at the single quantum emitter limit. Nat Commun **7** (2016). (cited on pages 8, 10, and 295)

[47] P. Goy, J. M. Raimond, M. Gross, and S. Haroche. Observation of cavity-enhanced single-atom spontaneous emission. Phys. Rev. Lett. **50**, 1903 (1983). (cited on p. 8)

[48] S. Haroche and J.-M. Raimond. *Exploring the quantum: atoms, cavities, and photons* (Oxford university press, 2006). (cited on pages 8, 23, and 109)

[49] E. Orgiu, J. George, J. Hutchison, E. Devaux, J. Dayen, B. Doudin, F. Stellacci, C. Genet, J. Schachenmayer, C. Genes, *et al.* Conductivity in organic semiconductors hybridized with the vacuum field. Nature Materials (2015). (cited on pages 9, 150, and 178)

[50] M. Pelton, C. Santori, J. Vučković, B. Zhang, G. S. Solomon, J. Plant, and Y. Yamamoto. Efficient source of single photons: A single quantum dot in a micropost microcavity. Phys. Rev. Lett. **89**, 233602 (2002). (cited on p. 9)

[51] Y.-S. Park, A. K. Cook, and H. Wang. Cavity qed with diamond nanocrystals and silica microspheres. Nano letters **6**, 2075 (2006). (cited on p. 9)

[52] P. Michler, A. Kiraz, C. Becher, W. Schoenfeld, P. Petroff, L. Zhang, E. Hu, and A. Imamoglu. A quantum dot single-photon turnstile device. Science **290**, 2282 (2000). (cited on p. 9)

[53] A. Kavokin and G. Malpuech. *Cavity Polaritons.* Thin Films and Nanostructures (Elsevier Science, 2003). (cited on pages 9, 110, and 124)

[54] H. Yokoyama and K. Ujihara. *Spontaneous Emission and Laser Oscillation in Microcavities.* Laser & Optical Science & Technology (Taylor & Francis, 1995). (cited on pages 9 and 89)

[55] F. Jahnke (editor) *Quantum Optics with Semiconductor Nanostructures.* Woodhead Publishing Series in Electronic and Optical Materials (Woodhead Publishing, 2012). (cited on pages 9 and 181)

[56] P. Lodahl, A. F. Van Driel, I. S. Nikolaev, A. Irman, K. Overgaag, D. Vanmaekelbergh, and W. L. Vos. Controlling the dynamics of spontaneous emission from quantum dots by photonic crystals. Nature **430**, 654 (2004). (cited on p. 9)

[57] M. D. Leistikow, A. P. Mosk, E. Yeganegi, S. R. Huisman, A. Lagendijk, and W. L. Vos. Inhibited spontaneous emission of quantum dots observed in a 3d photonic band gap. Phys. Rev. Lett. **107**, 193903 (2011). (cited on p. 9)

[58] L. Sanchis, M. J. Cryan, J. Pozo, I. J. Craddock, and J. G. Rarity. Ultrahigh purcell

factor in photonic crystal slab microcavities. Phys. Rev. B **76**, 045118 (2007). (cited on p. 9)

[59] A. Akimov, A. Mukherjee, C. Yu, D. Chang, A. Zibrov, P. Hemmer, H. Park, and M. Lukin. Generation of single optical plasmons in metallic nanowires coupled to quantum dots. Nature **450**, 402 (2007). (cited on pages 10, 71, 180, 181, 194, 198, 201, and 202)

[60] G. Di Martino, Y. Sonnefraud, M. S. Tame, S. Kéna-Cohen, F. Dieleman, i. m. c. K. Özdemir, M. S. Kim, and S. A. Maier. Observation of quantum interference in the plasmonic hong-ou-mandel effect. Phys. Rev. Applied **1**, 034004 (2014). (cited on p. 10)

[61] E. J. R. Vesseur, F. J. G. de Abajo, and A. Polman. Broadband purcell enhancement in plasmonic ring cavities. Phys. Rev. B **82**, 165419 (2010). (cited on p. 10)

[62] H. J. Kimble. The quantum internet. Nature **453**, 1023 (2008). (cited on pages 10, 16, 17, 203, and 211)

[63] S. Ritter, C. Nölleke, C. Hahn, A. Reiserer, A. Neuzner, M. Uphoff, M. Mücke, E. Figueroa, J. Bochmann, and G. Rempe. An elementary quantum network of single atoms in optical cavities. Nature **484**, 195 (2012). (cited on p. 11)

[64] M. Gaio, M. Moffa, M. Castro-Lopez, D. Pisignano, A. Camposeo, and R. Sapienza. Modal coupling of single photon emitters within nanofibre waveguides. ACS nano (2016). (cited on pages 11 and 295)

[65] P. Kolchin, N. Pholchai, M. H. Mikkelsen, J. Oh, S. Ota, M. S. Islam, X. Yin, and X. Zhang. High purcell factor due to coupling of a single emitter to a dielectric slot waveguide. Nano letters **15**, 464 (2014). (cited on pages 11 and 295)

[66] M. Arcari, I. Söllner, A. Javadi, S. Lindskov Hansen, S. Mahmoodian, J. Liu, H. Thyrrestrup, E. H. Lee, J. D. Song, S. Stobbe, and P. Lodahl. Near-unity coupling efficiency of a quantum emitter to a photonic crystal waveguide. Phys. Rev. Lett. **113**, 093603 (2014). (cited on pages 11, 12, 18, 97, 106, 209, 217, and 295)

[67] S. J. Kress, F. V. Antolinez, P. Richner, S. V. Jayanti, D. K. Kim, F. Prins, A. Riedinger, M. P. Fischer, S. Meyer, K. M. McPeak, *et al.* Wedge waveguides and resonators for quantum plasmonics. Nano letters **15**, 6267 (2015). (cited on pages 11, 210, 218, and 295)

[68] W. Bogaerts, R. Baets, P. Dumon, V. Wiaux, S. Beckx, D. Taillaert, B. Luyssaert, J. V.

Campenhout, P. Bienstman, and D. V. Thourhout. Nanophotonic waveguides in silicon-on-insulator fabricated with cmos technology. Journal of Lightwave Technology **23**, 401 (2005). (cited on p. 11)

[69] A. Politi, M. J. Cryan, J. G. Rarity, S. Yu, and J. L. O'Brien. Silica-on-silicon waveguide quantum circuits. Science **320**, 646 (2008). (cited on pages 11 and 17)

[70] P. Lodahl, S. Mahmoodian, and S. Stobbe. Interfacing single photons and single quantum dots with photonic nanostructures. Rev. Mod. Phys. **87**, 347 (2015). (cited on pages 12, 209, and 217)

[71] G. D. Marshall, A. Politi, J. C. F. Matthews, P. Dekker, M. Ams, M. J. Withford, and J. L. O'Brien. Laser written waveguide photonic quantum circuits. Opt. Express **17**, 12546 (2009). (cited on pages 12 and 17)

[72] I. Söllner, S. Mahmoodian, S. L. Hansen, L. Midolo, A. Javadi, G. Kiršanskė, T. Pregnolato, H. El-Ella, E. H. Lee, J. D. Song, *et al.* Deterministic photon–emitter coupling in chiral photonic circuits. Nature nanotechnology **10**, 775 (2015). (cited on pages 12, 17, 18, 19, 45, 61, 68, 94, 97, 100, 106, and 225)

[73] T. W. Ebbesen, C. Genet, and S. I. Bozhevolnyi. Surface-plasmon circuitry. Physics Today **61**, 44 (2008). (cited on p. 12)

[74] D. E. Chang, A. S. Sørensen, P. R. Hemmer, and M. D. Lukin. Strong coupling of single emitters to surface plasmons. Phys. Rev. B **76**, 035420 (2007). (cited on pages 12, 125, and 126)

[75] D. E. Chang, A. S. Sørensen, E. A. Demler, and M. D. Lukin. A single-photon transistor using nanoscale surface plasmons. Nature Physics **3**, 807 (2007). (cited on pages 12, 18, 36, 67, 105, 205, and 213)

[76] R. F. Oulton, V. J. Sorger, D. Genov, D. Pile, and X. Zhang. A hybrid plasmonic waveguide for subwavelength confinement and long-range propagation. Nature Photonics **2**, 496 (2008). (cited on pages 12 and 194)

[77] H. Zheng and H. U. Baranger. Persistent quantum beats and long-distance entanglement from waveguide-mediated interactions. Phys. Rev. Lett. **110**, 113601 (2013). (cited on pages 12, 56, 66, 67, 103, 205, 209, 213, and 218)

[78] B. Lounis and M. Orrit. Single-photon sources. Reports on Progress in Physics **68**, 1129 (2005). (cited on pages 13 and 122)

[79] Y. Sun, G. C. Welch, W. L. Leong, C. J. Takacs, G. C. Bazan, and A. J. Heeger. Solution-processed small-molecule solar cells with 6.7% efficiency. Nature materials **11**, 44 (2012). (cited on p. 13)

[80] F. J. Duarte, P. Kelley, L. W. Hillman, and P. F. Liao. *Dye laser principles* (Academic Press, 1990). (cited on p. 13)

[81] W. P. Ambrose, P. M. Goodwin, J. Enderlein, D. J. Semin, J. C. Martin, and R. A. Keller. Fluorescence photon antibunching from single molecules on a surface. Chemical Physics Letters **269**, 365 (1997). (cited on p. 13)

[82] L. Fleury, B. Sick, G. Zumofen, B. Hecht, and U. P. Wild. High photo-stability of single molecules in an organic crystal at room temperature observed by scanning confocal optical microscopy. Molecular Physics **95**, 1333 (1998). (cited on p. 13)

[83] A. Gruber, A. Dräbenstedt, C. Tietz, L. Fleury, J. Wrachtrup, and C. Von Borczyskowski. Scanning confocal optical microscopy and magnetic resonance on single defect centers. Science **276**, 2012 (1997). (cited on p. 13)

[84] M. W. Doherty, N. B. Manson, P. Delaney, F. Jelezko, J. Wrachtrup, and L. C. Hollenberg. The nitrogen-vacancy colour centre in diamond. Physics Reports **528**, 1 (2013). The nitrogen-vacancy colour centre in diamond.
(cited on pages 13, 181, and 183)

[85] Y. Dumeige, F. Treussart, R. Alléaume, T. Gacoin, J.-F. Roch, and P. Grangier. Photo-induced creation of nitrogen-related color centers in diamond nanocrystals under femtosecond illumination. Journal of luminescence **109**, 61 (2004). (cited on p. 14)

[86] S. Arroyo-Camejo, A. Lazariev, S. W. Hell, and G. Balasubramanian. Room temperature high-fidelity holonomic single-qubit gate on a solid-state spin. Nature communications **5** (2014). (cited on p. 14)

[87] K. Nemoto, M. Trupke, S. J. Devitt, B. Scharfenberger, K. Buczak, J. Schmiedmayer, and W. J. Munro. Photonic quantum networks formed from nv centers. Scientific Reports **6**, 26284 (2016). (cited on pages 14 and 181)

[88] P. N. Prasad. *Nanophotonics* (Wiley, 2004), 1 edition. (cited on p. 14)

[89] B. Mahler, P. Spinicelli, S. Buil, X. Quelin, J.-P. Hermier, and B. Dubertret. Towards non-blinking colloidal quantum dots. Nature materials **7**, 659 (2008). (cited on p. 14)

[90] V. V. Zhirnov, J. A. Hutchby, G. I. Bourianoff, and J. E. Brewer. Emerging research

memory and logic technologies. IEEE Circuits and Devices Magazine **21**, 47 (2005). (cited on p. 14)

[91] M. A. Nielsen and I. L. Chuang. *Quantum computation and quantum information* (Cambridge university press, 2010). (cited on pages 14, 15, 17, 23, 67, and 88)

[92] G. Rempe, R. J. Thompson, and H. J. Kimble. Cavity quantum electrodynamics with strong coupling in the optical domain. Physica Scripta **1994**, 67 (1994). (cited on p. 15)

[93] A. Wallraff, D. I. Schuster, A. Blais, L. Frunzio, R.-S. Huang, J. Majer, S. Kumar, S. M. Girvin, and R. J. Schoelkopf. Strong coupling of a single photon to a superconducting qubit using circuit quantum electrodynamics. Nature **431**, 162 (2004). (cited on pages 15 and 179)

[94] D. A. Lidar and K. Birgitta Whaley. *Decoherence-Free Subspaces and Subsystems*, 83–120 (Springer Berlin Heidelberg, Berlin, Heidelberg, 2003). (cited on p. 15)

[95] L. Jiang, A. M. Rey, O. Romero-Isart, J. J. García-Ripoll, A. Sanpera, and M. D. Lukin. Preparation of decoherence-free cluster states with optical superlattices. Phys. Rev. A **79**, 022309 (2009). (cited on p. 15)

[96] M. Freedman, A. Kitaev, M. Larsen, and Z. Wang. Topological quantum computation. Bulletin of the American Mathematical Society **40**, 31 (2003). (cited on p. 15)

[97] W. K. Wootters and W. H. Zurek. A single quantum cannot be cloned. Nature **299**, 802 (1982). (cited on p. 15)

[98] P. W. Shor. Scheme for reducing decoherence in quantum computer memory. Phys. Rev. A **52**, R2493 (1995). (cited on p. 15)

[99] R. P. Feynman. Simulating physics with computers. International journal of theoretical physics **21**, 467 (1982). (cited on p. 15)

[100] J. I. Cirac, P. Maraner, and J. K. Pachos. Cold atom simulation of interacting relativistic quantum field theories. Phys. Rev. Lett. **105**, 190403 (2010). (cited on p. 16)

[101] K. Kim, M.-S. Chang, S. Korenblit, R. Islam, E. Edwards, J. Freericks, G.-D. Lin, L.-M. Duan, and C. Monroe. Quantum simulation of frustrated ising spins with trapped ions. Nature **465**, 590 (2010). (cited on p. 16)

[102] I. Bloch, J. Dalibard, and S. Nascimbene. Quantum simulations with ultracold quantum gases. Nature Physics **8**, 267 (2012). (cited on p. 16)

[103] U. Schollwöck. The density-matrix renormalization group in the age of matrix product states. Annals of Physics **326**, 96 (2011). (cited on p. 16)

[104] R. Islam, E. Edwards, K. Kim, S. Korenblit, C. Noh, H. Carmichael, G.-D. Lin, L.-M. Duan, C.-C. J. Wang, J. Freericks, *et al.* Onset of a quantum phase transition with a trapped ion quantum simulator. Nature communications **2**, 377 (2011). (cited on p. 16)

[105] R. Blatt and D. Wineland. Entangled states of trapped atomic ions. Nature **453**, 1008 (2008). (cited on pages 16 and 23)

[106] D. Martín-Cano, A. González-Tudela, L. Martín-Moreno, F. J. García-Vidal, C. Tejedor, and E. Moreno. Dissipation-driven generation of two-qubit entanglement mediated by plasmonic waveguides. Phys. Rev. B **84**, 235306 (2011).
(cited on pages 16, 24, 25, 29, 66, 121, 203, and 211)

[107] A. Gonzalez-Tudela, D. Martin-Cano, E. Moreno, L. Martin-Moreno, C. Tejedor, and F. J. Garcia-Vidal. Entanglement of two qubits mediated by one-dimensional plasmonic waveguides. Phys. Rev. Lett. **106**, 020501 (2011).
(cited on pages 16, 24, 25, 29, 66, 203, and 211)

[108] J. Petersen, J. Volz, and A. Rauschenbeutel. Chiral nanophotonic waveguide interface based on spin-orbit interaction of light. Science **346**, 67 (2014).
(cited on pages 17, 19, 45, 61, 68, 90, and 225)

[109] P. Lodahl, S. Mahmoodian, S. Stobbe, P. Schneeweiss, J. Volz, A. Rauschenbeutel, H. Pichler, and P. Zoller. Chiral quantum optics. arXiv preprint arXiv:1608.00446 (2016). (cited on pages 17, 68, 204, and 212)

[110] A. A. High, E. E. Novitskaya, L. V. Butov, M. Hanson, and A. C. Gossard. Control of exciton fluxes in an excitonic integrated circuit. Science **321**, 229 (2008).
(cited on pages 17, 144, 145, and 178)

[111] D. Ballarini, M. De Giorgi, E. Cancellieri, R. Houdré, E. Giacobino, R. Cingolani, A. Bramati, G. Gigli, and D. Sanvitto. All-optical polariton transistor. Nature communications **4**, 1778 (2013). (cited on pages 17 and 110)

[112] H. Wei and H. Xu. Nanowire-based plasmonic waveguides and devices for integrated nanophotonic circuits. Nanophotonics **1**, 155 (2012). (cited on pages 17, 18, and 180)

[113] T. Tiecke, K. Nayak, J. Thompson, T. Peyronel, N. De Leon, V. Vuletić, and M. Lukin. Efficient fiber-optical interface for nanophotonic devices. Optica **2**, 70 (2015).

(cited on p. 17)

[114] S. Fan, P. R. Villeneuve, J. D. Joannopoulos, and H. A. Haus. Channel drop tunneling through localized states. Phys. Rev. Lett. **80**, 960 (1998). (cited on pages 18 and 89)

[115] K. C. Huang, M.-K. Seo, T. Sarmiento, Y. Huo, J. S. Harris, and M. L. Brongersma. Electrically driven subwavelength optical nanocircuits. Nat. Photonics **8**, 244 (2014). (cited on pages 18 and 180)

[116] E. Vetsch, D. Reitz, G. Sagué, R. Schmidt, S. T. Dawkins, and A. Rauschenbeutel. Optical interface created by laser-cooled atoms trapped in the evanescent field surrounding an optical nanofiber. Phys. Rev. Lett. **104**, 203603 (2010). (cited on p. 18)

[117] D. Schrader, I. Dotsenko, M. Khudaverdyan, Y. Miroshnychenko, A. Rauschenbeutel, and D. Meschede. Neutral atom quantum register. Phys. Rev. Lett. **93**, 150501 (2004). (cited on p. 18)

[118] B. Gouraud, D. Maxein, A. Nicolas, O. Morin, and J. Laurat. Demonstration of a memory for tightly guided light in an optical nanofiber. Phys. Rev. Lett. **114**, 180503 (2015). (cited on p. 18)

[119] D. O'Shea, C. Junge, J. Volz, and A. Rauschenbeutel. Fiber-optical switch controlled by a single atom. Phys. Rev. Lett. **111**, 193601 (2013). (cited on p. 18)

[120] J. Volz, M. Scheucher, C. Junge, and A. Rauschenbeutel. Nonlinear [pi] phase shift for single fibre-guided photons interacting with a single resonator-enhanced atom. Nature Photonics **8**, 965 (2014). (cited on pages 18, 205, and 213)

[121] K. Xia, G. Lu, G. Lin, Y. Cheng, Y. Niu, S. Gong, and J. Twamley. Reversible nonmagnetic single-photon isolation using unbalanced quantum coupling. Phys. Rev. A **90**, 043802 (2014). (cited on pages 18, 68, 206, and 214)

[122] X.-W. Chen, V. Sandoghdar, and M. Agio. Highly efficient interfacing of guided plasmons and photons in nanowires. Nano letters **9**, 3756 (2009). (cited on pages 18, 209, and 218)

[123] N. P. de Leon, M. D. Lukin, and H. Park. Quantum plasmonic circuits. IEEE Journal of Selected Topics in Quantum Electronics **18**, 1781 (2012). (cited on pages 18 and 180)

[124] M. S. Tame, K. McEnery, Ş. Özdemir, J. Lee, S. Maier, and M. Kim. Quantum plasmonics. Nature Physics **9**, 329 (2013). (cited on pages 18, 180, and 202)

[125] E. Bermúdez-Ureña, C. Gonzalez-Ballestero, M. Geiselmann, R. Marty, I. P. Radko, T. Holmgaard, Y. Alaverdyan, E. Moreno, F. J. García-Vidal, S. I. Bozhevolnyi, *et al.* Coupling of individual quantum emitters to channel plasmons. Nature Communications **6** (2015). (cited on pages 19, 188, 199, 200, 201, 209, and 218)

[126] J. V. Frangioni. New technologies for human cancer imaging. Journal of Clinical Oncology **26**, 4012 (2008). PMID: 18711192. (cited on p. 19)

[127] C. J. Brabec, N. S. Sariciftci, and J. C. Hummelen. Plastic solar cells. Advanced Functional Materials **11**, 15 (2001). (cited on p. 19)

[128] N. Lambert, Y.-N. Chen, Y.-C. Cheng, C.-M. Li, G.-Y. Chen, and F. Nori. Quantum biology. Nature Physics **9**, 10 (2013). (cited on pages 20 and 21)

[129] D. A. Goldman, J. Murray, and J. N. Munday. Nanophotonic resonators for inp solar cells. Opt. Express **24**, A925 (2016). (cited on p. 20)

[130] S. Mokkapati and K. R. Catchpole. Nanophotonic light trapping in solar cells. Journal of Applied Physics **112**, 101101 (2012). (cited on p. 20)

[131] F. Dimroth, M. Grave, P. Beutel, U. Fiedeler, C. Karcher, T. N. D. Tibbits, E. Oliva, G. Siefer, M. Schachtner, A. Wekkeli, A. W. Bett, R. Krause, M. Piccin, N. Blanc, C. Drazek, E. Guiot, B. Ghyselen, T. Salvetat, A. Tauzin, T. Signamarcheix, A. Dobrich, T. Hannappel, and K. Schwarzburg. Wafer bonded four-junction gainp/gaas//gainasp/gainas concentrator solar cells with 44.7% efficiency. Progress in Photovoltaics: Research and Applications **22**, 277 (2014). PIP-13-265.R1. (cited on p. 20)

[132] K. R. Catchpole and A. Polman. Design principles for particle plasmon enhanced solar cells. Applied Physics Letters **93**, 191113 (2008). (cited on p. 20)

[133] M. O. Scully. Quantum photocell: Using quantum coherence to reduce radiative recombination and increase efficiency. Phys. Rev. Lett. **104**, 207701 (2010). (cited on p. 20)

[134] A. J. Nozik, M. C. Beard, J. M. Luther, M. Law, R. J. Ellingson, and J. C. Johnson. Semiconductor quantum dots and quantum dot arrays and applications of multiple exciton generation to third-generation photovoltaic solar cells. Chemical reviews **110**, 6873 (2010). (cited on p. 20)

[135] Y. Zhang, L.-W. Wang, and A. Mascarenhas. "quantum coaxial cables" for solar energy

harvesting. Nano Letters **7**, 1264 (2007). (cited on p. 20)

[136] J. Simon, F. Flory, L. Escoubas, P. Torchio, Y.-J. Chen, and D. Duché. Nanophotonics for efficient photovoltaic solar cells. Journal of optoelectronics and advanced materials **12**, 31 (2010). (cited on p. 20)

[137] F. Flory, L. Escoubas, J. J. Simon, P. Torchio, J. L. Rouzo, and W. Vervisch. *Nanophotonics for Photovoltaics*, 1–12 (CRC Press, 2015). (cited on p. 20)

[138] J. Feist and F. J. Garcia-Vidal. Extraordinary exciton conductance induced by strong coupling. Phys. Rev. Lett. **114**, 196402 (2015).
(cited on pages 20, 21, 146, 147, 152, 174, and 177)

[139] J. Schachenmayer, C. Genes, E. Tignone, and G. Pupillo. Cavity-enhanced transport of excitons. Phys. Rev. Lett. **114**, 196403 (2015). (cited on pages 20, 21, 146, and 177)

[140] G. D. Scholes, G. R. Fleming, A. Olaya-Castro, and R. van Grondelle. Lessons from nature about solar light harvesting. Nature chemistry **3**, 763 (2011).
(cited on pages 21 and 145)

[141] E. Wientjes, J. Renger, A. G. Curto, R. Cogdell, and N. F. van Hulst. Nanoantenna enhanced emission of light-harvesting complex 2: the role of resonance, polarization, and radiative and non-radiative rates. Physical Chemistry Chemical Physics **16**, 24739 (2014). (cited on p. 21)

[142] G. S. Engel, T. R. Calhoun, E. L. Read, T.-K. Ahn, T. Mančal, Y.-C. Cheng, R. E. Blankenship, and G. R. Fleming. Evidence for wavelike energy transfer through quantum coherence in photosynthetic systems. Nature **446**, 782 (2007).
(cited on pages 21 and 145)

[143] H. Lee, Y.-C. Cheng, and G. R. Fleming. Coherence dynamics in photosynthesis: protein protection of excitonic coherence. Science **316**, 1462 (2007). (cited on p. 21)

[144] S. F. Huelga and M. B. Plenio. Vibrations, quanta and biology. Contemporary Physics **54**, 181 (2013). (cited on p. 21)

[145] R. Hildner, D. Brinks, J. B. Nieder, R. J. Cogdell, and N. F. van Hulst. Quantum coherent energy transfer over varying pathways in single light-harvesting complexes. Science **340**, 1448 (2013). (cited on p. 21)

[146] E. Wientjes, J. Renger, A. G. Curto, R. Cogdell, and N. F. van Hulst. Strong antenna-enhanced fluorescence of a single light-harvesting complex shows photon

antibunching. Nature communications **5** (2014). (cited on p. 21)

[147] F. Caruso, A. W. Chin, A. Datta, S. F. Huelga, and M. B. Plenio. Highly efficient energy excitation transfer in light-harvesting complexes: The fundamental role of noise-assisted transport. The Journal of Chemical Physics **131**, 105106 (2009). (cited on pages 21, 145, 171, and 177)

[148] F. A. Y. N. Schröder and A. W. Chin. Simulating open quantum dynamics with time-dependent variational matrix product states: Towards microscopic correlation of environment dynamics and reduced system evolution. Phys. Rev. B **93**, 075105 (2016). (cited on pages 21, 177, 208, and 217)

[149] Z. Ficek and R. Tanaś. Entangled states and collective nonclassical effects in two-atom systems. Physics Reports **372**, 369 (2002). (cited on pages 23, 27, and 28)

[150] R. Horodecki, P. Horodecki, M. Horodecki, and K. Horodecki. Quantum entanglement. Rev. Mod. Phys. **81**, 865 (2009). (cited on pages 23 and 31)

[151] Y. Makhlin, G. Schön, and A. Shnirman. Quantum-state engineering with josephson-junction devices. Rev. Mod. Phys. **73**, 357 (2001). (cited on p. 23)

[152] R. Hanson, L. P. Kouwenhoven, J. R. Petta, S. Tarucha, and L. M. K. Vandersypen. Spins in few-electron quantum dots. Rev. Mod. Phys. **79**, 1217 (2007). (cited on p. 23)

[153] S. De Franceschi, L. Kouwenhoven, C. Schönenberger, and W. Wernsdorfer. Hybrid superconductor-quantum dot devices. Nature Nanotechnology **5**, 703 (2010). (cited on p. 23)

[154] L. D. Contreras-Pulido and R. Aguado. Entanglement between charge qubits induced by a common dissipative environment. Phys. Rev. B **77**, 155420 (2008). (cited on p. 23)

[155] R. Ruskov and A. N. Korotkov. Entanglement of solid-state qubits by measurement. Phys. Rev. B **67**, 241305 (2003). (cited on p. 23)

[156] J. R. Weber, W. F. Koehl, J. B. Varley, A. Janotti, B. B. Buckley, C. G. Van de Walle, and D. D. Awschalom. Quantum computing with defects. Proceedings of the National Academy of Sciences **107**, 8513 (2010). (cited on p. 23)

[157] L. G. Herrmann, F. Portier, P. Roche, A. L. Yeyati, T. Kontos, and C. Strunk. Carbon nanotubes as cooper-pair beam splitters. Phys. Rev. Lett. **104**, 026801 (2010). (cited on p. 23)

[158] F. Galve, L. A. Pachón, and D. Zueco. Bringing entanglement to the high temperature limit. Phys. Rev. Lett. **105**, 180501 (2010). (cited on p. 23)

[159] D. Braun. Creation of entanglement by interaction with a common heat bath. Phys. Rev. Lett. **89**, 277901 (2002). (cited on p. 23)

[160] J. Majer, J. Chow, J. Gambetta, J. Koch, B. Johnson, J. Schreier, L. Frunzio, D. Schuster, A. Houck, A. Wallraff, A. Blais, M. Devoret, S. M. Girvin, and R. J. Schoelkopf. Coupling superconducting qubits via a cavity bus. Nature **449**, 443 (2007). (cited on pages 23 and 24)

[161] A. Imamoğlu, D. D. Awschalom, G. Burkard, D. P. DiVincenzo, D. Loss, M. Sherwin, and A. Small. Quantum information processing using quantum dot spins and cavity qed. Phys. Rev. Lett. **83**, 4204 (1999). (cited on p. 24)

[162] E. Gallardo, L. J. Martínez, A. K. Nowak, D. Sarkar, H. P. van der Meulen, J. M. Calleja, C. Tejedor, I. Prieto, D. Granados, A. G. Taboada, J. M. García, and P. A. Postigo. Optical coupling of two distant inas/gaas quantum dots by a photonic-crystal microcavity. Phys. Rev. B **81**, 193301 (2010). (cited on p. 24)

[163] A. Laucht, J. M. Villas-Bôas, S. Stobbe, N. Hauke, F. Hofbauer, G. Böhm, P. Lodahl, M.-C. Amann, M. Kaniber, and J. J. Finley. Mutual coupling of two semiconductor quantum dots via an optical nanocavity. Phys. Rev. B **82**, 075305 (2010). (cited on p. 24)

[164] M. V. G. Dutt, L. Childress, L. Jiang, E. Togan, J. Maze, F. Jelezko, A. S. Zibrov, P. R. Hemmer, and M. D. Lukin. Quantum register based on individual electronic and nuclear spin qubits in diamond. Science **316**, 1312 (2007). (cited on p. 24)

[165] S. Hughes. Modified spontaneous emission and qubit entanglement from dipole-coupled quantum dots in a photonic crystal nanocavity. Phys. Rev. Lett. **94**, 227402 (2005). (cited on p. 24)

[166] M. B. Plenio, S. F. Huelga, A. Beige, and P. L. Knight. Cavity-loss-induced generation of entangled atoms. Phys. Rev. A **59**, 2468 (1999). (cited on p. 24)

[167] A. S. Sørensen and K. Mølmer. Measurement induced entanglement and quantum computation with atoms in optical cavities. Phys. Rev. Lett. **91**, 097905 (2003). (cited on p. 24)

[168] E. Hagley, X. Maître, G. Nogues, C. Wunderlich, M. Brune, J. M. Raimond, and

S. Haroche. Generation of einstein-podolsky-rosen pairs of atoms. Phys. Rev. Lett. **79**, 1 (1997). (cited on p. 24)

[169] A. Barenco, D. Deutsch, A. Ekert, and R. Jozsa. Conditional quantum dynamics and logic gates. Phys. Rev. Lett. **74**, 4083 (1995). (cited on p. 24)

[170] D. Loss and D. P. DiVincenzo. Quantum computation with quantum dots. Phys. Rev. A **57**, 120 (1998). (cited on p. 24)

[171] T. Calarco, A. Datta, P. Fedichev, E. Pazy, and P. Zoller. Spin-based all-optical quantum computation with quantum dots: Understanding and suppressing decoherence. Phys. Rev. A **68**, 012310 (2003). (cited on p. 24)

[172] R. Hanson and G. Burkard. Universal set of quantum gates for double-dot spin qubits with fixed interdot coupling. Phys. Rev. Lett. **98**, 050502 (2007). (cited on p. 24)

[173] S. Diehl, A. Micheli, A. Kantian, B. Kraus, H. Büchler, and P. Zoller. Quantum states and phases in driven open quantum systems with cold atoms. Nature Physics **4**, 878 (2008). (cited on p. 24)

[174] F. Verstraete, M. M. Wolf, and J. I. Cirac. Quantum computation and quantum-state engineering driven by dissipation. Nature physics **5**, 633 (2009). (cited on p. 24)

[175] M. S. Kim, J. Lee, D. Ahn, and P. L. Knight. Entanglement induced by a single-mode heat environment. Phys. Rev. A **65**, 040101 (2002). (cited on p. 24)

[176] R. Tanaś and Z. Ficek. Entangling two atoms via spontaneous emission. Journal of Optics B: Quantum and Semiclassical Optics **6**, S90 (2004). (cited on p. 24)

[177] D. Solenov, D. Tolkunov, and V. Privman. Exchange interaction, entanglement, and quantum noise due to a thermal bosonic field. Phys. Rev. B **75**, 035134 (2007). (cited on p. 24)

[178] A. F. Alharbi and Z. Ficek. Deterministic creation of stationary entangled states by dissipation. Phys. Rev. A **82**, 054103 (2010). (cited on p. 24)

[179] M. J. Kastoryano, F. Reiter, and A. S. Sørensen. Dissipative preparation of entanglement in optical cavities. Phys. Rev. Lett. **106**, 090502 (2011). (cited on p. 24)

[180] H. Krauter, C. A. Muschik, K. Jensen, W. Wasilewski, J. M. Petersen, J. I. Cirac, and E. S. Polzik. Entanglement generated by dissipation and steady state entanglement of two macroscopic objects. Phys. Rev. Lett. **107**, 080503 (2011). (cited on p. 24)

[181] J. T. Barreiro, M. Müller, P. Schindler, D. Nigg, T. Monz, M. Chwalla, M. Hennrich, C. F. Roos, P. Zoller, and R. Blatt. An open-system quantum simulator with trapped ions. Nature **470**, 486 (2011). (cited on p. 24)

[182] B. Bellomo, R. L. Franco, S. Maniscalco, and G. Compagno. Two-qubit entanglement dynamics for two different non-markovian environments. Physica Scripta **2010**, 014014 (2010). (cited on p. 24)

[183] F. Le Kien, S. D. Gupta, K. P. Nayak, and K. Hakuta. Nanofiber-mediated radiative transfer between two distant atoms. Phys. Rev. A **72**, 063815 (2005). (cited on p. 24)

[184] T. Lund-Hansen, S. Stobbe, B. Julsgaard, H. Thyrrestrup, T. Sünner, M. Kamp, A. Forchel, and P. Lodahl. Experimental realization of highly efficient broadband coupling of single quantum dots to a photonic crystal waveguide. Phys. Rev. Lett. **101**, 113903 (2008). (cited on p. 24)

[185] P. Yao and S. Hughes. Macroscopic entanglement and violation of bell's inequalities between two spatially separated quantum dots in a planar photonic crystal system. Opt. Express **17**, 11505 (2009). (cited on p. 24)

[186] W. Chen, G.-Y. Chen, and Y.-N. Chen. Coherent transport of nanowire surface plasmons coupled to quantum dots. Opt. Express **18**, 10360 (2010). (cited on pages 24 and 33)

[187] D. Dzsotjan, A. S. Sørensen, and M. Fleischhauer. Quantum emitters coupled to surface plasmons of a nanowire: A green's function approach. Phys. Rev. B **82**, 075427 (2010). (cited on pages 24 and 120)

[188] J. Bleuse, J. Claudon, M. Creasey, N. S. Malik, J.-M. Gérard, I. Maksymov, J.-P. Hugonin, and P. Lalanne. Inhibition, enhancement, and control of spontaneous emission in photonic nanowires. Phys. Rev. Lett. **106**, 103601 (2011). (cited on p. 24)

[189] Q. Quan, I. Bulu, and M. Lončar. Broadband waveguide qed system on a chip. Phys. Rev. A **80**, 011810 (2009). (cited on pages 24 and 50)

[190] E. Rephaeli, J.-T. Shen, and S. Fan. Full inversion of a two-level atom with a single-photon pulse in one-dimensional geometries. Phys. Rev. A **82**, 033804 (2010). (cited on pages 26, 33, 36, 70, 205, and 213)

[191] M. Gross and S. Haroche. Superradiance: An essay on the theory of collective spontaneous emission. Physics Reports **93**, 301 (1982). (cited on p. 30)

[192] S. Hill and W. K. Wootters. Entanglement of a pair of quantum bits. Phys. Rev. Lett. **78**, 5022 (1997). (cited on p. 31)

[193] K. Stannigel, P. Rabl, and P. Zoller. Driven-dissipative preparation of entangled states in cascaded quantum-optical networks. New Journal of Physics **14**, 063014 (2012). (cited on p. 32)

[194] T. Shi and C. P. Sun. Lehmann-symanzik-zimmermann reduction approach to multiphoton scattering in coupled-resonator arrays. Phys. Rev. B **79**, 205111 (2009). (cited on pages 33, 104, 206, and 214)

[195] T. Shi, S. Fan, and C. P. Sun. Two-photon transport in a waveguide coupled to a cavity in a two-level system. Phys. Rev. A **84**, 063803 (2011). (cited on pages 33, 78, 206, and 214)

[196] J.-T. Shen and S. Fan. Theory of single-photon transport in a single-mode waveguide. i. coupling to a cavity containing a two-level atom. Phys. Rev. A **79**, 023837 (2009). (cited on pages 33, 34, 36, 204, and 211)

[197] A. W. Snyder and J. Love. *Optical waveguide theory* (Springer Science & Business Media, 2012). (cited on pages 33, 196, and 197)

[198] H. Zheng, D. J. Gauthier, and H. U. Baranger. Waveguide qed: Many-body bound-state effects in coherent and fock-state scattering from a two-level system. Phys. Rev. A **82**, 063816 (2010). (cited on pages 34, 36, 66, 76, 77, 102, 103, 205, 213, 232, and 234)

[199] J. T. Shen and S. Fan. Coherent photon transport from spontaneous emission in one-dimensional waveguides. Opt. Lett. **30**, 2001 (2005). (cited on pages 36, 103, 205, and 213)

[200] G. Zumofen, N. M. Mojarad, V. Sandoghdar, and M. Agio. Perfect reflection of light by an oscillating dipole. Phys. Rev. Lett. **101**, 180404 (2008). (cited on p. 36)

[201] Y. L. A. Rezus, S. G. Walt, R. Lettow, A. Renn, G. Zumofen, S. Götzinger, and V. Sandoghdar. Single-photon spectroscopy of a single molecule. Phys. Rev. Lett. **108**, 093601 (2012). (cited on pages 36, 70, 129, 207, and 215)

[202] P. Bermel, A. Rodriguez, S. G. Johnson, J. D. Joannopoulos, and M. Soljačić. Single-photon all-optical switching using waveguide-cavity quantum electrodynamics. Phys. Rev. A **74**, 043818 (2006). (cited on p. 36)

[203] D. E. Chang, L. Jiang, A. V. Gorshkov, and H. J. Kimble. Cavity qed with atomic

mirrors. New Journal of Physics **14**, 063003 (2012). (cited on p. 38)

[204] R. Mitsch, C. Sayrin, B. Albrecht, P. Schneeweiss, and A. Rauschenbeutel. Quantum state-controlled directional spontaneous emission of photons into a nanophotonic waveguide. Nature communications **5** (2014). (cited on pages 45, 68, and 90)

[205] R. Coles, D. Price, J. Dixon, B. Royall, E. Clarke, P. Kok, M. Skolnick, A. Fox, and M. Makhonin. Chirality of nanophotonic waveguide with embedded quantum emitter for unidirectional spin transfer. Nature communications **7** (2016). (cited on pages 45 and 68)

[206] B. Le Feber, N. Rotenberg, and L. Kuipers. Nanophotonic control of circular dipole emission. Nature communications **6** (2015). (cited on pages 45, 61, and 68)

[207] V. V. Klimov and M. Ducloy. Spontaneous emission rate of an excited atom placed near a nanofiber. Phys. Rev. A **69**, 013812 (2004). (cited on p. 50)

[208] A. Faraon, C. Santori, Z. Huang, K.-M. C. Fu, V. M. Acosta, D. Fattal, and R. G. Beausoleil. Quantum photonic devices in single-crystal diamond. New Journal of Physics **15**, 025010 (2013). (cited on p. 50)

[209] V. S. C. Manga Rao and S. Hughes. Single quantum-dot purcell factor and β factor in a photonic crystal waveguide. Phys. Rev. B **75**, 205437 (2007). (cited on p. 50)

[210] H. Thyrrestrup, L. Sapienza, and P. Lodahl. Extraction of the beta factor for single quantum dots coupled to a photonic crystal waveguide. Applied Physics Letters **96**, 231106 (2010). (cited on p. 50)

[211] J. Barthes, A. Bouhelier, A. Dereux, and G. C. des Francs. Coupling of a dipolar emitter into one-dimensional surface plasmon. Scientific reports **3** (2013). (cited on pages 50, 180, and 194)

[212] A. Blais, R.-S. Huang, A. Wallraff, S. M. Girvin, and R. J. Schoelkopf. Cavity quantum electrodynamics for superconducting electrical circuits: An architecture for quantum computation. Phys. Rev. A **69**, 062320 (2004). (cited on pages 56 and 179)

[213] M. Devoret, S. Girvin, and R. Schoelkopf. Circuit-qed: How strong can the coupling between a josephson junction atom and a transmission line resonator be? Annalen der Physik **16**, 767 (2007). (cited on p. 56)

[214] H. Pichler, T. Ramos, A. J. Daley, and P. Zoller. Quantum optics of chiral spin networks. Phys. Rev. A **91**, 042116 (2015). (cited on pages 57, 59, 68, 204, and 212)

[215] A. B. Young, A. C. T. Thijssen, D. M. Beggs, P. Androvitsaneas, L. Kuipers, J. G. Rarity, S. Hughes, and R. Oulton. Polarization engineering in photonic crystal waveguides for spin-photon entanglers. Phys. Rev. Lett. **115**, 153901 (2015). (cited on pages 61 and 68)

[216] H. Bernien, B. Hensen, W. Pfaff, G. Koolstra, M. Blok, L. Robledo, T. Taminiau, M. Markham, D. Twitchen, L. Childress, *et al.* Heralded entanglement between solid-state qubits separated by three metres. Nature **497**, 86 (2013). (cited on p. 66)

[217] A. Delteil, Z. Sun, W.-b. Gao, E. Togan, S. Faelt, and A. Imamoğlu. Generation of heralded entanglement between distant hole spins. Nature Physics (2015). (cited on p. 66)

[218] W. Gao, A. Imamoğlu, H. Bernien, and R. Hanson. Coherent manipulation, measurement and entanglement of individual solid-state spins using optical fields. Nature Photonics **9**, 363 (2015). (cited on p. 66)

[219] D. Roy. Few-photon optical diode. Phys. Rev. B **81**, 155117 (2010). (cited on p. 66)

[220] J.-T. Shen and S. Fan. Strongly correlated two-photon transport in a one-dimensional waveguide coupled to a two-level system. Phys. Rev. Lett. **98**, 153003 (2007). (cited on pages 66, 78, 103, and 234)

[221] K. Życzkowski, P. Horodecki, M. Horodecki, and R. Horodecki. Dynamics of quantum entanglement. Phys. Rev. A **65**, 012101 (2001). (cited on pages 66 and 83)

[222] T. Yu and J. H. Eberly. Finite-time disentanglement via spontaneous emission. Phys. Rev. Lett. **93**, 140404 (2004). (cited on pages 66 and 83)

[223] M. P. Almeida, F. de Melo, M. Hor-Meyll, A. Salles, S. P. Walborn, P. H. S. Ribeiro, and L. Davidovich. Environment-induced sudden death of entanglement. Science **316**, 579 (2007). (cited on pages 66 and 83)

[224] J.-S. Xu, C.-F. Li, M. Gong, X.-B. Zou, C.-H. Shi, G. Chen, and G.-C. Guo. Experimental demonstration of photonic entanglement collapse and revival. Phys. Rev. Lett. **104**, 100502 (2010). (cited on pages 66 and 83)

[225] L.-T. Shen, R.-X. Chen, H.-Z. Wu, and Z.-B. Yang. Distributed manipulation of two-qubit entanglement with coupled continuous variables. J. Opt. Soc. Am. B **32**, 297 (2015). (cited on p. 66)

[226] K. Eckert, O. Romero-Isart, M. Rodriguez, M. Lewenstein, E. S. Polzik, and A. Sanpera.

Quantum non-demolition detection of strongly correlated systems. Nature Physics **4**, 50 (2008). (cited on p. 66)

[227] J. Altepeter, E. Jeffrey, P. Kwiat, S. Tanzilli, N. Gisin, and A. Acín. Experimental methods for detecting entanglement. Physical Review letters **95**, 033601 (2005). (cited on p. 66)

[228] D. F. V. James, P. G. Kwiat, W. J. Munro, and A. G. White. Measurement of qubits. Phys. Rev. A **64**, 052312 (2001). (cited on pages 66, 205, and 213)

[229] S. Walborn, P. S. Ribeiro, L. Davidovich, F. Mintert, and A. Buchleitner. Experimental determination of entanglement with a single measurement. Nature **440**, 1022 (2006). (cited on p. 67)

[230] S. M. Lee, S.-W. Ji, H.-W. Lee, and M. Suhail Zubairy. Proposal for direct measurement of concurrence via visibility in a cavity qed system. Phys. Rev. A **77**, 040301 (2008). (cited on p. 67)

[231] L.-H. Zhang, Q. Yang, M. Yang, W. Song, and Z.-L. Cao. Direct measurement of the concurrence of two-photon polarization-entangled states. Phys. Rev. A **88**, 062342 (2013). (cited on p. 67)

[232] J. M. Chow, L. DiCarlo, J. M. Gambetta, A. Nunnenkamp, L. S. Bishop, L. Frunzio, M. H. Devoret, S. M. Girvin, and R. J. Schoelkopf. Detecting highly entangled states with a joint qubit readout. Phys. Rev. A **81**, 062325 (2010). (cited on p. 67)

[233] G. Romero, C. E. López, F. Lastra, E. Solano, and J. C. Retamal. Direct measurement of concurrence for atomic two-qubit pure states. Phys. Rev. A **75**, 032303 (2007). (cited on p. 67)

[234] L. Zhou and Y.-B. Sheng. Detection of nonlocal atomic entanglement assisted by single photons. Phys. Rev. A **90**, 024301 (2014). (cited on p. 67)

[235] L.-H. Zhang, M. Yang, and Z.-L. Cao. Directly measuring the concurrence of atomic two-qubit states through the detection of cavity decay. The European Physical Journal D **68**, 1 (2014). (cited on pages 67 and 88)

[236] D. Jalas, A. Petrov, M. Eich, W. Freude, S. Fan, Z. Yu, R. Baets, M. Popovic, A. Melloni, J. D. Joannopoulos, *et al.* What is—and what is not—an optical isolator. Nat. Photonics **7**, 579 (2013). (cited on p. 67)

[237] E. Mascarenhas, M. F. Santos, A. Auffèves, and D. Gerace. Quantum rectifier in a

one-dimensional photonic channel. Phys. Rev. A **93**, 043821 (2016). (cited on p. 67)

[238] F. Fratini, E. Mascarenhas, L. Safari, J.-P. Poizat, D. Valente, A. Auffèves, D. Gerace, and M. F. Santos. Fabry-perot interferometer with quantum mirrors: Nonlinear light transport and rectification. Phys. Rev. Lett. **113**, 243601 (2014). (cited on p. 67)

[239] F. Fratini and R. Ghobadi. Full quantum treatment of a light diode. Phys. Rev. A **93**, 023818 (2016). (cited on p. 67)

[240] J. Dai, A. Roulet, H. N. Le, and V. Scarani. Rectification of light in the quantum regime. Phys. Rev. A **92**, 063848 (2015). (cited on p. 67)

[241] X.-Y. Chen, F.-Y. Zhang, and C. Li. Single-photon quantum router by two distant artificial atoms. J. Opt. Soc. Am. B **33**, 583 (2016). (cited on p. 67)

[242] L. Yuan, S. Xu, and S. Fan. Achieving nonreciprocal unidirectional single-photon quantum transport using the photonic aharonov-bohm effect. Opt. Lett. **40**, 5140 (2015). (cited on p. 67)

[243] M. Hafezi and P. Rabl. Optomechanically induced non-reciprocity in microring resonators. Opt. Express **20**, 7672 (2012). (cited on p. 68)

[244] W.-B. Yan, B. Liu, L. Zhou, and H. Fan. All-optical router at single-photon level by interference. EPL (Europhysics Letters) **111**, 64005 (2015). (cited on pages 68 and 89)

[245] E. Mascarenhas, D. Gerace, D. Valente, S. Montangero, A. Auffèves, and M. F. Santos. A quantum optical valve in a nonlinear-linear resonators junction. EPL (Europhysics Letters) **106**, 54003 (2014). (cited on pages 68 and 108)

[246] Z. Shen, Y.-L. Zhang, Y. Chen, C.-L. Zou, Y.-F. Xiao, X.-B. Zou, F.-W. Sun, G.-C. Guo, and C.-H. Dong. Experimental realization of optomechanically induced non-reciprocity. arXiv preprint arXiv:1604.02297 (2016). (cited on p. 68)

[247] S. Rosenblum, O. Bechler, I. Shomroni, Y. Lovsky, G. Guendelman, and B. Dayan. Extraction of a single photon from an optical pulse. Nature Photonics **10**, 19 (2016). (cited on pages 68 and 108)

[248] Y. Huang, G. Veronis, and C. Min. Unidirectional reflectionless propagation in plasmonic waveguide-cavity systems at exceptional points. Opt. Express **23**, 29882 (2015). (cited on p. 68)

[249] F. Le Kien and A. Rauschenbeutel. Anisotropy in scattering of light from an atom into

the guided modes of a nanofiber. Phys. Rev. A **90**, 023805 (2014). (cited on pages 68 and 90)

[250] T. Ramos, B. Vermersch, P. Hauke, H. Pichler, and P. Zoller. Non-markovian dynamics in chiral quantum networks with spins and photons. Phys. Rev. A **93**, 062104 (2016). (cited on p. 68)

[251] B. Vermersch, T. Ramos, P. Hauke, and P. Zoller. Implementation of chiral quantum optics with rydberg and trapped-ion setups. Phys. Rev. A **93**, 063830 (2016). (cited on p. 68)

[252] T. Ramos, H. Pichler, A. J. Daley, and P. Zoller. Quantum spin dimers from chiral dissipation in cold-atom chains. Phys. Rev. Lett. **113**, 237203 (2014). (cited on p. 68)

[253] C. Sayrin, C. Junge, R. Mitsch, B. Albrecht, D. O'Shea, P. Schneeweiss, J. Volz, and A. Rauschenbeutel. Nanophotonic optical isolator controlled by the internal state of cold atoms. Phys. Rev. X **5**, 041036 (2015). (cited on pages 68 and 98)

[254] N. V. Corzo, B. Gouraud, A. Chandra, A. Goban, A. S. Sheremet, D. V. Kupriyanov, and J. Laurat. Large bragg reflection from one-dimensional chains of trapped atoms near a nanoscale waveguide. arXiv preprint arXiv:1604.03129 (2016). (cited on p. 68)

[255] Y. Shen, M. Bradford, and J.-T. Shen. Single-photon diode by exploiting the photon polarization in a waveguide. Phys. Rev. Lett. **107**, 173902 (2011). (cited on p. 68)

[256] M. V. Fedorov, M. A. Efremov, A. E. Kazakov, K. W. Chan, C. K. Law, and J. H. Eberly. Spontaneous emission of a photon: Wave-packet structures and atom-photon entanglement. Phys. Rev. A **72**, 032110 (2005). (cited on p. 70)

[257] U. Dorner and P. Zoller. Laser-driven atoms in half-cavities. Phys. Rev. A **66**, 023816 (2002). (cited on p. 70)

[258] D. E. Chang, A. S. Sørensen, P. R. Hemmer, and M. D. Lukin. Quantum optics with surface plasmons. Phys. Rev. Lett. **97**, 053002 (2006). (cited on pages 71 and 180)

[259] A. Laucht, S. Pütz, T. Günthner, N. Hauke, R. Saive, S. Frédérick, M. Bichler, M.-C. Amann, A. W. Holleitner, M. Kaniber, and J. J. Finley. A waveguide-coupled on-chip single-photon source. Phys. Rev. X **2**, 011014 (2012). (cited on p. 71)

[260] A. González-Tudela, V. Paulisch, H. Kimble, and J. Cirac. Reliable multiphoton generation in waveguide qed. arXiv preprint arXiv:1603.01243 (2016). (cited on p. 71)

[261] G.-Y. Chen, N. Lambert, C.-H. Chou, Y.-N. Chen, and F. Nori. Surface plasmons in a metal nanowire coupled to colloidal quantum dots: Scattering properties and quantum entanglement. Phys. Rev. B **84**, 045310 (2011). (cited on p. 73)

[262] W.-X. Lai, H.-C. Li, X. Lin, and X. Chen. Semiconductor-cavity qed-based optical beam splitter. Phys. Rev. A **79**, 023832 (2009). (cited on pages 74 and 89)

[263] M. Keller, B. Lange, K. Hayasaka, W. Lange, and H. Walther. Continuous generation of single photons with controlled waveform in an ion-trap cavity system. Nature **431**, 1075 (2004). (cited on p. 74)

[264] H. F. Hofmann, K. Kojima, S. Takeuchi, and K. Sasaki. Entanglement and four-wave mixing effects in the dissipation-free nonlinear interaction of two photons at a single atom. Phys. Rev. A **68**, 043813 (2003). (cited on p. 78)

[265] E. Rephaeli, i. m. c. E. Kocabaş, and S. Fan. Few-photon transport in a waveguide coupled to a pair of colocated two-level atoms. Phys. Rev. A **84**, 063832 (2011). (cited on pages 78, 103, 205, and 213)

[266] R. J. Coles, N. Prtljaga, B. Royall, I. J. Luxmoore, A. M. Fox, and M. S. Skolnick. Waveguide-coupled photonic crystal cavity for quantum dot spin readout. Opt. Express **22**, 2376 (2014). (cited on p. 89)

[267] M. G. Daly, P. E. Jessop, and D. Yevick. Crosstalk reduction in intersecting rib waveguides. Journal of Lightwave Technology **14**, 1695 (1996). (cited on p. 90)

[268] S. M. Musa. *Computational Nanophotonics: Modeling and Applications* (CRC Press Taylor & Francis Group, 2013). (cited on p. 90)

[269] C. Manolatou, S. G. Johnson, S. Fan, P. R. Villeneuve, H. A. Haus, and J. D. Joannopoulos. High-density integrated optics. J. Lightwave Technol. **17**, 1682 (1999). (cited on p. 90)

[270] E. Brion, L. H. Pedersen, and K. Molmer. Adiabatic elimination in a lambda system. Journal of Physics A: Mathematical and Theoretical **40**, 1033 (2007). (cited on p. 90)

[271] H. Zheng, D. J. Gauthier, and H. U. Baranger. Waveguide-qed-based photonic quantum computation. Phys. Rev. Lett. **111**, 090502 (2013). (cited on pages 94, 205, and 213)

[272] W.-B. Yan and H. Fan. Single-photon quantum router with multiple output ports. Scientific reports **4** (2014). (cited on p. 94)

[273] J. Lu, Z. H. Wang, and L. Zhou. T-shaped single-photon router. Opt. Express **23**, 22955 (2015). (cited on p. 94)

[274] Y. Chen, D. Jiang, L. Xie, and L. Chen. Quantum router for single photons carrying spin and orbital angular momentum. Scientific reports **6**, 27033 (2016). (cited on p. 94)

[275] T. Shi, D. E. Chang, and J. I. Cirac. Multiphoton-scattering theory and generalized master equations. Phys. Rev. A **92**, 053834 (2015). (cited on pages 104 and 236)

[276] T. Caneva, M. T. Manzoni, T. Shi, J. S. Douglas, J. I. Cirac, and D. E. Chang. Quantum dynamics of propagating photons with strong interactions: a generalized input-output formalism. New Journal of Physics **17**, 113001 (2015). (cited on p. 104)

[277] S. Xu and S. Fan. Input-output formalism for few-photon transport: A systematic treatment beyond two photons. Phys. Rev. A **91**, 043845 (2015). (cited on p. 104)

[278] G. S. Agarwal. Vacuum-field rabi oscillations of atoms in a cavity. J. Opt. Soc. Am. B **2**, 480 (1985). (cited on p. 109)

[279] R. J. Thompson, G. Rempe, and H. J. Kimble. Observation of normal-mode splitting for an atom in an optical cavity. Phys. Rev. Lett. **68**, 1132 (1992). (cited on p. 110)

[280] B. Deveaud. Polariton interactions in semiconductor microcavities. Comptes Rendus Physique – (2016). (cited on p. 110)

[281] Y. Yamamoto, H. Deng, and H. Haug. Bose-einstein condensation of exciton-polaritons. In *Pushing the Frontiers of Atomic Physics*, volume 1, 168–177 (2009). (cited on pages 110 and 124)

[282] S. Kéna-Cohen and S. Forrest. Room-temperature polariton lasing in an organic single-crystal microcavity. Nature Photonics **4**, 371 (2010). (cited on p. 110)

[283] A. Imamoğlu, R. J. Ram, S. Pau, and Y. Yamamoto. Nonequilibrium condensates and lasers without inversion: Exciton-polariton lasers. Phys. Rev. A **53**, 4250 (1996). (cited on p. 110)

[284] T. Birr, U. Zywietz, P. Chhantyal, B. N. Chichkov, and C. Reinhardt. Ultrafast surface plasmon-polariton logic gates and half-adder. Opt. Express **23**, 31755 (2015). (cited on p. 110)

[285] M. Sich, D. Krizhanovskii, M. Skolnick, A. V. Gorbach, R. Hartley, D. V. Skryabin, E. Cerda-Méndez, K. Biermann, R. Hey, and P. Santos. Observation of bright polariton

solitons in a semiconductor microcavity. Nature photonics **6**, 50 (2012). (cited on p. 110)

[286] A. Kavokin, G. Malpuech, and M. Glazov. Optical spin hall effect. Phys. Rev. Lett. **95**, 136601 (2005). (cited on p. 110)

[287] T. Karzig, C.-E. Bardyn, N. H. Lindner, and G. Refael. Topological polaritons. Phys. Rev. X **5**, 031001 (2015). (cited on p. 110)

[288] J. del Pino, J. Feist, and F. J. Garcia-Vidal. Quantum theory of collective strong coupling of molecular vibrations with a microcavity mode. New Journal of Physics **17**, 053040 (2015). (cited on pages 111, 171, 172, 177, 208, and 217)

[289] M. Fleischhauer and M. D. Lukin. Quantum memory for photons: Dark-state polaritons. Phys. Rev. A **65**, 022314 (2002). (cited on p. 111)

[290] L. Knoell, S. Scheel, and D.-G. Welsch. *QED in dispersing and absorbing media*, 1–63 (Wiley-VCH, 2001). (cited on pages 120 and 251)

[291] T. Gruner and D.-G. Welsch. Green-function approach to the radiation-field quantization for homogeneous and inhomogeneous kramers-kronig dielectrics. Phys. Rev. A **53**, 1818 (1996). (cited on p. 120)

[292] S. Scheel, L. Knöll, and D.-G. Welsch. Qed commutation relations for inhomogeneous kramers-kronig dielectrics. Phys. Rev. A **58**, 700 (1998). (cited on p. 120)

[293] M. Khanbekyan, L. Knöll, D.-G. Welsch, A. A. Semenov, and W. Vogel. Qed of lossy cavities: Operator and quantum-state input-output relations. Phys. Rev. A **72**, 053813 (2005). (cited on p. 120)

[294] S. Scheel, L. Knöll, and D.-G. Welsch. Spontaneous decay of an excited atom in an absorbing dielectric. Phys. Rev. A **60**, 4094 (1999). (cited on p. 120)

[295] H. T. Dung, L. Knöll, and D.-G. Welsch. Spontaneous decay in the presence of dispersing and absorbing bodies: General theory and application to a spherical cavity. Phys. Rev. A **62**, 053804 (2000). (cited on pages 120 and 121)

[296] A. González-Tudela, P. A. Huidobro, L. Martín-Moreno, C. Tejedor, and F. J. García-Vidal. Reversible dynamics of single quantum emitters near metal-dielectric interfaces. Phys. Rev. B **89**, 041402 (2014). (cited on p. 120)

[297] A. Delga, J. Feist, J. Bravo-Abad, and F. J. Garcia-Vidal. Quantum emitters near a

metal nanoparticle: Strong coupling and quenching. Phys. Rev. Lett. **112**, 253601 (2014). (cited on pages 120, 133, 146, and 159)

[298] A. Delga, J. Feist, J. Bravo-Abad, and F. J. Garcia-Vidal. Theory of strong coupling between quantum emitters and localized surface plasmons. Journal of Optics **16**, 114018 (2014). (cited on pages 120 and 146)

[299] A. González-Tudela, P. A. Huidobro, L. Martín-Moreno, C. Tejedor, and F. J. García-Vidal. Theory of strong coupling between quantum emitters and propagating surface plasmons. Phys. Rev. Lett. **110**, 126801 (2013). (cited on pages 121, 146, and 148)

[300] L. Landau, J. Bell, M. Kearsley, L. Pitaevskii, E. Lifshitz, and J. Sykes. *Electrodynamics of Continuous Media*. COURSE OF THEORETICAL PHYSICS (Elsevier Science, 2013). (cited on p. 121)

[301] S. A. Maier. Plasmonic field enhancement and sers in the effective mode volume picture. Opt. Express **14**, 1957 (2006). (cited on p. 121)

[302] R. Ruppin. Electromagnetic energy density in a dispersive and absorptive material. Physics Letters A **299**, 309 (2002). (cited on p. 121)

[303] A. F. Koenderink. On the use of purcell factors for plasmon antennas. Opt. Lett. **35**, 4208 (2010). (cited on p. 121)

[304] E. Thiel, C. Zander, and K. Drexhage. Incoherently pumped continuous wave dye laser. Optics Communications **62**, 171 (1987). (cited on p. 122)

[305] C. Santori, D. Fattal, and Y. Yamamoto. *Single-photon Devices and Applications*. Physics textbook (John Wiley & Sons, 2010). (cited on p. 122)

[306] Z. M. Wang. *One-dimensional nanostructures*, volume 3 (Springer Science & Business Media, 2008). (cited on pages 125 and 160)

[307] G. Beadie, M. Brindza, R. A. Flynn, A. Rosenberg, and J. S. Shirk. Refractive index measurements of poly(methyl methacrylate) (pmma) from $0.4 - 1.6\mu$m. Appl. Opt. **54**, F139 (2015). (cited on p. 125)

[308] R. Kumar, A. P. Singh, A. Kapoor, and K. N. Tripathi. Fabrication and characterization of polyvinyl-alcohol-based thin-film optical waveguides. Optical Engineering **43**, 2134 (2004). (cited on p. 125)

[309] J. Jackson. *Classical electrodynamics* (Wiley, 1975). (cited on pages 125, 185, 240, and 251)

[310] Q. Li and M. Qiu. Plasmonic wave propagation in silver nanowires: guiding modes or not? Opt. Express **21**, 8587 (2013). (cited on p. 126)

[311] J. Moll, S. Daehne, J. R. Durrant, and D. A. Wiersma. Optical dynamics of excitons in j aggregates of a carbocyanine dye. The Journal of Chemical Physics **102** (1995). (cited on pages 127, 136, and 150)

[312] S. Valleau, S. K. Saikin, M.-H. Yung, and A. A. Guzik. Exciton transport in thin-film cyanine dye j-aggregates. The Journal of Chemical Physics **137**, 034109 (2012). (cited on pages 127, 136, and 150)

[313] J. Bellessa, C. Bonnand, J. C. Plenet, and J. Mugnier. Strong coupling between surface plasmons and excitons in an organic semiconductor. Phys. Rev. Lett. **93**, 036404 (2004). (cited on pages 127, 145, and 146)

[314] D. Melnikau, D. Savateeva, A. Susha, A. L. Rogach, and Y. P. Rakovich. Strong plasmon-exciton coupling in a hybrid system of gold nanostars and j-aggregates. Nanoscale Research Letters **8**, 1 (2013). (cited on p. 127)

[315] T. Schwartz, J. A. Hutchison, J. Léonard, C. Genet, S. Haacke, and T. W. Ebbesen. Polariton dynamics under strong light–molecule coupling. ChemPhysChem **14**, 125 (2013). (cited on pages 127 and 150)

[316] G. Zengin, M. Wersäll, S. Nilsson, T. J. Antosiewicz, M. Käll, and T. Shegai. Realizing strong light-matter interactions between single-nanoparticle plasmons and molecular excitons at ambient conditions. Phys. Rev. Lett. **114**, 157401 (2015). (cited on pages 127 and 146)

[317] T. Taminiau, F. Stefani, F. Segerink, and N. Van Hulst. Optical antennas direct single-molecule emission. Nature Photonics **2**, 234 (2008). (cited on pages 129, 207, and 215)

[318] L. Piatkowski, N. Accanto, and N. F. van Hulst. Ultrafast meets ultrasmall: controlling nanoantennas and molecules. ACS Photonics (2016). (cited on p. 129)

[319] M. Pelton and G. Bryant. *Introduction to Metal-Nanoparticle Plasmonics*. A Wiley-Science Wise Co-Publication (Wiley, 2013). (cited on p. 135)

[320] P. W. Anderson, D. J. Thouless, E. Abrahams, and D. S. Fisher. New method for a

scaling theory of localization. Phys. Rev. B **22**, 3519 (1980). (cited on p. 137)

[321] J. Hernando, E. M. H. P. van Dijk, J. P. Hoogenboom, J.-J. García-López, D. N. Reinhoudt, M. Crego-Calama, M. F. García-Parajó, and N. F. van Hulst. Effect of disorder on ultrafast exciton dynamics probed by single molecule spectroscopy. Phys. Rev. Lett. **97**, 216403 (2006). (cited on p. 138)

[322] A. T. Black, J. K. Thompson, and V. Vuletić. On-demand superradiant conversion of atomic spin gratings into single photons with high efficiency. Phys. Rev. Lett. **95**, 133601 (2005). (cited on p. 144)

[323] H. Tanji, S. Ghosh, J. Simon, B. Bloom, and V. Vuletić. Heralded single-magnon quantum memory for photon polarization states. Phys. Rev. Lett. **103**, 043601 (2009). (cited on p. 144)

[324] D. M. Coles, N. Somaschi, P. Michetti, C. Clark, P. G. Lagoudakis, P. G. Savvidis, and D. G. Lidzey. Polariton-mediated energy transfer between organic dyes in a strongly coupled optical microcavity. Nature materials **13**, 712 (2014). (cited on pages 144 and 178)

[325] B. Nagorny, T. Elsässer, and A. Hemmerich. Collective atomic motion in an optical lattice formed inside a high finesse cavity. Phys. Rev. Lett. **91**, 153003 (2003). (cited on p. 145)

[326] M. Albert, J. P. Marler, P. F. Herskind, A. Dantan, and M. Drewsen. Collective strong coupling between ion coulomb crystals and an optical cavity field: Theory and experiment. Phys. Rev. A **85**, 023818 (2012). (cited on p. 145)

[327] F. Brennecke, T. Donner, S. Ritter, T. Bourdel, M. Köhl, and T. Esslinger. Cavity qed with a bose–einstein condensate. Nature **450**, 268 (2007). (cited on p. 145)

[328] Y. Colombe, T. Steinmetz, G. Dubois, F. Linke, D. Hunger, and J. Reichel. Strong atom–field coupling for bose–einstein condensates in an optical cavity on a chip. Nature **450**, 272 (2007). (cited on p. 145)

[329] D. G. Lidzey, D. Bradley, M. Skolnick, T. Virgili, S. Walker, and D. Whittaker. Strong exciton–photon coupling in an organic semiconductor microcavity. Nature **395**, 53 (1998). (cited on p. 145)

[330] Y. Dubi and M. Di Ventra. *Colloquium* : Heat flow and thermoelectricity in atomic and molecular junctions. Rev. Mod. Phys. **83**, 131 (2011). (cited on p. 145)

[331] S. M. Menke, W. A. Luhman, and R. J. Holmes. Tailored exciton diffusion in organic photovoltaic cells for enhanced power conversion efficiency. Nature materials **12**, 152 (2013). (cited on pages 145 and 178)

[332] S. Hofmann, T. C. Rosenow, M. C. Gather, B. Lüssem, and K. Leo. Singlet exciton diffusion length in organic light-emitting diodes. Phys. Rev. B **85**, 245209 (2012). (cited on p. 145)

[333] G. M. Akselrod, P. B. Deotare, N. J. Thompson, J. Lee, W. A. Tisdale, M. A. Baldo, V. M. Menon, and V. Bulović. Visualization of exciton transport in ordered and disordered molecular solids. Nat. Commun. **5**, 1 (2014). (cited on p. 146)

[334] P. Törmä and W. L. Barnes. Strong coupling between surface plasmon polaritons and emitters: a review. Reports on Progress in Physics **78**, 013901 (2015). (cited on pages 146, 207, and 216)

[335] P. Andrew and W. Barnes. Energy transfer across a metal film mediated by surface plasmon polaritons. Science **306**, 1002 (2004). (cited on p. 146)

[336] J. Zhang, Y. Fu, and J. R. Lakowicz. Enhanced förster resonance energy transfer (fret) on a single metal particle. The journal of physical chemistry C **111**, 50 (2007). (cited on p. 146)

[337] D. Martín-Cano, L. Martín-Moreno, F. J. García-Vidal, and E. Moreno. Resonance energy transfer and superradiance mediated by plasmonic nanowaveguides. Nano Letters **10**, 3129 (2010). PMID: 20698627. (cited on pages 146, 180, 186, 251, and 253)

[338] A. Trügler and U. Hohenester. Strong coupling between a metallic nanoparticle and a single molecule. Phys. Rev. B **77**, 115403 (2008). (cited on p. 146)

[339] E. Waks and D. Sridharan. Cavity qed treatment of interactions between a metal nanoparticle and a dipole emitter. Phys. Rev. A **82**, 043845 (2010). (cited on pages 146 and 160)

[340] C. Van Vlack, P. T. Kristensen, and S. Hughes. Spontaneous emission spectra and quantum light-matter interactions from a strongly coupled quantum dot metal-nanoparticle system. Phys. Rev. B **85**, 075303 (2012). (cited on p. 146)

[341] J. Dintinger, S. Klein, F. Bustos, W. L. Barnes, and T. W. Ebbesen. Strong coupling between surface plasmon-polaritons and organic molecules in subwavelength hole arrays. Phys. Rev. B **71**, 035424 (2005). (cited on p. 146)

[342] Y. Sugawara, T. A. Kelf, J. J. Baumberg, M. E. Abdelsalam, and P. N. Bartlett. Strong coupling between localized plasmons and organic excitons in metal nanovoids. Phys. Rev. Lett. **97**, 266808 (2006). (cited on p. 146)

[343] N. T. Fofang, T.-H. Park, O. Neumann, N. A. Mirin, P. Nordlander, and N. J. Halas. Plexcitonic nanoparticles: Plasmon- exciton coupling in nanoshell- j-aggregate complexes. Nano letters **8**, 3481 (2008). (cited on p. 146)

[344] T. K. Hakala, J. J. Toppari, A. Kuzyk, M. Pettersson, H. Tikkanen, H. Kunttu, and P. Törmä. Vacuum rabi splitting and strong-coupling dynamics for surface-plasmon polaritons and rhodamine 6g molecules. Phys. Rev. Lett. **103**, 053602 (2009). (cited on p. 146)

[345] P. Vasa, R. Pomraenke, G. Cirmi, E. De Re, W. Wang, S. Schwieger, D. Leipold, E. Runge, G. Cerullo, and C. Lienau. Ultrafast manipulation of strong coupling in metal- molecular aggregate hybrid nanostructures. Acs Nano **4**, 7559 (2010). (cited on p. 146)

[346] T. Schwartz, J. A. Hutchison, C. Genet, and T. W. Ebbesen. Reversible switching of ultrastrong light-molecule coupling. Phys. Rev. Lett. **106**, 196405 (2011). (cited on p. 146)

[347] A. E. Schlather, N. Large, A. S. Urban, P. Nordlander, and N. J. Halas. Near-field mediated plexcitonic coupling and giant rabi splitting in individual metallic dimers. Nano letters **13**, 3281 (2013). (cited on p. 146)

[348] R. Chikkaraddy, B. de Nijs, F. Benz, S. J. Barrow, O. A. Scherman, E. Rosta, A. Demetriadou, P. Fox, O. Hess, and J. J. Baumberg. Single-molecule strong coupling at room temperature in plasmonic nanocavities. Nature (2016). (cited on pages 146, 208, and 217)

[349] S. K. Saikin, A. Eisfeld, S. Valleau, and A. Aspuru-Guzik. Photonics meets excitonics: natural and artificial molecular aggregates. Nanophotonics **2**, 21 (2013). (cited on pages 146, 208, and 217)

[350] S. Kéna-Cohen, S. A. Maier, and D. D. C. Bradley. Ultrastrongly coupled exciton–polaritons in metal-clad organic semiconductor microcavities. Advanced Optical Materials **1**, 827 (2013). (cited on p. 146)

[351] *Transmission Lines & Waveguide* (McGraw-Hill Education (India) Pvt Limited, 2010). (cited on p. 148)

[352] T. Hümmer, F. J. García-Vidal, L. Martín-Moreno, and D. Zueco. Weak and strong coupling regimes in plasmonic qed. Phys. Rev. B **87**, 115419 (2013). (cited on p. 149)

[353] E. del Valle, F. P. Laussy, F. Troiani, and C. Tejedor. Entanglement and lasing with two quantum dots in a microcavity. Phys. Rev. B **76**, 235317 (2007). (cited on p. 149)

[354] E. del Valle, F. P. Laussy, and C. Tejedor. Luminescence spectra of quantum dots in microcavities. ii. fermions. Phys. Rev. B **79**, 235326 (2009). (cited on p. 149)

[355] E. del Valle. Steady-state entanglement of two coupled qubits. J. Opt. Soc. Am. B **28**, 228 (2011). (cited on pages 149 and 171)

[356] S. Kühn, U. Håkanson, L. Rogobete, and V. Sandoghdar. Enhancement of single-molecule fluorescence using a gold nanoparticle as an optical nanoantenna. Phys. Rev. Lett. **97**, 017402 (2006). (cited on pages 149 and 191)

[357] G. Wrigge, I. Gerhardt, J. Hwang, G. Zumofen, and V. Sandoghdar. Efficient coupling of photons to a single molecule and the observation of its resonance fluorescence. Nature Physics **4**, 60 (2008). (cited on p. 149)

[358] D. Manzano, M. Tiersch, A. Asadian, and H. J. Briegel. Quantum transport efficiency and fourier's law. Phys. Rev. E **86**, 061118 (2012). (cited on p. 149)

[359] J. Johansson, P. Nation, and F. Nori. Qutip 2: A python framework for the dynamics of open quantum systems. Computer Physics Communications **184**, 1234 (2013). (cited on p. 150)

[360] S. Wang, T. Chervy, J. George, J. A. Hutchison, C. Genet, and T. W. Ebbesen. Quantum yield of polariton emission from hybrid light-matter states. The journal of physical chemistry letters **5**, 1433 (2014). (cited on p. 151)

[361] P. Anger, P. Bharadwaj, and L. Novotny. Enhancement and quenching of single-molecule fluorescence. Phys. Rev. Lett. **96**, 113002 (2006). (cited on pages 159 and 191)

[362] C. F. Bohren and D. R. Huffman. *Absorption and scattering of light by small particles* (John Wiley & Sons, 2008). (cited on p. 160)

[363] W. Zhu, R. Esteban, A. G. Borisov, J. J. Baumberg, P. Nordlander, H. J. Lezec, J. Aizpurua, and K. B. Crozier. Quantum mechanical effects in plasmonic structures with subnanometre gaps. Nature communications **7** (2016). (cited on p. 169)

[364] M. B. Plenio and S. F. Huelga. Dephasing-assisted transport: quantum networks and biomolecules. New Journal of Physics **10**, 113019 (2008). (cited on p. 177)

[365] J. M. Moix, M. Khasin, and J. Cao. Coherent quantum transport in disordered systems: I. the influence of dephasing on the transport properties and absorption spectra on one-dimensional systems. New Journal of Physics **15**, 085010 (2013). (cited on p. 177)

[366] F. C. Spano. Optical microcavities enhance the exciton coherence length and eliminate vibronic coupling in j-aggregates. The Journal of Chemical Physics **142**, 184707 (2015). (cited on p. 177)

[367] F. Herrera and F. C. Spano. Cavity-controlled chemistry in molecular ensembles. Physical Review Letters **116**, 238301 (2016). (cited on pages 177, 208, and 217)

[368] J. A. Hutchison, T. Schwartz, C. Genet, E. Devaux, and T. W. Ebbesen. Modifying chemical landscapes by coupling to vacuum fields. Angewandte Chemie International Edition **51**, 1592 (2012). (cited on p. 178)

[369] J. Galego, F. J. Garcia-Vidal, and J. Feist. Suppressing photochemical reactions with quantized light fields. arXiv preprint arXiv:1606.04684 (2016). (cited on pages 178, 208, and 217)

[370] J. A. Hutchison, A. Liscio, T. Schwartz, A. Canaguier-Durand, C. Genet, V. Palermo, P. Samorì, and T. W. Ebbesen. Tuning the work-function via strong coupling. Advanced Materials **25**, 2481 (2013). (cited on p. 178)

[371] R. Hildner, D. Brinks, and N. F. van Hulst. Femtosecond coherence and quantum control of single molecules at room temperature. Nature Physics **7**, 172 (2011). (cited on p. 178)

[372] S. Haze, Y. Tateishi, A. Noguchi, K. Toyoda, and S. Urabe. Observation of phonon hopping in radial vibrational modes of trapped ions. Phys. Rev. A **85**, 031401 (2012). (cited on p. 178)

[373] M. Ramm, T. Pruttivarasin, and H. Häffner. Energy transport in trapped ion chains. New Journal of Physics **16**, 063062 (2014). (cited on p. 178)

[374] X. Hu, Y.-x. Liu, and F. Nori. Strong coupling of a spin qubit to a superconducting stripline cavity. Phys. Rev. B **86**, 035314 (2012). (cited on p. 179)

[375] A. Huck and U. Andersen. Coupling single emitters to quantum plasmonic circuits. Nanophotonics aop (2016). (cited on p. 179)

[376] W. L. Barnes, A. Dereux, and T. W. Ebbesen. Surface plasmon subwavelength optics. Nature **424**, 824 (2003). (cited on p. 180)

[377] D. K. Gramotnev and S. I. Bozhevolnyi. Plasmonics beyond the diffraction limit. Nature photonics **4**, 83 (2010). (cited on p. 180)

[378] C. Ropp, Z. Cummins, S. Nah, J. T. Fourkas, B. Shapiro, and E. Waks. Nanoscale imaging and spontaneous emission control with a single nano-positioned quantum dot. Nature communications **4**, 1447 (2013). (cited on pages 180 and 181)

[379] R. M. Dickson and L. A. Lyon. Unidirectional plasmon propagation in metallic nanowires. The Journal of Physical Chemistry B **104**, 6095 (2000). (cited on p. 180)

[380] H. Ditlbacher, A. Hohenau, D. Wagner, U. Kreibig, M. Rogers, F. Hofer, F. R. Aussenegg, and J. R. Krenn. Silver nanowires as surface plasmon resonators. Phys. Rev. Lett. **95**, 257403 (2005). (cited on p. 180)

[381] B. Wild, L. Cao, Y. Sun, B. P. Khanal, E. R. Zubarev, S. K. Gray, N. F. Scherer, and M. Pelton. Propagation lengths and group velocities of plasmons in chemically synthesized gold and silver nanowires. ACS Nano **6**, 472 (2012). PMID: 22185403. (cited on p. 180)

[382] P. Kusar, C. Gruber, A. Hohenau, and J. R. Krenn. Measurement and reduction of damping in plasmonic nanowires. Nano Letters **12**, 661 (2012). PMID: 22268794. (cited on p. 180)

[383] Y. Fang and M. Sun. Nanoplasmonic waveguides: towards applications in integrated nanophotonic circuits. Light: Science & Applications **4**, e294 (2015). (cited on p. 180)

[384] S. I. Bozhevolnyi, V. S. Volkov, E. Devaux, J.-Y. Laluet, and T. W. Ebbesen. Channel plasmon subwavelength waveguide components including interferometers and ring resonators. Nature **440**, 508 (2006). (cited on p. 180)

[385] D. F. P. Pile and D. K. Gramotnev. Channel plasmon–polariton in a triangular groove on a metal surface. Opt. Lett. **29**, 1069 (2004). (cited on p. 180)

[386] S. P. Burgos, H. W. Lee, E. Feigenbaum, R. M. Briggs, and H. A. Atwater. Synthesis and characterization of plasmonic resonant guided wave networks. Nano Letters **14**, 3284 (2014). (cited on p. 180)

[387] E. Moreno, F. J. Garcia-Vidal, S. G. Rodrigo, L. Martin-Moreno, and S. I. Bozhevolnyi. Channel plasmon-polaritons: modal shape, dispersion, and losses. Opt. Lett. **31**, 3447

(2006). (cited on pages 180 and 187)

[388] Z. Han and S. I. Bozhevolnyi. Radiation guiding with surface plasmon polaritons. Reports on Progress in Physics **76**, 016402 (2013). (cited on p. 180)

[389] D. F. Pile and D. K. Gramotnev. Plasmonic subwavelength waveguides: next to zero losses at sharp bends. Opt. Lett. **30**, 1186 (2005). (cited on p. 180)

[390] I. P. Radko, T. Holmgaard, Z. Han, K. Pedersen, and S. I. Bozhevolnyi. Efficient channel-plasmon excitation by nano-mirrors. Applied Physics Letters **99**, 213109 (2011). (cited on pages 180, 185, and 187)

[391] C. Gruber, A. Trügler, A. Hohenau, U. Hohenester, and J. R. Krenn. Spectral modifications and polarization dependent coupling in tailored assemblies of quantum dots and plasmonic nanowires. Nano Letters **13**, 4257 (2013). (cited on p. 181)

[392] R. Kolesov, B. Grotz, G. Balasubramanian, R. J. Stöhr, A. A. Nicolet, P. R. Hemmer, F. Jelezko, and J. Wrachtrup. Wave–particle duality of single surface plasmon polaritons. Nature Physics **5**, 470 (2009). (cited on pages 181 and 202)

[393] A. Huck, S. Kumar, A. Shakoor, and U. L. Andersen. Controlled coupling of a single nitrogen-vacancy center to a silver nanowire. Phys. Rev. Lett. **106**, 096801 (2011). (cited on p. 181)

[394] W. Pfaff, A. Vos, and R. Hanson. Top-down fabrication of plasmonic nanostructures for deterministic coupling to single quantum emitters. Journal of Applied Physics **113**, 024310 (2013). (cited on p. 181)

[395] S. Kumar, A. Huck, and U. L. Andersen. Efficient coupling of a single diamond color center to propagating plasmonic gap modes. Nano Letters **13**, 1221 (2013). PMID: 23414581. (cited on pages 181 and 194)

[396] S. Kumar, N. I. Kristiansen, A. Huck, and U. L. Andersen. Generation and controlled routing of single plasmons on a chip. Nano Letters **14**, 663 (2014). PMID: 24471714. (cited on p. 181)

[397] L. Robledo, L. Childress, H. Bernien, B. Hensen, P. F. Alkemade, and R. Hanson. High-fidelity projective read-out of a solid-state spin quantum register. Nature **477**, 574 (2011). (cited on p. 181)

[398] G. D. Fuchs, A. L. Falk, V. V. Dobrovitski, and D. D. Awschalom. Spin coherence during optical excitation of a single nitrogen-vacancy center in diamond. Phys. Rev.

Lett. **108**, 157602 (2012). (cited on p. 181)

[399] E. Togan, Y. Chu, A. S. Trifonov, L. Jiang, J. Maze, L. Childress, M. V. G. Dutt, A. S. Sorensen, P. R. Hemmer, A. S. Zibrov, and M. D. Lukin. Quantum entanglement between an optical photon and a solid-state spin qubit. Nature **466**, 730 (2010). (cited on p. 181)

[400] G. de Lange, Z. H. Wang, D. Ristè, V. V. Dobrovitski, and R. Hanson. Universal dynamical decoupling of a single solid-state spin from a spin bath. Science **330**, 60 (2010). (cited on p. 181)

[401] F. A. Inam, M. D. W. Grogan, M. Rollings, T. Gaebel, J. M. Say, C. Bradac, T. A. Birks, W. J. Wadsworth, S. Castelletto, J. R. Rabeau, and M. J. Steel. Emission and nonradiative decay of nanodiamond nv centers in a low refractive index environment. ACS Nano **7**, 3833 (2013). (cited on pages 183 and 188)

[402] A. Vial, A.-S. Grimault, D. Macías, D. Barchiesi, and M. L. de la Chapelle. Improved analytical fit of gold dispersion: Application to the modeling of extinction spectra with a finite-difference time-domain method. Phys. Rev. B **71**, 085416 (2005). (cited on p. 187)

[403] J. Lakowicz. *Principles of Fluorescence Spectroscopy* (Springer US, 2007). (cited on p. 188)

[404] F. Sala and S. D'Agostino. *Handbook of Molecular Plasmonics* (CRC Press, 2013). (cited on p. 188)

[405] A. Mohtashami and A. F. Koenderink. Suitability of nanodiamond nitrogen vacancy centers for spontaneous emission control experiments. New Journal of Physics **15**, 043017 (2013). (cited on p. 188)

[406] J.-M. Jin. *The finite element method in electromagnetics* (John Wiley & Sons, 2014). (cited on p. 191)

[407] Y. Chen, T. R. Nielsen, N. Gregersen, P. Lodahl, and J. Mørk. Finite-element modeling of spontaneous emission of a quantum emitter at nanoscale proximity to plasmonic waveguides. Phys. Rev. B **81**, 125431 (2010). (cited on pages 191 and 253)

[408] H. R. Phillip and E. A. Taft. Kramers-kronig analysis of reflectance data for diamond. Phys. Rev. **136**, A1445 (1964). (cited on p. 195)

[409] E. Moreno, S. G. Rodrigo, S. I. Bozhevolnyi, L. Martín-Moreno, and F. J. García-Vidal. Guiding and focusing of electromagnetic fields with wedge plasmon polaritons. Phys.

Rev. Lett. **100**, 023901 (2008). (cited on pages 196, 197, and 253)

[410] R. H. Brown and R. Q. Twiss. Correlation between photons in two coherent beams of light. Nature **177**, 27 (1956). (cited on p. 199)

[411] Y. A. Vlasov, M. O'Boyle, H. F. Hamann, and S. J. McNab. Active control of slow light on a chip with photonic crystal waveguides. Nature **438**, 65 (2005). (cited on p. 202)

[412] J. L. O'Brien, A. Furusawa, and J. Vučković. Photonic quantum technologies. Nature Photonics **3**, 687 (2009). (cited on p. 202)

[413] A. Goban, C.-L. Hung, S.-P. Yu, J. Hood, J. Muniz, J. Lee, M. Martin, A. McClung, K. Choi, D. Chang, *et al.* Atom–light interactions in photonic crystals. Nature communications **5** (2014). (cited on p. 202)

[414] Z. Jacob and V. M. Shalaev. Plasmonics goes quantum. Science **334**, 463 (2011). (cited on p. 202)

[415] E. Altewischer, M. Van Exter, and J. Woerdman. Plasmon-assisted transmission of entangled photons. Nature **418**, 304 (2002). (cited on p. 202)

[416] S. Fasel, F. Robin, E. Moreno, D. Erni, N. Gisin, and H. Zbinden. Energy-time entanglement preservation in plasmon-assisted light transmission. Phys. Rev. Lett. **94**, 110501 (2005). (cited on p. 202)

[417] A. Huck, S. Smolka, P. Lodahl, A. S. Sørensen, A. Boltasseva, J. Janousek, and U. L. Andersen. Demonstration of quadrature-squeezed surface plasmons in a gold waveguide. Phys. Rev. Lett. **102**, 246802 (2009). (cited on p. 202)

[418] P.-O. Guimond, H. Pichler, A. Rauschenbeutel, and P. Zoller. Chiral quantum optics with v-level atoms and coherent quantum feedback. Phys. Rev. A **94**, 033829 (2016). (cited on pages 204 and 212)

[419] A. González-Tudela and D. Porras. Mesoscopic entanglement induced by spontaneous emission in solid-state quantum optics. Physical review letters **110**, 080502 (2013). (cited on pages 204 and 212)

[420] I. M. Mirza and J. C. Schotland. Multiqubit entanglement in bidirectional - chiral - waveguide qed. Phys. Rev. A **94**, 012302 (2016). (cited on pages 204 and 212)

[421] A. Javadi, I. Söllner, M. Arcari, S. L. Hansen, L. Midolo, S. Mahmoodian, G. Kiršanskė, T. Pregnolato, E. Lee, J. Song, *et al.* Single-photon non-linear optics with a quantum

dot in a waveguide. Nature communications **6** (2015). (cited on pages 205 and 213)

[422] P. Kolchin, R. F. Oulton, and X. Zhang. Nonlinear quantum optics in a waveguide: Distinct single photons strongly interacting at the single atom level. Phys. Rev. Lett. **106**, 113601 (2011). (cited on pages 205 and 213)

[423] M. Scheucher, A. Hilico, E. Will, J. Volz, and A. Rauschenbeutel. Quantum optical circulator controlled by a single chirally coupled atom. arXiv preprint arXiv:1609.02492 (2016). (cited on pages 206 and 214)

[424] P. Longo, P. Schmitteckert, and K. Busch. Few-photon transport in low-dimensional systems: Interaction-induced radiation trapping. Phys. Rev. Lett. **104**, 023602 (2010). (cited on pages 206 and 214)

[425] E. Sánchez-Burillo, D. Zueco, J. Garcia-Ripoll, and L. Martin-Moreno. Scattering in the ultrastrong regime: Nonlinear optics with one photon. Physical review letters **113**, 263604 (2014). (cited on pages 206 and 214)

[426] G. H. Lodden and R. J. Holmes. Electrical excitation of microcavity polaritons by radiative pumping from a weakly coupled organic semiconductor. Phys. Rev. B **82**, 125317 (2010). (cited on pages 207 and 215)

[427] T. W. Hughes and S. Fan. Plasmonic circuit theory for multi-resonant light funneling to a single spatial hot spot. Nano Letters (2016). (cited on pages 208 and 216)

[428] A. Shalabney, J. George, J. Hutchison, G. Pupillo, C. Genet, and T. W. Ebbesen. Coherent coupling of molecular resonators with a microcavity mode. Nature communications **6** (2015). (cited on pages 208 and 216)

[429] L. Piatkowski, J. T. Hugall, and N. F. van Hulst. Raman spectroscopy: Watching a molecule breathe. Nature Photonics **8**, 589 (2014). (cited on pages 208 and 217)

[430] T. Rudolph. Why i am optimistic about the silicon-photonic route to quantum computing. arXiv preprint arXiv:1607.08535 (2016). (cited on pages 209 and 217)

[431] M. Castro-Lopez, A. Manjavacas, J. G. de Abajo, and N. van Hulst. Propagation and localization of quantum dot emission along a gap-plasmonic transmission line. Optics express **23**, 29296 (2015). (cited on pages 210 and 218)

[432] D. A. Steck. *Quantum and Atom Optics (revision 0.10.7)* (2016). (cited on pages 239, 240, 241, 246, 247, and 248)

[433] Y. Aharonov and D. Bohm. Significance of electromagnetic potentials in the quantum theory. Phys. Rev. **115**, 485 (1959). (cited on p. 240)

[434] I. Vágó. On the interface and boundary conditions of electromagnetic fields. Periodica Polytechnica Electrical Engineering **38**, 79 (1994). (cited on p. 244)

[435] M. Göppert-Mayer. Über elementarakte mit zwei quantensprüngen. Annalen der Physik **401**, 273 (1931). (cited on p. 247)

[436] E. A. Power and S. Zienau. Coulomb gauge in non-relativistic quantum electro-dynamics and the shape of spectral lines. Philosophical Transactions of the Royal Society of London A: Mathematical, Physical and Engineering Sciences **251**, 427 (1959). (cited on p. 247)

[437] A. Y. Nikitin, F. Guinea, F. J. Garcia-Vidal, and L. Martin-Moreno. Fields radiated by a nanoemitter in a graphene sheet. Phys. Rev. B **84**, 195446 (2011). (cited on p. 251)

[438] C. A. Marocico and J. Knoester. Effect of surface-plasmon polaritons on spontaneous emission and intermolecular energy-transfer rates in multilayered geometries. Phys. Rev. A **84**, 053824 (2011). (cited on p. 251)

[439] J. Barthes, G. Colas des Francs, A. Bouhelier, J.-C. Weeber, and A. Dereux. Purcell factor for a point-like dipolar emitter coupled to a two-dimensional plasmonic waveguide. Phys. Rev. B **84**, 073403 (2011). (cited on p. 253)

[440] D. Marcuse (editor) *Theory of Dielectric Optical Waveguides (Second Edition)* (Academic Press, 1991), second edition. (cited on p. 253)

List of Figures

List of publications

Publications related to the content of this Thesis:

1. *Non-reciprocal few-photon devices based on chiral waveguide-emitter couplings.* **C Gonzalez-Ballestero**, Esteban Moreno, F. J. Garcia Vidal, and A. Gonzalez-Tudela, arXiv:1608.04928 (2016) (Accepted in Physical Review A)

2. *Uncoupled dark states can inherit polaritonic properties.* **C Gonzalez-Ballestero**, J. Feist, E. Gonzalo-Badia, Esteban Moreno, and F. J. Garcia-Vidal, Physical Review Letters 117, 156402 (2016)

3. *Chiral route to spontaneous entanglement generation.* **Carlos Gonzalez-Ballestero**, Alejandro Gonzalez-Tudela, Francisco J. Garcia-Vidal, and Esteban Moreno, Physical Review B 92, 155304 (2015).

4. *Harvesting excitons through plasmonic strong coupling.* **Carlos Gonzalez-Ballestero**, Johannes Feist, Esteban Moreno, and Francisco J. Garcia-Vidal. Physical Review B 92, 121402(R) (2015).

5. *Coupling of individual quantum emitters to channel plasmons.* Esteban Bermúdez-Ureña, **Carlos Gonzalez-Ballestero**, Michael Geiselmann, Renaud Marty, Ilya P Radko, Tobias Holmgaard, Yury Alaverdyan, Esteban Moreno, Francisco J García-Vidal, Sergey I Bozhevolnyi, and Romain Quidant, Nature Communications 6, 7783 (2015).

6. *Generation, manipulation, and detection of two-qubit entanglement in waveguide QED.* **C Gonzalez-Ballestero**, E Moreno, and FJ Garcia-Vidal, Physical Review A 89, 042328 (2014).

7. *Non-Markovian effects in waveguide-mediated entanglement.* **C Gonzalez-Ballestero**, F. J. Garcia-Vidal and Esteban Moreno, New Journal of Physics 15, 073015 (2013).